Titre: Title:	Innovative Microwave and Millimetre-Wave Components and Sub-Systems Based on Substrate Integration Technology
Auteur: Author:	Fanfan He
Date:	2011
Type:	Mémoire ou thèse / Dissertation or Thesis
Référence: Citation:	He, F. (2011). Innovative Microwave and Millimetre-Wave Components and Sub-Systems Based on Substrate Integration Technology [Thèse de doctorat, École Polytechnique de Montréal]. PolyPublie. https://publications.polymtl.ca/524/

URL de PolyPublie: PolyPublie URL:	https://publications.polymtl.ca/524/
Directeurs de recherche: Advisors:	Ke Wu
Programme: Program:	génie électrique

UNIVERSITÉ DE MONTRÉAL

INNOVATIVE MICROWAVE AND MILLIMETRE-WAVE COMPONENTS AND SUB-SYSTEMS BASED ON SUBSTRATE INTEGRATION TECHNOLOGY

FANFAN HE

DÉPARTEMENT DE GÉNIE ÉLECTRIQUE

ÉCOLE POLYTECHNIQUE DE MONTRÉAL

THÈSE PRÉSENTÉE EN VUE DE L'OBTENTION

DU DIPLÔME DE PHILOSOPHIAE DOCTOR (Ph.D.)

(GÉNIE ÉLECTRIQUE)

MARS 2011

UNIVERSITÉ DE MONTRÉAL

ÉCOLE POLYTECHNIQUE DE MONTRÉAL

Cette thèse intitulée:

INNOVATIVE MICROWAVE AND MILLIMETRE-WAVE COMPONENTS AND SUB-SYSTEMS BASED ON SUBSTRATE INTEGRATION TECHNOLOGY

présentée par : Fanfan He

en vue de l'obtention du diplôme de : Philosophiae Doctor

a été dûment acceptée par le jury d'examen constitué de :

M. Laurin, Jean-Jacques, Ph. D, président

M. Wu, Ke, Ph. D, membre et directeur de recherche

M. Caloz, Christophe, Ph. D, membre

M. Sebak, Razik, Abdel, Ph. D, membre externe

DEDICATION

To my parents,

To my wife Sixu Mao

To my daughter Jennifer Meiyan He

ACKNOWLEDGMENT

First of all, I would like to express my gratitude to my Ph.D. advisors, Prof. Ke Wu and Prof. Hong Wei, who offered me support whenever I needed it. Their passion for research, their persistence, and their innovative ideas gave me the drive and the motivation to explore new frontiers and to accomplish this thesis.

I would also like to thank all the personnel at the Poly-Grames Research Center when I studied in Canada, in particular Mr. Jules Gauthier and Mr. Steve Dubé, whose technical assistance was essential for the realization of the prototypes. A special thank is extended to Mrs. Ginette Desparois and Mrs. Nathalie Lévesque for guiding me through the administration and to Mr. Jean-Sébastien Décarie for assistance with computer trouble.

I would also like to thank all the personnel at the millimetre-wave key lab in Southeast University when I studied in China. A special thank is extended to Mrs. Zhang, Mrs. Li and Mr. Huo for supporting a good working environment.

I am also indebted to my student colleagues and friends for all the professional and personal advice, and to everybody who contributed directly or indirectly to this thesis.

A special thank goes to the members of the examination jury, who took their time to read the thesis and provided very valuable comments.

Finally, I would like to extend my gratitude to my parents and my wife, who supported my decision to study for the Ph.D. degree.

RÉSUMÉ

Avec le rapide développement des technologies microondes et millimétriques, les spécifications de conception des circuits et systèmes sont de plus en plus exigeantes. La tendance pour le développement des systèmes de communication se dirige vers un poids minimisé, une taille réduite, de multiples fonctions, une fiabilité accrue et un faible coût. Ainsi, des technologies microondes et millimétriques faibles coûts, performantes et convenant à une production de masse sont critiques pour développer avec succès des systèmes commerciaux. La technologie à guide d'ondes rectangulaire a toujours été parmi les plus populaires pour la fabrication des systèmes millimétriques. Cependant, une difficulté majeure est reliée à leur intégration avec des composants actifs et les autres types de lignes de transmission conventionnelles, telle que microruban ou coplanaire… Les technologies de Circuits Intégrés au Substrat (CISs), incluant la technologie Guide Intégré au Substrat (GIS), qui peut être intégrée dans les substrats diélectriques avec de faibles pertes d'insertion et de radiation, sont une famille de nouvelles structures à ondes guidées. Ces dernières permettent de faire un pont entre les structures planaires et non-planaires. Jusqu'à maintenant, les composants et les sous-systèmes micro-ondes basés sur la technologie GIS ont été largement étudiés et développés.

Dans cette thèse, nous étudions d'avantage la technologie GIS afin de proposer et développer divers composants actif et passif micro-ondes et millimétriques innovant et originaux. Ces structures de composants innovants peuvent améliorer l'intégration entre les composants GIS et les autres composants planaires. Ainsi, un certain nombre de structures et composants sont proposés et appliqués dans la conception et la démonstration d'un réseau d'antennes intégré en ondes millimétriques et un sous-système d'antennes intelligentes à 60 GHz. Il est à noter que plusieurs composants étudiés dans ce travail ont été proposés et démontrés à des fréquences micro-ondes plus basses afin de faire une preuve de concept en permettant une fabrication facile des structures et des circuits. Ces circuits en basses fréquences peuvent facilement être adaptés pour des applications aux fréquences plus hautes.

Dans le chapitre 1, trois composants passifs incluant un T-magique, un filtre large bande et une antenne large bande sont étudiés et développés. Premièrement, nous proposons une transition de ligne à fentes à GIS, qui a permis le développement d'une jonction en « T » et d'un T-magique. Tous ont été simulés, conçus, fabriqués et mesurés dans la bande X. Ensuite, nous avons utilisé à

notre avantage les caractéristiques passe-haut d'une ligne GIS à Demi Mode (GISDM) pour réaliser un filtre à bande très large en cascadant une section de ligne GISDM avec un filtre microstrip passe-bas. Une autre application large bande du concept des CISs est une antenne de type ALTSA alimentée par un guide d'onde à plaque parallèle.

Dans le chapitre 2, nous avons mis à profit les technologies CISs dans la conception d'oscillateurs contrôlables par tension (VCO, pour Voltage Controlled Oscillator), amplificateurs de puissance et mélangeurs. Les résonateurs ajustables proposés réalisent non seulement une fonction d'ajustement en fréquence en contrôlant une tension DC polarisant une diode, mais maintient un facteur de qualité inhérent élevé des cavités résonantes GIS et GISDM. Un VCO en bande X basé sur une cavité résonante réflective GIS a été développé et réalisé. À part des oscillateurs, la technologie GIS peut aussi être appliquée à la conception d'amplificateur de puissance. Un amplificateur multi-section GIS est investigué, et les résultats montrent que les harmoniques peuvent être supprimées. Les mélangeurs sont une autre application importante de la technologie GIS. Comme démonstration directe, un mélangeur en bande X utilisant notre « T-magique » est conçu. De bonnes performances ont été obtenues en mesure.

Dans le chapitre 3, trois sortes de réseaux d'antennes actifs intégrés sont développés basés sur l'antenne ALTSA GIS. Premièrement, un amplificateur de puissance spatial en bande X présentant et réalisé. Deuxièmement, un réseau d'antennes élévateur 2x2 en bande Ka, pouvant être vue comme un transmetteur faible coût pour les courtes distances de communication, est présenté. Enfin, un réseau rectenna (pour rectifier antenna) 1x4 en bande Ka est introduit. Il peut être utilisé afin de convertir la puissance RF en puissance DC pour la transmission de puissance microonde pour les futurs satellites de collecte d'énergie solaire, les stations spatiales ou le recyclage d'énergie RF dans les environnements électromagnétiques présents.

Enfin dans le dernier chapitre, une autre application majeure est le développement d'un sous-système récepteur à faisceau contrôlé à 60 GHz basé sur les résultats de recherche de la technologie GIS. C'est la première réalisation d'un récepteur à faisceau variable employant un front-end à 60 GHz conçu à partir de la technologie GIS. Ce récepteur utilise une matrice de Butler 4x4 en technologie GIS et une antenne GIS. Pour diminuer le coût du sous-système, une source LO GIS à 30 GHz et un mélangeur abaisseur de fréquence GIS sont développés. Les signaux IF obtenus sont traités dans la chaine IF et un DSP extrait les signaux de contrôle. Le

faisceau du sous-système est contrôlé de façon adaptative par le signal de contrôle afin d'obtenir le maximum de puissance en réception.

ABSTRACT

The tendency of modern microwave and millimetre-wave communication system development is towards small size, light weight, reliable, multifunctional and low-cost. Moreover, low-cost, mass producible, high-performance and high-yield microwave and millimetre wave technologies are crucial for developing successful commercial microwave and millimetre wave systems. Rectangular waveguide has always been among the most popular choices for the making of millimetre-wave circuits and systems. A major challenge, however, is related to its integration with active devices and other conventional planar transmission lines, such as microstrip or coplanar waveguide (CPW), etc. Substrate Integrated Circuits (SICs) techniques including substrate integrated waveguide (SIW), which can be integrated in planar dielectric substrate with low insertion loss, high Q and low radiation loss, present a family of novel guided wave structures. This scheme provides a bridge between planar and non-planar structures. Up to now, microwave components and sub-systems based on SIW technology have been widely studied and developed.

In this thesis, we take a further study of SIW technology to propose and develop various innovative and original microwave and millimetre-wave passive and active components. These innovative component structures can improve the integration between SIW components and other planar components. Then, a certain number of proposed structures or components are applied in the design and demonstration of millimetre-wave integrated antenna arrays and 60 GHz smart antenna sub-system. Note that many components studied in this work were proposed and demonstrated at different lower microwave frequencies for the proof of concept purpose with easy-to-fabricate structures and circuits. Those low-frequency circuits can easily be scaled up for high-frequency applications.

In Chapter 1, three passive components such as magic-T, wideband filter and antenna are studied and developed. First, we propose a slotline-to-SIW transition which is investigated, leading to the development of 180^0 reverse-phase T-junction and planar magic-Ts. Next, we take the advantage of high-pass characteristics of the half-mode substrate integrated waveguide (HMSIW) to realize a super wideband band-pass filter by cascading a section of HMSIW with a microstrip low-pass filter. Another wideband application of SICs concept is related to an antipodal linearly tapered

slot antenna (ALSTA) structure fed by a substrate parallel plate waveguide as TEM mode transmission line.

In Chapter 2, we make use of SICs techniques in the design of PA, mixer and voltage controlled oscillator (VCO). First of all, planar tunable reflective SIW and HMSIW cavity resonators are developed. An X-band low phase noise VCO based on SIW tunable reflective cavity resonator has been developed and realized. Besides oscillator applications, SIW can also be applied to PA design. A multi-section SIW is investigated, and results show that any harmonics could be suppressed. As a practical and straightforward demonstration, an X-band singly balanced mixer using our proposed modified magic-T is designed and measured with good performances.

In Chapter 3, three kinds of integrated active antenna array are developed based on the SIW ALTSA in the work. First, an X-band spatial power amplifier is proposed and realized. Second, a Ka-band 2×2 up-converter antenna array which can be seen as a low-cost transmitter for millimetre-wave short distance communications. Finally, a Ka-band 1×4 rectenna array is introduced.

In the thesis, another major application of SICs as described in Chapter 4 is to develop a 60 GHz switched-beam receiver sub-system based on the above-discussed research results of the SIW technology. This is the first time to realize and demonstrate a 60 GHz beamforming receiver system employing 60 GHz front-end mainly using the SIW technology. This receiver makes use of an SIW 4×4 Butler matrix network and an SIW antenna to construct the sub-system. To decrease the cost of the sub-system, 30 GHz SIW LO sources and SIW sub-harmonically down-converter mixers are developed. As a result, IF signals obtained in the chain are processed within IF circuitry and a DSP core to extract controlled signals. Consequently, beam of the sub-system is adaptively switched by the controlled signals according to the criterion of maximum received signal. The thesis will be finally concluded with various remarks in connection with key concepts and original contributions presented in this work as well as discussions on future research and development on this SICs topic.

TABLE OF CONTENTS

LIST OF TABLE

LIST OF FIGURES

LIST OF ACRONYMS AND ABBREVIATIONS

2-D	Two-Dimensional
3-D	Three-Dimensional
ADC	Analog-to-Digital Converter,
ADS	Advanced Design System
AIA	Active Integrated Antenna
ALSTA	Antipodal Linearly Tapered Slot Antenna
AM	Amplitude Modulation
ARM	Advanced RISC Machine
CAD	Computer Aided Design
CBCPW	Conductor-Backed Co-Planar Waveguide.
CPW	Coplanar Waveguide
CST-MWS	Microwave Studio® (Computer Simulation Technology)
CTL	Control Track Longitudinal
DC	Direct Current
DRLA	Dual-Rhombic-Loop Traveling-Wave Rectifying Antenna
DSP	Digital Signal Processor
EBG	Electromagnetic Band Gap
EIRP	Equivalent Isotropic Radiated Power
FET	Field-Effect Transistor
FHMSIW	Folded Half Mode Substrate Integrated Waveguide
FOM	Figure of Merit
FSIW	Folded Substrate Integrated Waveguide
HB	Harmonic Balance

HFSS	High Frequency Structure Simulator
HMSIW	Half Mode Substrate Integrated Waveguide
IF	Intermediate Frequency
IM3	Third-order Intermodulation
IML	Inverted Microstrip Line
IMPATT	IMPact ionization Avalanche Transit-Time
IP3	Third-order Intercept Point
LNA	Low Noise Amplifier
LO	Local Oscillator
MEMS	Micro Electro Mechanical systems
MICs	Microwave Integrated Circuits
MMICs	Microwave Monolithic Integrated Circuits
MPT	Microwave Power Transmission
MW	Magnetic Wall
PA	Power Amplifier
PAE	Power Added Efficiency
PCB	Printed Circuits Board
pHEMT	Pseudomorphic High Electron Mobility Transistor
RF	Radio Frequency
SIC	Substrate Integrated Circuits
SINRD	Substrate Integrated Non-Radiative Dielectric Guide
SIIG	Substrate Integrated Image Guide
SIW	Substrate Integrated Waveguide
TE	Transverse Electric

TEM	Transverse Electric Magnetic
TM	Transverse Magnetic
TSA	Tapered Slot Antenna
TTL	Transistor–Transistor Logic
VCO	Voltage Controlled Oscillator
VNA	Vector Network Analyzer
WPAN	Wireless Personal Area Network Communication Technologies

INTRODUCTION

Following the rapid development of modern microwave technology, design specifications of microwave and millimetre-wave circuits and systems become more and more demanding. The development tendency of modern microwave and millimetre-wave communication systems is towards small size, low weight, reliable, multifunctional, low cost etc. Low-cost, mass-producible, high-performance and high-yield microwave and millimetre-wave technologies are crucial for developing successful commercial microwave and millimetre-wave broadband systems. Over the millimetre-wave frequency bands, in particular, circuit-building blocks including antenna elements are closely related to each other via electromagnetic coupling and interconnect. In this case, the circuit design should be made with a system consideration. The classical waveguide technology is still the main stream for designing high-performance millimetre-wave systems. However, this matured scheme is not suitable for low cost mass production. Tedious and expensive post-fabrication tuning and mechanical assembling become a real problem for manufacturers. In addition, the waveguide technique cannot be used to reduce the weight and volume. On the other hand, challenging problems are often encountered in the design of low loss ICs, e.g., high Q resonator for VCO, band-pass filter and diplexers, to which the planar technique is fundamentally limited in performance. As such, non-planar structures such as the classical metallic waveguide are usually needed, thus hybrid schemes of planar and non-planar structures become attractive. In fact, an easy-to-handle low cost hybrid design strategy is of critical importance for the development of high-volume millimetre-wave ICs and systems. Hence, it is necessary to develop novel microwave and millimetre-wave integrated techniques.

In order to solve the mentioned problems, the substrate should not only serve as support for hybrid circuits, it should also be the medium out of which three-dimensional waveguides are formed. This technology was named as “Substrate Integrated Circuits” (SICs), a combination of various planar and synthesized non-planar waveguides in planar form, which complement one another in their favourable properties [1]. The most popular and widely used one of such waveguide structures is the Substrate Integrated Waveguide (SIW), an embedded version of the dielectric filled metallic rectangular waveguide [2]-[6]. Other SIW-like guided wave structures are Substrate Integrated Non-Radiative Dielectric Guide (SINRD) [7], Substrate Integrated Image

Guide (SIIG) [8], half-mode SIW (HMSIW) [9]-[15], folded HMSIW (FHMSIW) [16], and folded SIW (FSIW) [17][18], ridge SIW [19] etc. This research work is mainly focused on novel components and sub-system based on SIW technology.

The SIW technique which can be integrated in dielectric substrate with low insert loss and low radiation loss presents a guided-wave structure developed in recent years. Using this technique, passive components and active devices can be efficiently integrated together, and then the size of microwave and millimetre-wave systems is effectively reduced and the whole system can be fabricated in the same PCB or package. Thus, the cost of such systems is effectively cut down. Since the propagation properties in SIW are similar to those in conventional rectangular waveguide, the millimetre-wave and sub-millimetre wave SIW components and sub-systems possess similar merits such as high-Q, high power capability and easy integration etc. Additionally, since SIW components are totally constructed by metallic vias or discrete metallic posts in the dielectric substrate, these components can be fabricated using printed circuits board (PCB), low temperature co-fired ceramic (LTCC) process or even thin film process and integrated with other planar microwave circuits and chips without expensive assembling. Compared to the fabrication cost of traditional waveguide microwave and millimetre wave components, the cost of SIW components which does not need tedious post-fabrication tuning is very low, and they are very suitable for the design and mass-production of microwave and millimetre wave integrated circuits.

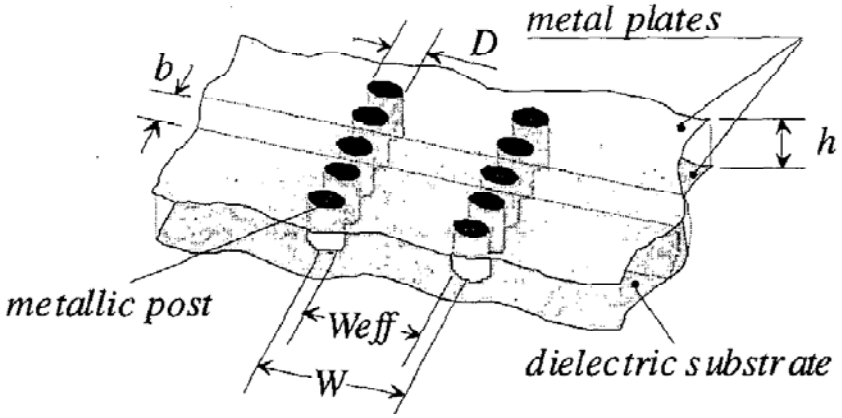

Figure 1: Topology of an SIW guide realized on a dielectric substrate

The rectangular waveguide is synthesized by placing two rows of metalized hole in the substrate as illustrated in Figure 1. Diameter *D* of the holes, spacing *b* between the holes and spacing *W* between the two rows of metallic vias are physical parameters necessary for the design of the guide. Period *b* must be kept small to reduce potential leakage loss between adjacent vias. However, via diameter *D* is also subject to the loss problem. As a result, ratio *D/b* is considered to be more critical than the period length because the via's diameter and the period length are interrelated to each other. Due to the synthesis, the SIW can no longer be regarded as a normal homogeneous waveguide, and it is in fact an artificial periodic waveguide. Therefore, the via diameter may significantly affect the return loss of the waveguide section in view of its input port. Two rules have been deducted of different SIW geometries [8]:

$$\begin{aligned} D &< \lambda_g / 5 \\ b &\le 2D \end{aligned} \tag{1.1}$$

Propagation properties of the TE_{10}-like mode in SIW are very similar to the TE_{10} mode of a rectangular waveguide. As a result, the SIW can be designed by using the following equations [20]:

$$W_{eff} = W - \frac{D^2}{0.95b} \tag{1.2}$$

Equation (1.2) is valid for $b < \lambda_0 \times \sqrt{\varepsilon_r}/2$ and $b < 4D$, where *D* is the diameter of the metallic holes. Note that because of the small thickness of the dielectric substrate, only modes with no field variation along this vertical direction take place in the frequency band of interest.

In this thesis, we take a further study of SIW technology to propose and develop various original and innovative microwave and millimetre-wave passive and active components based pm SICs technology, and then apply a part of proposed components to design millimetre-wave integrated antenna arrays and 60 GHz smart antenna sub-system. The other proposed components are proposed and demonstrated at lower microwave frequency as innovative and original concepts. They could be scaled to millimetre-wave frequency band for other millimetre-wave systems.

Chapter 1 presents novel passive components including planar magic-T, wide-band filter and wideband ALTSA. Chapter 2 focuses on applying SIW technology to active components that include oscillators, PA and mixer. Chapter 3 provides three kinds of active antenna array for

power combining. Chapter 4 then presents a 60 GHz beamforming receiver sub-system employing some of the above-proposed structures and other SIW components. Finally, the last chapter concludes the thesis by highlighting and summarizing the key concepts and contributions developed in this work as well as the future work in connection with this research project.

CHAPTER 1 MICROWAVE AND MILLIMETRE-WAVE SUBSTRATE INTEGRATED PASSIVE COMPONENTS DESIGN

This chapter presents some novel passive components employing the SICs concept. The main works are focused on three parts including magic-T, wide-band filter and wide-band antenna. In section 1.1, a slotline-to-SIW transition, an 180^0 phase-reverse slotline-to-SIW T-junction and two types of magic-T are presented separately. Section 1.2 describes how to take the advantage of the high-pass characteristic of HMSIW to easily realize a super wideband band-pass filter by cascading a section of HMSIW and a microstrip low-pass filter. In the end, an ALSTA structure fed by a substrate parallel plate waveguide is shown in section 1.3.

1.1 Planar Magic-T using SIC Concept

1.1.1 Review of Magic-T

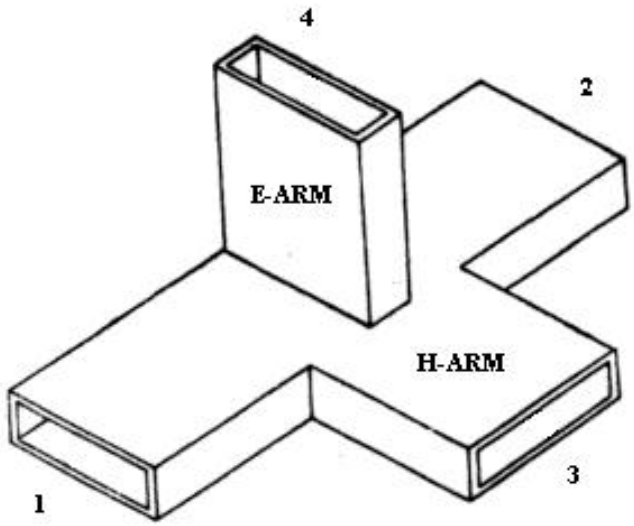

Figure 1.1: Configuration of rectangular waveguide magic-T

A magic T (hybrid-T) is a hybrid or 3dB coupler which plays a very important role in the design of a large number of microwave circuits such as multiplexers, power dividers, couplers, shifters, band-stop filters, mixers, power combiner, antenna array, etc [21]. The magic-T was originally

developed in World-War II, and first published by W. A. Tyrell (of Bell Labs) in 1947 [2]. Robert L. Kyhl and Bob Dicke independently created magic-Ts around the same period of time.

The magic-T is a combination of E and H plane tees as shown in Figure 1.1. Arms 1 and 2 are sometimes called the side or collinear arms. Port 3 is called the H-plane port, and is also called the Σ port, sum port or the P-port (for Parallel). Port 4 is the E-plane port, and is also called the Δ port, difference port, or S-port (for Series). To function correctly, the magic-T must incorporate an internal matching structure. This structure typically consists of a post inside the H-plane tee and an inductive iris inside the E-plane limb. Thus, the dependence on the matching structure means that the magic tee will only work over a limited frequency band. The name magic-T is derived from the way in which power is divided among various ports. A signal injected into the H-plane port will be divided equally between ports 1 and 2, and will be in phase. A signal injected into the E-plane port will also be divided equally between ports 1 and 2, but subject to 180 degrees out of phase. If signals are fed in through ports 1 and 2, they are added at the H-plane port and subtracted at the E-plane port [22]. Thus, with the ports numbered as shown, and within a phase factor, the full scattering matrix for an ideal magic-T is

$$[S]=\frac{1}{\sqrt{2}}\begin{bmatrix}0 & 1 & 1 & 0\\ 1 & 0 & 0 & -1\\ 1 & 0 & 0 & 1\\ 0 & -1 & 1 & 0\end{bmatrix} \tag{1.1}$$

With the increasing complexity of microwave systems, high-density interconnects in microwave integrated circuits (MICs) and microwave monolithic integrated circuits (MMICs) are required [23]. More and more integrated planar magic-Ts have been proposed with different techniques. In 1964, Kraker proposed a magic-T [24] which is constructed with an asymmetric coupled transmission line directional coupler and Shiffman's phase-shift network. Another type of MIC magic-T was proposed by de Ronde in 1970 [25], using a combination of microstrip and slot lines. Thereafter, CPW or microstrip to slot line mode conversion techniques [26]-[29] are widely incorporated in magic-T to produce a broadband out-of-phase power combiner or divider such that the slotline transmission becomes the main part of these magic-Ts. Since a slotline has less field confinement than a microstrip or a CPW, slotline radiation can cause high insertion loss in these magic-Ts. In addition, the magic-T constructed from CPW transmission lines requires the

bonding process for air bridges which increases fabrication complexity. Although aperture-coupled magic-Ts [30] have a small slot area, they require three metal layers. Another type of MIC magic-T was proposed in a multilayer configuration [31]-[32]. This type of magic-T makes use of back-to-back microstrip lines coupled through aperture in the common ground plane. Due to the electrically short slot used, the operating bandwidth tends to be narrow.

Following intensive investigations of SIW components and systems in the past ten years, more and more attentions are being paid to integrate the conventional magic-T based on SIW technology. Some SIW-based magic-T structures have been proposed and studied [33-34]. In [33-34], magic-T design techniques were developed using multilayer Low-Temperature Co-Fired Ceramics (LTCC) or PCB processes. However, planar SIW magic-T has not been developed so far. In this thesis work, our goal is therefore to develop planar magic-T using SIW technology.

Described in section 1.2.2 are the simulation, design and experiments of the proposed slotline-to-SIW transition. In section 1.2.3, the analysis and discussions of the proposed 180^0 phase-reverse slotline-to-SIW T-junction with its simulated and measured results are introduced. In section 1.2.4 and 1.2.5, a magic-T and a modified magic-T are proposed and measured, separately. All the structures in this section are simulated with the full-wave computer aided design (CAD) software Ansoft high frequency structure simulator (HFSS) and designed on Rogers/duroid 6010 substrate with a dielectric constant of 10.2 and a thickness of 0.635 mm. In slotline circuits design, high permittivity substrate is a good choice to avoid the big radiation loss.

1.1.2 Slotline-to-SIW Transition

The transitions from SIW to other planar structures [35]-[36] have been investigated theoretically and experimentally. Nevertheless, direct slotline-to-SIW transition, which is very important part for magic-T, has not been reported so far. So we firstly proposed a slotline-to-SIW transition.

Figure 1.2(a) depicts the physical configuration of the proposed slotline-to-SIW transition, where D and S are the diameter and period of metallic vias, and W_{SIW} stands for the SIW width that determines its cut-off frequency and thus the working frequency range of TE_{10} mode, W_S is the slotline width designed for 50 Ω characteristic impedance. The slotline and SIW are set up to cross with each other at a right angle where the slotline extends one quarter-wavelength into the metallic cover of the SIW with a short-circuited termination. The distance between the end of

SIW and slotline is one half-wavelength of half mode substrate integrated waveguide (HMSIW). λ_{gHMSIW} is the guided wavelength of HMSIW as described in [37]-[39]. Two via posts with the diameter of D_2 are used to optimize the return loss of the transition. When slotline extends into SIW, metallic vias around slot is removed because these vias will suppress slot mode at the plane B-B'. Figure 1.2(b) shows the direction of electric field plotted in the cross section at the B-B' plane. The electric field of the slotline is horizontally-polarized. When the signal is transmitted from slotline into the SIW at the B-B' plane, the horizontally-polarized electric field of the slotline is converted to the vertically-polarized field of the HMSIW because of overlapped metallic covers on the top and bottom of the SIW. Moreover, electric fields at both sides of the slotline in the SIW have a reversed phase. Figure 1.2(c) shows the equivalent transmission line model of the slotline-to-SIW transition. The model is similar to that of the λ/4 slotline-to-microstrip transition.

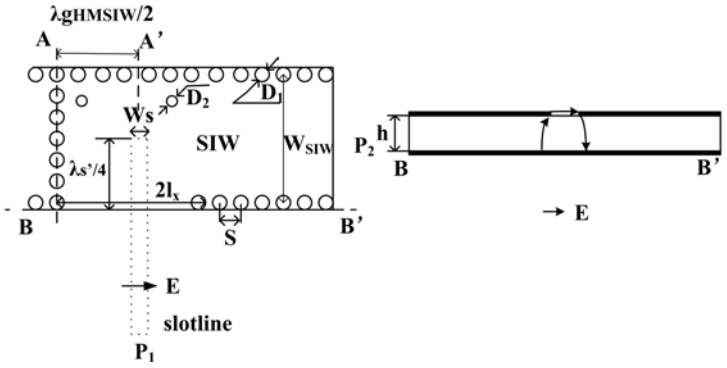

(a) (b)

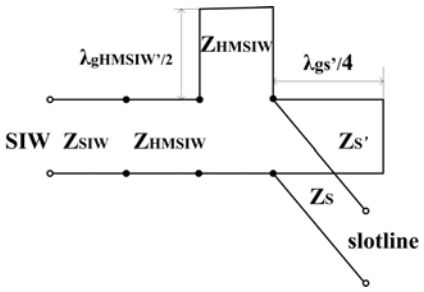

(c)

Figure 1.2 (a) Physical description and parameters of the slotline-to-SIW transition. (b) Cross section at the B-B' plane (c) Equivalent transmission line model of the slotline-to-SIW transition

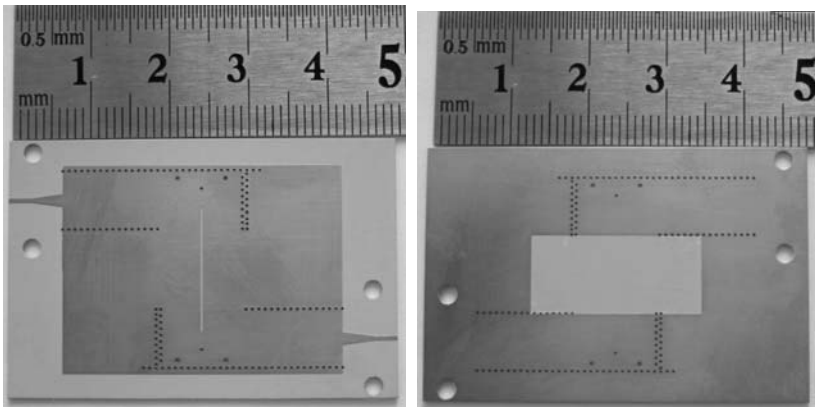

Figure 1.3: Photograph of the back-to-back transition

Figure 1.3 shows the top view and bottom view of a back-to-back transition photograph. Simulated and measured results of the back-to-back transition are shown in Figure 1.4. It is found that the insertion loss is less than 1 dB from 8.7 to 9.0 GHz. Measured return loss is less than -15 dB from 8.75 to 9 GHz.

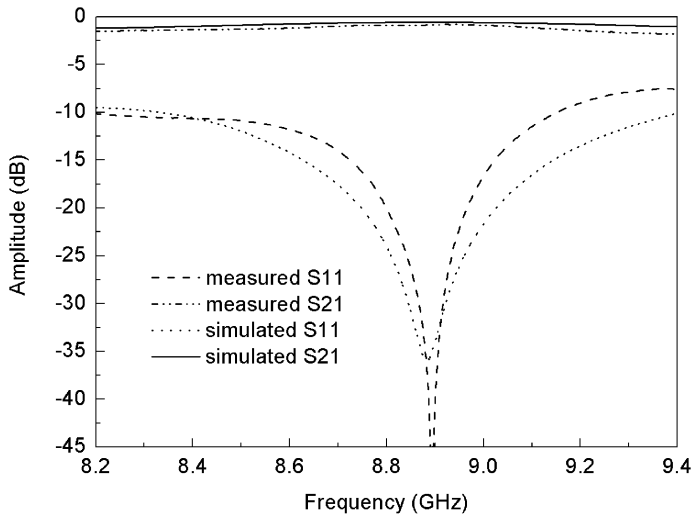

Figure 1.4: Simulated and measured insertion and return losses of the proposed slotline-to-SIW transition

1.1.3 Slotline-to-SIW Reverse-phase T Junction

In this section, we describe the slotline-to-SIW T-junction that acts as a mode converter between slotline and SIW. Figure 1.5 depicts the physical 3D configuration of the slotline-to-SIW T-

junction, where W_S is the width of metallic slot as the SIW metallic wall, W_{SIW} is the SIW width, and W_{SLOT} is the slotline width. The gray and dark coloured layers are the top metal cover and bottom metal cover, respectively. The light gray area stands for substrate. The slotline and SIW structures intersect with each other in which the slotline extends length L_g into the metallic cover of the SIW with a short-circuited termination. Two via posts with the diameter of D are used to optimize the return loss of the T-junction. Figure 1.6 shows the cross section at the A-A' plane, where the orientation of electric fields is sketched. Slotline is excited by slotline-to-microstrip line transition for measurement. When the signal is coupled from the slotline into the SIW at the A-A' plane, the electric fields of the slotline mode are converted to those of HMSIW because of overlapped metallic covers on the top and bottom of the SIW. The mode conversion process of the T junction is similar to that of the slotling-to-SIW transition. As such, two phase-reverse waves come out of ports P2 and P3.

Figure 1.7 shows the equivalent circuit model of the T-junction. The model is similar to that of an E-plane waveguide T-junction due to their similar electric field conversion. Y_S and Y_H are the characteristic admittances of the slotline and HMSIW, respectively. In the equivalent circuit, Y_H is used instead of the SIW characteristic admittance because both of them have almost the same value. Based on the above principle, parameters jB_d, jB_c and jB_b are mainly dependent on slotline's length L_g, width W_{SLOT} and L_X at the slotline port (port 1) and jB_a mainly depends on the SIW width $W_{SIW.}$ Therefore, the relationship between parameters of the equivalent circuit and return loss at port 1 is replaced by that between parameters of physical configuration and return loss at port 1. In order to minimize any potential radiation loss while transmitting signal from the slotline to the SIW, a possible minimum width of the slot line is chosen as W_{SLOT}=0.2 mm. All parameters are W_{SLOT}=0.2 mm, W_{SIW}=7.3 mm, D=0.6 mm, L_X = 4.6mm, L_g =4 mm and W_D=8 mm.

Figure 1.8 shows simulated and measured frequency responses of power dividing and return loss of the 180^0 phase-reversal slotline-to-SIW T-junction. The imbalance in amplitude and phase are respectively 0.3 dB and 3^o as shown in Figure 1.9. These results suggest that the junction have broadband characteristics. Figure 1.10 gives the photograph of the T-junction.

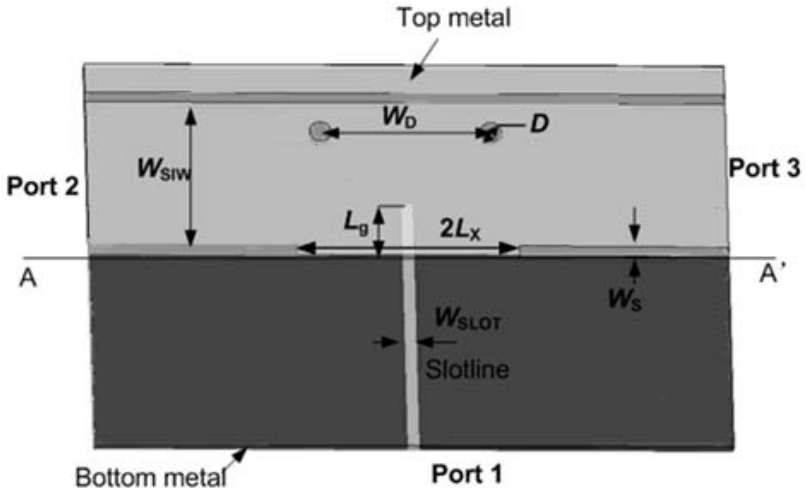

Figure 1.5: Physical description and parameters of the slotline-to-SIW T-junction

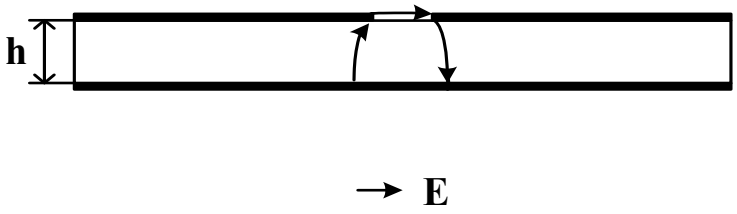

Figure 1.6: Electric field distributions at cross section A-A' plane

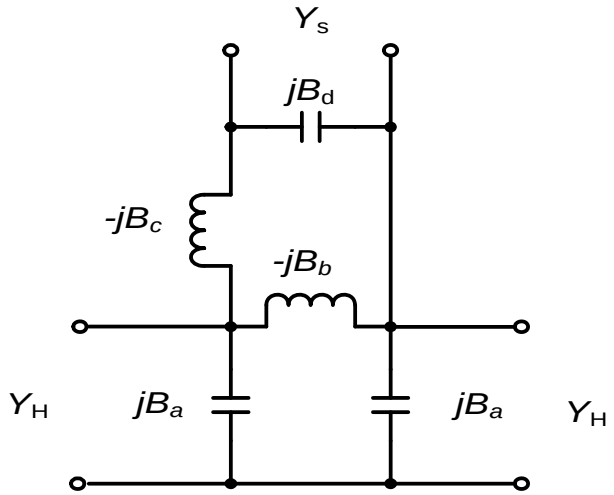

Figure 1.7: Equivalent circuits for the slotline-to-SIW T-junction

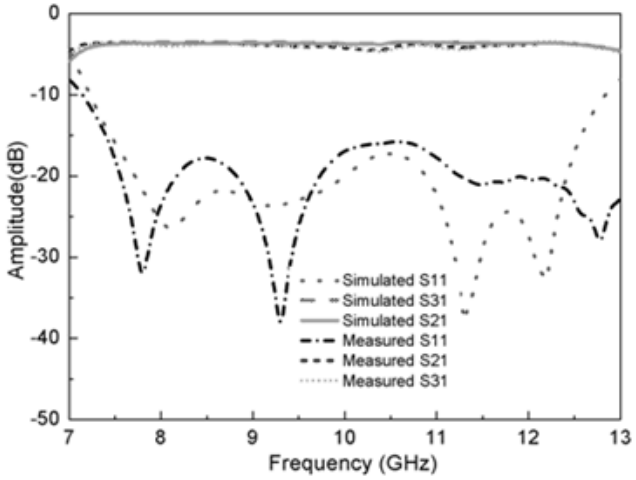

Figure 1.8: Simulated and measured frequency responses of power dividing and return loss for the180^0 slotline-to-SIW T-junction

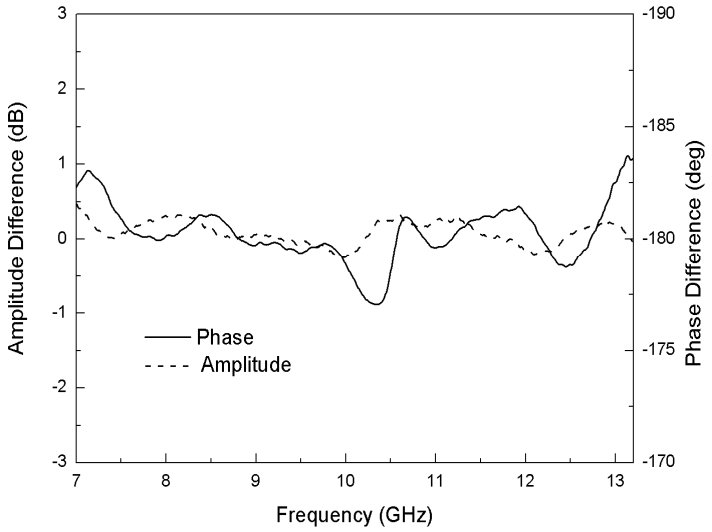

Figure 1.9: Measured amplitude and phase imbalances of the slotline-to-SIW T-junction

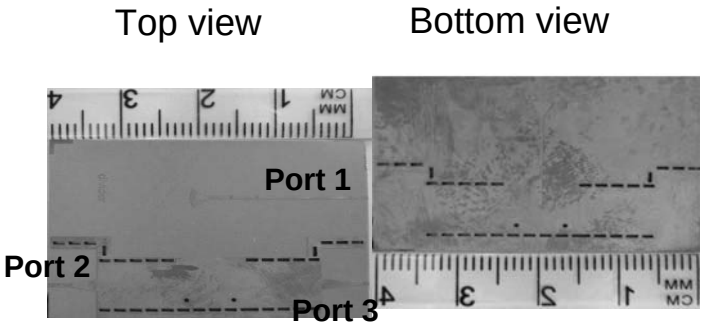

Figure 1.10: Photograph of the slotline-to-SIW T-junction

1.1.4 Planar SIW Magic-T

Figure 1.11 and Figure 1.12 describe the physical configuration and photograph of the proposed magic-T. This magic-T consists of an SIW T-junction, a slotline T-junction and two phase-reverse slotline-to-SIW T-junctions. Ports 1 and 4 present the sum and difference ports respectively, while ports 2 and 3 are the power dividing arms. When a signal is imposed on port 1, the symmetry plane A-B becomes a virtual magnetic wall and the input signal is then split into two in-phase components at ports 2 and 3 while port 4 is isolated where $L_S=\lambda_{slot}/2$. Contrarily, the plane A-B becomes a virtual electric wall when a signal is imposed on port 4. The input signal is split into two equal and out-of-phase signals at ports 2 and 3, and port 1 is isolated in this case where $L_W=\lambda_{gHMSIW}/2+n\times\lambda_{SIW}/2,(n=1,2,3,\ldots)$. The extra via posts are also used to optimize the return loss of SIW T-junction and slotline-to-SIW transition proposed in section 1.1.2.

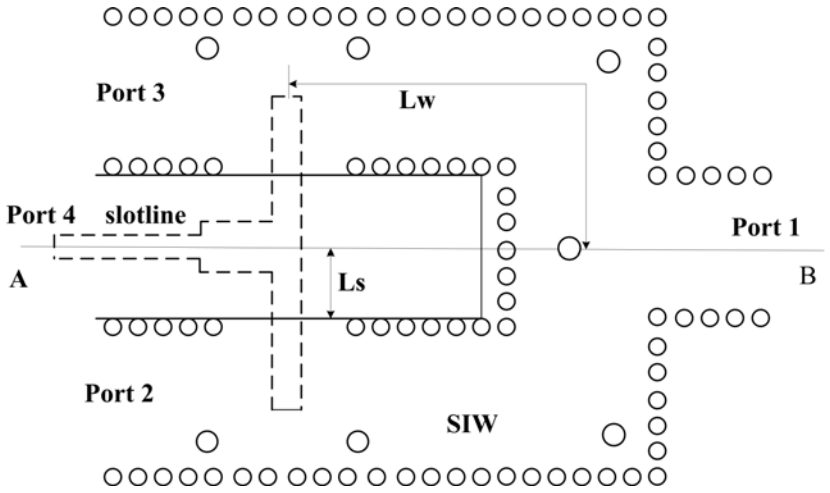

Figure 1.11: Physical configuration of the proposed magic-T. L_S=5.15mm and L_W=23.45mm

The magic-T is designed at center frequency of 8.9 GHz. Figure 1.13 (a) and (b) depict simulated and measured frequency responses of the insertion loss for in-phase and out-of-phase cases, respectively. In the in-phase case, the insertion loss is less than 0.6 dB at 8.9 GHz. While in the out-of-phase case, the insertion loss is less than 0.7 dB at 8.9 GHz. As shown in Figure 1.14 (a) and (b), the maximum phase and amplitude imbalances within the frequency range of 8.4-9.4 GHz for both in-phase and out-of-phase cases are less than 1.5^o and 0.2 dB, respectively.

Simulated and measured isolation characteristics are plotted in Figure 1.15. Within the frequency range of 8.4-9.4 GHz, the isolation is better than 30 dB between ports 1 and 4, and better than 15 dB between ports 2 and 3. Simulated results of isolation between port 1 and port 4 do not agree very well with measured results because simulated results with a very small value is sensitive to the fabrication tolerance. Measured results show that this kind of magic-T has narrow band characteristic.

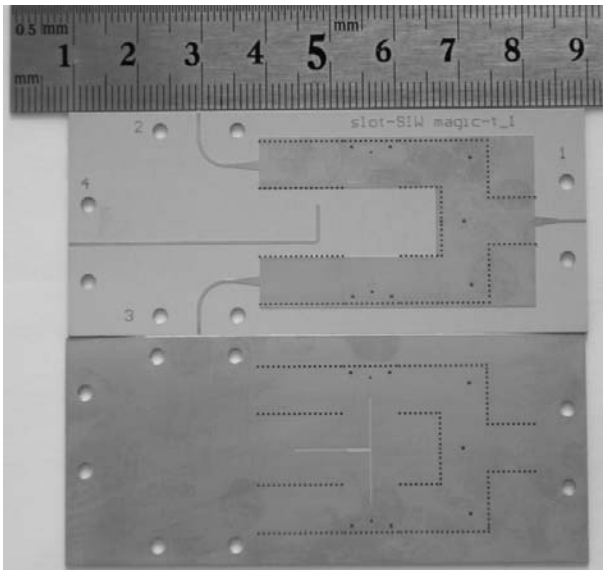

Figure 1.12: Photograph of the proposed magic-T

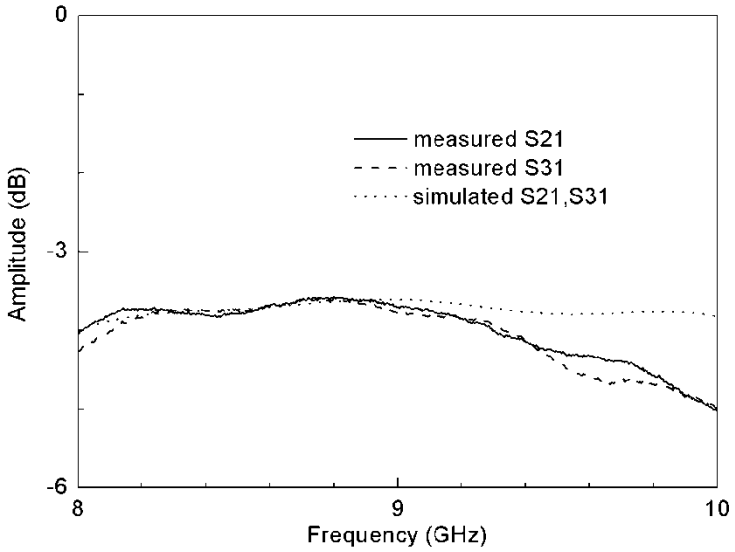

(a)

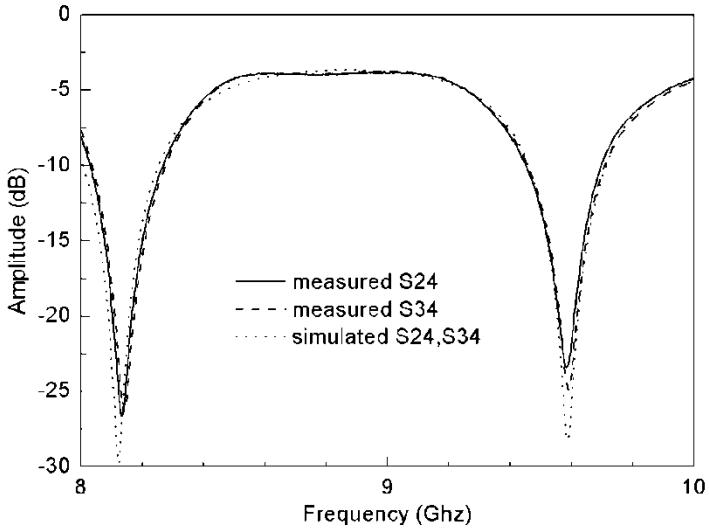

(b)

Figure 1.13: Simulated and measured frequency responses of power dividing (a) in-phase (b) out-of-phase

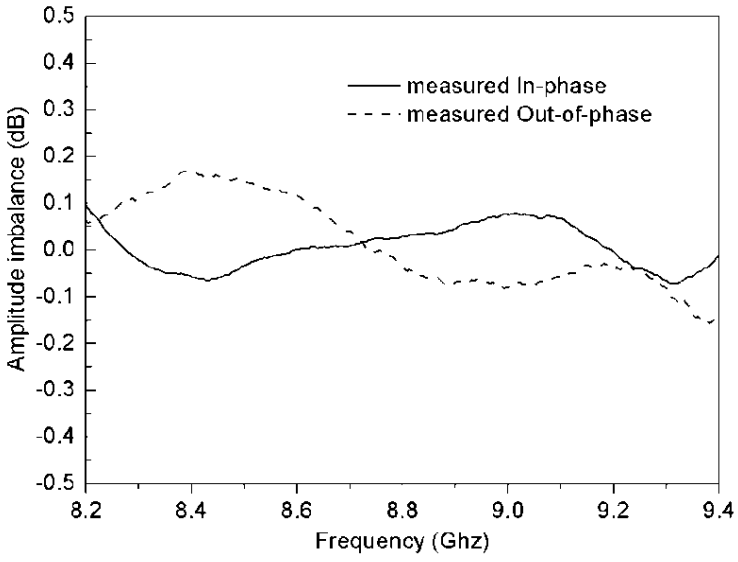

(a)

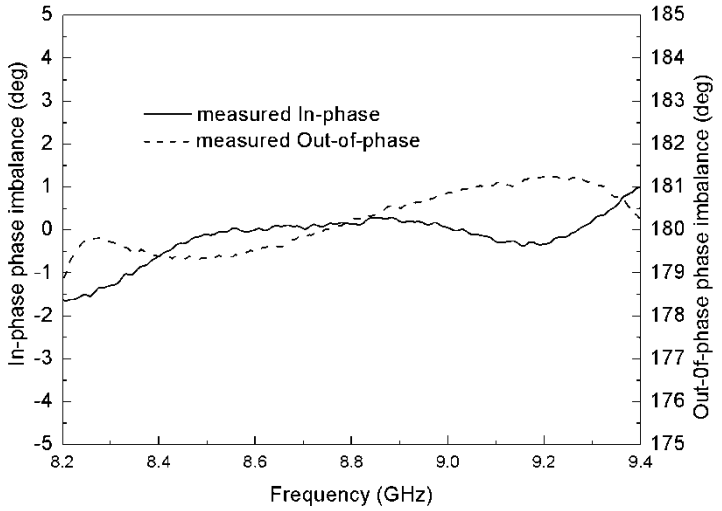

(b)

Figure 1.14: Measured results of amplitude and phase imbalance characteristics of the magic-T. (a) amplitude (b) phase

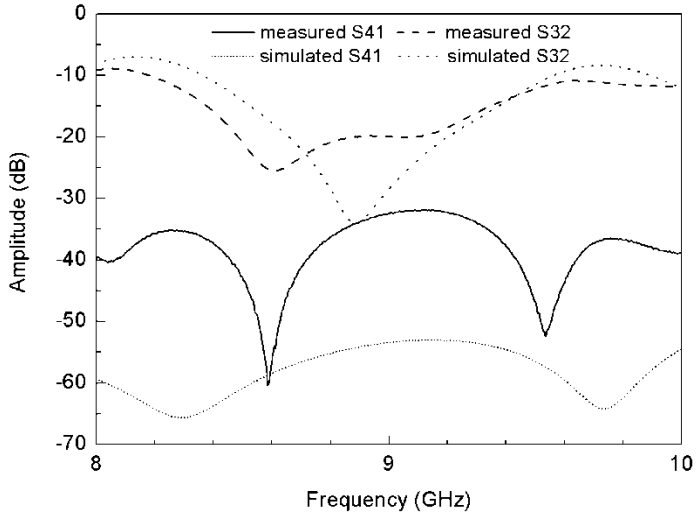

Figure 1.15: Simulated and measured isolation characteristics of the magic-T

1.1.5 Modified Planar SIW Magic-T

The above-discussed magic-T consists of an SIW T-junction, a slotline T-junction and two phase-reverse slotline-to-SIW T-junctions, and it has an about 8% bandwidth centered at 9 GHz with 0.2 dB amplitude and 1.5^{o} phase imbalances. In order to obtain smaller size and wider band, a modified version of planar SIW magic-T, which only consists of a phase-reverse slotline-to-SIW T-junction and an H-plane SIW T-junction, is proposed and presented as shown in Figure 1.16.

The gray and dark coloured layers mark the top metal cover and bottom metal cover, respectively. The light gray area again stands for substrate. The light dark areas are metallic slots for the SIW. Such two T-junctions share the two common arms with 45-degree rotation. Metallic vias V1 and V2 with diameter *D* are used to construct SIW H-plane T-junction. Ports 1(H port) and 4(E port) are sum and difference ports, respectively, while ports 2 and 3 are power dividing arms. Without the microstrip-to-SIW and slotline-to-microstrip transitions, the size of the magic-T is about 20mm×20mm. A signal applied to port 1 is split into two in-phase components by metallic via V1. The two components cancel each other at the slotline while port 4 is isolated. In this case, the 4-port junction works as an SIW H-plane T-junction and the symmetrical plane becomes a virtual open plane. Otherwise, the 4-port junction works as a slotline-to-SIW T-junction and the plane A-B becomes a virtual ground plane when a signal is applied to port 4. The input signal is naturally split into two equal and out-of-phase signals at ports 2 and 3, and port 1 is isolated in this case.

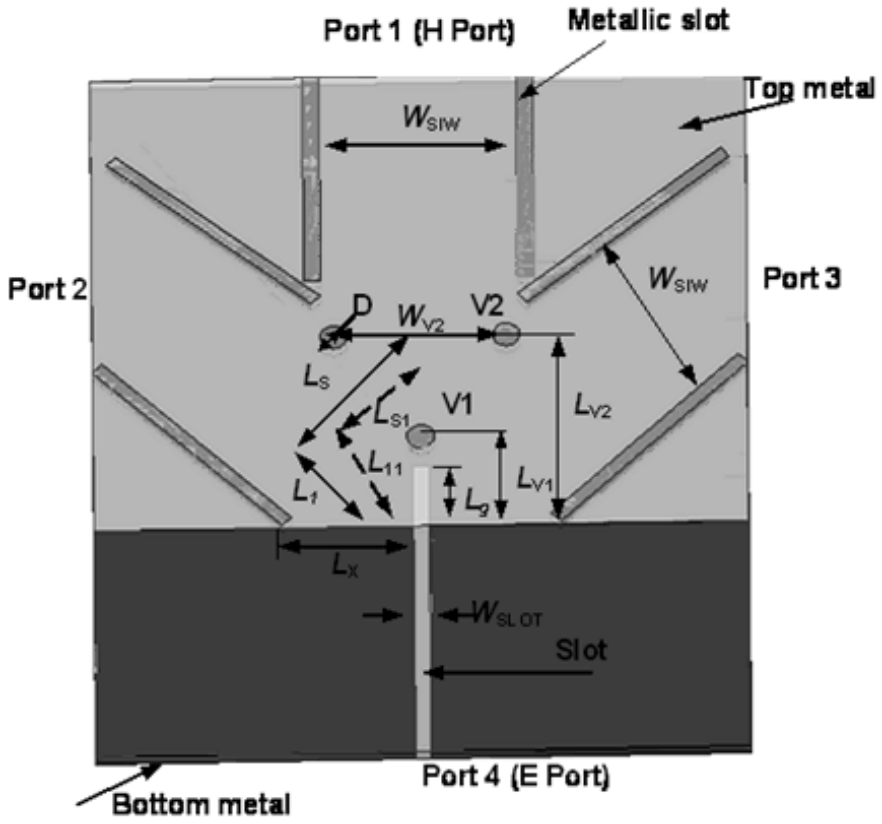

Figure 1.16: Physical 3D configurations of the modified magic-T

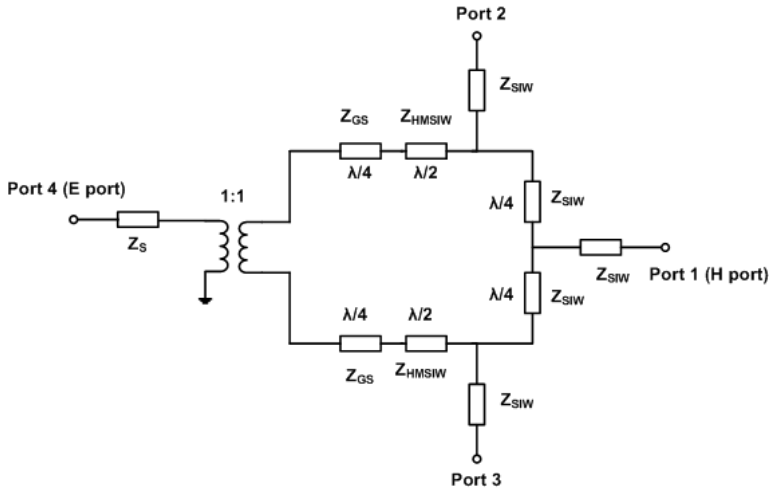

Figure 1.17: Corresponding equivalent circuit of the magic-T

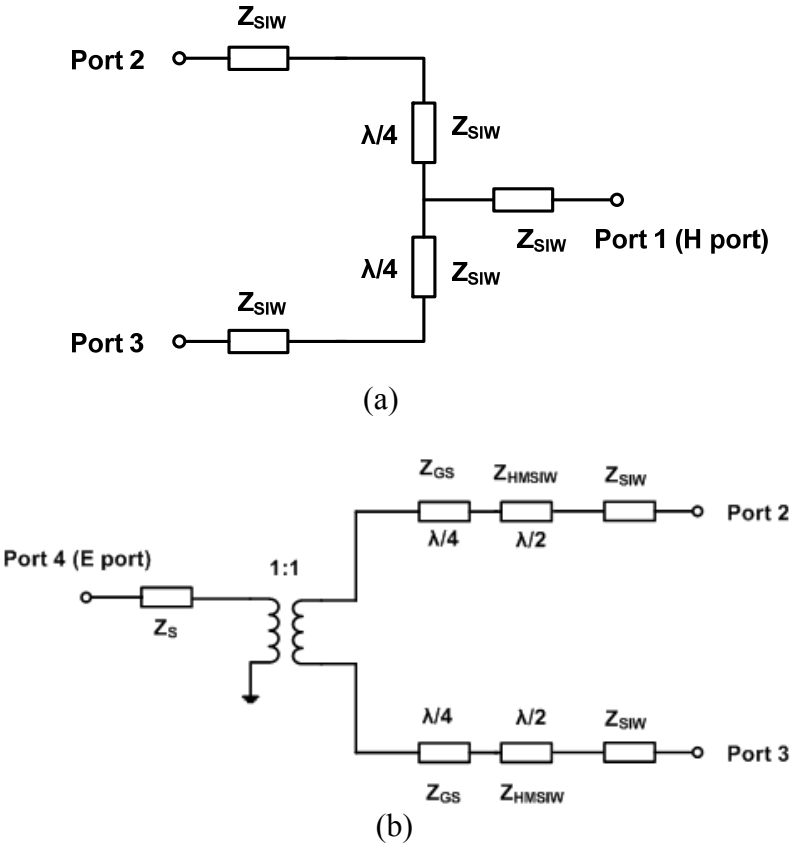

Figure 1.18: Simplified equivalent circuits of the magic-T: (a) in-phase (b) out-of-phase

The operating principle of the modified magic-T can also be well explained by its corresponding equivalent circuit at the working frequency shown in Figure 1.17, where the slot-to-SIW T-junction can be seen as an ideal transformer and the SIW H-plane T-junction as a divider. Parameters Z_S, Z_{GS}, Z_{HMSIW}, Z_{SIW} stand for the characteristic impedances the slotline, ground slotline, HMSIW, SIW, respectively. In the in-phase case, the equivalent circuit model will further be simplified as depicted in Figure 1.18(a), when $L_I=\lambda_{SIW}/2+\lambda_{HMSIW}/4$ at the working frequency. In the out-of-phase case, the simplified equivalent is shown in Figure 1.18(b), where $L_S=\lambda_{SIW}/4$. On the basis of the above discussion, distances L_I and L_S should depend on the positions of the three metallic vias in the magic-T circuit.

Based on the above-stated principle, two magic-T structures are designed and fabricated on RT/Duroid 6010LM substrate, respectively, with narrow-band and wide-band characteristics. So the narrow-band and wide-band cases of the magic-T will be discussed separately. Figure 1.19 shows the top view and bottom views of the modified magic-T's photograph. From this photograph, we can estimate that the size of the magic-T is reduced by near 50% with reference to above magic-T.

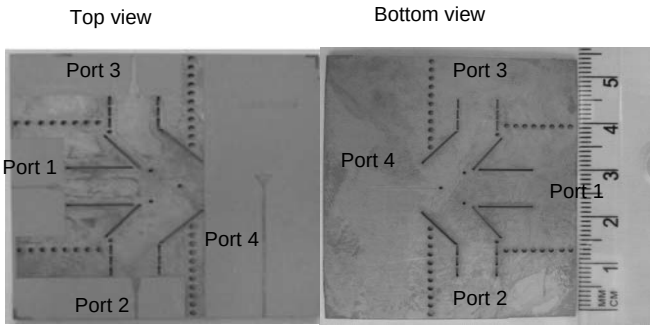

Figure 1.19: Photograph of the modified magic-T

The two out-of-phase signals cancel each other at port 1 as described in the operating principle, and simultaneously distance L_S is equal to a quarter of guide wavelength of the SIW at the working frequency. So the working bandwidth of the return loss at port 4 should be narrow in a similar manner to the above-studied magic-T. However, the working bandwidth judging from the return loss at port 1 should be wider because the two in-phase signals cancel each other in the slotline at port 4. In this demonstration, the magic-T was designed at 9 GHz. All design parameters of the magic-T are listed in Table 1.1.

Figure 1.20 shows the return loss and insertion loss of the fabricated narrow-band magic-T. S_{11} is lower than -15 dB from 8.7 to 9.4 GHz with a 7.8% bandwidth which has validated the above discussion. Within the frequency range of interest, the minimum insertion loss is 0.7 dB and it is less than 0.8 dB in both in-phase and out-of-phase cases. The isolation is better than 30 dB between ports 1 and 4, and better than 20 dB between ports 2 and 3 over the entire frequency range. As shown in Figure 1.21(a) and (b), the maximum phase and amplitude imbalances for both in-phase and out-of-phase cases are less than 1.5^{o} and 0.5 dB in the working band, respectively. Simulated and measured isolation characteristics are described in Figure 1.22.

Table 1.1: Dimension of the modified narrow-band magic-T

$\boldsymbol{D}$ (mm)	0.60	$\boldsymbol{W_{SLOT}}$ (mm)	0.20
$\boldsymbol{L_{V1}}$ (mm)	5.09	$\boldsymbol{L_{V2}}$ (mm)	9.29
$\boldsymbol{L_g}$ (mm)	3.78	$\boldsymbol{L_X}$ (mm)	4.91
$\boldsymbol{W_{SIW}}$ (mm)	7.30	$\boldsymbol{W_{V2}}$ (mm)	6.40

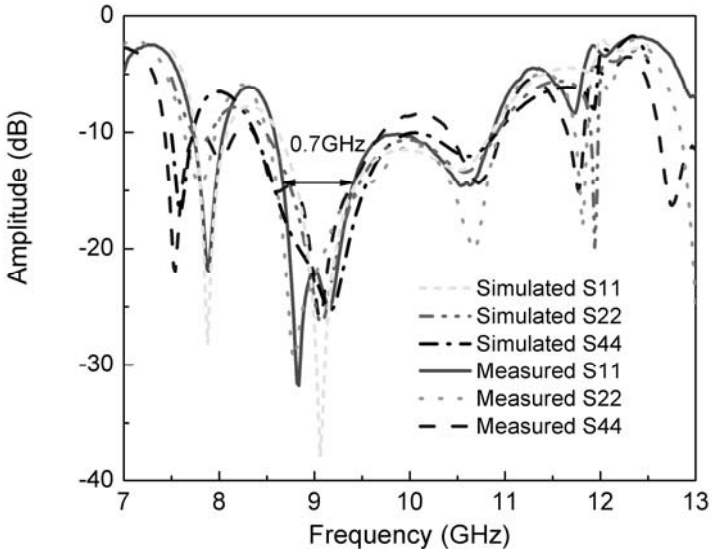

(a)

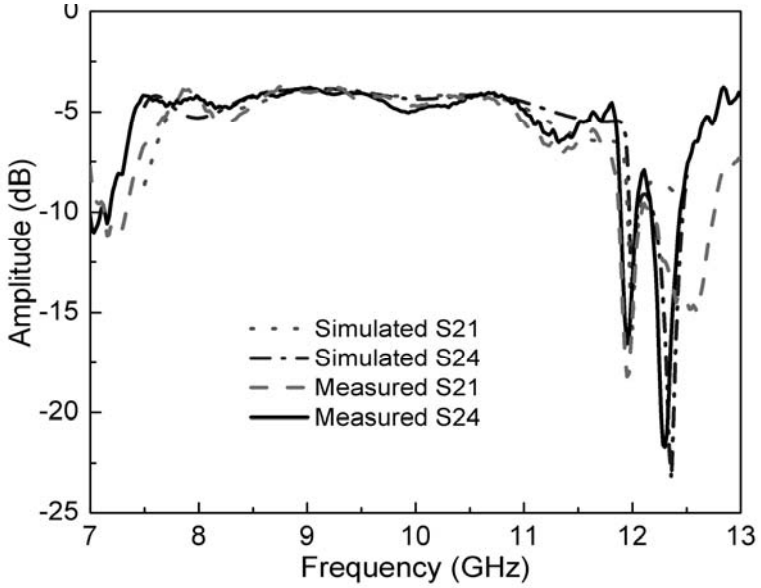

(b)

Figure 1.20: Simulated and measured frequency responses of the magic-T (a) return loss (b) insertion loss

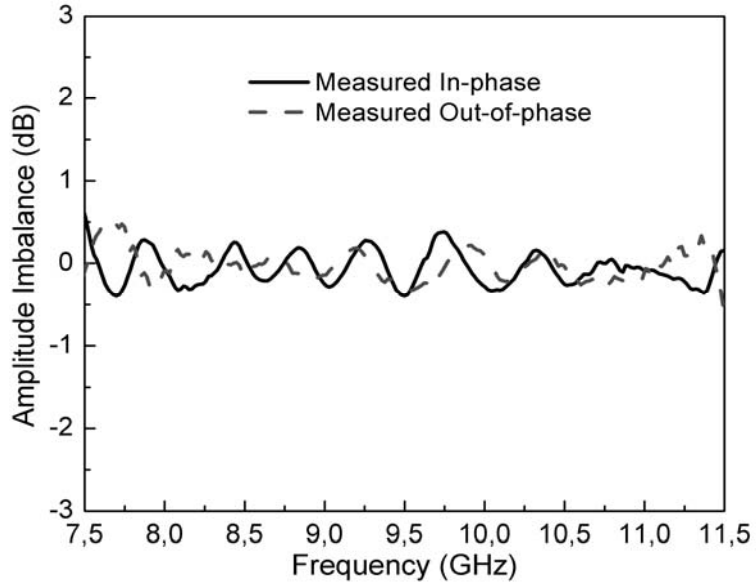

(a)

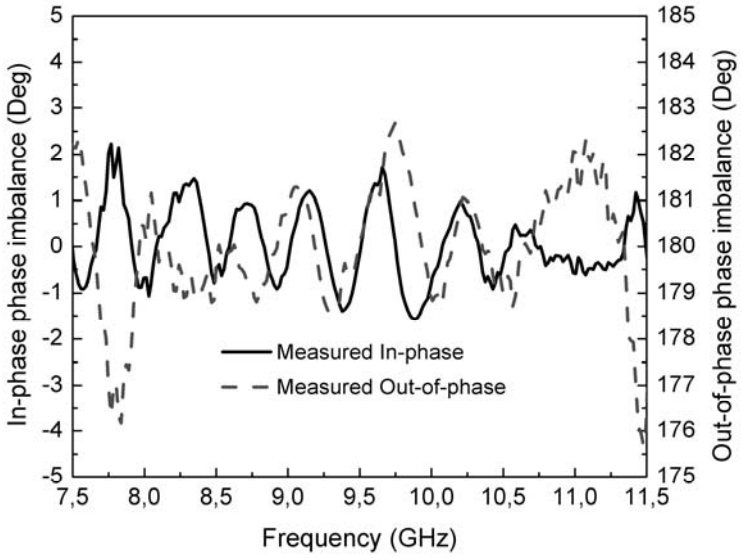

(b)

Figure 1.21: Measured results of amplitude and phase imbalance characteristics of the magic-T: (a) amplitude (b) phase

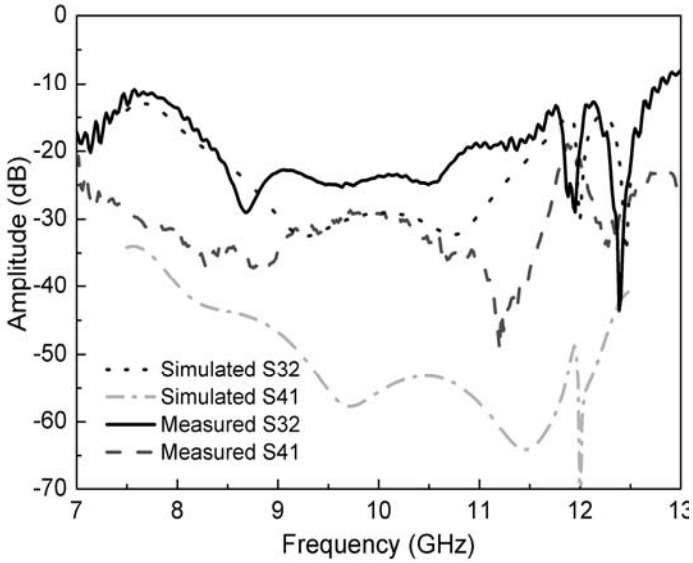

Figure 1.22: Simulated and measured isolation characteristics of the magic-T

The narrow-band characteristics of this magic-T have well been confirmed in the above discussion. However, an interesting outcome can be observed in that the return-loss defined bandwidth can be broadened by optimizing the parameter values of L_{V1}, L_{V2}, W_{V2} and L_g. When

the signal flows into the SIW from the slotline in this slotline-to-SIW structure, it would be split into two components and each of them will propagate along line L_I at the working frequency as shown in Figure 1.16. Nevertheless, the propagating directions being different slightly at different frequencies provide a possibility of broadening the bandwidth of the magic-T. It works like a filter which has two different resonate frequency. In other words, it is possible for the magic-T to simultaneously realize L_I, $L_{I1}=\lambda_{SIW}/2+\lambda_{HMSIW}/4$ and L_S, $L_{S1}=\lambda_{SIW}/4$ at two different frequencies. In our proposed broadband design, these two frequencies are set at 8.7 GHz and 9.8 GHz. Through optimization, some geometrical parameters of magic-T are changed such that L_{V1}=3.89 mm, L_{V2}=8.45 mm, W_{V2}=6.36 mm, and L_g=3.24 mm.

Figure 1.23(a) shows the newly-designed magic-T's simulated and measured return losses at each port. Among the results, simulated S_{44} indicates that the above two geometrical conditions for achieving broadband performances are readily satisfied at 8.7 GHz and 9.8 GHz. Measured return loss is better than 15 dB from 8.4 to 10.6 GHz with 23.2% bandwidth. In this broadband frequency range, the insertion loss is less than 0.9 dB and the minimum insertion loss is 0.7 dB in both in-phase and out-of-phase cases as shown in Figure 1.23(b). Measured and simulated isolation curves between port 1 and port 4 or port 2 and port 3 are plotted in Figure 1.24. In addition, the amplitude and phase imbalances of the magic-T are 2^o and 0.5 dB, respectively, as shown in Figure 1.25(a) and (b). Measured results of all circuits agree well with their simulated counterparts.

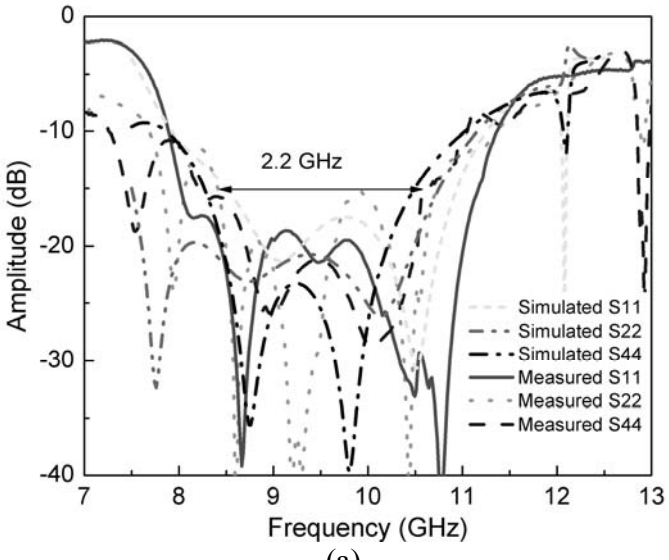

(a)

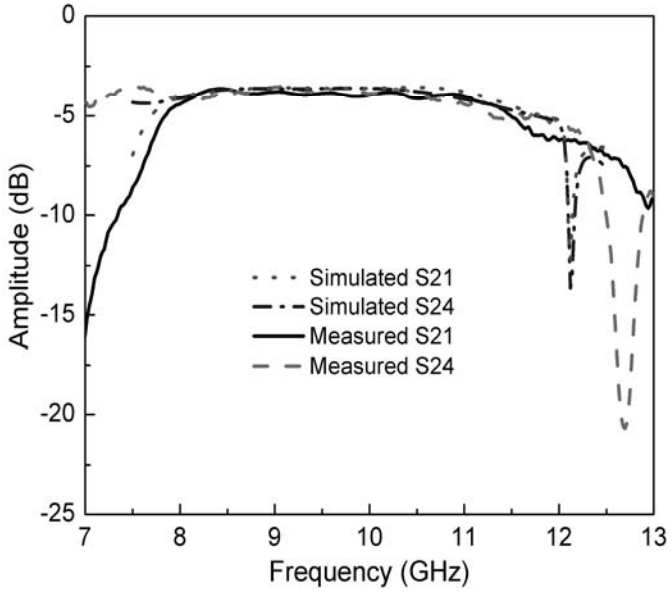

(b)

Figure 1.23: Simulated and measured frequency responses of the magic-T (a) return loss (b) insertion loss

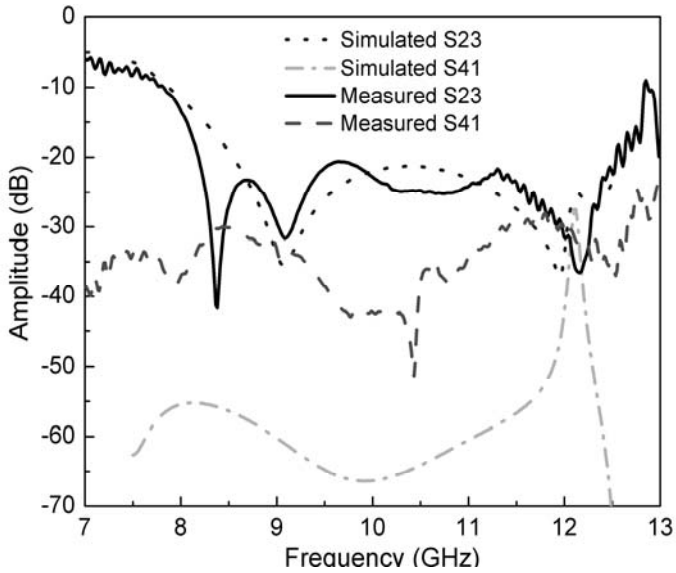

Figure 1.24: Simulated and measured isolation characteristics of the magic-T

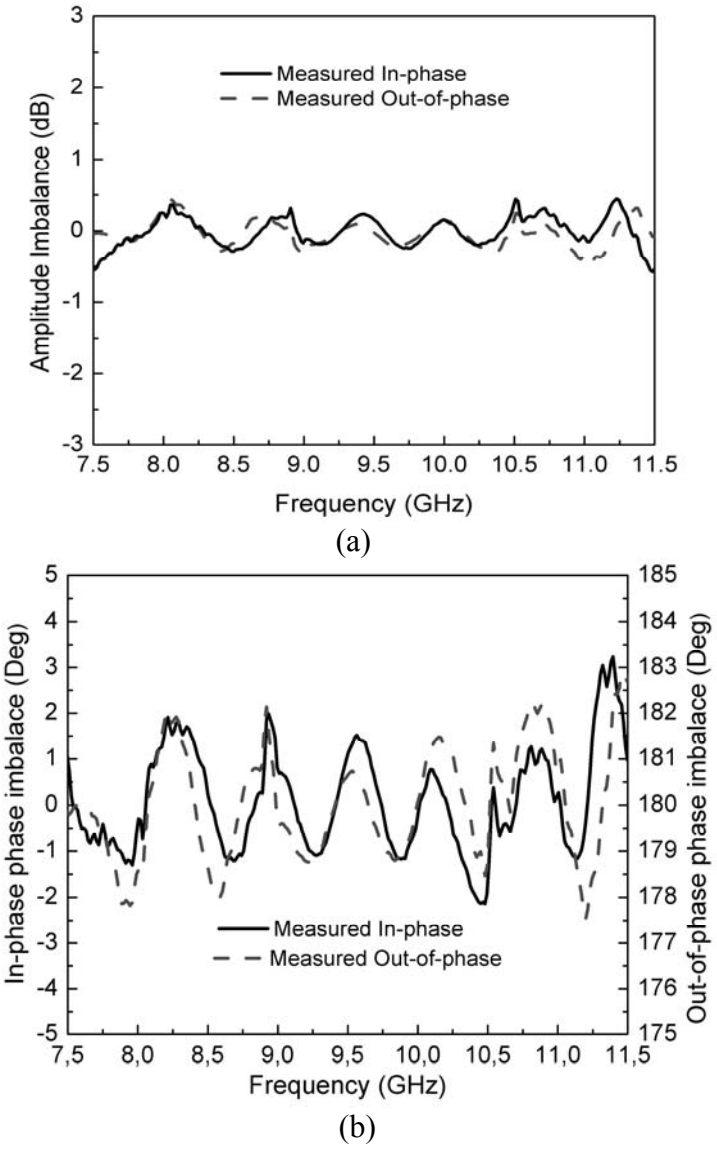

Figure 1.25: Measured results of amplitude and phase imbalance characteristics of the magic-T: (a) amplitude (b) phase

1.2 HMSIW Wideband Band-pass Filter

1.2.1 Review of Wideband Band-pass Filter

Wideband band-pass filter technology plays a critical role in the development of modern radar and high data-rate communications systems [40]-[41]. Wideband solutions for microwave filters, performing very efficient signal selections by properly suppressing out-of-band additive noise,

external (out-of-system) and internal (inter-channel) interferences, and nonlinear-distortion perturbations, are required in RF front-ends supporting these applications.

Over the last years, classic microwave band-pass filter theory has become well established in designing narrow and reasonably moderate bandwidth filters. However, it is not suitable for filters with a large pass-band width. One example is the design of parallel-coupled transmission-line resonator filters [42]. Since the developed synthesis methods for these structures are based on equivalent-circuit models of the coupled-line section only that exact at the center frequency such as K- and J-inverters, they are not useful in wideband situations. Recently, various methods and designs to make ultra-wideband filters have been proposed.

In addition to parallel-coupled lines and stepped-impedance resonators, the ground-plane aperture was employed to improve the coupling coefficient [43], while the capacitive loading is used to enhance the rejection in the higher stop-band [44]. Multiple-mode resonator and quarter-wavelength parallel-coupled lines at the input and output ports are adopted in [45] and [46] to achieve the goals shown in [43] and [44]. The dual-mode ring resonator cascaded with orthogonal feed lines is used in [47], double-sided parallel-strip lines are presented in [48], and three-line microstrip structures are utilized in [49]. References [50] and [51] make use of transmission zeros on both sides of the pass-band skirts to realize ultra-wideband filters. The hybrid microstrip and coplanar waveguide structure are proposed to make ultra-wideband filters in [52]-[54]; however, there are complicated design procedures with the double-sided structure. In [55] and [56], short-circuited stubs and a low-pass filter are utilized for better performance in an ultra-wideband filter. For flatter group delay in a wideband band-pass filter, short-circuited stubs are employed in [57]-[59]. In order to achieve broader bandwidth and better selectivity, filters based on composite low-pass and high-pass topology were developed in [60].

1.2.2 Introduction of the HMSIW

In order to reduce the size of the SIW devices, a novel technique named HMSIW was proposed [61]. As shown in Figure 1.26, the HMSIW is realized by cutting the SIW along the center plane where can be considered as an equivalent magnetic wall when the SIW is used with a dominant mode. The HMSIW can keep the original performance of SIW with nearly a 50% reduction in size. In addition, the HMSIW has the wider-bandwidth dominant mode range than the SIW

because the former cannot intrinsically support the $TE_{(2m)n}$ modes as well as TM modes. Some devices based on the HMSIW were realized with good performances [37]-[39].

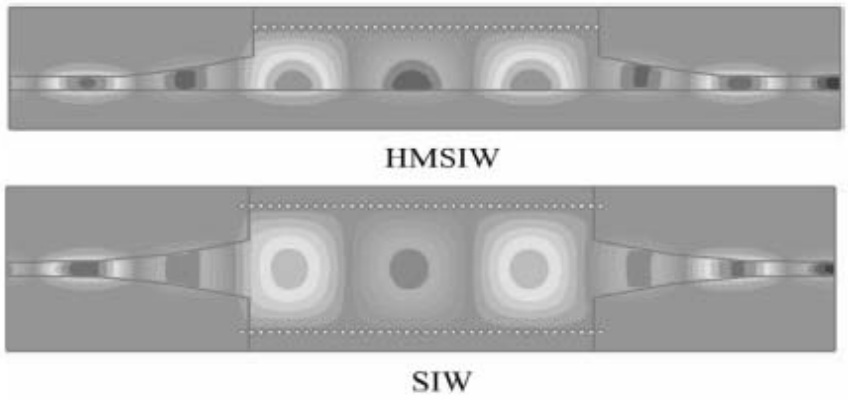

Figure 1.26: Dominant field distribution in HMSIW and SIW

The SIW and HMSIW are high-pass transmission line because they have the inherent cutoff frequency as the metal rectangular waveguide. The inherent sharp cutoff behavior in low side can be used to develop some SIW or HMSIW devices such as filters [39] and [62]. In [62], the high-pass behavior was used to develop a super wideband band-pass filter by combining EBG structures into the SIW, where EBG and SIW provide the band-stop and high-pass behaviors, respectively. So the HMSIW's characteristics of high-pass and rejection of $TE_{(2m)n}$ modes can be used with a low-pass filter to build up a wide-band filter.

In this thesis work, we take the advantages of high-pass behaviour of the HMSIW to easily realize a super wideband band-pass filter by serially connecting the microstrip low-pass filter. The HMSIW and microstrip low-pass filter decide the lower side and upper side of amplitude response of the wideband band-pass filter, respectively. First, the width of the HMSIW is determined for the cutoff frequency. In other words, the lower side of frequency response of the wideband band-pass filter is determined by the width of the HMSIW. Second, the microstrip low-pass filter is designed to determine the upper side of the frequency response. Finally, the wide-band band-pass filter is developed, simulated and measured.

1.2.3 Wideband Filter by Integrating HMSIW and Lowpass Filter

Figure 1.27 shows the schematics of synthesizing the proposed wideband band-pass filter that consists of a low-pass filter and a high-pass filter. The stop-band frequencies of the low-pass filter and high-pass filter are the upper side and lower side stop-band frequencies of the wideband band-pass filter, respectively. Meanwhile, the group delay of the designed filter is the sum of those of the low-pass filter and the high-pass filter. In this design, the stepped-impedance Butterworth low-pass filter is selected because it has a good performance judging from its group delay. The filter is simulated and designed with full-wave CAD software CST, and fabricated on Rogers/duroid 5880 substrate with dielectric constant of 2.2 and a thickness of 0.5mm.

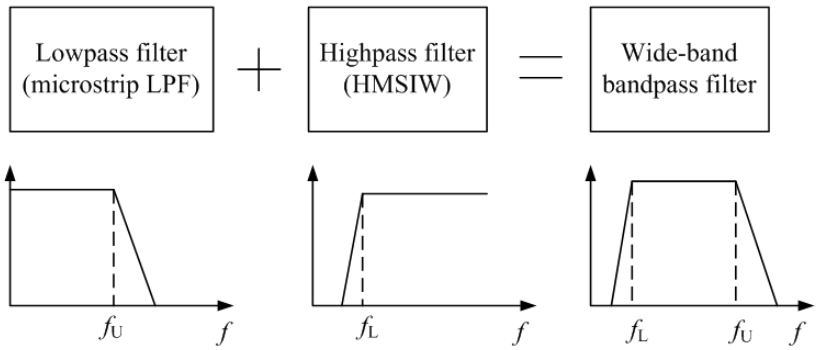

Figure 1.27: Schematics of the forming process of the wide-band band-pass filter

Figure 1.28 depicts the layout of HMSIW with a cutoff frequency of 7.1 GHz, where D and S are the diameter and period of metallic vias, and W_{HMSIW} stands for the HMSIW width that determines its cutoff frequency. This cutoff frequency is also that of the lower side of the wideband band-pass filter. The SIW-microstrip transition is used for connecting 50Ω testing system, where W_{50} and W_{taper} are the widths at both ends of the microstrip taper, and L_{taper} is the length of the taper. Dimensions of the HMSIW are determined by D=0.4 mm, S=0.8 mm, W_{HMSIW}=7.1 mm, W_{50}=1.5 mm, W_{taper}=2.5 mm and L_{taper}=14 mm.

As shown in Figure 1.29, simulated results indicate that the HMSIW has a good high-pass behaviour with a low insertion loss in pass-band and sharp cutoff. The return loss over 7.1-19 GHz is better than -10 dB and the insertion loss (rejection) is more than 30 dB below 5 GHz.

As stated above, the stepped-impedance low-pass filter has a maximally flat response. The specifications of this filter are: cutoff frequency of 16.6 GHz; impedance of 50 Ω; the highest practical line impedance is 125 Ω, the lowest is 20 Ω; the insertion loss (out-of-band rejection) is more than 30 dB at 20 GHz. To satisfy these specifications, an eleven-order low-pass filter is designed as shown in Figure 1.31. W_1, W_2 and L_i are the physical microstrip widths and lengths of low impedance and high impedance lines, respectively. Dimensions of the low-pass filter are W_1=5.31 mm, W_2=0.27 mm, L_1=0.08 mm, L_2=0.40 mm, L_3=0.57 mm, L_4=0.84mm, L_5=0.85 mm and L_6=1.00 mm.

Simulated results of the low-pass filter are shown in Figure 1.31. It is found that the insertion loss is less than 0.3 dB and the return loss is more than 15 dB. Simulated performance of the low-pass filter can satisfy specifications proposed in advance.

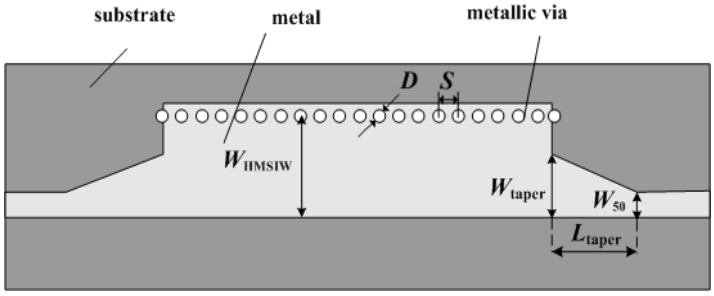

Figure 1.28: Configuration and dimensions of the HMSIW

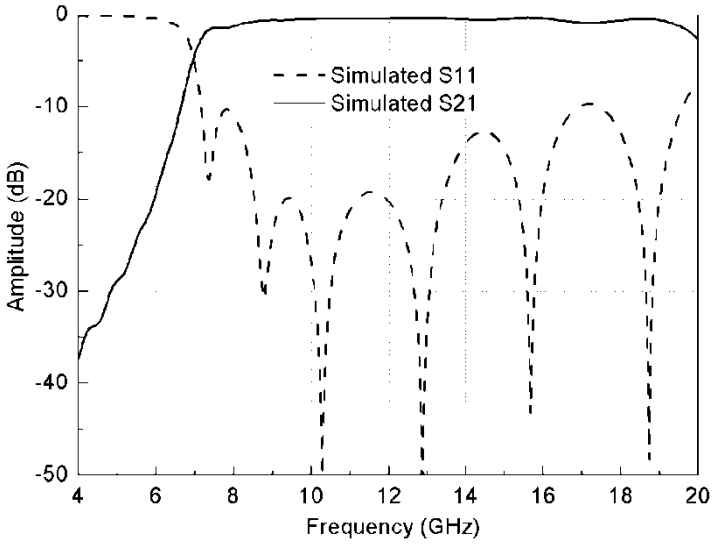

Figure 1.29: Simulated frequency responses of the HMSIW

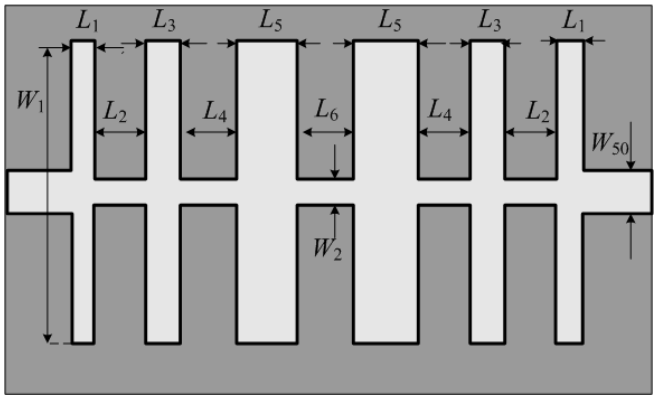

Figure 1.30: Configuration and dimensions of the low-pass filter

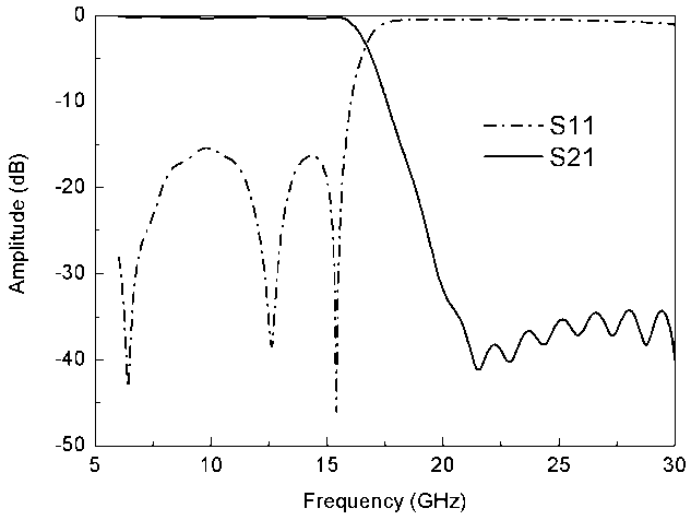

Figure 1.31: Simulated frequency responses of the low-pass filter

As shown in Figure 1.32, the wide-band band-pass filter is formed when the low-pass filter and the HMSIW are serially connected. Meanwhile, the performance of the wide-band band-pass filter is already determined by the low-pass filter and HMSIW. The predicted center frequency and bandwidth are 12.85 GHz and 74%, because the cutoff frequency of the low-pass filter and HMSIW are 7.1 GHz and 16.6 GHz, respectively. The upper side and lower side stop-band frequency response should be the same as that of the low-pass filter and HMSIW.

As can be seen from Figure 1.33, simulated and measured results agree with the predicted results very well. The lower side stop-band is within 0-7.1 GHz, while the insertion loss (rejection) is more than 30 dB below 5 GHz. In the pass band, the insertion is about 1±0.4 dB and the return loss is better than 10 dB. The wideband band-pass filter also has a wide stop band at upper side from 16.6 to 30 GHz, while the insertion loss (out-of-band rejection) more than 30 dB within 19-30 GHz. Figure 1.34 shows measured and simulated group delays which are flat over the pass-band.

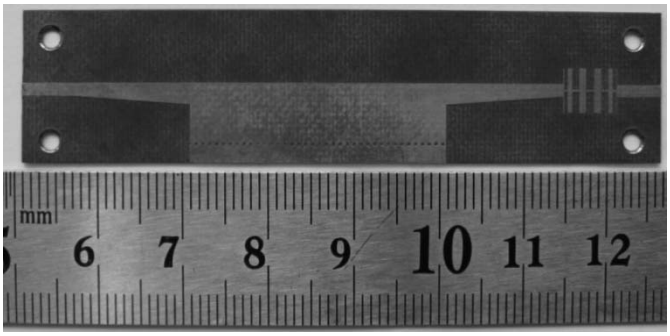

Figure 1.32: Photograph of the proposed wideband band-pass filter

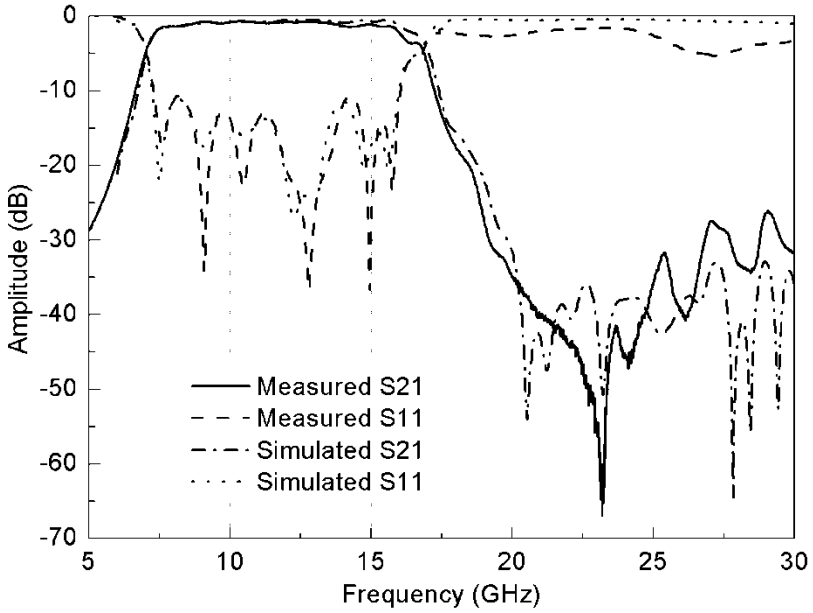

Figure 1.33: Simulated and measured frequency responses of the wideband band-pass filter

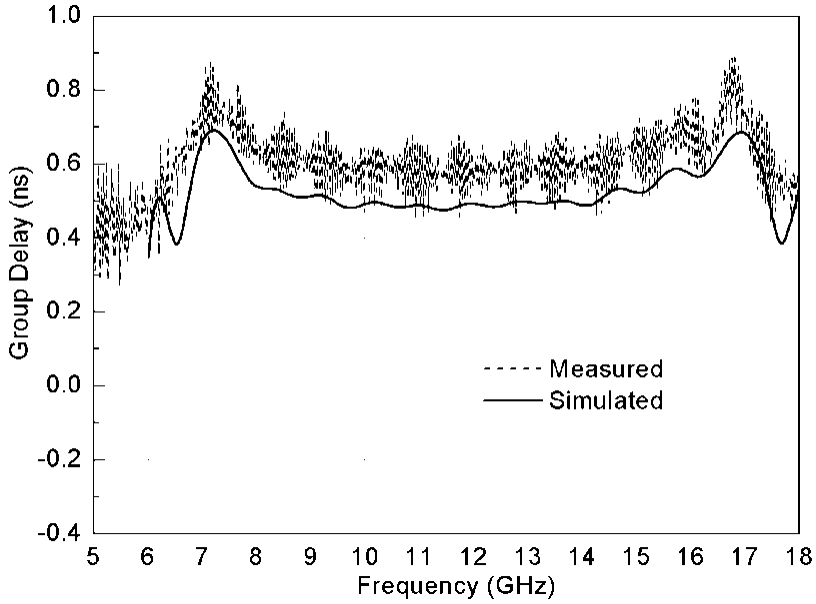

Figure 1.34: Simulated and measured group delays

1.3 Antipodal Linearly Tapered Slot Antenna (ALTSA) System Using Substrate Parallel Plate Waveguide Feeding Structure

The linearly tapered slot antenna (LTSA) has attracted much interest in many practical applications due to its attractive features such as narrow beam width, high element gain, wide bandwidth and small transverse spacing between elements in arrays [63]-[65]. To design an LTSA, the most important part is how to develop the feeding structure which determines the performances of this antenna. So far, many feeding structures such as fin line, inverted microstrip, coplanar waveguide, microstrip to slot line transition, balanced microstrip and SIW have been proposed and designed [66]-[68]. Generally speaking, some of the above-mentioned feeding structures such as SIW and microstrip transition have the limitation for wide bandwidth LTSA.

As is well known, the parallel plate waveguide as a TEM mode transmission line has many applications in wide-band components [69]-[70]. Therefore, a wide-band LTSA excited by parallel plate waveguide is proposed in this work. The parallel plate waveguide is fabricated on substrate while it has a small size feature with finite ground planes. The propagation

characteristics of the substrate parallel plate waveguide are relatively easy to analyze. This structure is found to be a good candidate for microwave and millimetre-wave applications. Details of the LTSA with substrate parallel plate waveguide feeding mechanism including the prototype, simulated and measured results are presented as follows.

1.3.1 Substrate Parallel Plate Waveguide

The substrate parallel plate waveguide is inspired and developed from the concept of substrate integrated waveguide with four additional air gaps, as shown in Figure 1.35. Four air gaps allow isolating the central flat plates from the side metallic walls. Metallic walls can suppress any potential radiation of the signal on the fringes of the two central flat plates. Moreover, metallic walls can reduce the size of the central plates. Figure 1.36 shows the electric fields over the cross section related to the working mode. Through 2D simulations, the propagation constant of this structure can be obtained, as shown in Figure 1.387. The results show that this substrate parallel plate waveguide can support three TEM modes. In the design, we will use microstrip line to excite the parallel plate mode and suppress another two TEM mode.

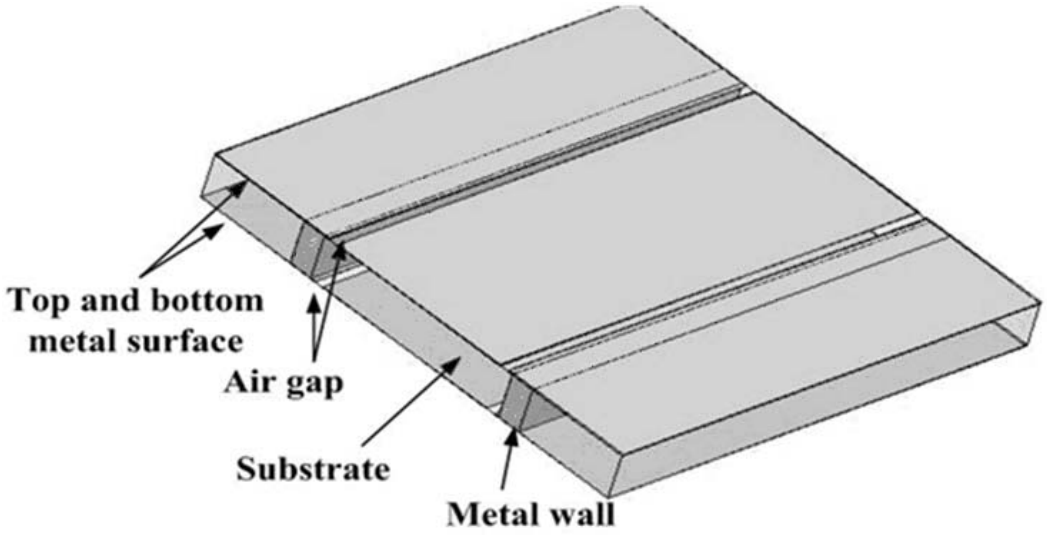

Figure 1.35: 3D schematic of the substrate parallel plate waveguide

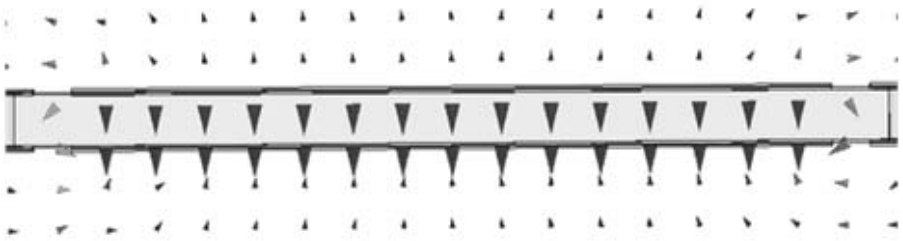

Figure 1.36: Electric fields over the cross section

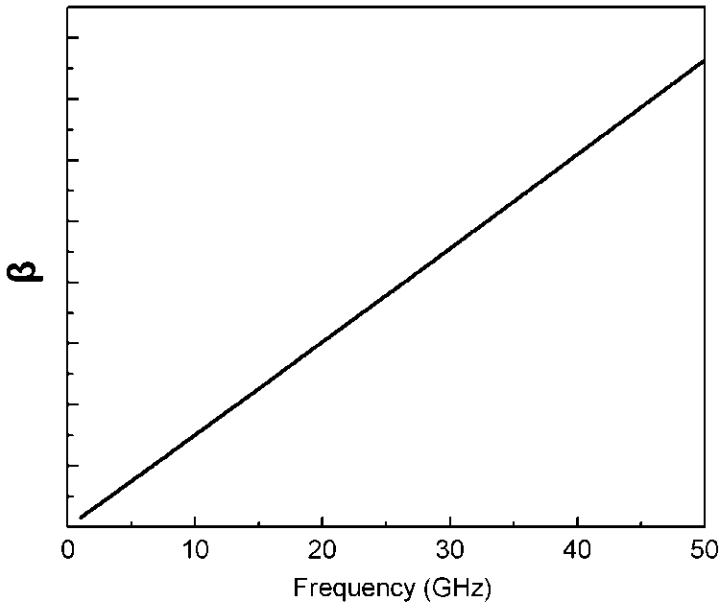

Figure 1.37: Qualitative dispersion behaviour of substrate parallel plate waveguide mode

1.3.2 Design of the Proposed ALTSA

First of all, the operation principle of the proposed ALTSA is described in this section. Figure 1.38 depicts the physical 3D configuration of an ALTSA with substrate parallel plate waveguide feeding structure and microstrip-to-parallel plate waveguide transition, where the dielectric constant and substrate thickness are denoted by ε_r and t, respectively. The light gray and dark gray areas identify the substrate area and metal covers of the substrate, respectively. The parallel plate waveguide-microstrip transition is used for connecting 50 Ω measurement system, W_{50} and W_{strip} are the widths at the both ends of the microstrip taper for matching the antenna impedance

to 50 Ω, and L_{taper} is the length of the taper. The parallel plate waveguide section simply transforms the unbalanced microstrip to the balanced parallel plate waveguide feeding system for ALTSA, where D and S are the diameter and period of the metallic vias used to form an equivalent metal wall similar to the case of SIW, W_h is the distance between two rows of metallic vias, W_{gap} is the air gap width and L_P is the length of parallel plate waveguide section. The ALTSA has a flare angle of 2α and a length of L_{ant}.

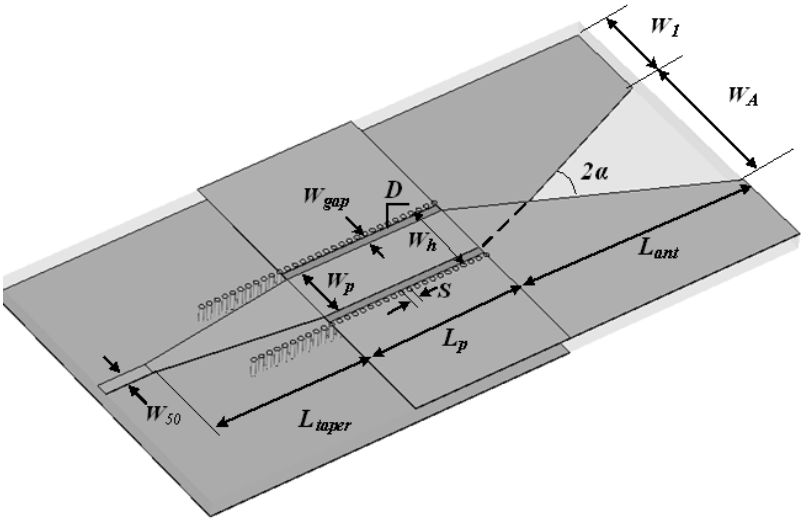

Figure 1.38: Physical 3D configuration and parameters of the proposed ALTSA

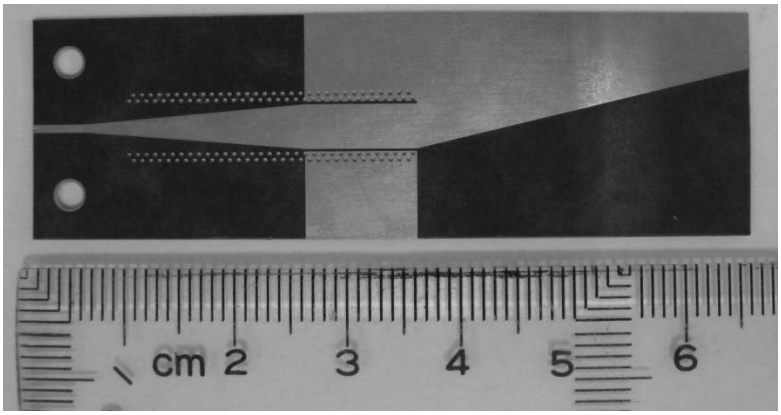

Figure 1.39: Photograph of the proposed ALTSA

In Figure 1.37, the substrate parallel plate waveguide is designed to support TEM mode free from cut-off frequency. The ATLSA is designed by gradually flaring the metallic covers on opposite sides of the substrate by an angle of 2α. In order to match the high impedance of ALTSA with the low impedance parallel plate waveguide, the flaring metal covers are overlapped with each other. The metallic covers gradually stretch out on the opposite side of the substrate by angle 2α. Linear tapers from the overlapped metallic covers to tapered slot antenna can change the vertical field polarization of the parallel plate waveguide to the horizontal field polarization of the ALTSA. A good impedance matching can be obtained by adjusting length L_{ant} and angle 2α. If a good matching performance cannot be obtained, we may match the ALTSA with air by adjusting width W1, consequently the entire ALTSA matching can be adjusted to its optimal performance. The gain of an ALTSA is mainly determined by length L_{ant} [64].

In this work, the proposed ALTSA is designed only for demonstration purpose. The parameters of the antenna are D=0.3 mm, S=0.6 mm, L_p=10 mm, W_p=4 mm, W_{50}=0.75 mm, W_{gap}=0.2 mm, L_{taper}=20 mm, L_t=40 mm, W_h=4.8 mm, α=19.8^0, W_1=5 mm and W_A=5 mm.The antenna is designed and fabricated on Rogers/duroid 5880 substrate with ε_r=2.2 and t=0.254 mm. Figure 1.39 shows the photograph of the fabricated ALTSA sample.

The ALTSA using substrate parallel plate waveguide as feeding structure is simulated by the full-wave CAD software (CST in our case). Simulated and measured return losses are shown in Figure 1.40, which show a very good agreement. Measured return loss S_{11} is lower than -10 dB from 12 to 50 GHz. Actually simulated return loss is lower than -10 dB from 12.5 to 80 GHz. The highest measured frequency is limited by the measurement system. The results show that the proposed antenna has a very wide bandwidth.

The antenna gain is measured from 10 to 40 GHz because certain measurement equipment above 40 GHz was not available during this work. Figure 1.41 shows simulated and measured antenna gains versus frequency. Both simulated and measured results indicate that the antenna gain slowly increases from 6 to 12 dBi as the working frequency is swept from 10 to 40 GHz.

Figure 1.42 shows the measured radiation patterns of the ALTSA with the substrate integrated parallel plate antenna feeding structure at 18 GHz and 30 GHz respectively. The sidelobe is below than -10 dB at both frequencies. The E-plane radiation pattern has a 3 dB beamwidth of 50 degree and 28 degree at 18 GHz and 30 GHz, respectively. The H-plane radiation pattern has a 3

dB beamwidth of 78 degree and 57 degree at 18 GHz and 30 GHz, respectively. At these two frequencies, antenna gain is 8 dBi and 9.5 dBi as shown in Figure 1.41. The results indicate that the ALTSA using the proposed feeding structure can yield wideband characteristics.

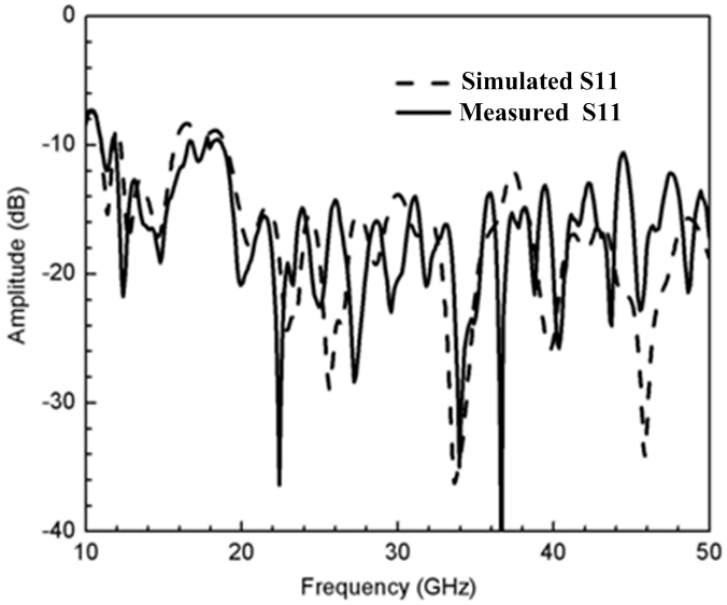

Figure 1.40: Simulated and measured return losses of the proposed ALTSA cell

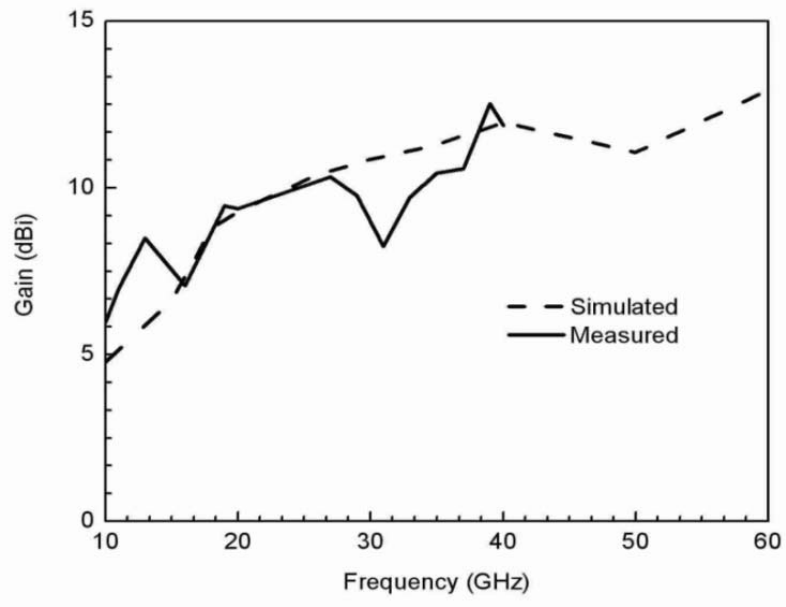

Figure 1.41: Simulated and measured gains versus frequency

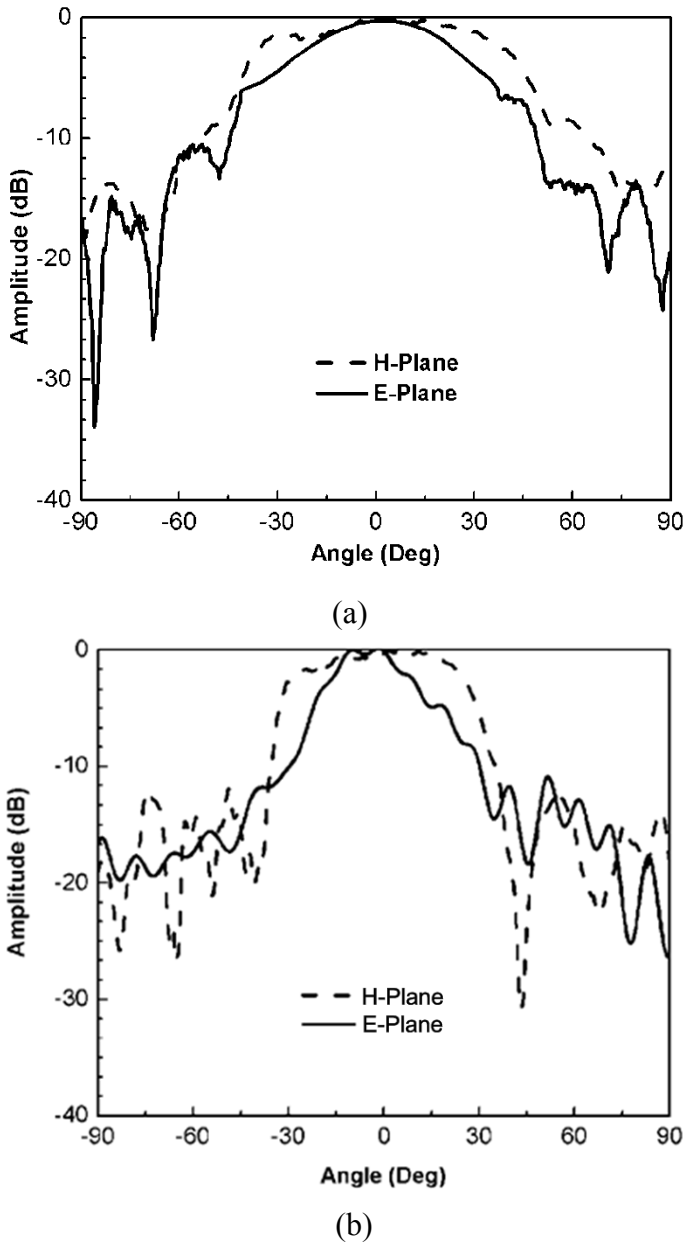

Figure 1.42: Measured normalized radiation patterns for the proposed ALTSA. (a) Radiation patterns at 18 GHz. (b) Radiation patterns at 30 GHz

1.4 Conclusion

In this chapter, three novel passive components employing the SICs concept are developed. Firstly, the slotline-to-SIW transition and magic-T circuits are proposed, simulated, fabricated and measured. There are two types of magic-Ts: one is a narrow band of 8% and not a compact size, modified one is a wide band of 23.4% and 50% smaller size comparing to the former one.

Good performances related to the insertion loss, isolation and balance are observed for our fabricated samples designed over X-band. Those novel structures are important components for designing integrated microwave and millimetre wave circuits and systems such as mixer, antenna feed network and mono-pulse radar. Second, we provide a simple method to develop a wideband BPF by a section of HMSIW and a LPF being cascaded together. This wideband BPF is simulated, fabricated and measured. Good performance related to the insertion loss, return loss cutoff characteristic and group delay are observed for our fabricated samples designed from 5 to 30 GHz. In the end, the antipodal linearly tapered slot antenna using the substrate parallel plate waveguide feeding structure has been designed, fabricated and tested. The proposed substrate parallel plate waveguide supporting TEM mode, can be used in not only wideband antenna but also other wideband components such as wideband divider, coupler, etc. For the purpose of demonstration, the substrate integrated parallel plate waveguide feeding the ALTSA is tested with return loss S_{11} lower than -10 dB from 12 to 50 GHz. The results indicate that the ALTSA using the proposed feeding structure has a wideband characteristic.

CHAPTER 2 MICROWAVE AND MILLIMETRE-WAVE SUBSTRATE INTEGRATED ACTIVE COMPONENTS DESIGN

In this chapter, a series of novel active components based on SIW are presented. First, a low-impedance SIW bias line is proposed to suppress 2nd and 3rd harmonics in power amplifier (PA). Next, a singly balanced mixer, which employs the modified magic-T proposed in Chapter 2, is developed. Then, we propose electrically tunable SIW and HMSIW reflective cavity resonators. Finally, a VCO on the basis of such novel tunable SIW cavity resonators are developed and measured.

2.1 Power Amplifier Using λ/4 Low-Impedance SIW Bias Line

2.1.1 Summary of Bias Line of Power Amplifier

Microwave PA, which converts DC energy to microwave energy and thus amplifies microwave signal amplitude, is a very important component for microwave applications. It has been under constant research to improve its linearity, power added efficiency, output power and integration aspects.

In the design of PA circuits, bias lines, which are generally designed as low-pass filter, used to provide DC bias to solid-states devices are important. Usually, inductors are used as RF-choke for bias at low frequency, and at high frequency, λ/4 high-impedance transmission lines terminated with chip capacitor or radial stub are used as bias lines. However, when λ/4 high-impedance transmission lines terminated with chip capacitor or radial stub are used, only even harmonic components can be blocked. It has been well known that the consideration of odd harmonic components are much more critical in the design of high-performance PA as they will degrade the linearity and power added efficiency of PA. This problem still remains largely unsolved.

To provide a high isolation between signal transmission line and bias line, the characteristic impedance of bias line should be higher than that of transmission line. As has been well known, a higher impedance transmission line has a narrower width. However, the DC bias line usually needs to carry a large current in the design of a high power PA. Therefore, a bias line of narrower

width can only carry a weaker current or produces more DC loss. This is the second problem affecting power added efficiency (PAE). A relationship between the current capability and the width of bias line was discussed [71] in detail.

In this thesis work, a low-impedance SIW bias line is proposed and developed for the first time to tackle the above-mentioned two problems. Simulation, design and experiments of the proposed SIW bias are described in section 1.1.2. In section 1.2.3, the performance of the proposed PA is discussed with comparison to the PA using conventional λ/4 high-impedance microstrip terminated with chip capacitor.

2.1.2 Design of SIW Bias Line

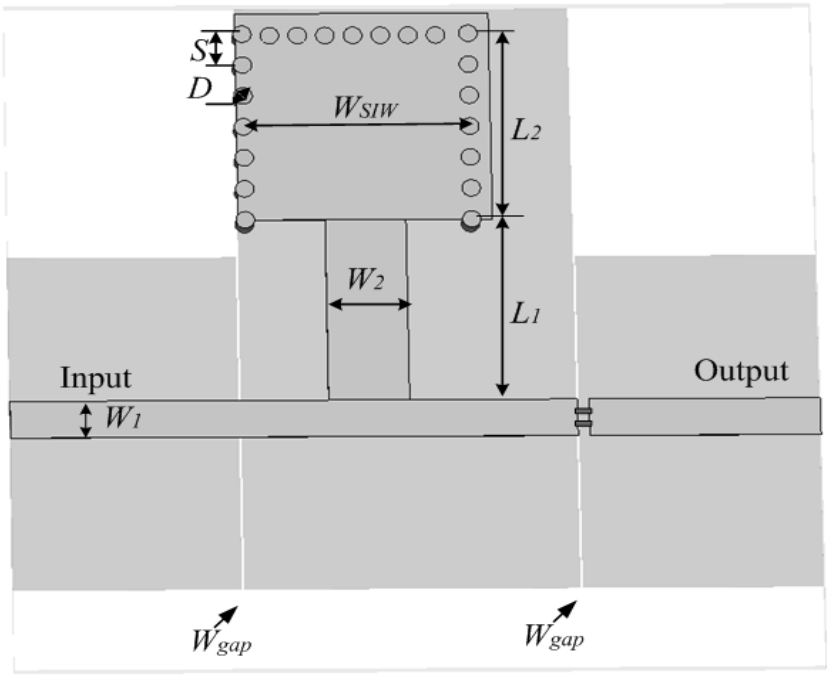

Figure 2.1: Three-dimensional view of the proposed λ/4 SIW bias line connected with 50Ω microstrip line

Figure 2.1 depicts the three-dimensional configuration of the proposed SIW bias line, where the light and dark gray areas stand for the top and bottom metal covers of the substrate, respectively. *D* and *S* are the diameter and period of the metallic vias of the SIW, and W_{SIW} is the SIW width that determines its cut-off frequency and thus the working frequency range of TE_{10} mode. W_1 is

the microstrip width that is chosen for 50 Ω. W_2 and L_1 are the width and length of λ/4 low-impedance bias line, respectively. L_2 is the length of the SIW. Gaps, whose width is W_{gap}, are used to isolate the ground and DC source in the ground because the metallic vias of the SIW contact the metal top and bottom covers of the substrate. The parameters of this structure are: S =0.8 mm, D=0.4 mm, W_{SIW}=9.4 mm, W_1=1.75 mm, W_2=3.5 mm, L_1=8.7 mm, L_2=8.4 mm, and W_{gap}=0.2 mm. However, in order to guarantee the RF signal continuous flow in the ground, chip capacitors whose value is 3 pF are used in gaps under the microstrip. A gap along the microstrip is used to block DC at the output port, and the value of the capacitor in this gap is also 3 pF.

In this work, let us define f for the amplifier working frequency. When the fundamental component f and 2nd harmonic component 2f are lower than the inherent cut-off frequency of the SIW, they are both shorted at the input port of the SIW. If L_1 is $\lambda_f/4=\lambda_{2\times f}/2$, the 2nd harmonic component 2f becomes shorted by this bias line as can be seen from the input to output but the fundamental component f will go through. It is similar to a λ/4 high-impedance transmission line terminated with radial stub. In order to suppress 3rd harmonic component 3f which is in the working frequency range of the SIW, this SIW is shorted by the metallic vias, where electrical length of L_1+ electrical length of L_2=n×pi (n=2,3,4…). Therefore, the 2nd and 3rd harmonic components are suppressed simultaneously in this case. In addition, the shorted SIW will effectively filter the signal, multi-tone products and harmonics generated by the PA from low to high frequencies for the DC source.

The circuits are simulated with the full-wave electromagnetic software Ansoft-HFSS and designed on substrate with a relative permittivity of 3.5 and a thickness of 0.8mm. The characteristic impedance of λ/4 low-impedance bias line is 11.5Ω when W2=3.5mm. This broad bias line with a width of 3.5mm can handle maximum current of 45A.

Figure 2.2 shows simulated and measured frequency responses of λ/4 low-impedance SIW bias line connected with 50Ω microstrip. The fundamental frequency is 4GHz. The results indicate that the fundamental frequency can pass through the microstrip while 2nd or 3rd harmonic components can be significantly reduced with this simple scheme.

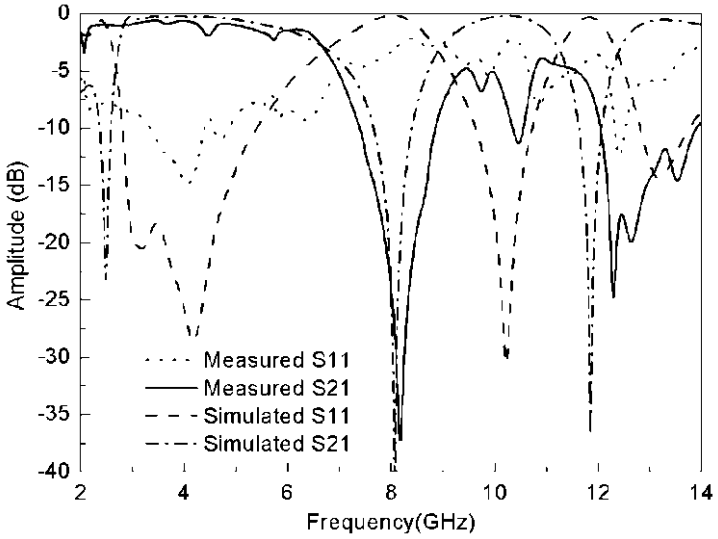

Figure 2.2: Simulated and measured frequency responses of λ/4 low-impedance SIW bias line connected with 50 Ω microstrip

2.1.3 Implementation of a C-band Power Amplifier Using SIW Bias Line

In the design of a PA with SIW bias line for demonstration purpose, a Eudyna's C-band power GaAs FET FLM3742-4F internally matched is used, where the working frequency range is from 3.7 to 4.2 GHz. The recommended bias voltage V_{GS}, V_{DS} and current I_{DS} are -1.06 V, 10 V and 1.1 A, respectively. In the test procedure, a pre-amplifier with a gain of 40 dB at 4 GHz and a 30 dB power attenuator are used too. For comparison with our proposed amplifier, a demo PA using λ/4 high-impedance microstrip terminated with 3 pF chip capacitor is measured. The demo PA is provided by Eudyna Devices Inc.

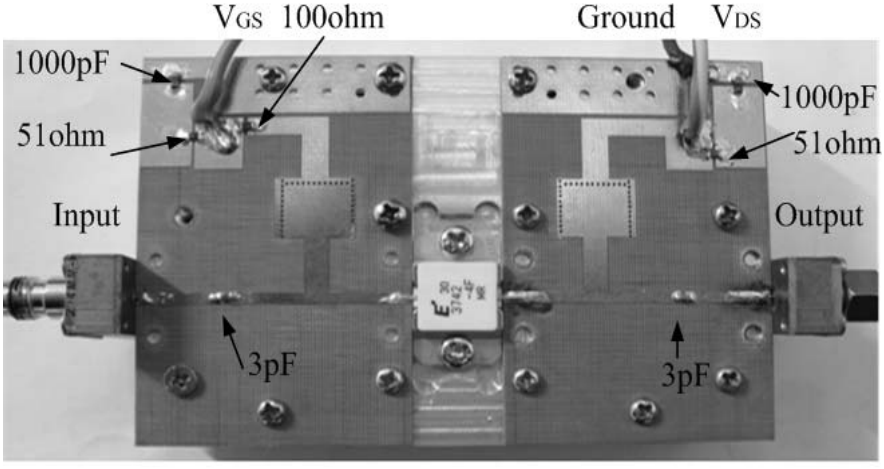

Figure 2.3: Photograph of the fabricated PA using λ/4 SIW bias line

The photograph of the fabricated PA using λ/4 SIW bias line is shown in Figure 2.3. Some chip capacitors and resistances are required for bias circuits and DC block. The value of the chip capacitor blocking DC is 3 pF.

Figure 2.4 displays measured small signal gains and return losses of two PAs. Demo PA has a gain of 14.5 dB at 4 GHz, similar to our proposed PA. However, our proposed PA has a higher gain from 3.4 to 3.6 GHz. When the input power is 20 dBm, 2^{nd} or 3^{rd} harmonic suppression with reference to the fundamental component of two PAs are measured. The measured results are listed in Table 2.1. The 2^{nd} or 3^{rd} harmonic components suppressions to the fundamental component of demo PA are 43 dBc and 45 dBc, while in our proposed PA, significant improvements in those suppressions reach to 22 dB and 13 dB, respectively. It is obvious that the 2^{nd} or 3^{rd} harmonic components can effectively be rejected by the SIW bias line. This phenomenon of harmonic suppression can also be found in Figure 2.2 and Figure 2.4.

Figure 2.5 plots two PAs' output powers and PAEs versus input power. In our proposed PA, the 1-dB output compression point is measured and determined at 35.1 dBm, which is higher than that of the demo PA by 0.2 dB. Figure 2.5 indicates that the improvement in output power and PAE are 0.3-0.8 dB and 0.5-3.3%, respectively.

This type of bias line can not only handle a high DC current, but also suppress the 2^{nd} and 3^{rd} harmonic components. Moreover, the proposed method is simple, low-cost and easy-to-use in the design of PA, which can be seen with many advantageous aspects in DC power handling and harmonic suppressions as well as PA performance improvement.

Table 2.1 Measured 2nd or 3rd Harmonic Suppressions to Fundamental Component of the Two PAs

Pin=20 dBm	**$P(f_0)$-$P(2f_0)$**	**$P(f_0)$-$P(3f_0)$**
Demo PA	43 dBc	45 dBc
Proposed PA	65 dBc	58 dBc
Improvement	22 dB	13 dB

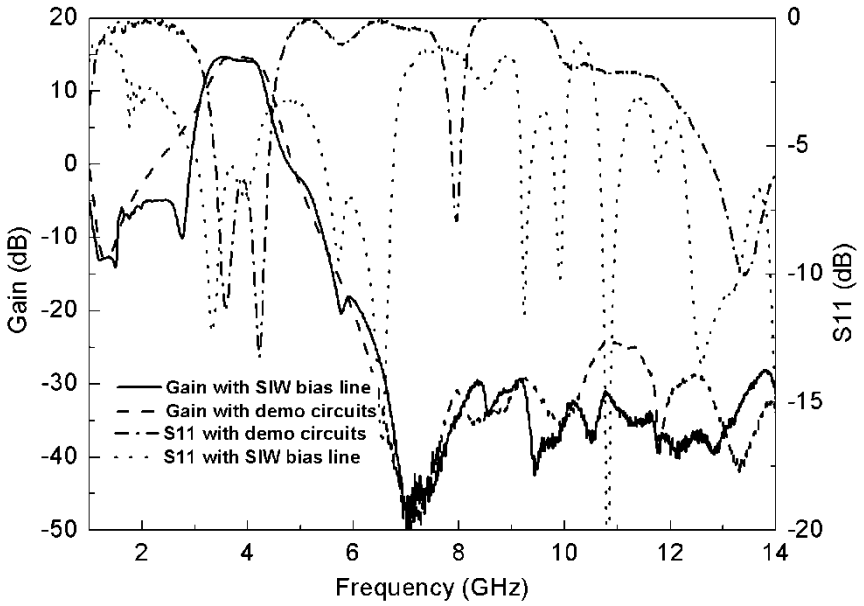

Figure 2.4: Measured small gains and return losses of the two PAs

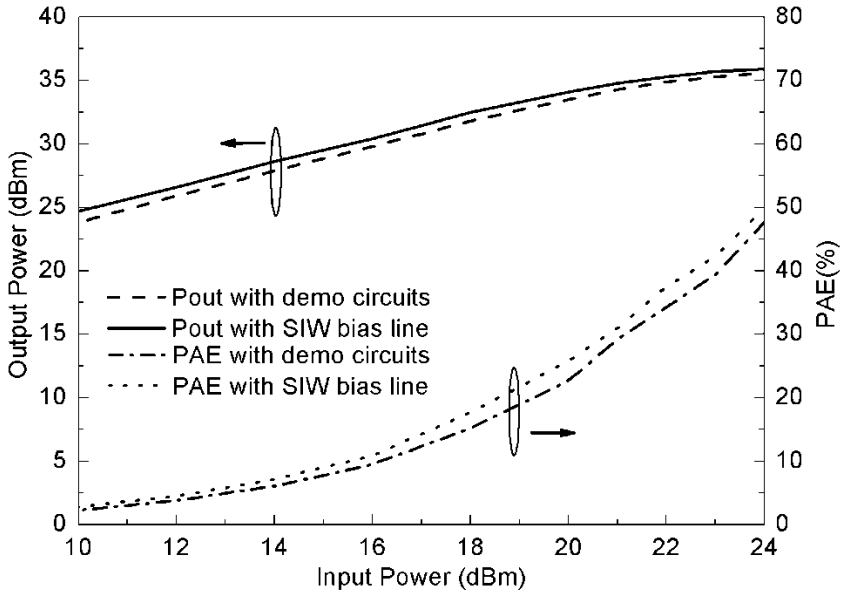

Figure 2.5: Measured output power and PAE versus input power of the two PAs

2.2 Singly Balance Mixer Using the Modified SIW Magic-T

2.2.1 Introduction of the Singly Balanced Mixer

Figure 2.6 shows conceptually one basic type of balanced mixers, which use 180 degree hybrids. In this case, the balanced mixer consists of two complete single diode mixers, represented by diode symbol, connected to mutually isolated ports of the hybrid. The other two ports, which are also mutually isolated, are used for the RF and LO inputs. Typically, the IF outputs from the two mixers are simply connected in parallel, although they sometimes are combined with another hybrid. Differences in performance between individual designs are related to their hybrids.

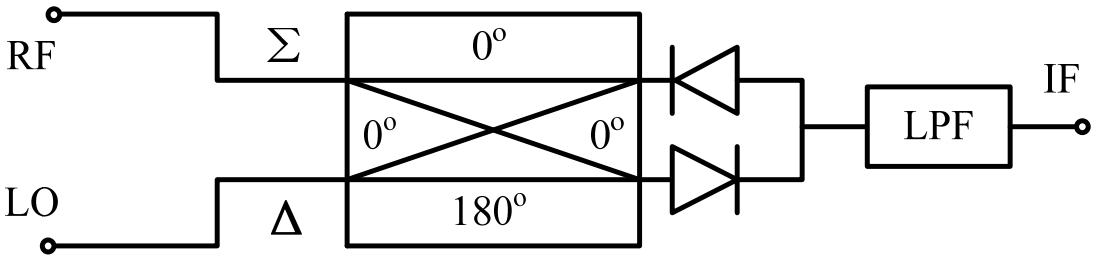

Figure 2.6: 180-degree singly balanced mixer

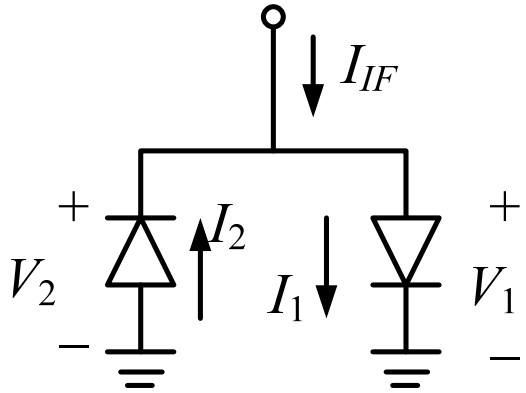

Figure 2.7: Currents and voltages in the diode with the *I/V* characteristic expressed by a power series.

From the viewpoint of electrical current, IF current I_{IF} can be represented by two exponential nonlinearity of the diode junction shown in Figure 2.7. I_1 and I_2 can be expressed by the following power series:

$$I_1 = aV_1 + bV_1^2 + cV_1^3 + dV_1^4 + \ldots \tag{2.1}$$

$$I_2 = -aV_2 + bV_2^2 - cV_2^3 + dV_2^4 + \ldots \tag{2.2}$$

where V_1 is the total AC voltage across diode no.1 (i.e., the RF plus the LO voltages), I_1 is the current, and lower-case letters represent constants; they are derived from the diode I/V characteristic and the DC bias voltage. If the diode is reversely polarized (the applied voltage is reversed), the signs of the odd-power terms become negative as shown (2.2).

From Figure 2.7, the IF current is

$$I_{IF} = I_1 - I_2 \tag{2.3}$$

With the LO applied to the delta port of the hybrid,

$$V_1 = -V_L \cos(\omega_p t) + V_{RF} \cos(\omega_S t) \tag{2.4}$$

$$V_2 = V_L \cos(\omega_p t) + V_{RF} \cos(\omega_S t) \tag{2.5}$$

Equations (2.4) and (2.5) are substituted into (2.1) and (2.2), and these, are in turn, substituted into (2.3), after some liberal use of trigonometric identities, the following generalizations are found to be true:

1. *k*th-order spurious responses, those arising from mixing between $mf_{RF} + nf_{LO}$ where m+n=*k*, arise only from the terms of *k*th power in (2.1) and (2.2).
2. All (m, n) spurious responses, where m and n are even, are eliminated.
3. The (2, 1) spurious response (m=±2, n=±1) is eliminated, but not the (1, 2).

If the LO and RF ports are reversed, the mixer has the same conversion loss and noise temperature as before. The AM LO noise rejection occurs because the additive (AM) LO noise is completely cancelled. The same is true for AM spurious signals on the LO.

2.2.2 Implementation of a X-band Singly Balance Mixer

As a practical and straightforward demonstration of our modified magic-T applications, a singly balanced mixer is designed as shown in Figure 2.8. An anti-parallel pair of serially connected diodes (SMS7630-006LF from Skyworks Inc) is adopted. Generally, a quarter-wavelength short stub in matching circuit is needed for providing a DC-return and good IF-to-RF and IF-to-LO isolations. However, a matching circuit can be designed between diode and SIW without using a quarter-wavelength short stub because the SIW is grounded inherently. Two $\lambda_{RF}/4$ open-circuited stubs on the right side of the diodes pair are used to provide terminal virtual grounding point for LO frequency and RF frequency simultaneously. In addition, a low pass filter is designed to suppress LO and RF signals at IF port. The mixer is designed and simulated by the Harmonic Balance (HB) method in Agilent ADS software combined with measured S-parameters of the wideband magic-T structure. Figure 2.9 shows the photograph of the proposed mixer.

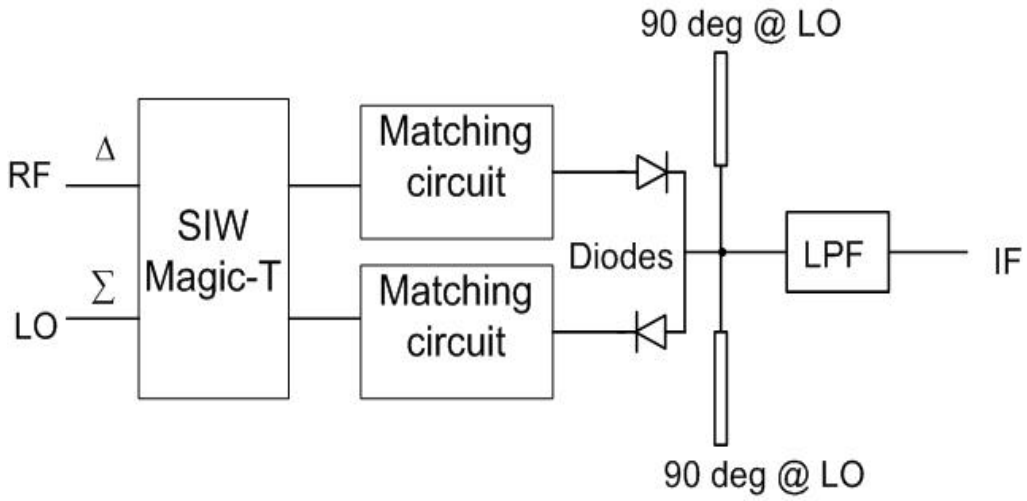

Figure 2.8: Circuit topology of the proposed mixer

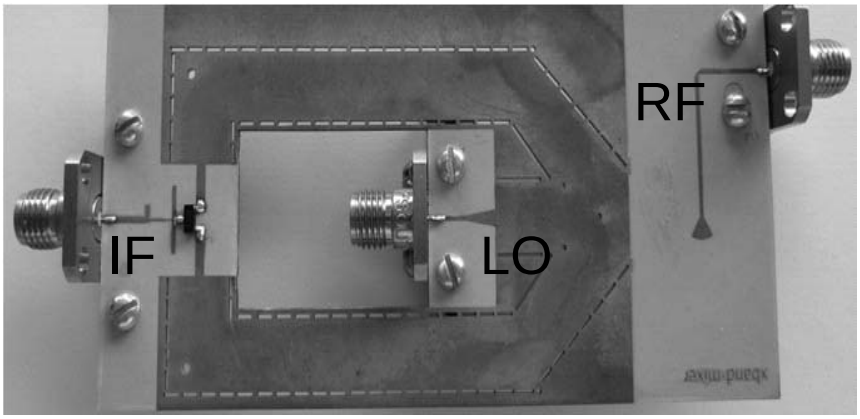

Figure 2.9: Photograph of the mixer

Figure 2.10 depicts the measured conversion loss versus LO input power level when IF signal is fixed at 1 GHz with an input power level of -30 dBm and LO frequency is fixed at 10.2 GHz. When LO input power level is larger than 13 dBm, the conversion loss remains around 7.4 dB. Figure 2.11 shows the measured conversion loss versus IF frequency when IF signal is swept from 0.1 to 4 GHz (RF is from 10.1to 6.2 GHz) with a constant input power level of -30 dBm and LO signal is fixed at the frequency of 10.2 GHz with 13 dBm power level. The measured conversion loss is about 8±0.6 dB over the IF frequency range of 0.1-3 GHz (RF is from 7.2 to 10.1 GHz). Figure 2.12 plots the measured conversion loss versus input RF power level, where RF frequency is set at 9.2 GHz and LO frequency is at 10.2 GHz with a power level of 13 dBm, input RF power level is swept from -30 to 5 dBm. The output IF power almost increases with the RF power linearly when the RF power level stays lower than -3 dBm. On the other hand, when the RF power level is larger than 0 dBm, the mixer is driven into its non-linearity region. From this figure, it can also be seen that the input 1-dB compression point is around 3 dBm. Moreover, the LO-to-IF isolation is about 40 dB. All the measurement results dictate that this mixer is suitable for wideband applications.

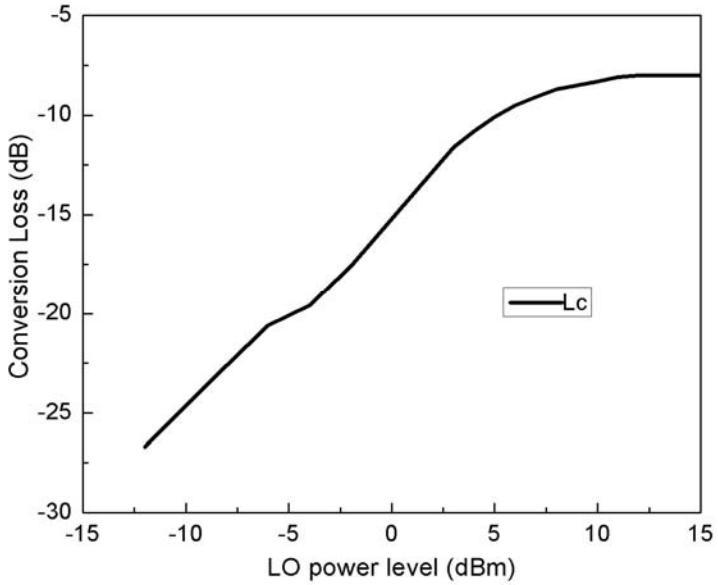

Figure 2.10: Measured conversion loss versus LO input power

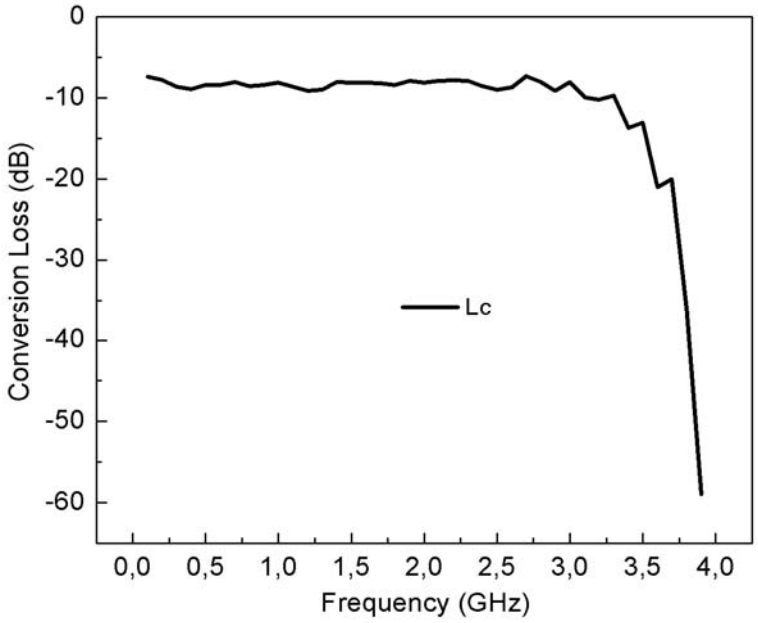

Figure 2.11: Measured conversion loss versus IF frequency

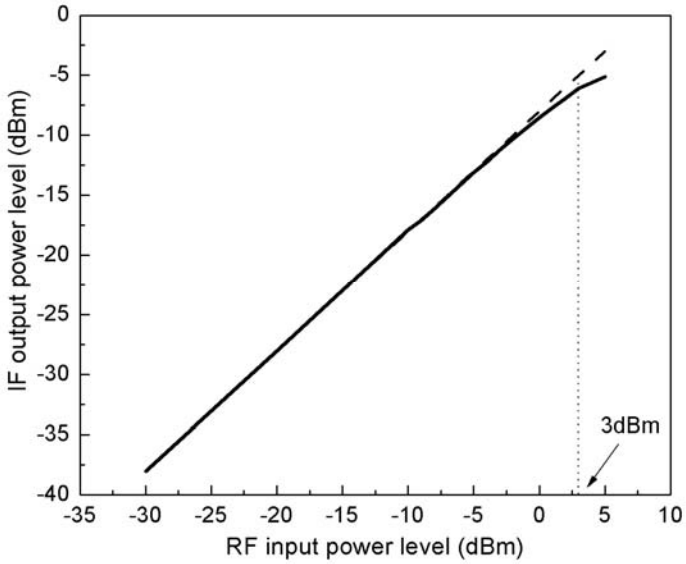

Figure 2.12: Measured IF output power versus RF input power

2.3 Reflective Transistor Oscillators Using Novel SIW Resonators

2.3.1 Introduction of Transistor Oscillator

A microwave oscillator converts DC power to RF power, and so is one of the most basic and essential components in a microwave system. A solid-state oscillator requires an active device, such as diode or transistor, in conjunction with a passive circuit to produce a sinusoidal steady-state RF signal. At startup, however, oscillation is triggered by transients or noise, after which a properly designed oscillator will reach a stable oscillation state. This process requires that the active device be nonlinear. In addition, since the device is producing RF power, it must have negative resistance. Because of this active and nonlinear element, the complete analysis of an oscillator operation is very difficult. Usually, one-port negative resistance oscillators use IMPATT or Gunn diodes. For transistor oscillator, either an FET or bipolar device is operated with a passive termination that produces a negative resistance at its input port. That is, the transistor is operated in an unstable region.

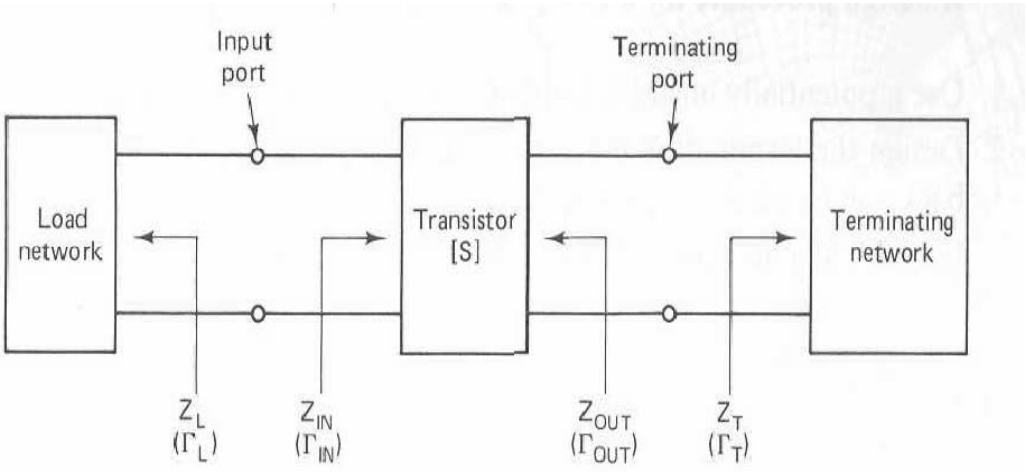

Figure 2.13: Two-port network configuration of transistor oscillator

Two-port network configuration is shown in Figure 2.13. The two-port network is characterized by the S parameters of the transistor, terminating impedance Z_T, and load impedance Z_L. The actual power output port can be on either side of the transistor. For an oscillator, we require a device with a high degree of instability. Typically, common source or common gate FET configurations are used, often with positive feedback to enhance the instability of the device. After a transistor configuration is selected, the output stability circle can be drawn in the Γ_T plane, and Γ_T is then selected to produce a large value of negative resistance at the input of transistor. Then load impedance Z_L can be chosen to match Z_{in} because such a design uses small-signal S parameters, and because R_{in} will become less negative as the oscillator power builds up, it is necessary to choose R_L so that $R_L + R_{in} < 0$. Otherwise, oscillation will cease when the increasing power raises R_{in} up to the point where $R_L + R_{in} > 0$. In practice, a value of

$$R_L = \frac{-R_{in}}{3} \tag{2.6}$$

is typically used. The reactive part of Z_L is chosen to resonate the circuit,

$$X_L = -X_{in} \tag{2.7}$$

When oscillation occurs between the load network and the transistor, oscillation will simultaneously occur at the output port, which we can show as follows. For steady-state oscillation at the input port, we must have $\Gamma_L\Gamma_{in}=1$. Then we have

$$\frac{1}{\Gamma_L} = \Gamma_{in} = S_{11} + \frac{S_{12}S_{21}\Gamma_T}{1 - S_{22}\Gamma_T} = \frac{S_{11} - \Delta\Gamma_T}{1 - S_{22}\Gamma_T} \tag{2.8}$$

where $\Delta = S_{11}S_{22} - S_{12}S_{21}$. Solving for Γ_L gives,

$$\Gamma_T = \frac{1 - S_{11}\Gamma_L}{S_{22} - \Delta\Gamma_L} \tag{2.9}$$

Then we have

$$\Gamma_{out} = S_{22} + \frac{S_{12}S_{21}\Gamma_L}{1 - S_{11}\Gamma_L} = \frac{S_{22} - \Delta\Gamma_L}{1 - S_{11}\Gamma_L} \tag{2.10}$$

which shows that $\Gamma_T\Gamma_{out}=1$, and hence $Z_T = -Z_{out}$. Thus the condition for oscillation of the terminating network is satisfied. Note that appropriate S parameters to use in the above development are generally large-signal parameters of the transistor.

2.3.2 Overview of Microwave Resonators

Resonant structures are extensively used as network elements in the realization of microwave oscillators and filter circuits. Microwave energy can be stored in resonator circuit consisting of either lumped elements or distributed elements. Whatever the type is, the following basic resonator parameters have resonant frequency, equivalent models and quality factor Q [72].

Resonant frequency is the frequency at which the electric and magnetic stored energies are equal; i.e. the input impedance of the circuit is purely a real value. It is more convenient to present the resonant frequency definition through the concept of lumped element models. Physical unloaded resonators may be approximated by lumped element series or parallel RLC circuits in the vicinity of their resonant frequency, as shown in Figure 2.14. The input reactance X_{in} reflects the ideal behavior of the resonator, while the resistance R represents the loss mechanisms inside that resonator. It is known that a parallel resonance presents its highest impedance magnitude to the input port at the resonant frequency f_0 , while a series resonance presents its lowest impedance magnitude at f_0 . A series RLC model has a constant resistance, while a parallel RLC model displays a constant conductance. In the case of a series resonance, the input reactance is

$$X_{in} = \frac{-1}{\omega C} + \omega L \tag{2.11}$$

While at resonant frequency ω_0 , X_{in} =0 and thus

$$\omega_0 = \frac{1}{\sqrt{LC}} \tag{2.12}$$

In the case of a parallel resonance model,

$$X_{in} = \frac{\omega L}{1 - \omega^2 LC} \tag{2.13}$$

Therefore, the resonance frequency of the simplest lumped-element model with parallel or series components is always given by:

$$f_0 = \frac{1}{2\pi\sqrt{LC}} \tag{2.14}$$

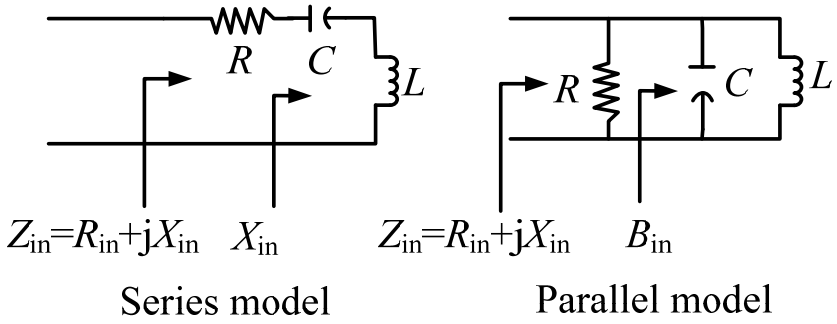

Figure 2.14: Simplest series and parallel lumped-models for an unloaded resonator

From another point of view, resonators may be divided into one port (reflection type) and two port (transmission) types. Therefore, in one port case, the resonance frequency can be defined as the frequency at which minimum reflection occurs; i.e. the energy absorbed in the resonator is at its maximum. One the other hand, the resonance frequency of two ports is the frequency at which maximum transmission occurs; i.e. the energy absorbed in the resonator is the minimum.

The main characteristic of the resonator is the quality factor. In terms of energy ratio it is defined as [73]:

$$Q = \omega \frac{\left(time - averaged \quad energy \quad stored \quad in \quad the \quad resonator \right)}{\left(engergy \quad loss \quad per \text{ second } in \quad the \quad resonator \right)} \tag{2.15}$$

The amplitude of the stored energy will decay because of the resonator circuit's electrical resistance. The rate of decay depends on the resonator's quality factor Q. The lower the Q, the greater the rate of decay. It is clear that the higher the Q of series resonators, the lower its minimum Z_{in}, while the higher the Q of parallel resonators, the larger its Z_{in}. High-Q resonators can be used to build very stable, low noise oscillators. Low-Q resonators are employed in broadband tuned oscillators.

For distributed resonator circuits, the total energy stored in the resonator is obtained by integrating the energy density over the resonator volume. The electric and magnetic energies are given by [74]:

$$W_e = \frac{\varepsilon}{2} \int_v |E|^2 dv \tag{2.16}$$

$$W_m = \frac{\mu}{2} \int_v |H|^2 dv \tag{2.17}$$

At resonance both energies should be equal, i.e.

$$W_e = W_m = W$$

On the other hand, the sources of losses inside a resonator may be due to conductor, dielectric or radiation losses. The average conductor power loss in a metallic resonator is obtained by integrating the power density over the inner metal surface of the resonator.

$$P_{lc} = \frac{R_S}{2} \int_S |H_t|^2 da \tag{2.18}$$

where R_S is the surface resistance of the resonator.

Thus, Q_c due to the conductor loss, assuming lossless dielectric filling, can be obtained as follows

$$Q_C = \frac{\omega W}{P_{lc}} = \frac{\omega\mu \int_v |H|^2 \, dv}{R_S \int_S |H_t|^2 \, da} \tag{2.19}$$

where H_t is the peak value of the tangential magnetic intensity.

Q_d is the Q when a lossy dielectric medium is present but the walls are perfectly conducting assuming no radiation;

$$Q_d = \frac{\omega W}{P_{ld}} \tag{2.20}$$

where P_{ld} is the power loss due to the dielectric only.

Q_r is the quality factor due to radiation losses:

$$Q_r = \frac{\omega W}{P_{rad}} \tag{2.21}$$

where P_r is the power loss due to the dielectric only

Thus the resultant unloaded Q, denoted Q_u of resonant cavity is given by

$$\frac{1}{Q_u} = \frac{1}{Q_c} + \frac{1}{Q_d} + \frac{1}{Q_r} \tag{2.22}$$

Q_u is called unloaded Q because the dissipated power is calculated inside the structure only excluding any coupling to an external load. But, in a practical situation, the resonant circuit is coupled to a load that also dissipates power. If the power dissipation is calculated inside the external load, only the quality factor will be denoted $Q_{ext.}$ On the other hand, if the Q is due to both load coupling and resonator losses it will be denoted as loaded quality factor Q_L. The loaded quality factor Q_L is given by

$$\frac{1}{Q_L} = \frac{1}{Q_u} + \frac{1}{Q_{ext}} \tag{2.23}$$

Planar resonators are used in MMICs such as oscillators but also in filters. A microstrip resonator is a planar conductor, which is deposited on a dielectric substrate. Commonly, microstrip shapes are rectangular, circular disk, circular ring, triangular and rhombus resonators. The amplitude of the current that flows on structure becomes significant when the signal frequency is close to a

resonance. But they offer low Q values. For example, such planar resonator's Q is still limited (less than 300) [75].

As we all know, a rectangular waveguide presents a high Q value of more than thousands because it has conducting enclosures or cavities without any dielectric losses. They are difficult to tune, however. In general, the main disadvantage of cavity resonators is their bulky volume and hence their unsuitability for small size requirements in many modern applications. However, dielectric-filling versions of this class of resonators are very promising and can be readily implanted in packaging environments such as SIW by replacing the vertical metallic walls by closely spaced via posts as shown in Figure 2.15.

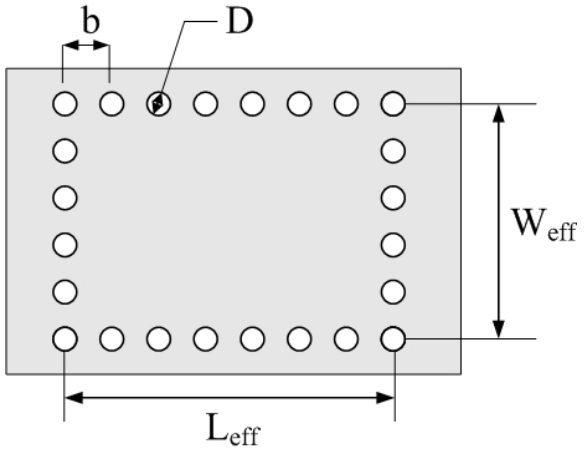

Figure 2.15: Typical top view of an SIW cavity structure

Microwave and millimetre-wave components based on SIW, which can easily be integrated with other planar circuits, have the advantages of high Q-factor, low insertion loss, and high power capability and etc. A number of applications based on the SIW technology have been reported [76]-[84], especially a high Q resonator that was designed with such a technique [84]. So far, oscillators based on this resonator have been developed [84].

A typical SIW cavity resonator is shown in Figure 2.15. According to [76], propagation properties of a TE_{10}-like mode in the SIW are very similar to the TE_{10} mode of a rectangular waveguide. As a result, an SIW cavity can be designed by using the following equations

$$F_R(TE_{moq}) = \frac{c_0}{2\sqrt{\varepsilon_r}}\sqrt{(m/W_{eff})^2 + (q/L_{eff})^2} \tag{2.24}$$

Where W_{eff} and L_{eff} are the effective width and length of the SIW cavity.

Note that because of a small thickness of the dielectric substrate, only modes with no variation along this direction take place in the frequency band of interest. The unloaded quality factor of the cavity can be approximated by the following equation:

$$\frac{1}{Q_u} = \frac{1}{Q_c} + \frac{1}{Q_d} + \frac{1}{Q_{leakage}} \tag{2.25}$$

where quantities Q_c and Q_d are designated for a rectangular waveguide cavity. $Q_{leakage}$ is Q factor due to leakage losses from between metallic vias. If $b < \lambda_0 \times \sqrt{\varepsilon_r}/2$ and $b < 4D$ are satisfied, $Q_{leakage}$ will be neglected. An estimate of Q_u is obtained by using effective dimensions of the SIW cavity in (2.26). Figure 2.16 shows electric field distribution of the fundamental mode for the SIW cavity. The maximum electric field strength is placed at the center of the SIW cavity while magnetic fields surround the center of the cavity.

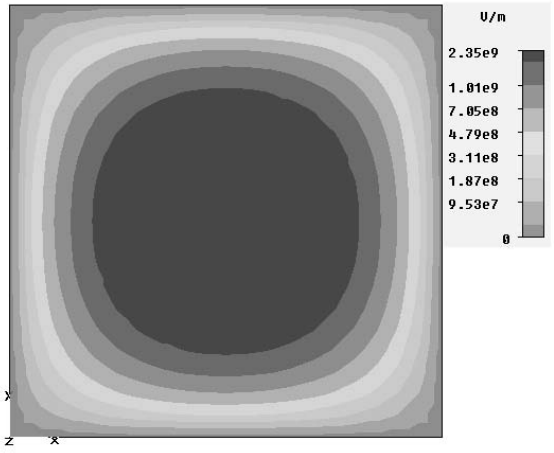

Figure 2.16: Electric field distribution of the fundamental mode for the SIW cavity

2.3.3 Tunable SIW Cavity Resonator

Presently, many studies of SIW resonator and its applications have been carried out for filters and oscillators. However, only few tunable SIW resonators have been studied because it is difficult to integrate SIW resonator with other tuning devices such as varactor. Although one tunable SIW

resonator was developed in [85], it cannot be tuned continuously. In this thesis work, we have proposed a continuously electrically tunable SIW reflective cavity resonator that can be used to design tunable devices such as VCOs and tunable filters. This resonator makes use of a typical SIW cavity resonator that is combined with a surface mounted varactor to realize the desired tuning function. Compared to the coaxially packaged components combined with the SIW [85], the fabrication complexity decreases greatly in this case.

Figure 2.17 illustrates the top view of the physical configuration of an electrically tunable SIW reflective cavity resonator. The white and gray areas stand for substrate surfaces and metal covers of the substrate, respectively. The separate circular metal cover is used to provide a DC bias for the varactor. The resonator is designed and fabricated on Rogers/duroid 6002 substrate with ε_r=2.94 and t=0.508 mm. Parameters in this structures are W=13.6 mm, L=13.8 mm, W_A=2.6 mm, W_P=0.2 mm, L_P=3.0 mm, W_G=0.2 mm, L_d=1.8 mm, R=1.2 mm, L_G=0.4 mm, L_S=0.6 mm, W_S=0.3 mm and W_m=1 mm. In the following section, we will explain how to mount the varactor and set the DC bias line in detail. As for circuit design, the cavity and its external coupling to the cavity using microstrip are firstly developed, and then the cavity coupling to the varactor is designed.

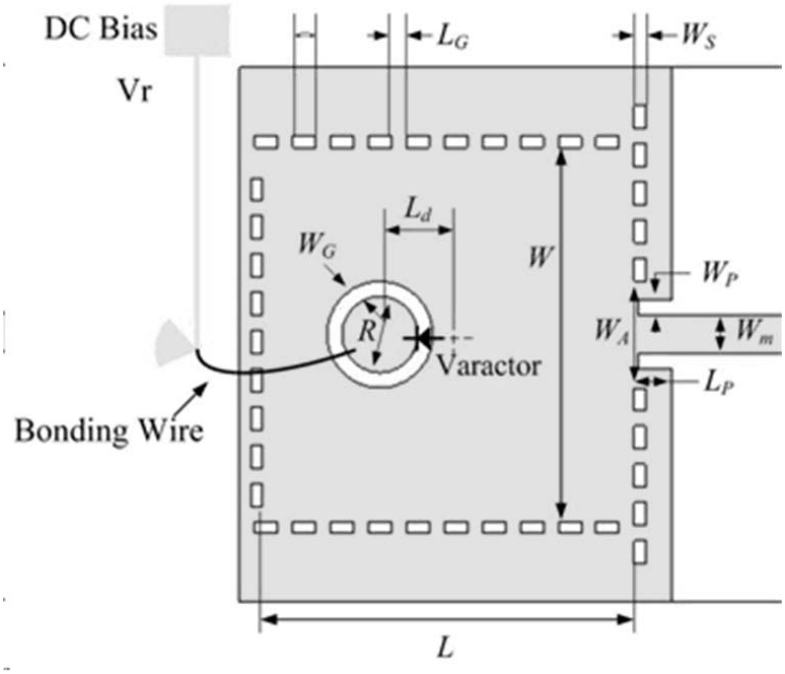

Figure 2.17: Top view of the physical configuration of an electrically tunable SIW reflective cavity resonator

As shown in Figure 2.17, the metallic holes are replaced by metallized slot trenches for brevity, where W_S is the width of these slots. The resonant frequency of the H101 mode is 9.01 GHz for W=13.6 mm and L=13.8 mm. An estimate of Q_u is obtained by using effective dimensions of the SIW cavity in the above formulas. In this case, we can use (2.25) to calculate the unloaded Q-factor of the H_{101} mode SIW cavity to be 374.

The energy is coupled to the cavity by means of effective current probes with microstrip line. The current probes are built by removing metallic slots on one side of the cavity to make place for an insert as illustrated in Figure 2.18. The probe is merely a prolongation of the microstrip in the cavity that is then shorted-circuit. As the probes are comparable in size to the cavity, they can change the frequency of resonance. A three-dimensional (3-D) electromagnetic simulator is necessary to accurately design the cavity. The strength of the coupling of a current probe mainly depends on depth L_P, width W_P and W_A of the probe.

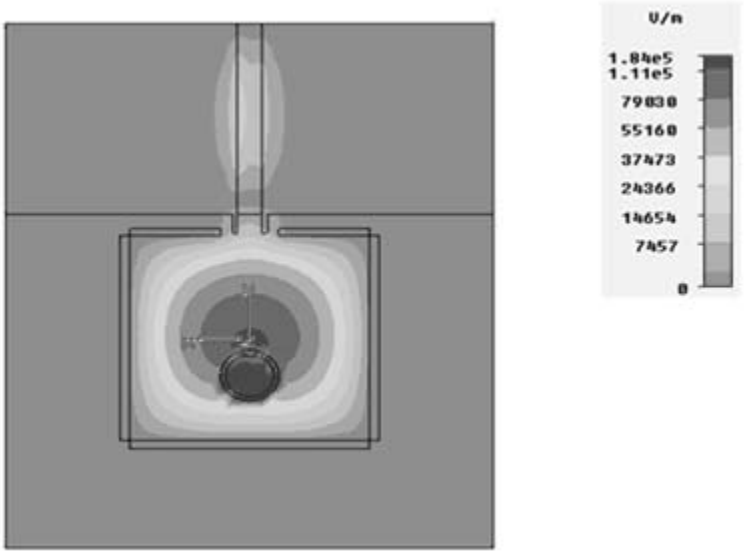

Figure 2.18: Electric field distribution of the electrically tunable SIW reflective cavity resonator.

Figure 2.19 and Figure 2.20 show the simulated and measured S11. We can see that the simulated and measured resonant frequencies are slightly different because of the deviation in dielectric constant and fabrication error. The measured resonant frequency is 8.955 GHz. In [86], a one-

port reflection technique was proposed to extract the unloaded Q_U and loaded Q_L from the measured return loss. At the resonant frequency, the coupling coefficient can be obtained from return loss as:

$$\mathbf{RL}o = -20\log\left|\frac{1-\beta}{1+\beta}\right| \tag{2.26}$$

where RLo is the return loss at the resonant frequency. From the equation above, we can generate,

$$\beta = \frac{1-10^{-\frac{RLo}{20}}}{1+10^{-\frac{RLo}{20}}} < 1 \tag{2.27}$$

or

$$\beta = \frac{1+10^{-\frac{RLo}{20}}}{1-10^{-\frac{RLo}{20}}} > 1 \tag{2.28}$$

Coupling coefficients β in equations (2.27) and (2.28) correspond to the under-coupling case and the over-coupling case, respectively. Through the response circle in the Smith Chart (Figure 2.20), these two solutions can easily be distinguished. Usually, a small response circle excluding the origin of the Smith Chart signifies an under-coupling case; for the over-coupling case, the response circle is large and encloses the origin. In this design, the over-coupling is indicated as shown in Figure 2.20. According to RLo=5.36 dB, β=3.35 has been calculated from (2.26). Figure 2.19 and (2.38) also helps us to calculate the loaded Q_L=90. Therefore, the unloaded Q_U=390 can be calculated by

$$Q_U = Q_L(1+\beta) \tag{2.29}$$

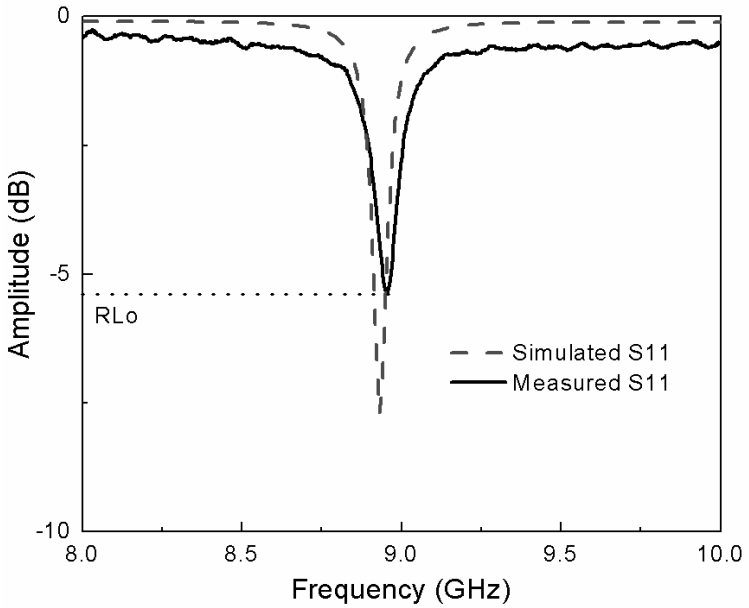

Figure 2.19: Simulated and measured return losses of the reflective SIW cavity resonator.

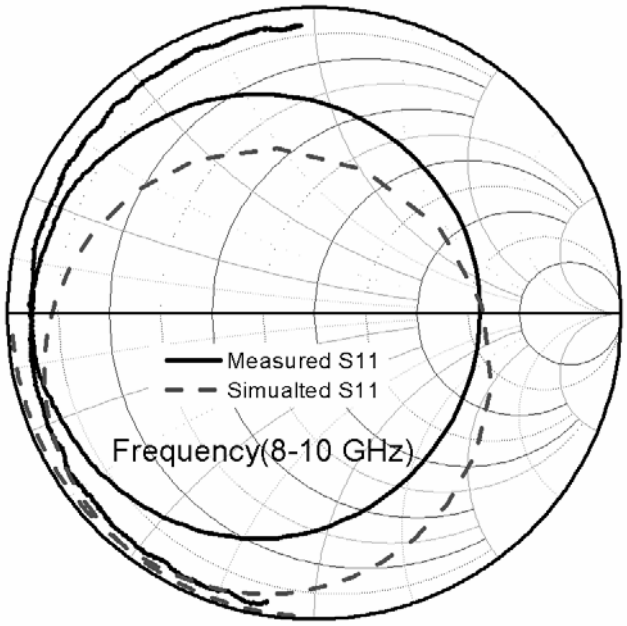

Figure 2.20: Measured and simulated return losses of the SIW cavity resonator in the Smith Chart.

In the SIW structure, the metallic slots connect the top metallic cover to the bottom metallic cover, and so the top metallic cover cannot be used for DC bias line or connected with DC bias line of active devices. Therefore, it is necessary to use a separated metallic cover to connect DC bias for active devices. In our instance, the circular metallic cover with a diameter of R is used for DC bias, where W_G is the width of the gap and L_d is the distance from the centre of the separated circle to the centre of the cavity. The bias line outside of the cavity can be connected to the circle metallic cover through a bonding wire. Since the circle metallic cover provides DC bias for the varactor, while its cathode is connected on the circle metallic cover and its anode is connected on the other top metallic cover (ground). Figure 2.18 shows that the electric field in the cavity can be coupled to the separated metallic cover through the gap, so the varactor will mainly be excited by a electrical coupling. If distance L_d changes from 0.6 to 3 mm, the simulated resonant frequency will shift downward from 9.17 to 9.03 GHz, but Q_L almost keeps constant. When L_d equals to 1.8 mm, the measured oscillation frequency is 9.113 GHz and Q_L equals to 125. Measured and simulated results indicate that the ring slot will increase the resonant frequency and Q_L of the SIW cavity.

Table 2.2: Parameters of the varactor diode

Model	**V_{BR} MIN V**	**C_T**			**Q MIN**
		MIN (30 V) pF	**NOM (4 V) pF**	**MAX (0 V) pF**	
MSV34060-0805-2	30	0.3	0.46	1	6300
Package	C_P Typ pF	**Tuning Ratio MIN**		**Rs MAX Ω**	**L_P Typ nH**
0805-2	0.06	3.0		1.3	0.4

In the following part, we will investigate how physical length L_d and the tuning capacitance of varactor C_T affect the tuning range of resonant frequency. Figure 2.21 shows simulated S11 of

the two cases when C_T is swept from 1.1 to 0.3 pF. When L_d equals to 3 mm, the resonant frequency varies from 8.441 to 8.861 GHz, which results in a tuning range of 4.85%; when L_d equals to 0.6 mm, the resonant frequency increases from 8.510 to 9.005 GHz and the tuning is about 5.65%. Simulated results indicate that the tuning range will increase as distance L_d decreases. The increment of the tuning range also indicates that the coupling strength increases between cavity and capacitor C_T.

In the design of electrically tunable SIW cavity resonators for the demonstration purpose, an aeroflex/metelics silicon varactor diode MSV34060-0805-2 is used. Parameters of the varactor diode are listed in Table I. The tuning capacitance of varactor C_T can be obtained about from 0.3 to 1 pF when the reverse voltage varies from 30 to 0 V. Distance L_d=1.8 mm is chosen in this case.

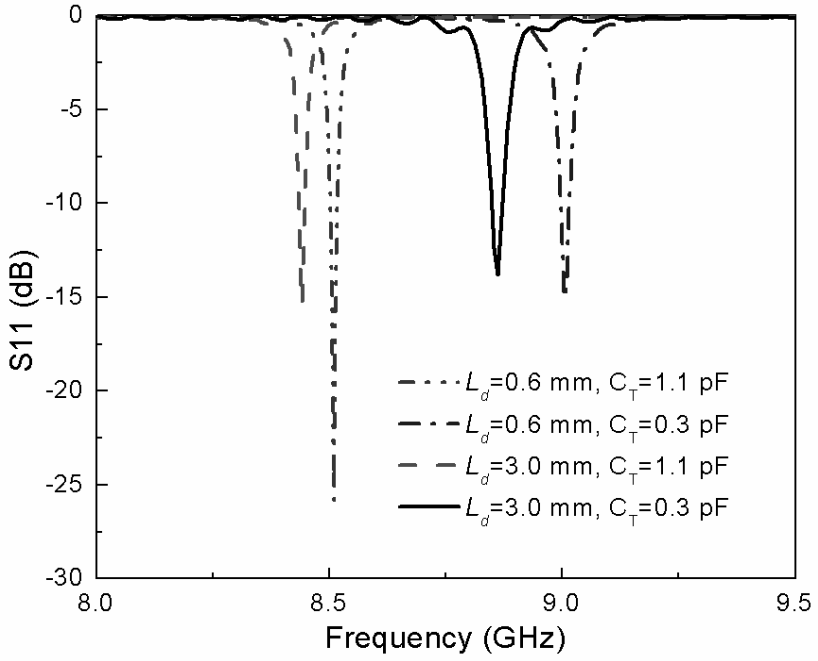

Figure 2.21: Simulated S11 versus C_T when L_d =3 mm and L_d=0.6 mm

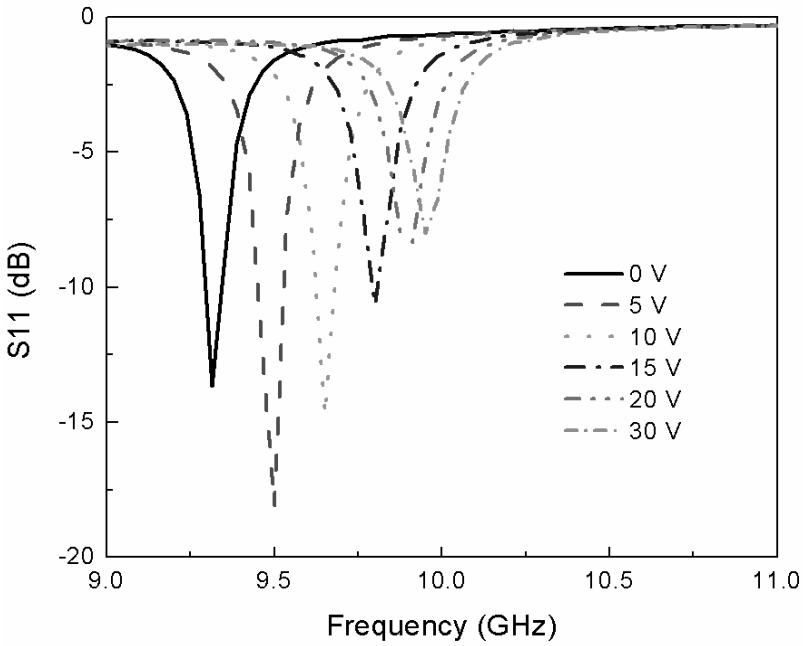

Figure 2.22: Measured S11 of the reflective tunable resonator

Figure 2.22 displays measured S11 versus DC bias voltage for the varactor. The resonant frequency of the tunable reflective resonator changes from 9.32 to 9.95 GHz while the DC bias voltage is swept from 0 V to 30 V. The tuning range is about 630 MHz or 6.54% and Q_L changes from 55 to 53. So if the varactor is mounted, the unloaded Q therefore varies from 132 to 138. Compared to characteristics of the SIW resonant cavity, the varactor has some side effects on the unloaded Q of this resonator. In the design, measured results do not agree well with simulated results due to the parasitic effects introduced to circuit after the mounting of varactor and connection of the DC biasing line. These parasitic effects are very hard to model since they are not consistent. So we do not propose an equivalent circuit of the tunable resonator in this thesis work. Finally, this proposed resonator provides a way to resolve the problem of tuning of the SIW cavity. The measured results will be used to simulate the proposed VCO in the following section.

2.3.4 Tunable HMSIW Cavity Resonator

This section presents a novel electronically tunable HMSIW cavity resonator at microwave frequency. The resonant frequency of the cavity resonator is tuned with different DC biasing voltage applied over a varactor coupled to the HMSIW cavity like SIW tunable cavity resonator in the above section.

In chapter 1, HMSIW concept was described. We know that a HMSIW cavity resonator also retains the advantages of high Q-factor while it has a compact size compared with its conventional SIW counterpart. Figure 2.23 shows electric field distributions of the fundamental mode for the HMSIW and SIW cavities. The maximum electric field strength is located at the center of the SIW cavity while magnetic fields surround the center of the cavity. So the HMSIW cavity resonator is realized by cutting the cavity along its symmetric line. Moreover, the resonant frequency of the HMSIW cavity almost remains the same as that of the SIW cavity while the former is formed by cutting the latter. The HMSIW cavity, therefore, is designed as a normal SIW cavity. The tunable cavity in this thesis is simulated with a full-wave CAD software Ansoft-HFSS12 and designed on Duroid 6002 substrate with a dielectric constant of 2.94 and a thickness of 0.254mm.

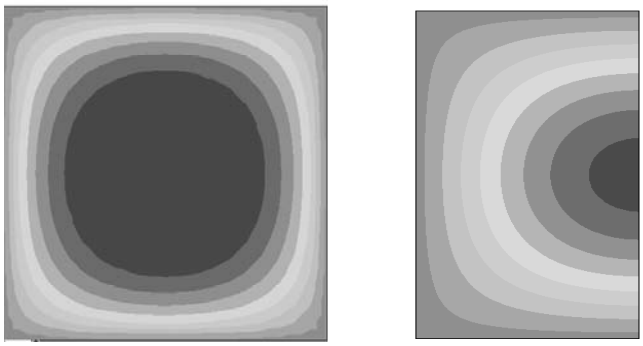

Figure 2.23: Electric field distribution of the fundamental mode for the SIW and HMSIW cavitie

Figure 2.24 depicts the top view of physical configuration of the electrically tunable HMSIW reflective cavity resonator. The white and yellow areas stand for the substrate and metal covers of the substrate, respectively. The HMSIW cavity can be designed by using the following equation as an SIW cavity:

$$F_R(TE_{moq}) = \frac{c_0}{2\sqrt{\varepsilon_r}}\sqrt{(m/W)^2 + (q/2L)^2} \qquad (2.30)$$

As shown in Figure 2.24, the metallic holes are replaced by metallic slots, where W_S is the width of these slots. Resonant frequency is 9.88GHz if W=10.6 mm and L=8 mm. So we can use Equation (2.25) to calculate the unloaded Q-factor of the H_{101} mode HMSIW cavity, which is 250.

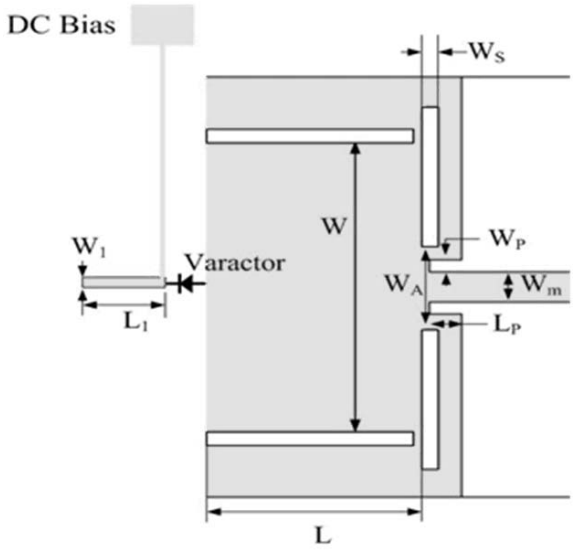

Figure 2.24: Top view of physical configuration of the electrically tunable HMSIW reflective cavity resonator

The energy is coupled to the cavity by means of a current probe with the microstrip line as in the same case as the SIW cavity design in the above section. The strength of the coupling of a current probe will mainly depend on depth Lp, width Wp and W_A of the probe. In this work, we use a weak coupling to calculate the loaded Q_L of the cavity. Figure 2.25 illustrates the equivalent circuit for an HMSIW cavity coupled to a microstrip line which has a characteristic impedance of 50 Ohm.

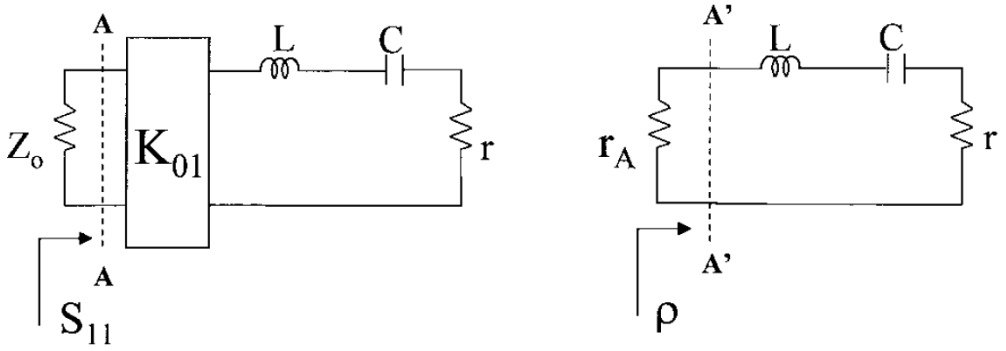

Figure 2.25: Equivalent circuit of an HMSIW cavity without varactor

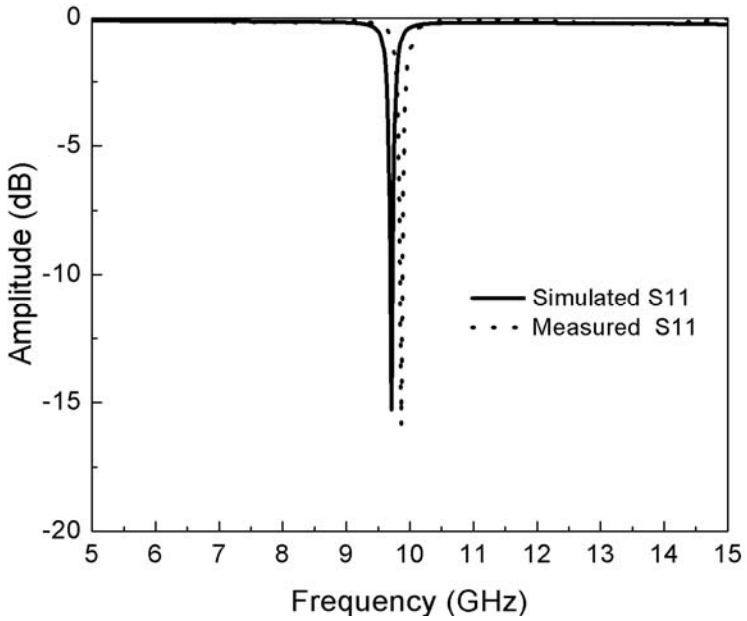

Figure 2.26: Simulated and measured return losses of the HMSIW cavity

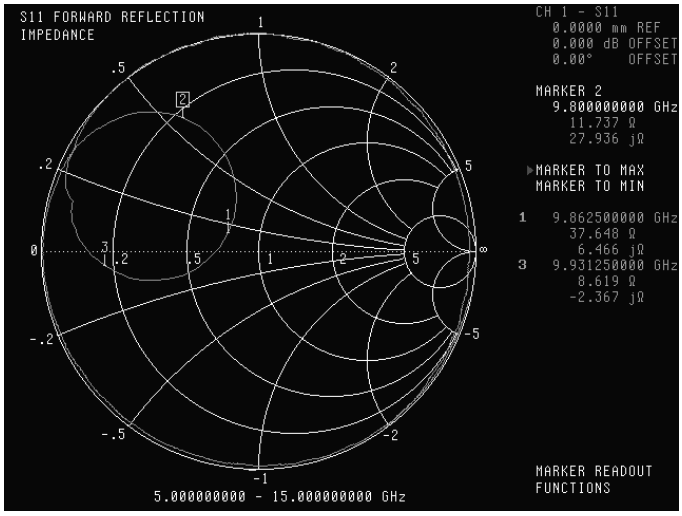

Figure 2.27: Measured return loss of the HMSIW cavity in Smith Chart

Figure 2.26 and Figure 2.27 show the simulated and measured S11, which indicate the simulated and measured resonant frequencies are slightly different because of the difference of dielectric constant and fabrication tolerance. The measured resonant frequency is about 9.86 GHz. In this design, the under-coupling is indicated as shown in Figure 2.27. According to RLo=16 dB and (2.27)-(2.29), β=0.75 has been calculated. Figure 2.26 also helps us calculate the loaded Q_L=95. Until now, the unloaded Q can be calculated by (2.29). Consequently, Q_U =166. We may notice

that measured unloaded Q is lower than the unloaded Q which is calculated from Equation (2.25) due to radiation loss introduced by non-ideal magnetic wall (MW) of the HMSIW cavity while the resonance is taking place.

For the HMSIW resonant cavity, the varactor can be integrated with it on MW by adding a piece of metallic cover that can be used to mount the active device, as shown in Figure 2.24. In the HMSIW structure, the metallic slots connect the top metallic cover to the bottom metallic cover, so the top metallic cover cannot be used for DC bias line or connected with DC bias line of active devices, as explained in one of the previous sections. Therefore, anode of the varactor is connected to MW and its cathode is connected to a ¼ wavelength microstrip open stub that acts as an open-short circuit for virtual grounding. So the DC reverse voltage can be provided for varactor by the stub. In our example, the open stub has a width of W_1 and a length of L_1. According to the physical diagram, the varactor series connection to cavity is assumed.

Figure 2.28 gives the photograph of the fabricated electrically tunable HMSIW reflective resonant cavity. For our demonstration purpose, an Aeroflex/Metelics silicon varactor diode MSV34060-0805-2 is used to design this electrically tunable HMSIW cavity resonator. Parameters of the varactor diode that was tested with 4V reverse voltage are listed in Table 2.2. The tuning capacitance of varactor C_T can be obtained from 0.25 to 1 pF while the reverse voltage varies from 30 to 0 V.

In the following, we will discuss the relationship between the tuning range of frequency and tuning capacitance of C_T. Figure 2.29 shows simulated and measured S11 of the two cases when C_T is swept from 0.25 to 1 pF. Measured results agree well with simulated results. Measured S11 indicates that the resonant frequency of the tunable reflective resonator changes from 10.06 to 10.42 GHz while the DC bias voltage is changed from 0 to 30 V. That is, the tuning range can be calculated as 3.52%. A larger tuning range can be expected by decreasing C_T. When C_T equals to 0.15 pF, the resonance takes place at 10.8 GHz. However, the resonant frequency is 10.1 GHz if C_T is fixed as 1.5 pF. On the other side, the changing trend of the resonant frequency versus C_T demonstrates the capacitor is connected to the cavity in series. When the resonant frequency sweeps from 10.06 to 10.42 GHz, the loaded Q changes from 81 to 86. So with the varactor, the unloaded Q sweeps from 145 to 156 using equation (2.30). Compared to characteristics of the HMSIW resonant cavity, the varactor has only little effect on the unloaded Q of this resonator.

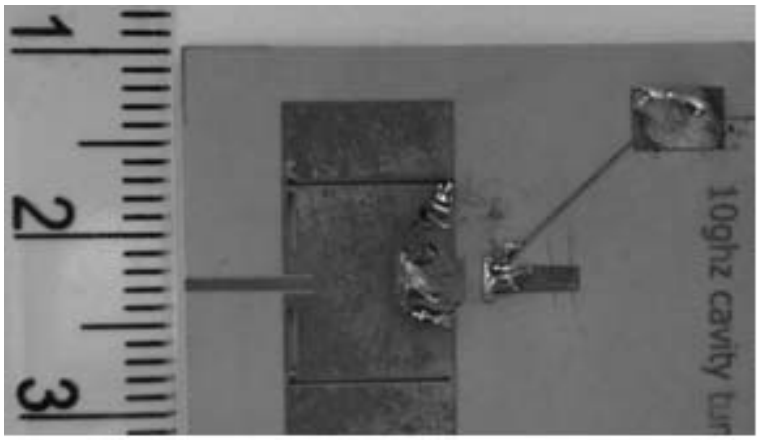

Figure 2.28: Photograph of the fabricated electrically tunable HMSIW reflective cavity resonator

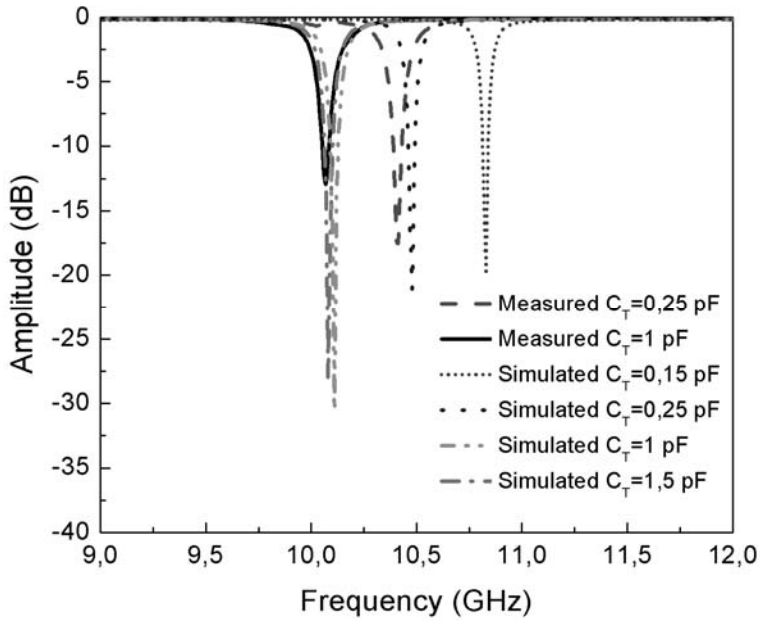

Figure 2.29: Simulated and measured return losses of the tunable resonator

For a further study of the HMSIW tunable resonator, it is important to establish an equivalent circuit of this resonator. According to the above analysis and the equivalent circuit of the varactor listed in Table 2.2, the equivalent circuit is built up as described in Figure 2.30. Inductor L, capacitor C and resistor r constitutes the HMSIW resonant circuit plus some additional parasitic parameters. Through resonant frequency $F_0=1/(2\times Pi(L_0\times C_0)^{0.5})$ and unloaded $Q=(L_0/C_0)^{0.5}/R$, we can establish a system of equations using different resonant frequency with different C_T. Then

solving the system of equations leads to the equivalent circuit development. In this design, r=3.1 Ohm, L=8.2 nH and C=0.03 pF have been obtained. Because C is very small, the tuning range can be broadened using a varactor with small C_T.

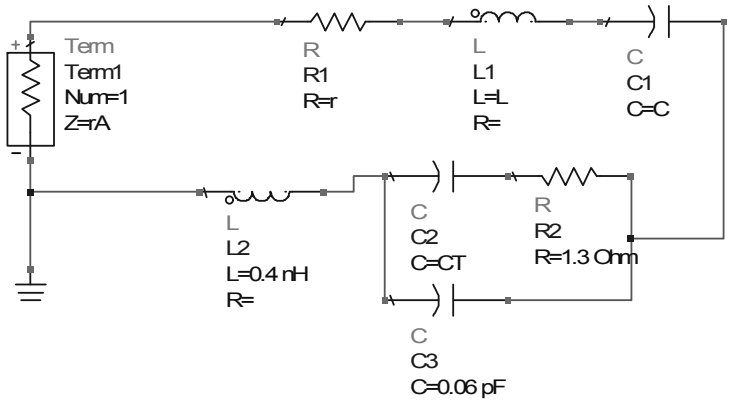

Figure 2.30: Equivalent circuit of an HMSIW cavity with varactor

2.3.5 Implementation of an X-band VCO

As is well known, the SIW has advantages of high-Q as described in the above sections. Therefore, many studies on filters and oscillators, which make use of such advantages, have been presented so far. For instance, based on the SIW resonator, several microwave and millimetre-wave oscillators with fixed oscillation frequencies have been investigated and developed. In [87], a feedback-type oscillator using an SIW cavity resonator as the frequency selector, which has a phase noise of 73 dBc/Hz at 100-kHz offset, was developed. A Ka-band Gunn diode oscillator with a phase noise lower than 91.23 dBc/Hz at 100-kHz offset was also reported in [88]. Moreover, SIW cavity resonator oscillators have been developed on the analysis of a relationship between Q-factor and phase noise [89]. However, most radar and communication applications need a VCO as the LO source. So far, VCOs based on SIW resonator have not been reported because it is difficult to design tunable SIW resonators. In this thesis work, we propose a VCO based on the tunable SIW cavity resonator introduced in section 2.3.3.

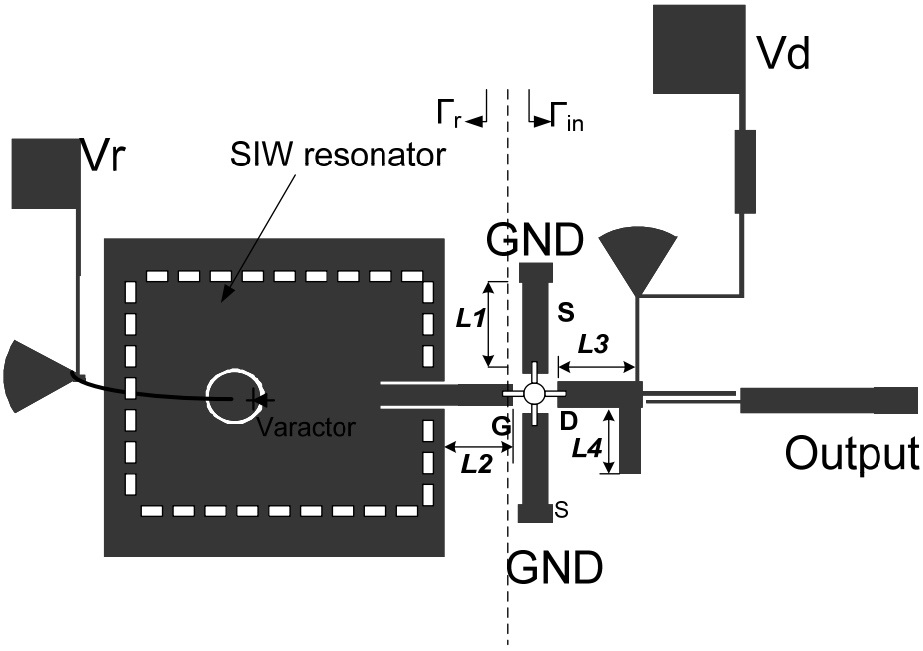

Figure 2.31: Physical configuration of the reflective SIW VCO

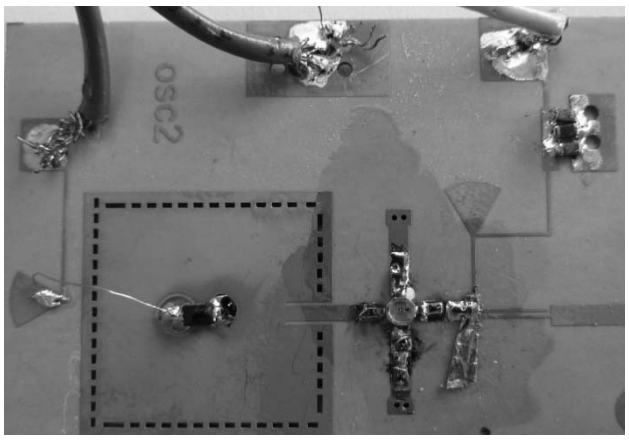

Figure 2.32: Photograph of the fabricated VCO

Figure 2.31 describes the physical configuration of the proposed reflective SIW resonator VCO. This configuration consists of a reflective tunable SIW cavity resonator and a transistor with an output matching network and a quarter-wavelength interdigital capacitor. On the other hand, the VCO design is based on the negative resistance concept using a common-source series feedback element to generate the negative resistance. The active device used is an Agilent ATF36077 ultra low noise pseudomorphic high electron-mobility transistor (HEMT). The feedback element

generating instability in the VCO is a short stub with length *L1*. A 65-Ω microstrip with length *L2* used at the gate side is to establish the required negative conductance and meet the oscillation conditions $|\Gamma_r| \bullet |\Gamma_{in}| > 1$ and $Arg(\Gamma_r) = Arg(1/\Gamma_{in})$. The frequency tuning is realized with a variable capacitance mounting on the SIW tunable cavity. Since the SIW is inherently grounded, this oscillator has the gate voltage Vgs=0. Dimensions of the VCO are *L1*=4.6 mm, *L2*=3.2 mm, *L3*=4 mm and *L4*=4.1 mm. Figure 2.32 shows the photograph of the fabricated VCO.

The proposed VCO is measured using a test fixture (Wiltron 3680) and a spectrum analyzer (Agilent E4440A) with respect to major performance parameters including the oscillation frequency, the output power, the second harmonic suppression and the phase noise. Figure 2.33 shows the measured oscillation frequency and the output power versus the reverse bias voltage V_r applied on the varactor, while the applied bias voltages of the pHEMT is Vd=1.5 V and Id=20 mA. The power consumption is about 37 mW. The tuning range of the oscillation frequency varies from 9.356 GHz (0 V) with an output power of 6.4 dBm to 9.816 GHz (13.3 V) with an output power of 9.3 dBm. The centre oscillation frequency is 9.586 GHz (6 V) and the tuning range is 4.8%. When voltage V_r is more than 13.3 V, the oscillation frequency suddenly changes to and keeps at 9.98 GHz. This phenomenon indicates that the oscillation conditions are just met at 9.98 GHz if we apply V_r more than 13.3 V. Measured phase noise of the VCO is better than 88 dBc/Hz at an offset frequency of 100-kHz over the all tuning frequency range as shown in Figure 2.34. The second harmonic is suppressed by more than 33 dBc compared to the fundamental oscillation frequency. The best suppression of 50 dBc occurs at 9.816 GHz (13.3 V). Therefore, the second harmonic has little effect on the fundamental oscillation. Figure 2.35 plots measured phase noise smoothed when the oscillation frequency is 9.4425 GHz (2 V).

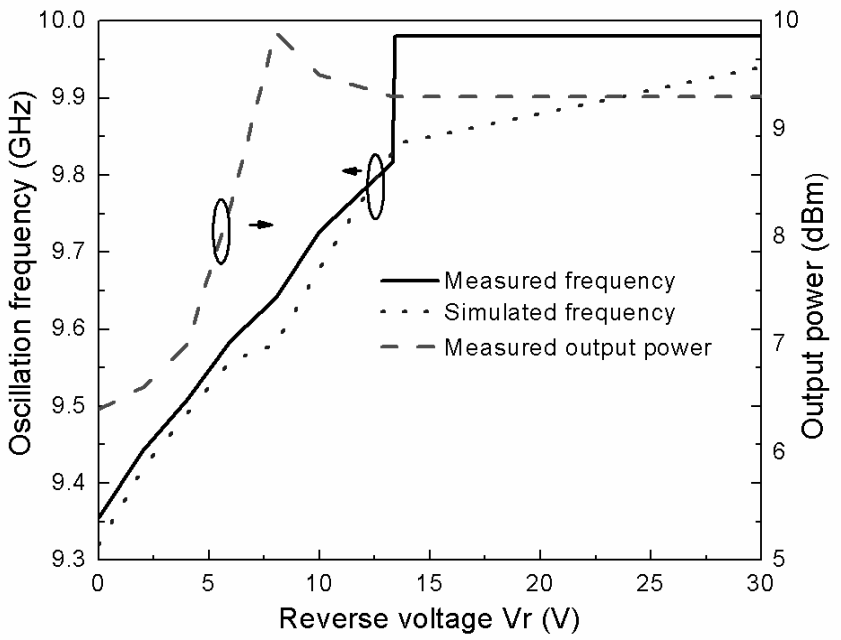

Figure 2.33: Measured and simulated oscillation frequencies and measured output power versus the reverse bias voltage V_r

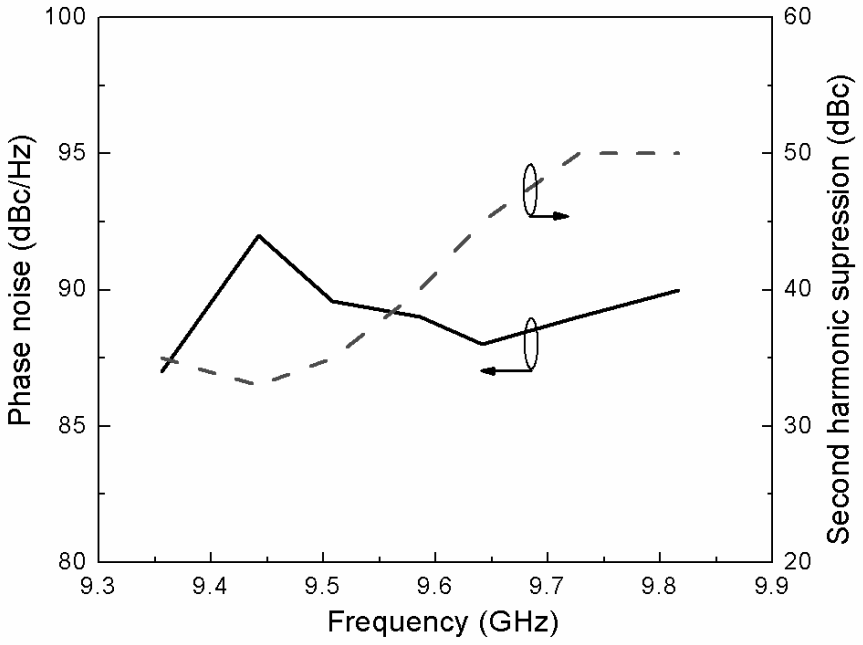

Figure 2.34: Measured phase noise@100-kHz offset and second harmonic suppression

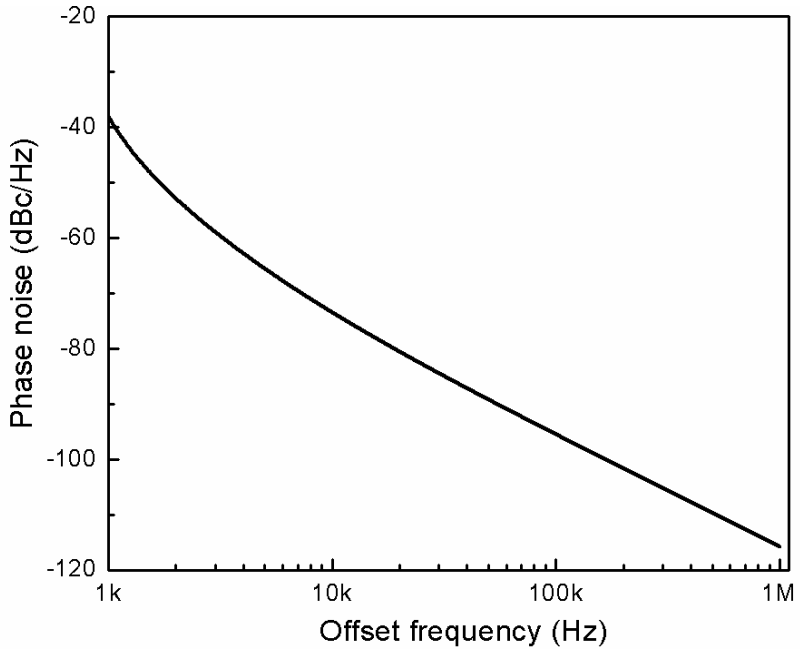

Figure 2.35: Measured phase noise when V_r=2 6V

Table 2.3: Performance of reported VCOs

Ref.	Fc (GHz)	Pout (dBm)	L@1MHz (dBc/Hz)	Offset (MHz)	FOM (dB)	Technology
[90]	11.8	-7	-123	1	183.9	0.5 um SiGe
[91]	7.8	1.92	-125.3	1	192.5	0.25 um SiGe
[92]	10.81	-8.83	-116.6	1	185.2	0.25 um COMS
[93]	9			3	177	180 nm COMS
This work	9.5	7.5	-117	1	184	SIW PCB

For comparison among other VCOs, the figure of merit (FOM) is used as

$$\mathrm{FOM} = -\mathrm{L}(\Delta \mathrm{f}) + 20\log(\frac{\mathrm{f}_0}{\Delta \mathrm{f}}) - 10\log(\mathrm{P}) \tag{2.31}$$

where f_0 is the oscillation frequency, Δf is the offset, L (Δf) is the phase noise at offset Δf and P (mW) is the DC power consumption of the VCO. The measured X-band VCO has a FOM of 184

dBc/Hz. Table 2.3 lists the performance of state-of-art VCOs based on IC technology. Measured results show that our proposed VCO has many advantages such as low cost, easy planar integration and low phase noise. The VCO will be very useful in cost-effective wireless systems.

2.4 Conclusion

In this chapter, a series of novel active components based on SIW are presented. First, The PA using λ/4 low-impedance SIW bias line is proposed and developed for the first time with a prototype measured in C-band. This type of bias line can not only handle a high DC current, but also suppress the 2nd and 3rd harmonic components by 22dB and 13dB as indicated in our case study. The output power, 1-dB output compression point and PAE of our proposed PA are higher than those of the demo PA by 0.3-0.8dB, 0.2dB and 0.5-3.3%, respectively. The proposed method is simple, low-cost and easy-to-use in the design of PA, which can be seen with many advantageous aspects in DC power handling and harmonic suppressions as well as PA performance improvement. Next, a singly balanced mixer, which employs the modified magic-T proposed. The measured conversion loss is about 8±0.6 dB over the IF frequency range of 0.1-3 GHz. Other performances of this mixer are also measured. All the measurement results dictate that this mixer is suitable for wideband applications. Finally, we propose electrically tunable SIW and HMSIW reflective cavity resonators. The tunable SIW and HMSIW cavity resonator have been proposed and analyzed. Proposed tunable resonators not only realize a tuning function by adjusting the DC biasing voltage of the varactor but also retain the inherent high Q characteristics of the SIW cavity resonator. Then, a novel planar VCO based on the proposed SIW tunable resonator is designed and fabricated. Measured results show that our proposed VCO has many advantages such as low cost, easy planar integration and low phase noise. The VCO may be very useful in cost effective wireless systems.

CHAPTER 3 ACTIVE INTEGRATED ANTENNA ARRAY USING SIW ALTSA

In this chapter, active integrated antenna (AIA) arrays, which are used for power combining, are presented using SIW ALTSA. The concept of AIA and design of the SIW ALTSA are introduced in the first and second sections, respectively. Next, three types of AIA array on the basis of the SIW ALTSA, including rectenna array, sub-harmonically up-converter antenna array and spatial PA, are proposed. In these three parts, we will begin the presentation of an X-band spatial PA that is proposed, designed and fabricated in this work. Next, a Ka-band sub-harmonically pumped up-converter antenna array is proposed, which can be considered as a transmitter due to its low cost, high dynamic range and high linearity. Finally, the proposed Ka-band rectenna array is used to convert RF energy to DC energy in microwave power transmission or RF energy recycling system.

3.1 Introduction of AIA

The AIA has been a growing area of research in recent years, as the microwave integrated circuits (MICs) and monolithic microwave integrated circuits (MMICs) technologies has become more matured allowing for high-level integration. From a microwave engineer's viewpoint, an AIA can be regarded as an active microwave circuit in which the output or input port is related to free space instead of a conventional 50- interface. In this case, the antenna can provide certain circuit functions such as resonating, filtering, and duplexing, in addition to its original role as a radiating element. On the other hand, from an antenna designer's point-of-view, the AIA is an antenna that possesses built-in signal and wave-processing capabilities such as mixing and amplification. A typical AIA consists of active devices such as Gunn diodes or three-terminal devices to form an active circuit, and planar antennas such as dipoles, microstrip patches, bowties, or slot antennas. Looking back into history, the idea of using active antennas can be traced back to as early as 1928 [94]. At that time, a small antenna with an electron tube was commonly used in radio broadcast receivers around 1 MHz. After the invention of high-frequency transistors, the study of active antennas received much more attention and several pioneering works were reported [95]-[104] in the 1960s and 1970s. Several advantages of implementing the active devices in passive radiating elements were discussed in [105]. For instance, these works include increasing the

effective length of short antenna and increasing antenna bandwidth, decreasing the mutual coupling between array elements, and improving the noise factor.

Over the past ten years, the major driving forces for the research on AIAs are the development of novel efficient quasi-optical power combiners [106]-[107]. The original purpose for the quasi-optical power combining is to combine the output power from an array of many solid-state devices in free space to overcome combiner loss limitations, which are significant at millimetre-wave frequencies [108]-[109]. Most solid device components of spatially combined arrays are oscillators and amplifiers. In the designed oscillator arrays, for example, an external reference signal or a high Q-factor external cavity was added to lock the oscillator element [110]. They have also shown an interesting functionality of beam control. Compared with oscillator arrays, PA arrays are more attractive because of its stabilization and lower noise. 120W X-band and 36W 61GHz spatial PA combiners were developed [111]-[112]. Other spatially combined arrays using phase shifters, frequency multipliers and mixers were developed with special features [113]-[115]. In those cases, each output power with the same amplitude and phase is combined in space through the far field of antenna. So the combining efficiency mainly depends on the array factor and the coherence of array elements. This combiner usually has a larger size, but also can less restricted requirement on dimensional accuracy.

In microwave and millimetre-wave region, SIW is such a technology that high-performance SIW antenna and other SIW active and passive components can easily be designed and developed such as mixer and filter. Therefore, various AIA arrays based on SIW technology are considered in our work. In this thesis, all AIA arrays are proposed on the basis of SIW-ALTSA, which is a high-performance antenna with high-gain and wide-band. This antenna will be described and designed in the following section.

3.2 Design of SIW ALTSA

The LTSA has been reported for years. Due to its salient features such as narrow beam width, high element gain, wide bandwidth and small transverse spacing between elements in arrays, it has attracted much interest in many applications [116]-[120]. Practically, the performance of the LTSA is mainly determined by the feeding system. In the previous research, some feeding strategies such as balanced microstrip, fin line, coplanar waveguide (CPW), microstrip to slot line transition, and inverted microstrip line (IML) have been reported, and some good performances

have been demonstrated. However, conventional microstrip-like feeding systems suffer from significant tradeoff problems between cost and performance at microwave and millimetre-wave frequency. Like printed-circuit transmission lines, SIW components are low-cost, small size and mass-producible. Unlike printed-circuit transmission lines, which suffer from inherently significant losses at high frequency, SIWs have high Q-factors and high-integrations. Thus, the SIW feeding system presents an excellent candidate for microwave and millimetre-wave applications [121]. The results of this SIW-ALSTA show that it has features of wide-band and high-gain. In this thesis, details and design procedure of the proposed feeding system of constructed prototype are presented.

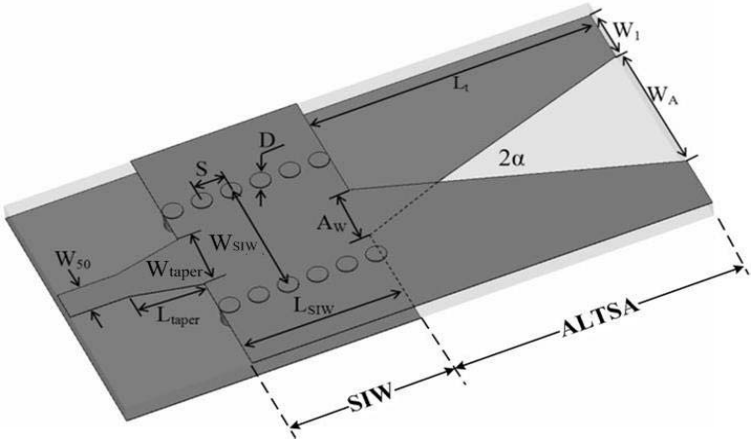

Figure 3.1 : Physical 3D configuration and parameters of SIW ALTSA

Figure 3.1 depicts the physical 3D configuration of an ALTSA with SIW feeding system and microstrip-SIW transition where the dielectric constant and thickness of substrate are denoted by ε_r and t, respectively. The light gray and dark gray areas mean the substrate and metal covers of the substrate, respectively. The SIW-microstrip transition is used for connecting the active circuits to the antenna, W_{50} and W_{taper} are the widths at both ends of the microstrip taper for matching the antenna impedance to 50Ω, and L_{taper} is the length of the taper. The SIW section simply transforms the unbalanced microstrip to the balanced SIW feeding system for the ALTSA, where D and S are the diameter and period of the metallic vias, respectively, and W_{SIW} is the SIW width which determines its cut-off frequency and thus the working frequency range of TE_{10} mode. Length L_{SIW} of the SIW section should be chosen properly to minimize the insertion loss and return loss. For the ALTSA, the metallic covers gradually stretch out on the opposite sides of the

substrate by angle 2α. Linear tapers from the overlapped metallic covers to tapered slot antenna can change the vertical field polarization of the SIW to the horizontal field polarization of the tapered slot antenna (TSA), and also match the low input impedance of the SIW to the high input impedance of TSA. A good impedance matching can be obtained by adjusting width A_w, length L_t and angle 2α. If a good matching performance cannot be obtained, we may match the ALTSA to air by adjusting width W_1, consequently the entire ALTSA matching can be adjusted to its optimal performance. The gain of an ALTSA is mainly determined by length L_t .

From references [115]-[119], one can identify an approximate optimum range of about 0.005 to 0.03 for the effective dielectric thickness t_{eff} of a substrate normalized to the free-space wavelength λ_0, which is defined by

$$\frac{t_{eff}}{\lambda_0} = \left(\sqrt{\varepsilon_r} - 1\right)\frac{t}{\lambda_0} \qquad (3.1)$$

where t is the actual substrate thickness.

The design procedure of the SIW-ALTSA can be summarized as follows:

a) Given the working frequency and the gain of ALTSA with the SIW feeding system.

b) According to a), substrate thickness t, via diameter D, period S, and width W_{SIW} will be determined by using formula (3.1).

c) On the basis of b), W_{taper} and L_{taper} can be designed and optimized to yield a good performance of the return loss [122].

d) Choose a proper value of L_{SIW}, then L_t, A_w and 2α will be optimized to obtain a good antenna performance.

3.3 Design of Spatial PA

Over the last two decades, spatial power combining and quasi-optical techniques for microwave and millimetre-wave applications have rapidly been developed [123]-[124]. Many spatial power combiners have made use of active antennas or integrated antennas incorporating solid state devices to build up the architecture of arrays. Since there are no additional dielectric and metal

losses in space, the spatial power combining technology provides a much higher combining efficiency by coupling the components to beams or modes in free space than its circuit-levelled counterparts such as corporate combining, especially when the number of combined solid-state devices is large. For instance, the insertion loss of 1-dB will decrease the combining efficiency to about 78%. In 1993, R.N.Simons and R.Q.Lee firstly proposed 3-elements spatial PA by integrating LTSAs and MMIC PAs [125]. This spatial PA consisting of 11dBi LTSA and 11 dB gain MMIC PA has 30 dB gain at 20 GHz. But microstrip feeding LTSA has parasitic radiations which increase mutual coupling and affect far-field radiation pattern.

In this section, an X-band spatial PA using active SIW-ALTSAs is proposed, designed and fabricated, the measured gain is 32dB. Each of the antenna elements has a gain of about 11dBi and the mutual coupling between antenna elements has been analyzed. The design is suitable for constructing a large array using monolithic integration techniques.

3.3.1 Performance of X-band SIW ALTSA

In section 3.2, we described the working principle and design procedure of SIW ALTSA. Here the performance of the X-band SIW ALTSA for the spatial PA is introduced.

The antenna is designed and fabricated on the substrate with ε_r=2.2 and t=1 mm. Dimensions of the designed Ka-band SIW-ALTSA are D=0.4 mm, S=0.8 mm, L_{SIW}=10 mm, W_{SIW}=16.8 mm, W_{taper}=8 mm, L_{taper}=5 mm, L_t=90 mm, A_W=8 mm, W_1=7 mm, W_A=40 mm, $\alpha=15.2^0$. The SIW feeding system is determined by the cut-off frequency of 6.56 GHz and the working frequency range 8.2~12.4 GHz of TE_{10} mode. The SIW-ALTSA cell is simulated with a full-wave CAD software (Ansoft-HFSS in our case). Measured return loss and gain are shown in Figure 3.2. From 8.2~12.5 GHz, measured return loss S_{11} is lower than -10 dB and measured gain is larger than 12 dBi. Figure 3.3 shows the measured radiation patterns of the SIW-ALTSA at 8.5 GHz.

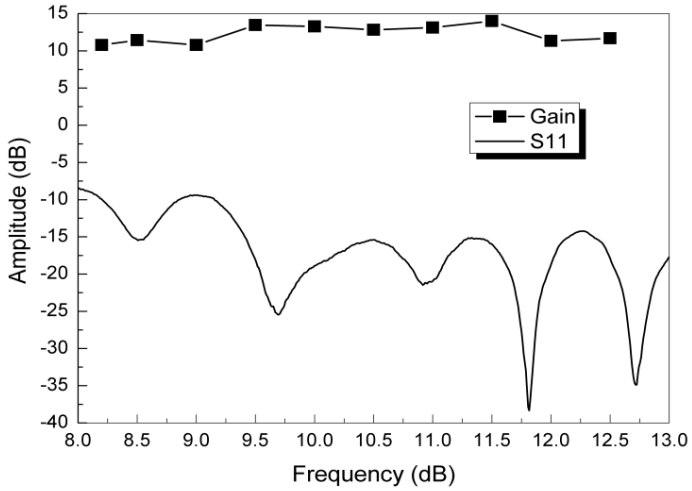

Figure 3.2: Measured return loss and gain of an SIW ALTSA cell

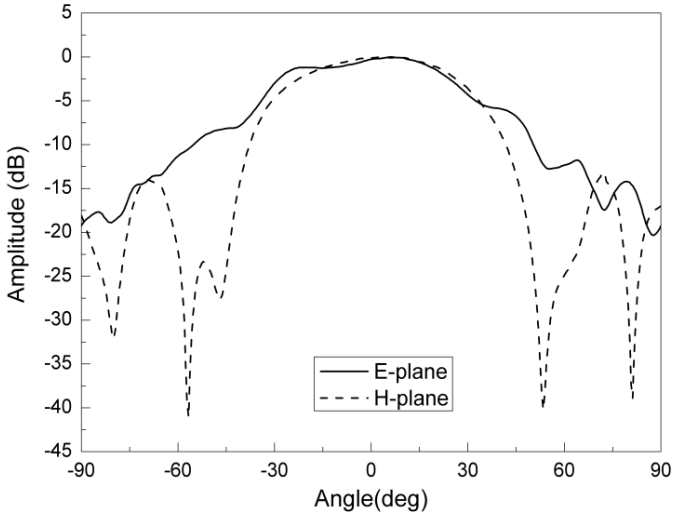

Figure 3.3: Measured normalized radiation patterns at 8.5 GHz

3.3.2 Mutual Coupling

Mutual coupling between antennas in array is a very important factor for consideration in designing a high-performance spatial PA. Strong coupling will induce self-oscillation between PAs and affect the antenna's performance significantly. Before the spatial PA is designed, the relationship between the mutual coupling and the distance of antennas in array is analyzed by experiments. Figure 3.4 and Figure 3.5 show S21 is less than -20 dB in the working frequency

range while center-to-center distance d between antennas is longer than 30 mm (d=30 mm is $0.85\lambda_0$, λ_0 is the space wavelength at 8.5 GHz). When two antennas are placed vertically, distance d is limited to 30mm due to the size of the antenna cell. Measured results show that the mutual coupling will decrease while the frequency increases because the electrical length becomes larger at the same time. When the distance d is larger than $0.85\lambda_0$, both antenna and PA will be slightly affected by the mutual coupling in both vertical and horizontal cases.

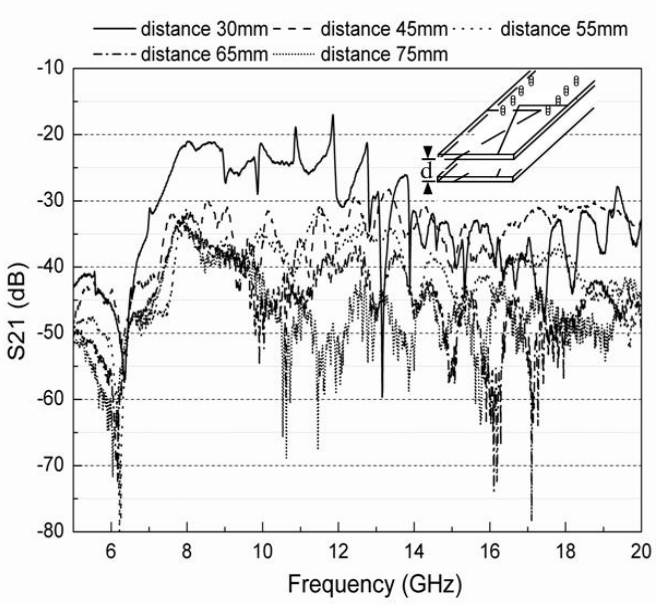

Figure 3.4: Relationship between mutual coupling and distance between two antennas in vertical case

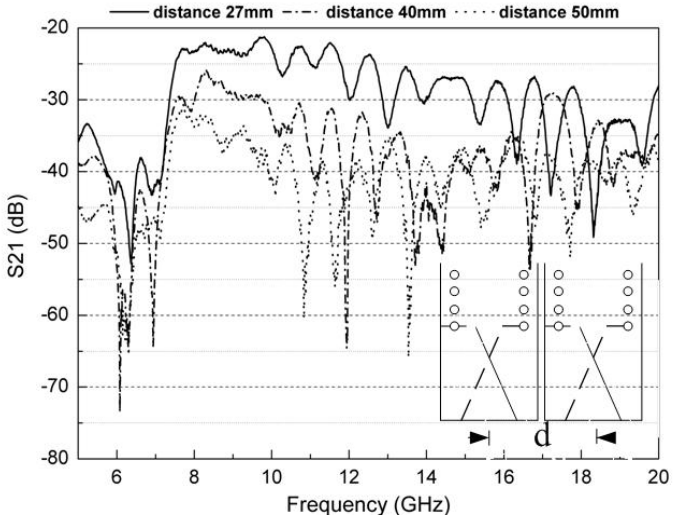

Figure 3.5: Relationship between mutual coupling and distance between two antennas in horizontal case

3.3.3 Implementation of X-band Spatial PA

In this approach, an array of active antenna modules constructed from SIW ALSTA and GaAs MMIC amplifiers receives signals at lower power, and after amplification reradiates signals into free space. Two advantages of the spatial amplifier over the spatial oscillator are that only a single stable lower power source is required (thus greatly simplifying the construction of combiner) and that the amplifiers can be individually optimized. Figure 3.6 schematically illustrates a possible arrangement for space power amplification. The photograph of the experimental two-element array module is shown in Figure 3.7. The array elements are constructed by integrating a GaAs MMIC PA between two SIW ALTSAs. A simple measurement procedure has been developed to estimate the gain of the space amplifier. This procedure involves the ALTSAs at the input terminals are space-fed from a single horn antenna while those at the output terminals radiate into free space. The free space radiation is picked up by a second horn antenna which is placed at a far field distance from the array. The ratio of the measured received power with and without bias to the MMIC amplifiers provides an estimate of the gain of the space amplifier. In the setup, the two horn antennas are orthogonally polarized but the ALTSAs are oriented to have the same polarization as their respective horn antennas, thus a good isolation between the transmitting and the receiving horn antennas is established.

In this design, measured gain of the MMIC PA is shown as Figure 3.8. At 8.5 GHz, the amplifier's gain is 13 dB. The gain is greater than 12 dB over the frequency range of 7.7 to 9.6 GHz.

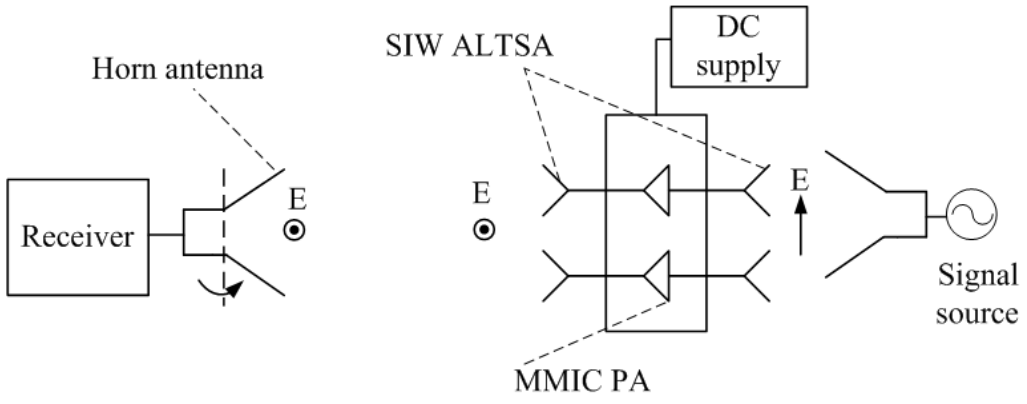

Figure 3.6: Schematic illustrating an arrangement for spatial amplifier

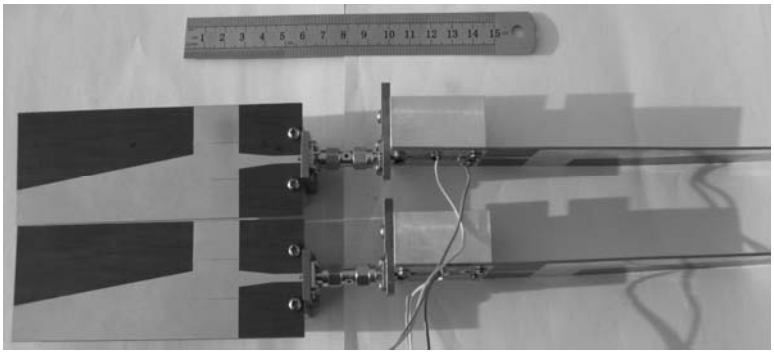

Figure 3.7: Photograph of the spatial amplifier

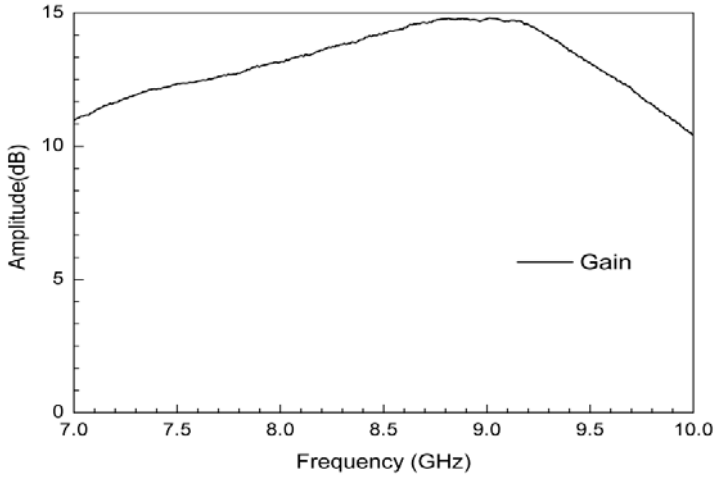

Figure 3.8: Measured gain of a commercial MMIC PA

In this experiment, the SIW ALTSAs at the amplifier input and output are oriented with the H and E vectors of the receiving horn, respectively as shown in Figure 3.6. This arrangement allows the horn to excite the two SIW ALTSAs with equal amplitude. In this design, distance d between the two SIW ALTSAs is about 35 mm (about 0.9 λ_0 at 8.5 GHz). According to the analysis of mutual coupling in section 4.3.2, the mutual coupling in this distance has a very little effect on the spatial amplifier. Measured radiation pattern is shown in Figure 3.9 with the amplifiers turned ON and OFF, respectively. The gain increases by as much as 32 dB when the amplifiers are turned ON. The radiation pattern is measured for receiver horn antenna in H-plane.

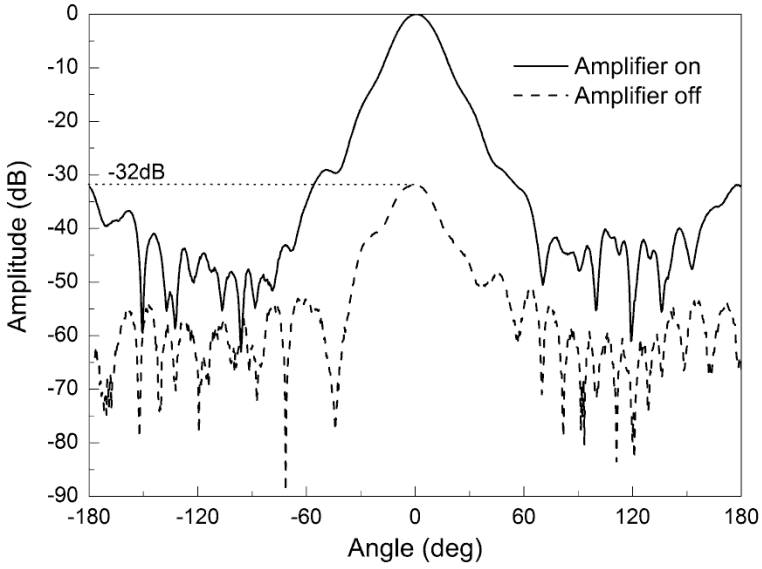

Figure 3.9: Measured radiation pattern of the horn antenna showing space power amplification

3.4 Integrated Sub-harmonically Up-converter Antenna Array

Up to now, the spatial combining classes can be defined according to different combined solid-state device components or active antennas. Most solid device components of spatially combined arrays are oscillators and amplifiers. In this section, a Ka-band sub-harmonically pumped up-converter antenna employing the SIW technology is proposed and used to realize a low cost transmitter together with spatial power combining architecture. A single Ka-band sub-harmonically pumped up-converter using SIW band-pass filter is developed, exhibiting a conversion loss of about 7dB. Based on the designed up-converter and SIW ALTSA, the integrated up-converter antenna is designed and fabricated. Measured results of equivalent isotropic radiated power (EIRP) and radiation patterns are given. Finally, a 2×2 up-converter antenna array are designed and fabricated.

3.4.1 Performance of Ka-band SIW ALTSA

Here, a Ka-band SIWALTSA is designed for up-converter antenna array. The antenna is designed and fabricated on Rogers/duroid 5880 substrate with ε_r=2.2 and t=0.508mm, then (3.1) gives rise to t_{eff}/λ_0 that is equal to 0.032 for 30 GHz or 0.028 for 35 GHz, respectively. The SIW feeding system is determined by the cut-off frequency of 18GHz and the working frequency range 26~40 GHz of TE_{10} mode.

The SIWALTSA cell is simulated with a full-wave CAD software (Ansoft-HFSS in our case) as in the case of the above X-band SIW ALTSA. Simulated and measured return losses are shown in Figure 3.10, which show a very good agreement. Measured return loss S_{11} is lower than -10 dB from 22.5 to 40 GHz. Figure 3.11 shows that the antenna gain slowly increases with frequency and also the 3 dB beam width of E-PLANE and H-PLANE becomes narrower rapidly. The trend regarding these curves is coincident with the Zucker's standard curves for TSA. Figure 3.12 shows the measured radiation patterns of the SIW ALTSA at 30 GHz, 35 GHz and 40 GHz, respectively. Figure 11 and Figure 12 also indicate the broadband features of radiation pattern. Dimensions of the designed Ka-band SIW-ALTSA are D=0.4 mm, S=0.8 mm, L_{SIW}=5 mm, W_{SIW}=5.8 mm, W_{taper}=2.3 mm, L_{taper}=1.5 mm, L_t=30 mm, A_W=2.1 mm, W_I=2.86 mm, W_A=12.07 mm, $\alpha=13.2^0$.

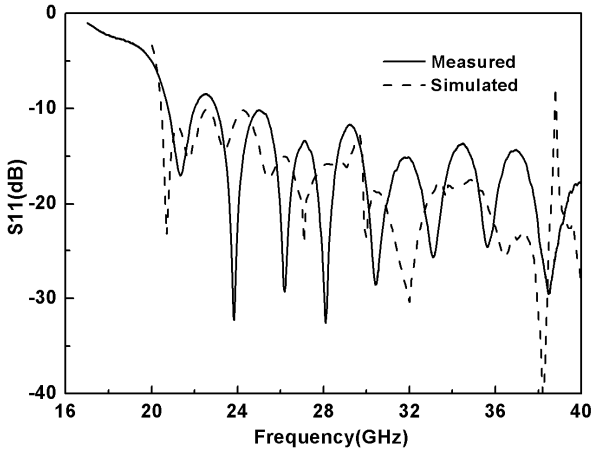

Figure 3.10: Simulated and measured return losses of an SIW ALTSA cell

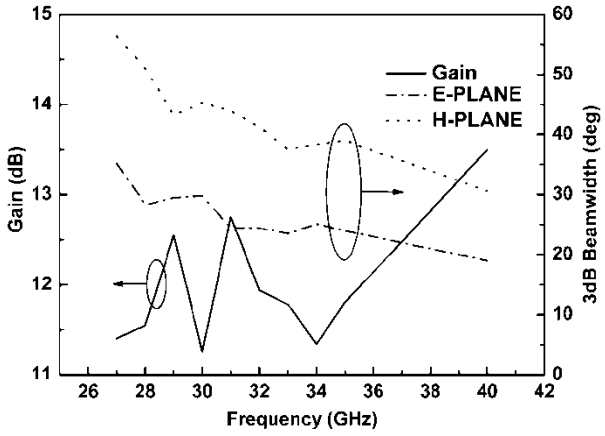

Figure 3.11: Antenna gain and 3 dB beam width versus frequency

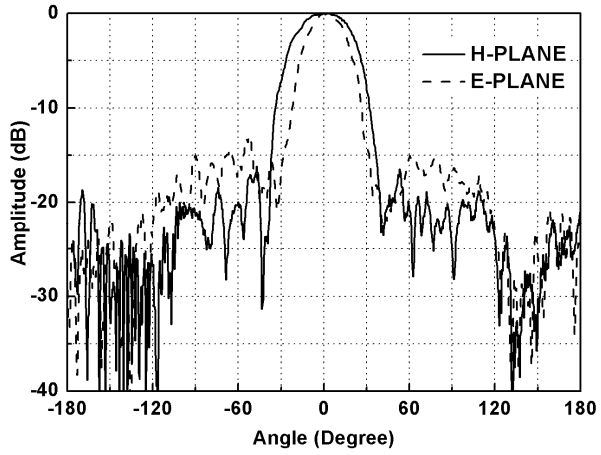

(a)

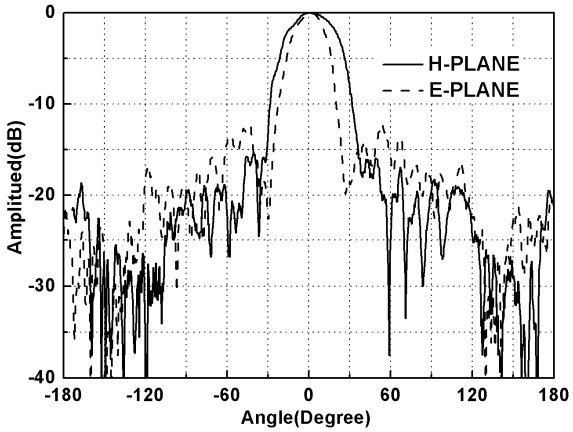

(b)

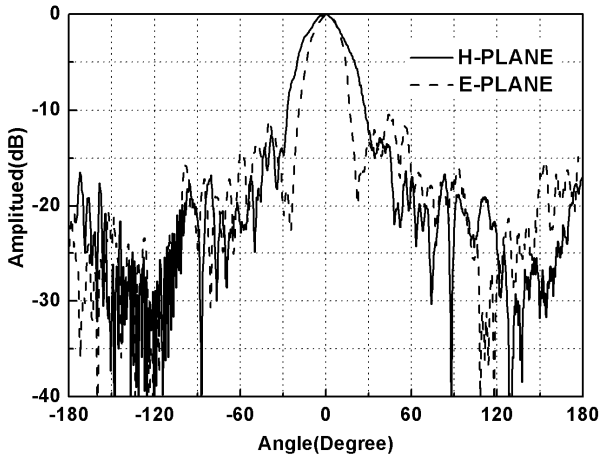

(c)

Figure 3.12: Measured normalized radiation patterns for an SIW feeding ALTSA, (a) Radiation patterns at 30 GHz. (b) Radiation patterns at 35 GHz. (c) Radiation patterns at 40 GHz

3.4.2 SIW Sub-harmonically Up-converter

Figure 3.13 describes the layout of the proposed SIW sub-harmonically pumped up-converter. A $\lambda_{LO}/4$ short stub on the left side of a diode pair and a $\lambda_{RF}/2$ open stub on the right side of a diode pair are used to provide shorted terminals for LO frequency and RF frequency, respectively. IF signal is imposed on the RF side through a low-pass filter prevented RF and LO leakage to IF port. Since SIW filter has a high Q-factor [126], this type of filter is a good choice for integration with planar active circuits. A band-pass filter is realized by four metallic posts embedded in an SIW, which is used to suppress image frequency, LO frequency and IF at the RF port. The SIW-microstrip transition is used for connecting the filter to diodes. W_{50} and W_t are the widths at both ends of the microstrip taper for matching the filter impedance to 50Ω, and L_t is the length of the taper. The SIW section produces the filter and simply transforms the unbalanced microstrip to the balanced SIW feeding system for ALTSA which will be discussed in the following part, where D and S are the diameter and period of metallic vias, and W_{SIW} is the SIW width which determines its cut-off frequency, thus the working frequency range of TE_{10} mode. Parameters of the up-converter are D=0.4, S=0.8, $s1$=4.43, $s2$=4.92, $d1$=1.14, $D1$=0.8, W_{SIW}=5.8, W_t=2.2, L_t=2 and W_{50} =1.6 (unit: mm).

In this design, an up-converter has been designed with LO frequency of 13.3 GHz and IF frequency of 0.8 GHz. The circuit is designed and fabricated on Rogers/duroid 5880 substrate with dielectric constant of 2.2 and thickness of 0.5mm. The Schottky anti-parallel diode pair used is DMK2308 from Alpha Industry. According to working frequency band of the up-converter, an SIW filter of 1GHz bandwidth centered at 27.4 GHz has been designed, fabricated and measured. The filter is simulated with a full-wave CAD software HFSS. Figure 3.14 shows simulated and measured frequency responses of the filter. The insertion loss and the return loss in the pass band are around 1.1 dB and lower than -15 dB, separately. The result indicates that the image frequency of 25.8 GHz can be suppressed by about 28 dB. Since the LO frequency is lower than the inherent cut-off frequency of the SIW, the LO becomes blocked.

The up-converter is designed and simulated by the Harmonic Balance (HB) method of Agilent ADS software, and the IF low-pass filter are simulated by the Momentum software package in the ADS platform. In the measurement, the LO, IF and RF are imposed into and take out from the sub-converter by SMA coaxial connectors. Simulated and measured conversion losses remain 7

dB when LO input power level is larger than 6 dBm, where IF signal is fixed at 0.8 GHz with input power level of -30 dBm and LO frequency is 13.3 GHz. Therefore, the minimized LO input power level of 6 dBm is chosen to pump. Figure 3.15 shows simulated and measured conversion losses versus IF frequency when IF signal is swept from 0.1 to 1.8 GHz with a constant input power level of -30 dBm and LO signal is fixed at the frequency of 13.3 GHz with 6 dBm power level. The measured conversion loss is less than 9 dB over the IF frequency range of 0.2-1.1 GHz. The lowest conversion loss is measured at 0.9 GHz and is equal to 6.6 dB. Figure 3.16 plots simulated and measured conversion losses versus input IF power level, where IF frequency is set at 0.8 GHz and LO frequency is 13.3 GHz with 6 dBm power level, input IF power level is swept from -60 to 5 dBm. The measured conversion loss is around 7 dB over a large dynamic range. Below IF power level of -15 dBm, the conversion loss is almost constant. Beyond IF power level of -10 dBm, the conversion loss increases quickly. The reason is that the diodes are driven into their saturation region. From this figure, it can also be seen that the input 1-dB compression point is around -6 dBm. The designed up-converter has a good linearity and a wide input/output dynamic range of larger than 55dB.

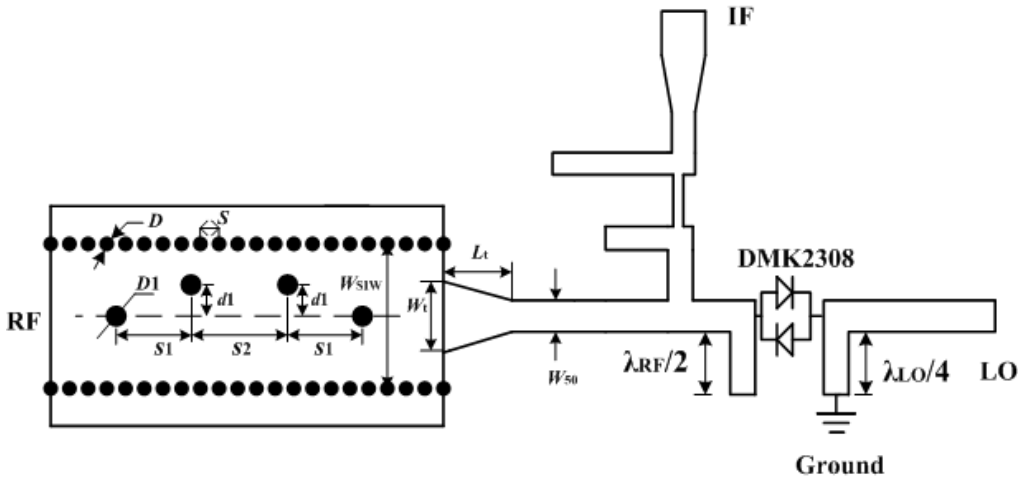

Figure 3.13: Physical description of the SIW sub-harmonically pumped up-converter

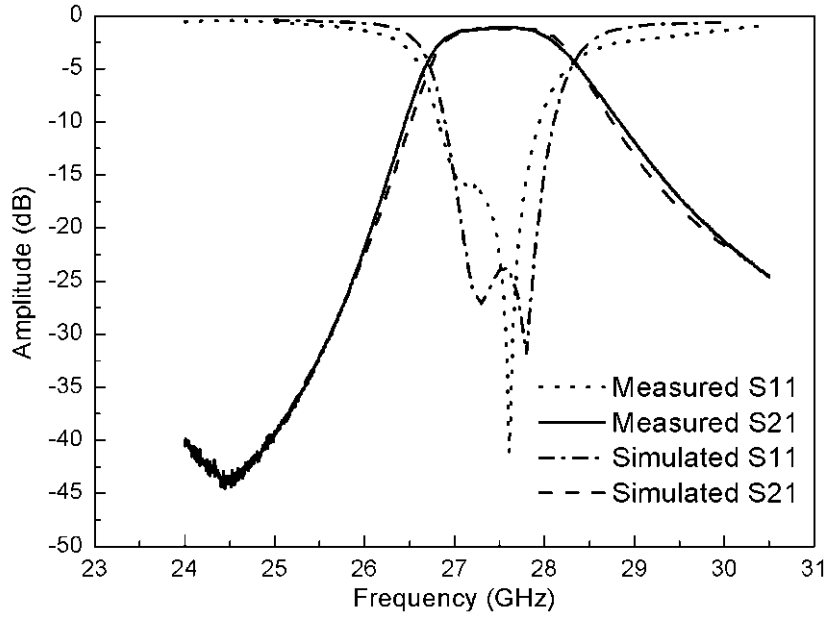

Figure 3.14: Simulated and measured frequency responses of the SIW band-pass filter

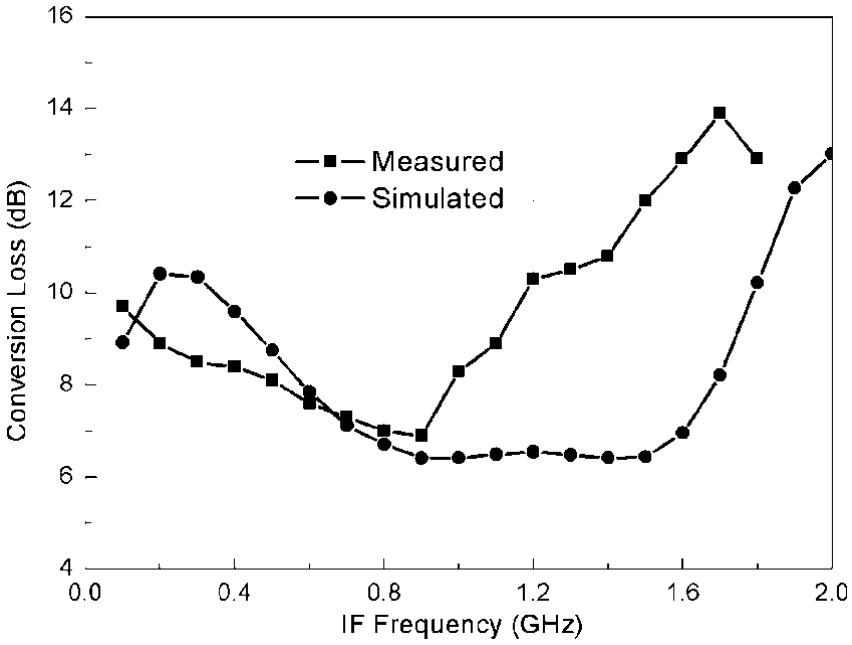

Figure 3.15**:** Simulated and measured conversion losses versus IF frequency

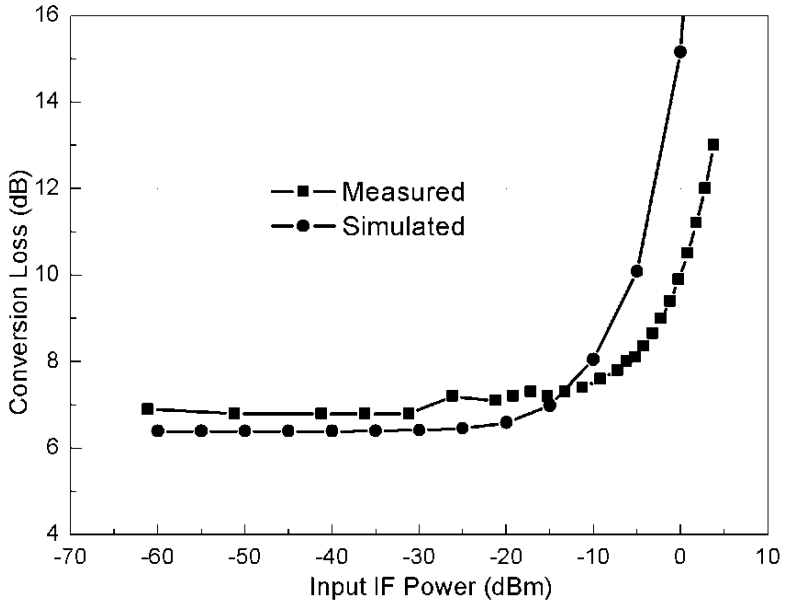

Figure 3.16: Simulated and measured conversion losses versus IF input power

3.4.3 SIW Sub-harmonically Up-converter Integrated Antenna

In this AIA design, the SIW up-converter and SIW-ALSTA are directly integrated to form the integrated up-converter antenna. Simulated and measured antenna gains are 12 dBi and 11.5 dBi at 27.4 GHz, respectively. The SIW ALSTA is a wide band antenna, which was designed in section 3.4.1. Therefore, the bandwidth of the integrated up-converter antenna mainly depends on the up-converter and the matching circuits between the up-converter and antenna. For the AIA and array, an important figure-of-merit is related to EIRP, which can be determined by measuring the power received by a standard gain horn placed in the far field of the transmitting antenna element or array. The EIRP is expressed as

$$EIRP = P_{trans} G_{trans} = \frac{P_{rec}}{G_{rec}} \left(\frac{\lambda_0}{4\pi R}\right)^{-2} \tag{3.2}$$

where P_{rec} is the power received by the standard gain horn, G_{rec} is the gain of the standard gain horn, and R is the distance between the standard gin horn and the integrated antenna element or array.

To measure the output power produced by the integrated up-converter antenna, a standard gain horn was placed at one meter away from the antenna. The spectrum analyzer is used to measure the received signal power and spectrum. Similar to the measurement of the above SIW up-

converter, EIRPs versus IF signal frequency are measured and shown in Figure 3.17. According to formula (3.2), we define equivalent conversion loss L_{eff}=EIRP/G_{trans} -P_{IF}. G_{trans} is the gain of the transmitted antenna, P_{IF} is the IF input power. Results of L_{eff} are also plotted in Figure 3.17. When IF signal is at 0.8 GHz with power level of -7.2 dBm and LO signal is at 13.3 GHz with power level 6 dBm, the value of L_{eff} is 8dB which is the same as that of up-converter shown in Figure 3.16. The up-converter antenna is excited by two IF input signal tones (819.5 MHz and 820.5 MHz) having equal magnitude and closely spaced frequencies of 1 MHz. The input third-order intercept point (IP3) EIRP is determined to be 6.5 dBm under the 6 dBm LO driving at a fixed LO of 13.3 GHz shown in Figure 3.18.

Radiation patterns of the integrated up-converter antenna in the E-and H-planes are also measured with a distance of 10 meters between receive antenna and the integrated up-converter antenna. The integrated up-converter antenna is fixed on the stepping motor driven rotational stage which rotates from -90 to +90 degree in 30 seconds. The results including passive and the integrated up-converter antenna radiation patterns at 27.4 GHz are shown in Figure 3.19. The E-plane and H-plane radiation patterns of the integrated up-converter antenna agree well with those of the passive antenna. The E-plane and H-plane have a half-power beamwidth of 26.6^o and 40^o, respectively. The sidelobes of both planes of the integrated antenna are lower than -13 dB. Different test environments and some radiation from the microstrip parts may have caused the difference of radiation patterns between up-converter antenna and passive antenna.

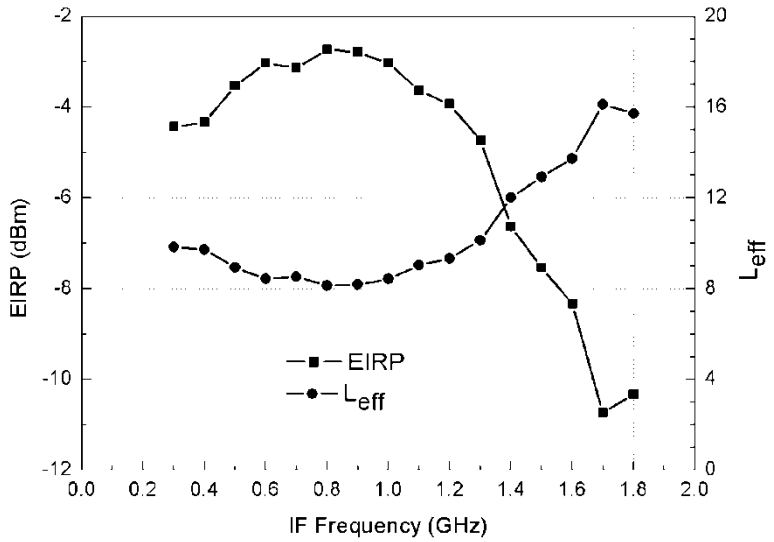

Figure 3.17: Measured EIRP and L_{eff} versus IF input frequency

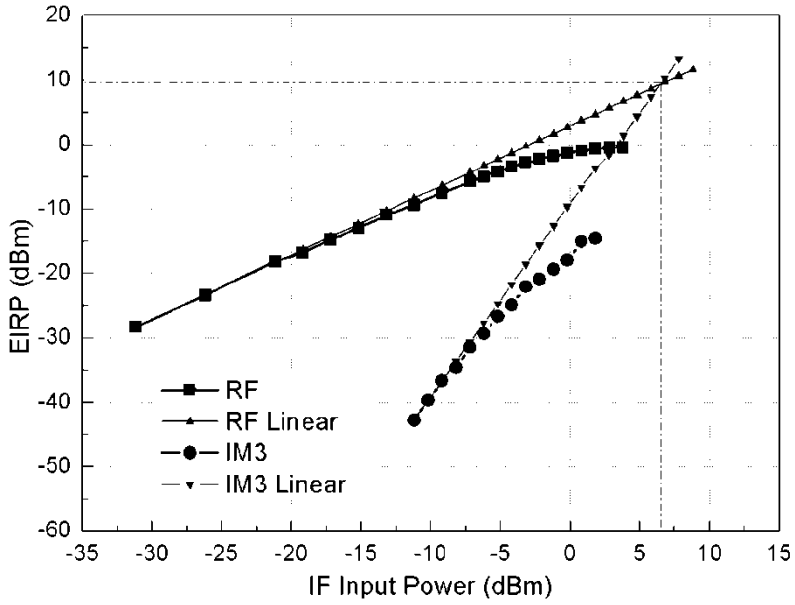

Figure 3.18: Measured RF EIRP and IM3 EIPR versus IF input power

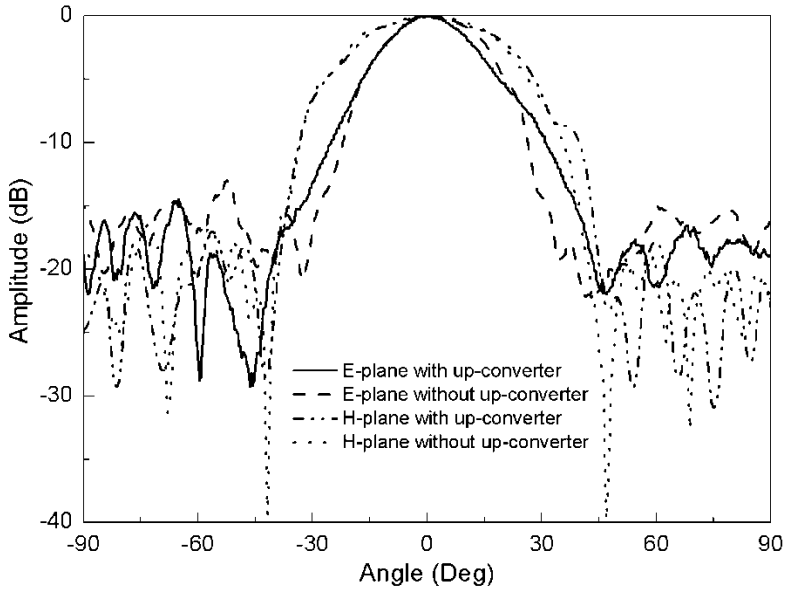

Figure 3.19: Measured radiation patterns for the antenna with and without the up-converter

3.4.4 Implementation of A Ka-band 2×2 Up-converter Antenna Array

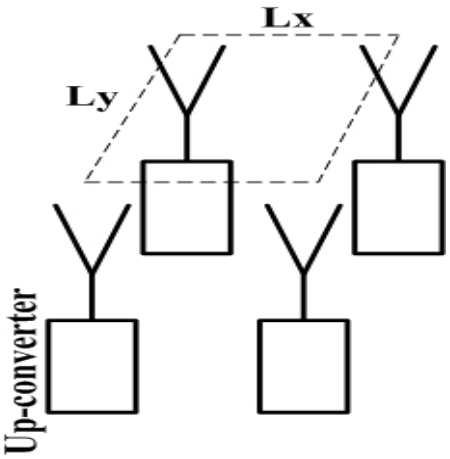

Figure 3.20: Simple configuration of the array

Figure 3.20 shows a simple arrangement of 2×2 array. The spacing between elements is one wavelength in both E-plane and H-plane directions (Lx=Ly=11mm). For the integrated up-converter antenna array, it does not need external signal or mutual coupling for injection-locking the array such as oscillator antenna arrays. Therefore, the combining efficiency of this array is determined by 1-to-2 LO and 1-to-4 IF power dividers and array factor. Here LO and IF power dividers are both Wilkinson power dividers. Each arm of the dividers has the almost same amplitude and phase responses and very low insertion losses of 0.2 dB. The insertion loss of the LO divider does not affect the combining efficiency of the array because LO power can be increased. According to array factor, the array gain is determined to be 17.3 dBi at 27.4 GHz. The ideal gain for four elements is 17.3 dBi. Therefore, the calculated combining efficiency is 97.7%. The measured combining efficiency can be determined by

$$\eta = \frac{P_{array}}{4 \times P_{element}} \times 100\% \tag{3.3}$$

where P_{array} is the power of the array received by the standard gain horn, P_{element} is the element's power received by the standard gain horn.

The injected LO power is set as 12.2 dBm for the array. Measured results are shown in Figure 3.21-3.23. Figure 3.21 shows measured output RF EIRP and IM3 EIPR versus the IF input power level for the up-converter antenna array. The input IP3 point of the array is 7 dB higher than that

of the single up-converter antenna element. The 1-dB input compression point is also improved by 5.5dB as shown in Figure 3.18 and Figure 3.21. Figure 3.22 plots the measured EIRP and combining efficiency versus input IF frequency, when the IF input frequency is swept from 0.2 to 1.8 GHz and the LO signal is fixed at 13.3 GHz with 12.2 dBm power level. It is also shown that the combining efficiency is larger than 90% due to the fact that RF powers are combined in free space with IF or LO signals having almost same amplitude and phase responses. Measured results display a very good linearity and a higher 1-dB compression point. This up-converter array can provide enhanced RF efficiency by coupling a number of components into beams in free space so that the spatial up-converter array has a higher dynamic range at input port and a larger output power at output port.

Figure 3.23 shows the radiation patterns of the designed 2×2 up-converter array in E-plane and H-plane, respectively. The measured half-power beamwidth in E-plane and H-plane are 18.2^{o} and 26^{o}, respectively. The beam sharpens in both planes because the array is arranged in two directions. Sidelobes of both planes are lower than -15 dB. But it is normally impossible that the sidelobes of the array are lower than that of the single device. We believe that the above phenomenon may be caused by performance difference of diodes or circuits. Figure 3.24 shows the photograph of 2×2 up-converter array.

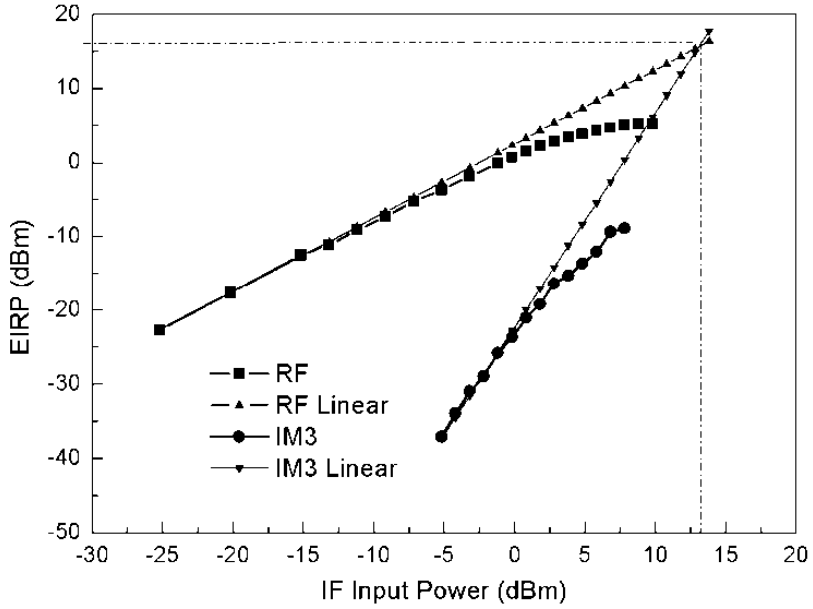

Figure 3.21: Measured RF EIRP and IM3 EIPR versus IF input power for the integrated up-converter antenna array

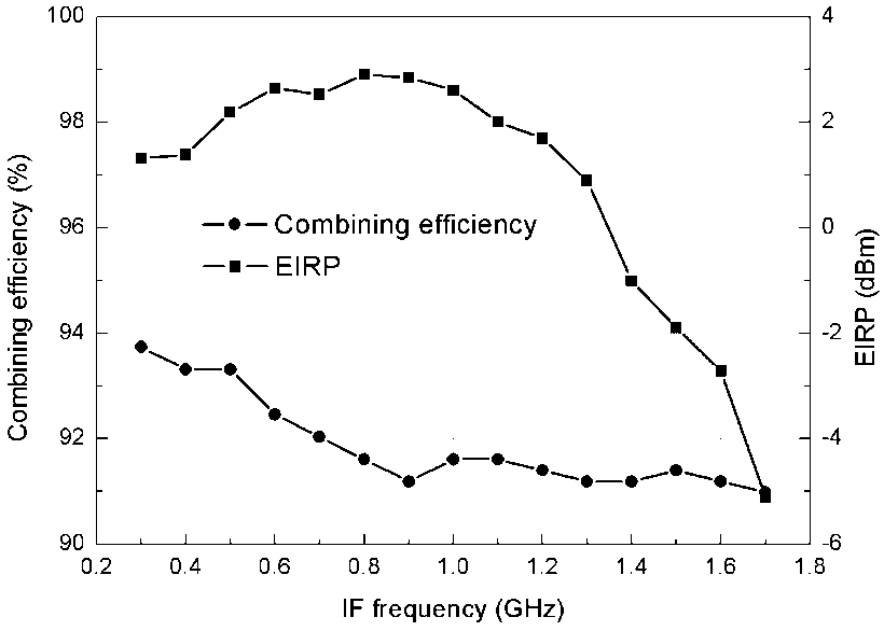

Figure 3.22: Measured RF EIRP and combining efficiency for the integrated up-converter antenna array

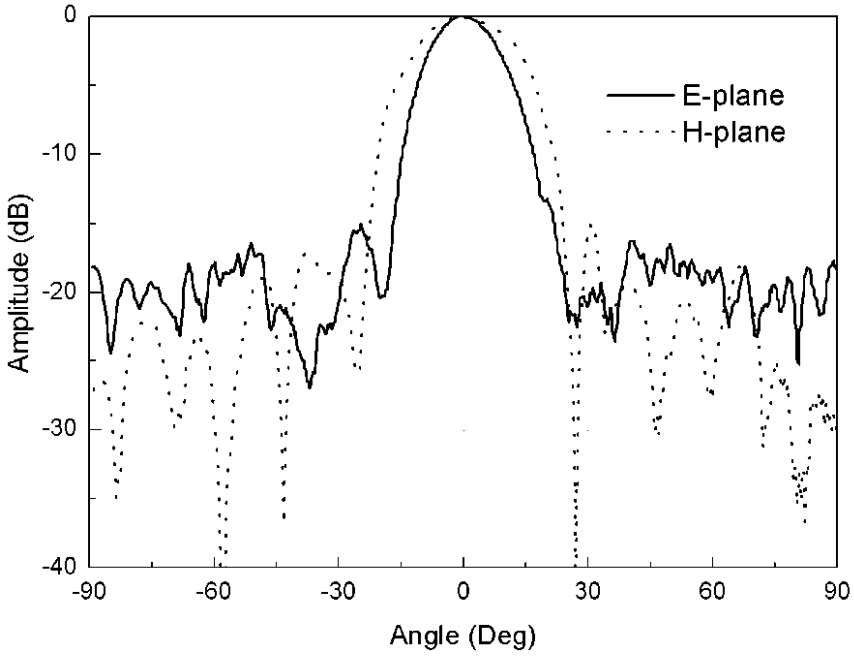

Figure 3.23: Measured radiation patterns for the integrated up-converter antenna array

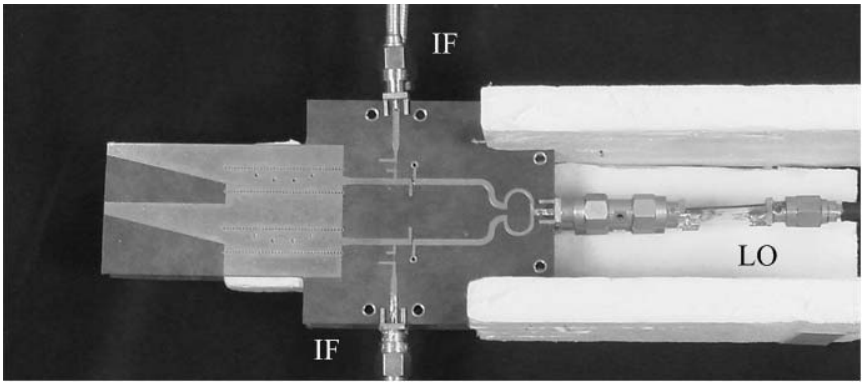

Figure 3.24: Photograph of 2×2 up-converter array

A low cost transmitter made of 2×2 integrated up-converter antenna array using the SIW technology is proposed and developed over Ka-band. Since the SIW structure can easily be integrated with active circuits in a planar form, the SIW up-converter circuit and the SIW-ALTSA are effectively designed and integrated together to form the integrated SIW up-converter antenna. The performances of a single integrated up-converter antenna and the whole integrated up-converter antenna array are shown and discussed with measured results. It can be postulated that the four element array is expandable to a larger array in two dimensions simply by a geometric arrangement. The proposed spatial integrated up-converter antenna array could be very useful for base station applications, especially for millimetre-wave transmitter design.

3.5 SIW Rectenna Array for Space Power Transmission

3.5.1 Introduction to Rectenna

Microwave power transmission (MPT) is an important technology for delivering power from space to space or space to ground such as systems of the future solar power satellites, spaced-based stations and others [127]-[129]. In the MPT, the DC power is firstly converted into RF power, which is then radiated into space with narrow beam and subsequently received by a special antenna array which finally converts the received RF power back into DC power. One of the main components in these systems was first proposed by Brown [130], which is called as rectifying antenna or rectenna.

Since the 1960s, rectennas have been studied and widely developed by many researchers. The first rectenna was designed by using a half-wave dipole antenna at 2.45GHz in the early 1960s

[130]. In 1977, Brown pioneered a microwave rectenna with the highest recorded conversion efficiency of 91.4% [131]. A great deal of designs and experiments on rectenna at 2.45 GHz have intensively been realized for nearly forty years. From the 1980s, researchers have looked into higher frequency, dual and circular polarization, and printed-circuit format for rectenna design and implementation. It is known that electromagnetic waves generally have a larger attenuation at higher frequency, but at the same time rectenna has a smaller aperture areas and narrower beam which are of benefit to point-to-point microwave power transmission. In 1992, X-band and Ka-band rectennas were developed with the conversion efficiency of 60% and 39%, respectively [132]. K. Chang and his group developed a 5.8 GHz rectenna with high conversion efficiency in 1998 [133]. In [134] and [135], dual-polarized rectennas were also investigated. In addition, a number of researchers looked into various circular polarized rectenna elements or arrays because the circular polarization can ensure the receiving antenna effectively captures the microwave or millimetre wave energy from the transmitted antenna when the antenna is rotated [136]-[139].

Usually, dipoles or patch antennas of low gain were adopted for the design of rectenna element or arrays in the past. In order to generate a higher output DC power, a large number of rectenna elements or rectifying diodes should be fabricated in the system. For example, 2304 rectenna elements were used for microwave energy transmission at 2.45GHz in [140]. High gain antenna is a good way to decrease the number of diodes. A high gain rectenna array was developed using Circularly Polarized Dual-Rhombic-Loop Traveling-Wave Rectifying Antenna （DRLA）array at 5.8GHz, and 82% RF-to-DC conversion efficiency was achieved [141].

In order to yield a narrow beam width with a high gain rectenna, proposed in this thesis work is a Ka-band 1×4 rectenna array on the basis of SIW technology in the form of the SIW ALTSA. As has been well known, the SIW ALTSA preserves the advantageous features of the LTSA as well as the SIW, and implements a smooth unbalance-to-balance transition from the SIW to the LSAT, which feeds electromagnetic wave energy into rectifying devices. Additionally, the SIW can suppress potential parasitic radiation that affects radiation patterns. Here, the SIW also is a part of matching circuit of the rectifier for providing a good DC return pass by the metal posts inherent to the SIW structure. The metal posts in the SIW will not affect matching circuit, but those of microstrip short stub for matching circuit will introduce some parasitic parameters in the millimetre-wave region. Finally, the converted DC power of four rectennas array is combined by

DC combining circuit and then the RF-to-DC conversion efficiency is analyzed by comparing with the results of a single rectifying circuit.

3.5.2 Design of Ka-band SIW Rectifier

The basic principle of the microwave power conversion by this rectifying circuit is analogous to a diode clamping circuit or a large signal mixer at microwave frequencies. The diode is the most critical component to achieve high efficiencies because it is the main source of loss. Increasing series resistance will increase the power dissipated in the diode. Because we cannot get the GaAs Schottky diodes, and a Ka-band zero-bias small signal detector Si Schottky diode with high series resistance is adopted to validate the idea of the new rectifier based on SIW technology. From the analysis of [131], it is well known that the power conversion efficiency of rectifier is mainly determined by three parameters of the diode. These parameters are decided by diode material properties. Diode parameters include parasitic resistance R_S=45 Ω, zero-bias junction capacitance C_{jo}=0.08 PF, inductance of the bonding wire (two parallel wires) L=0.5 nH and breakdown voltage of 4V. Figure 3.25 is the schematic configuration of rectifier with a series diode in this design. λ/4 RF open stub (open-short circuit) was a simple 60 deg radial stub with the radius of 2.3mm, which is used to choke RF signal, but not the 2nd harmonic signal which affects the RF-to-DC efficiency slightly [135].

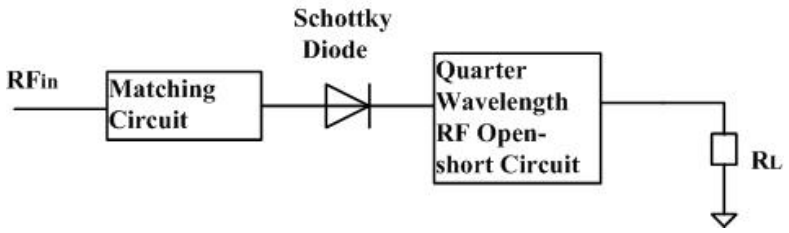

Figure 3.25: Schematic configuration of rectifier circuit

In the design of the rectifier, nonlinear equivalent circuit parameters of diode are firstly determined using a vector network analyzer when input RF power is 10 mW. Fig 3.26 shows the measured diode's scattering parameters, and Z0 is the 50 Ω. Secondly, the matching circuits are designed according to the measured diode's scattering parameters, and then dimensions of the matching circuit are set as the initial values. Finally, the matching circuit and load are optimized by the HB method to yield a high efficiency of the rectifier.

As shown in Figure 3.27, the input matching circuit has two parts: part 1 is microstrip matching circuit that is used to match the diode to 50 Ω microstrip transmission line at 30 GHz, and part 2 is the SIW-microstrip transition, matching the rectifier and antenna. Part 2 is used to provide a good DC return passing through metal posts of the SIW. The Ka-band millimetre-wave rectifier is designed and simulated by the Harmonic Balance method of ADS software, and part 2 of the matching circuits and λ/4 RF open-short circuit are simulated in ADS.

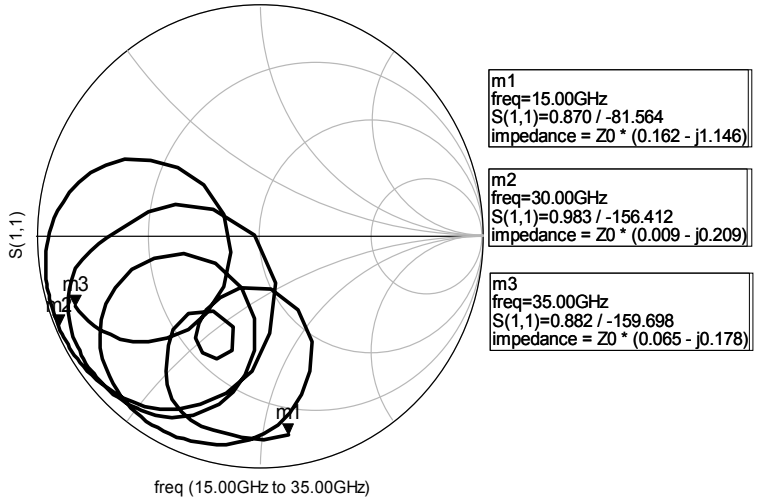

Figure 3.26: Measured diode's scattering parameters

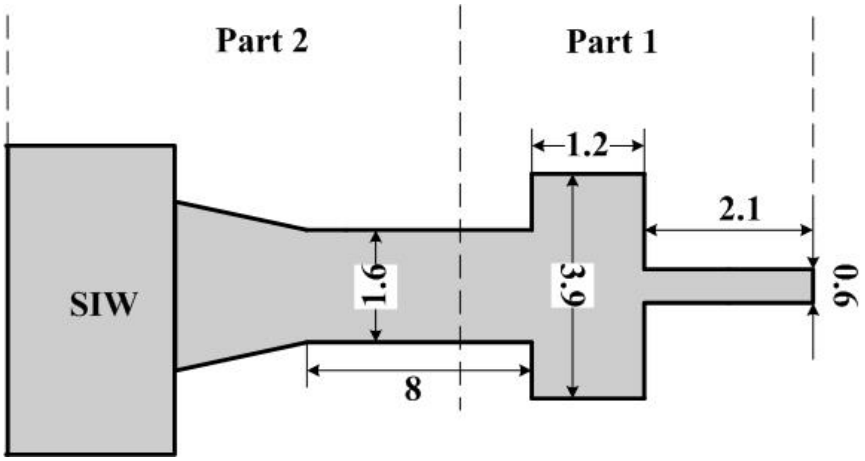

Figure 3.27: Configuration and parameters of the matching circuits (unit: mm)

The RF-to-DC conversion efficiency is defined by

$$\eta = \frac{P_{DC}}{P_{in}} \tag{3.3}$$

where P_{in} is the input power, and

$$P_{DC} = \frac{V_{out}^2}{R_L}. \tag{3.4}$$

When the input power is set to be 1.6 mW, 8 mW and 79.4 mW at 30 GHz, simulated and measured output DC powers with different load resistance are presented in Figure 3.28, indicating that the highest RF-to-DC efficiency can be obtained around R_L =240 Ω with different input power. Figure 3.29 shows curves of the RF-to-DC efficiency versus input power. The maximum conversion efficiency measured with R_L=240 Ω is 27.4% at the input power of 79.4 mw due to the maximum output power of the signal generator is 79.4 mW. Because of a larger R_S of the Si diode, it is difficult to achieve a higher RF-to-DC conversion efficiency.

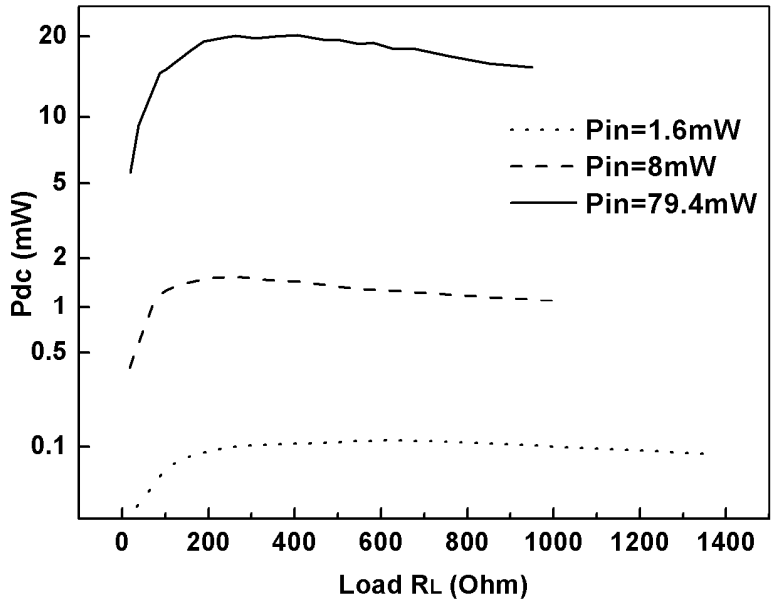

Figure 3.28 : Rectifying DC power versus load with different input power

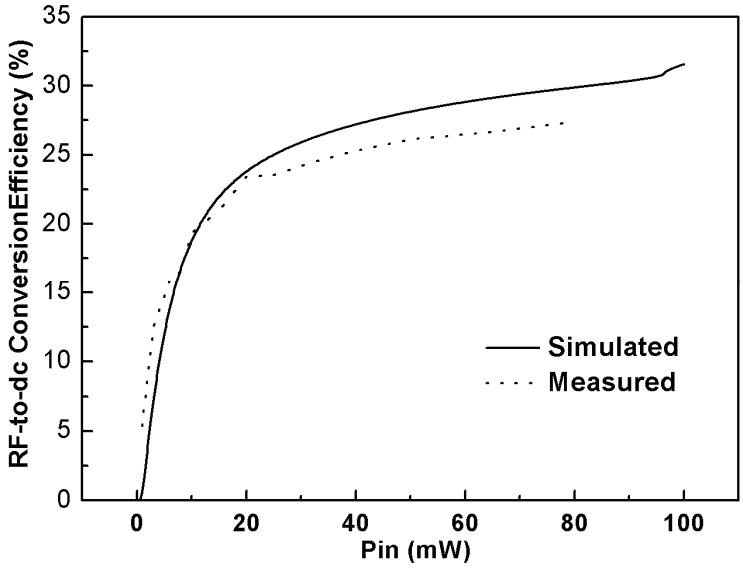

Figure 3.29: Simulated and measured single rectifier efficiency curves at 30 GHz for 240 Ω loading condition.

3.5.3 Design of Ka-band 1×4 Rectenna Array

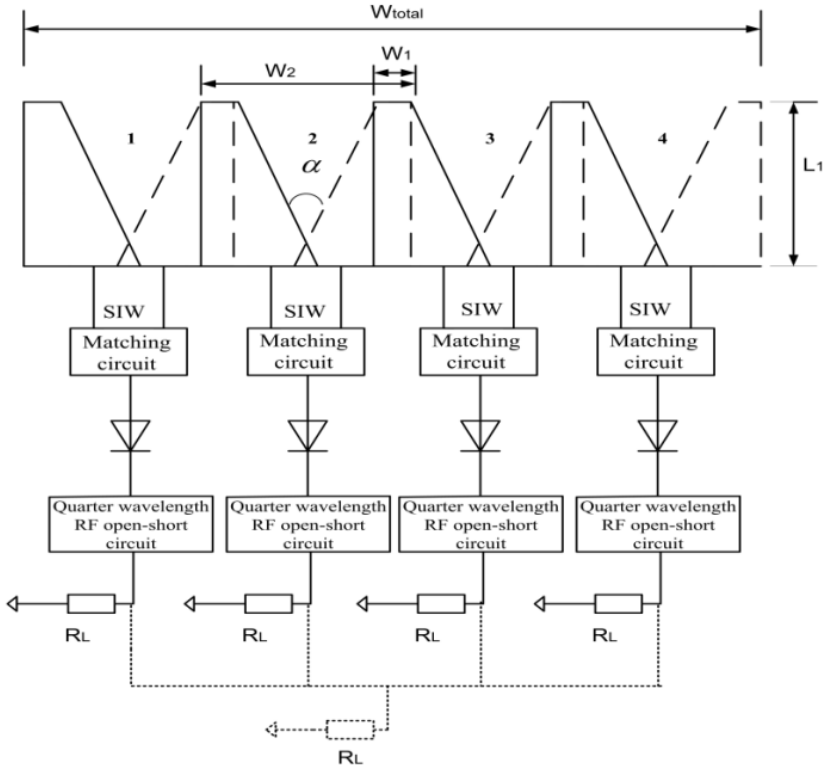

Figure 3.30: Layout of the rectenna array based on the SIW ALTSA array

Four rectenna elements are connected in parallel together to form a 1×4 rectenna array as shown in Figure 3.30. Each SIW- ALTSA is directly connected to a rectifier since the port impedance of the antenna-side is 50Ω, and also the same is for the rectifier-side input port impedance. The area related to width W_1 is one metallic cover on the bottom ground plane overlapped with the other metallic cover on the upper side. The decreasing of the distance between two adjacent antennas, which is caused by overlapped area W_1, can ensure that the adjacent rectenna effective aperture is closer to each other. In other words, a closer spacing aperture can decrease the undesirable void region. And also a closer distance between the array elements allows reception of the same microwave power and the same RF-to-DC conversion efficiency of each element. Due to the above reason, we can properly minimize width W_1 but still ensuring the antenna performance. By optimizing the spacing between antennas, the mutual coupling of each antenna is less than about -20dB in the array. So the interference between antennas can be neglected.

The DC output combining circuit should carefully be designed in order to achieve an optimal DC combining efficiency. Each rectenna produces a DC voltage or current, which can be seen as a DC Thevenin source. For a series connected array, all DC voltages are added together in a terminated load, meanwhile a larger matched load is required. However, a parallel connected array leads to smaller matched loads. Since one rectifier has an optimal output load R_L of 240 Ω, the 1×4 row rectenna array has an output load resistance R_L of 60 Ω. All the generated DC currents are added up at the end of the circuit. In Figure 3.30, each element is measured with loading R_L of 240 Ω, denoted by solid line and array elements are combined, denoted by dot line.

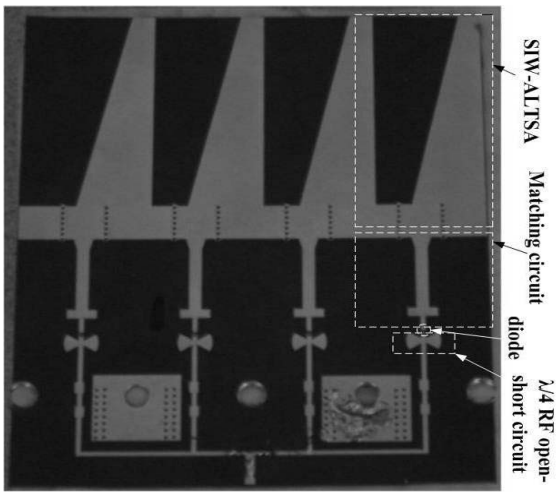

Figure 3.31: Photo for the rectenna array based on the SIW ALTSA array

The measurement setup for measuring performances of the rectenna array is shown in Figure 3.32. The millimetre-wave signal which is up-converted from a low frequency signal is transmitted through a linearly polarized standard horn antenna, and illuminates the rectenna array. Roughly speaking, each SIW ALTSA of the array should receive the same amount of power from an illuminated plane wave. In order to focus the radiated power to the rectenna array without using a high power millimetre-wave source, the rectenna array is placed in proximity of the standard horn antenna during experiments. Due to the non-plane incident wave, it is difficult for us to obtain the RF-to-DC conversion efficiency directly by using the power density. Therefore, the antenna array as used in the rectenna array is placed at the same position of the rectenna array for obtaining the total power received by the rectenna array. The input power received by antenna element is measured using power meter when the other antenna elements are matched with 50 Ohm. Antennas 2 and 3 or 1 and 4 receive the same input power. At the same time, the input power received by antenna 2 or 3 is twice as that received by antenna 1 or 4.

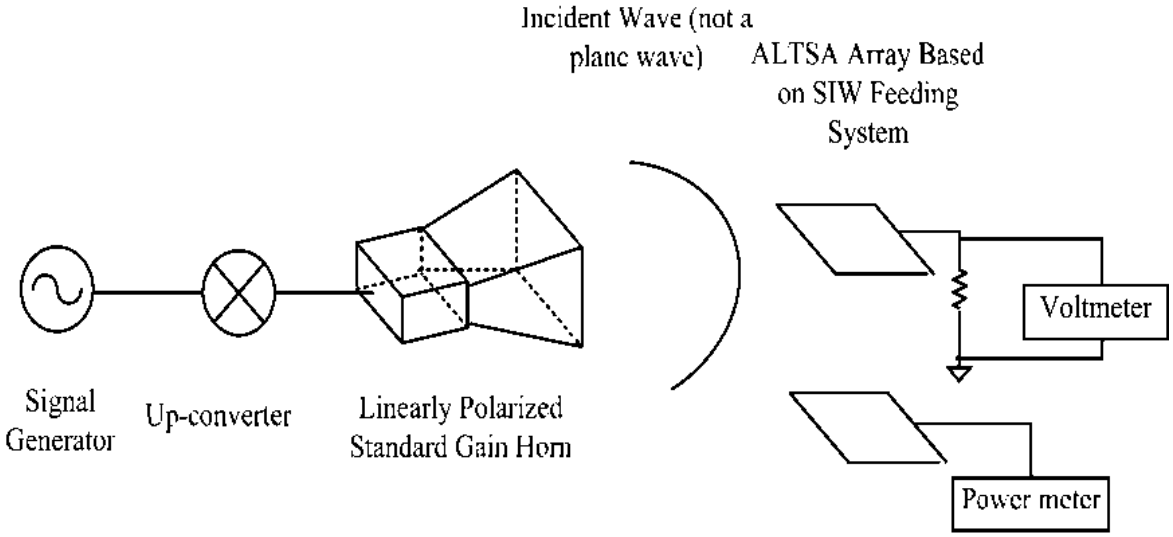

Figure 3.32: Rectenna array measurement setup

The measured DC power/voltage of each rectenna in the array and the total DC power/voltage of the array are shown in Figure 3.33, where P_{in} is the total RF power received by the SIW ALTSA array. Pi and vi (i=1, 2, 3, 4) denote the antenna from left to right. The DC power/voltage of each antenna in the array is independently measured with load R_L =240 Ω as well as total power/voltage of the array with load R_L =240 Ω and R_L =60 Ω. The rectified DC powers of antennas 1 and 4 are nearly identical, but different from antennas 2 and 3. Since the input powers

to antenna 2 and antenna 3 are the same, the DC power difference between such two antennas should be caused by the difference of Schottky diode parameters. If the DC output power is combined, the total DC powers are a small difference corresponding to load R_L=60 Ω and R_L=240 Ω when P_{in}<2 mW. When the RF power received by the rectenna array is more than 3mW, the total output DC power with load R_L= 60 Ω will be larger than that with load R_L = 240 Ω. The phenomenon can be explained in section 3.5.2. Figure 3.33 indicates that a higher load than 240Ω is needed in order to obtain the maximum rectifying DC power for a low input power. When the total received microwave power is 6 mW, 1 mW and 2 mW microwave powers are received by rectenna 1(or 4) and rectenna 2(or 3), which correspond to the RF-to-DC conversion efficiency of about 5% and 10%, respectively. The result coincides with the conversion efficiency of the single circuit as shown in Figure 3.29. The 1×4 rectenna array produces 0.45 mW of DC output power with 6 mW input RF power, it is approximately the summation of the DC powers of the four rectennas. The total RF-to-DC conversion efficiency of the array is 7.5%, which is a half of the sum of above two rectenna's conversion efficiencies (5% &10%). If the method of a far-field measurement is used, four antenna elements can receive the same power.

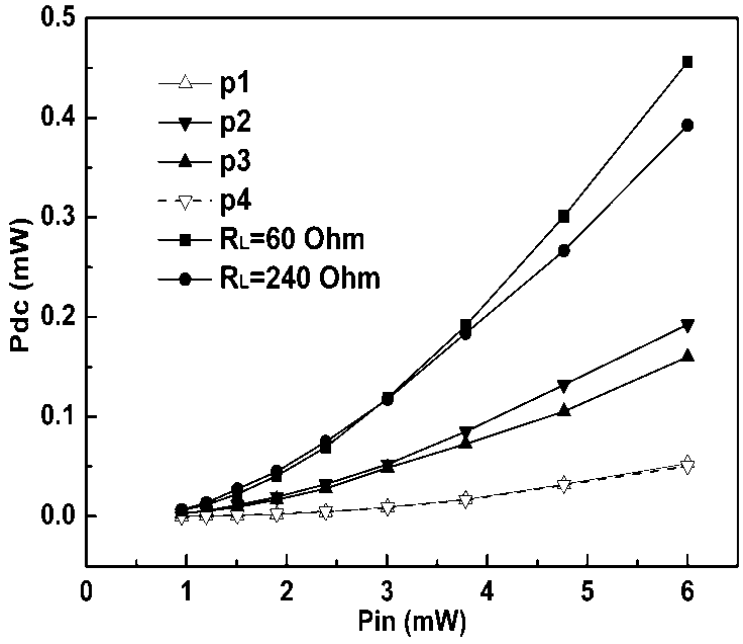

(a)

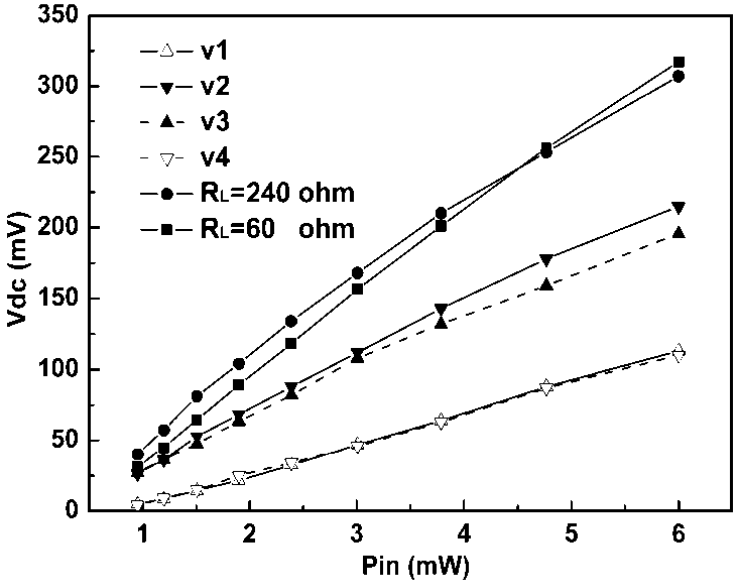

(b)

Figure 3.33: (a) Rectifying output DC power versus the total input power received by array. Four rectennas from left to right produce DC powers p1, p2, p3 and p4 respectively. The total DC power produced by the array is combined for R_L=60 Ω or R_L=240 Ω. (b) Rectifying output DC voltages versus the total input power received by the array. Four rectennas from left to right produce DC powers v1, v2, v3 and v4, respectively. The total DC voltage produced by the array is combined for R_L= 60 Ω or R_L= 240 Ω.

3.6 Conclusion

This chapter presented three active integrated antenna (AIA) array, which are used for power combining. Three types of AIA array on the basis of the SIW ALTSA, including rectenna array, sub-harmonically up-converter antenna array and spatial PA, are proposed. In these three parts, the mutual coupling between SIW ALTSA is discussed and an X-band spatial PA is proposed, designed and fabricated with the measured gain of 32dB. Next, a 2×2 up-converter antenna array is designed and fabricated. Measured result shows the array has a power combining efficiency of above 90% and IM3 EIRP of 16 dBm. In close-range point-to-point communication and radar systems, the demonstrated millimetre-wave sub-harmonically pumped up-converter antenna array can be considered as a transmitter because of its low cost, high dynamic range and high linearity.

Finally, A1×4 Ka-band linearly polarized rectifying antenna array based on the SIW technology is used to convert RF energy to DC energy in microwave power transmission or RF energy recycling system. The RF-to-DC conversion efficiency of single SIW-ALTSA rectenna and the whole rectenna array is shown and discussed with measured results. It is postulated that the four element array is expandable to a larger array in two dimensions simply by a geometric arrangement. The conversion efficiency can be improved by using better performance diodes.

CHAPTER 4 60 GHZ BEAMFORMING RECEIVER SUB-SYSTEM

This chapter describes the design of a 60 GHz beamforming receiver sub-system based on the SIW technology. We realize a 60 GHz beamforming receiver system including 60 GHz front-end mainly using SIW components including antenna array, Butler matrix, band-pass filter, sub-harmonically pumped mixer and 30 GHz LO source. Consequently, the beam of the sub-system is adaptively switched by the controlled signals according to the criterion of maximum received signal.

4.1 Motivation

The worldwide introduction of the unlicensed frequency band around 60 GHz has opened new avenues and created new opportunities for high data rate wireless applications [142]-[143]. The massive amount of available spectrum extending from 57–64 GHz range in the U.S. is larger than the total of all other unlicensed spectrums which leads to a low-cost implementation of high data rate demanding wireless applications [144]-[145]. Being much higher than the power limits of other unlicensed spectrums, the equivalent isotropic radiated power (EIRP) limit on the transmit signal imposed by FCC is 40 dBm which increases the attractiveness of this spectrum [142]. Possible applications include but are not limited to wireless high quality video transfer including uncompressed HDTV signals, point to point wireless data links replacing optical links, video/music transfer from/to portable devices, all of which are required to provide link speeds in the Gb/s range [146]-[147]. The main limitations associated with the 60 GHz frequency range are high propagation loss including oxygen absorption, immaturity of the circuit technology, high directivity of the antennas, and limited wall penetration. According to [144] and [145], 60 GHz signals are not able to propagate through walls and diffract around objects without significant power losses.

These limitations, however, can also be desirable because they reduce the interference, increase the frequency reuse, and hence, the network security. The possibility of reduced interference and higher frequency reuse makes the 60 GHz band an attractive solution for short range indoor broadband communications where many transmitters can be deployed in a small space. There are two factors causing high propagation losses in 60 GHz band. First, the free-space loss is directly proportional to the square of frequency as dictated by Friis' equation. Second, the water vapor in

the atmosphere brings an additional 15 dB/km of attenuation [144]. Although the FCC regulations permit high transmit powers, the RF front-end technology has not evolved enough to provide the required output powers to overcome these high propagation losses [148]. Use of several highly directive antennas and selecting the antenna with the highest power have been proposed by the authors to overcome the high propagation losses and provide antenna diversity to fight human shadowing [148]-[150]. Many sector antenna designs have come up to serve this goal [151], [152].

While helping in overcoming the high propagation losses, the employment of highly directive antennas with high gain in communication systems necessitate a perfect beam alignment of the transmitter and receiver as a small mismatch can cause signal degradation in terms of several dB [153], [154]. The degradation in signal power changes with the motion of the receiver in an arc around the transmitter and this phenomenon has been named as the “scalloping effect” in the antenna literature [151]. Manual beam alignment mechanisms such as the use of a laser pointer [148] can be sufficient for experimental applications, but an automatic beam alignment system is necessary for indoor 60 GHz communications systems since the locations of the transmitter or the receiver may change frequently.

A smart-antenna system can solve the alignment problem by adaptively steering the beams of the transmitter or the receiver to maximize the signal power at all times. Moreover, the employment of an antenna array at the receiver or transmitter results in distribution of power amplification over several channels thus overcoming the high output power requirements of 60 GHz LNAs which cannot be realized using current technology [148]. Many authors attempted to overcome the power requirement and alignment challenges of the 60 GHz systems using antenna arrays [153]-[155]. Although smart-antenna systems can solve the alignment and propagation loss problems, the more additional channels to the radio frequency (RF) front-end will increase the already high hardware costs several folds whilst exponentially increasing the computational requirements of the system. Low gain large beamwidth array elements are extensively used in [156]-[158] to increase the angular coverage, but similar requirement for a large number of RF channels makes the situation worse. Therefore, much simpler antenna switching systems, employing several highly directional elements, is desirable to steer the beam to predefined directions with negligible computational complexity and costs. The switched-beam antenna with

the Butler matrix network [155]-[160] is a cost effective approach to implementing an adaptive antenna in microwave and millimetre-wave range.

In this chapter, we propose a low cost 60 GHz switched-beam receiver system employing all 60 GHz components based on SIW technology, such as slot antenna, 4×4 Butler matrix network, band-pass filter, sub-harmonically pumed mixer and LO source. In this system, not only IF control circuits block, but also adaptive algorithm in advanced RISC machine (ARM) core are developed. Finally, our system is demonstrated by experiment: beam is switched adaptively through comparing four received signals in the control circuits and ARM based on maximum received power criterion.

4.2 System Considerations on 60 GHz Beamforming Receiver Sub-system

Figure 4.1 shows the configuration of the proposed switched-beam smart antenna system. The 60 GHz base-station receiver consists of three sectors, each of which covers 120 degree area. So each sector is composed of one 4×4 Butler matrix antenna sub-system. In this sub-system, we integrate the SIW slot antenna, the SIW Butler matrix and the SIW band-pass filter together into one substrate. This design can overcome the interconnection problem between millimetre-wave circuits.

Here, an SIW linear slot array antenna is chosen thanks to its more than 120^{o} 3-dB beamwidth in E-plane and a higher gain than microstrip patch antenna, which is very important in millimetre-wave application. The working frequency of this antenna is from 58 to 60.5 GHz. In order to avoid grating lobes, an array spacing of a half wavelength in free space is normally chosen. Four SIW linear slot array slot antennas are connected with a 4×4 SIW Butler matrix which is used to form four fixed beams covering the 120^{o} area. Then, an SIW band-pass filter working from 58.5 to 63 GHz is connected with each input port of the Butler matrix. To amplifying received signals, a ceramic substrate with 10 mil thickness is necessary to be used to wire bond the 60 GHz LNA chip die. So how to interconnect the LNA and the filter with good insertion loss and return loss is another challenge. In this design, we make use of BCCPW in both input of the LNA circuits and the output of the filter. Because both circuits designed on two very different substrates, an additional 50 Ω BCCPW line is inserted between the LNA and the filter for matching them. To down-convert the 60 GHz signals to IF (1.5 GHz), a sub-harmonically pumped mixer using anti-parallel diode pairs is designed, which considers low mutual coupling effects. It is well known

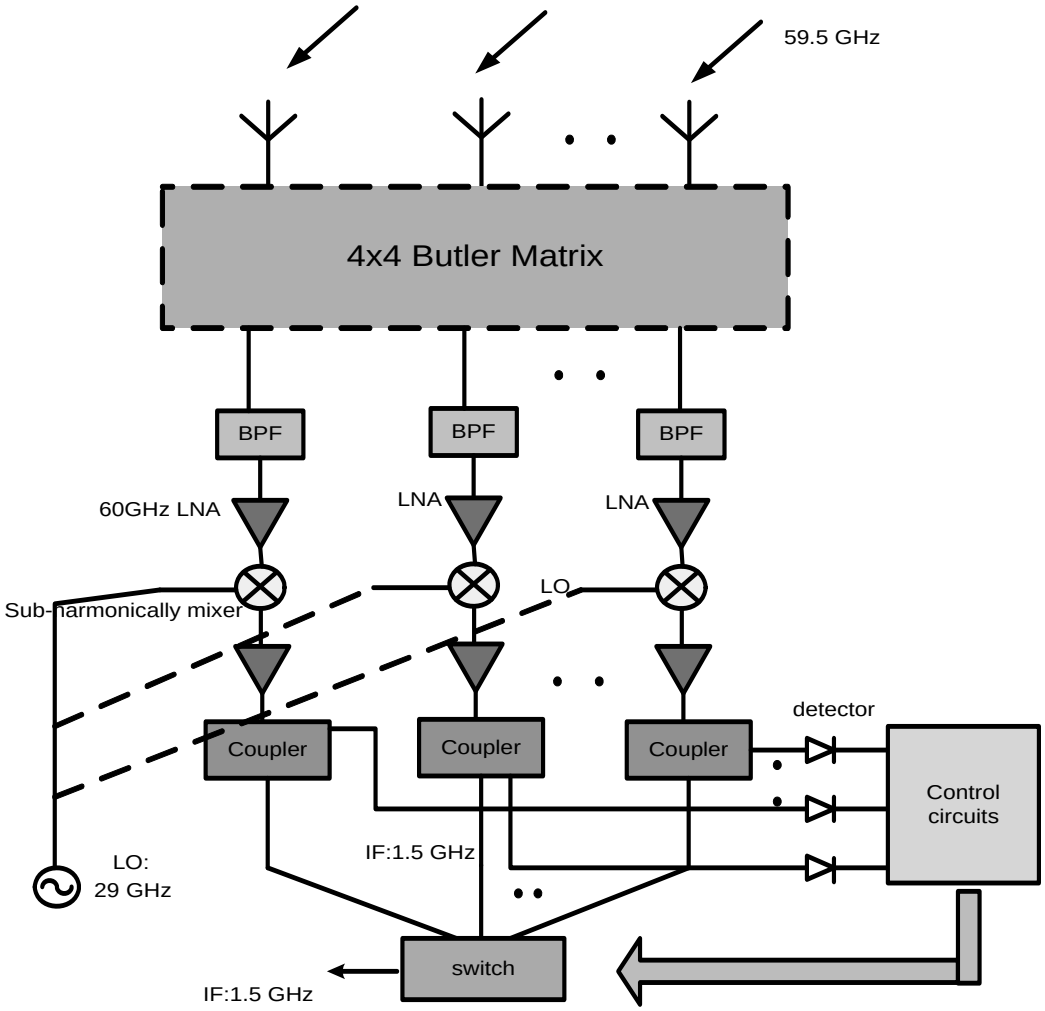

Figure 4.1: Configuration of the proposed switched-beam smart antenna sub-system

that a high power 60 GHz signal source is very expensive and difficult to design. Therefore, a sub-harmonically pumped mixer is substituted which can use a low pumping frequency, and then decrease the cost of the system. In addition, this mixer provides AM noise suppression and no requirement of DC bias circuits. Instead of a 60 GHz LO source, a 30 GHz LO source is developed to drive the sub-harmonically pumped mixer. This LO circuit consists of the SIW 10 GHz VCO proposed in Chapter 3, drive amplifiers and a10-to-30 GHz SIW tripler. After frequency down-conversion of four 60 GHz signals, we obtain four IF signals. Here we define RF chains in the sub-system as channel 1 to 4 from left to right as shown in Figure 4.1. Each IF signal is filtered, amplified, coupled to detector and finally sent to ARM processor to judge the maximum received power among the four IF signals by a algorithm of comparison. After the comparison of the four IF signals, control signals will be able to get feedbacked to the SP4T

switch and the beam is pointed to the main beam of the transmitted antenna. That is to say, the arriving 60 GHz RF signal can effectively tracked. Details of circuits in the system are described in the following sections.

In this project, the receiver system is a heterodyne structure. The second IF-to-baseband down-conversion is neglected because we only consider how to switch the beam automatically in the work. So this is also called IF adaptive beam-switched system. 60 GHz band is deployed for Gb/s communication system, the IF adaptive structure decreases the cost and complexity of the baseband circuits. Meanwhile, IF adaptive structure is also much better than RF adaptive structure because presently it is difficult to design a low-cost 60 GHz switch and a detector with a good performance compared with IF components. This is the reason why we choose the IF adaptive structure for 60 GHz band instead of RF or baseband adaptive structure.

4.3 60 GHz SIW Slot Antenna Design

To date, a vast amount of different planar antennas have been studied for millimetre-wave radio and radar applications. Although high gain operations have been demonstrated with microstrip patch antenna arrays, these configurations suffer from serious loss in the millimetre-wave band; the efficiency decreases as the gain and/or frequency becomes higher even though those antenna design techniques are basically mature. It was roughly estimated that the efficiency of microstrip arrays with gain of 35 dBi would be lower than 20% in the 60GHz band [161]. On-chip antennas also have other drawbacks. Their radiation efficiency on conductive high-permittivity silicon is poor and in spite of the short wavelength, they still occupy a non-negligible area on an MMIC chip, which is an important cost factor. The situation is even worse if arrays are required to achieve necessary gain of about 15 to 20 dBi in order to bridge intended distances of up to 10 meters in a WPAN environment [162].

Waveguide slot antenna arrays are the most attractive candidates for high-gain planar antennas, due to smallest conductor loss among all the planar feeding structures [163]. Single-layer waveguides for a mass reproducible planar array were presented in [163]-[165]. The antenna based on the SIW scheme can easily be integrated with other circuits, which leads to the cost-effective sub-system. Some SIW slot antenna arrays and beamforming networks have been developed [166]-[169]. We proposed 60 GHz SIW slot antenna array with the maximum gain of 22 dBi and corresponding efficiency of about 68% [170].

In the system design, SIW slot antenna array is employed. With consideration on the dielectric properties and temperature properties of dielectric substrate, Rogers/duroid 6002 with 0.5 oz. rolled copper foil, 20 mil thickness and dielectric constant ε_r=2.94 is used in this work. Generally, a thick substrate should be used to reduce the losses in connection with the top and bottom conductors and obtain appropriate offset for the design of radiating slots. This antenna consists of 12 radiation slots etched on the broad wall of SIW. The SIW structure is terminated with a short wall three-quarter guided wavelength beyond the centre of the last radiation slot. In order to allocate the slots at the standing wave peaks and excite all the slots with the same phase condition (in-phase), the slots in a linear array are placed half a guided wavelength at the required centre frequency and the adjacent slots have the opposite offset with respect to the SIW centre line. The width of radiation slots should be much smaller than the slot length, usually between one tenth and one twentieth of slot length. This, of course, depends on the bandwidth requirements. The detailed design procedure similar to that presented in [171] is as follows.

When a longitudinal slot on the broad wall of SIW is designed around resonance and slot offset is not very big or very small, the forward and backward wave scatterings from the slot are symmetrical in SIW and then the slot can be equivalent to shunt admittance on transmission line. According to Stegen's factorisation [172], the equivalent shunt admittance can be given as follows

$$\frac{Y(x,y)}{G_0} = \frac{G_r}{G_0} \cdot \frac{G + jB}{G_r} = g(x)h(y) = g(x)\left[h_1(y) + jh_2(y)\right] \tag{4.1}$$

where x is the offset of slot, $g(x) = G_r/G_0$ is the resonant conductance normalized to the conductance G_0 of SIW, $h(y) = h_1(y) + jh_2(y) = (G + jB)/G_r$ is the ratio of slot admittance to resonant conductance, $y = l/l(x, f)$ is the ratio of length to resonant length, $l(x, f) = \lambda \cdot v(x)/2\pi = c_0 \cdot v(x)/2\pi f$ is the resonant length. In this way, the calculation of the equivalent slot admittance is reduced to the calculation of three single variable functions $g(x)$, $v(x)$, and $h(y)$. Commercial full-wave simulator package HFSS is used to extract $g(x)$, $v(x)$, and $h(y)$ of the isolated longitudinal slot. In our work, slot width is 0.18mm and SIW width a is 2.4 mm. Figure 4.3 (a) and (b) show $g(x/a)$ and $v(x/a)$ for a discrete number of relative offsets x/a in the range 0.03-0.1. Curve fitting has been applied to approximate $g(x/a)$ and $v(x/a)$ in a continuum which can be directly used in the design of the slot array by the classical iteration procedure [173]. For each offset, function $h(y)$ as shown in Figure 2 (c) has also been extracted for y in the range 0.82-1.18. A table-look-up

method for $h(y)$ is used in the design procedure of the slot array. It is clear that $h_1(y)$ and $h_2(y)$ rapidly change with the y around the matching point y=1, which shows that the bandwidth of the SIW slot array is smaller than the bandwidth of conventional rectangular waveguide slot array [174].

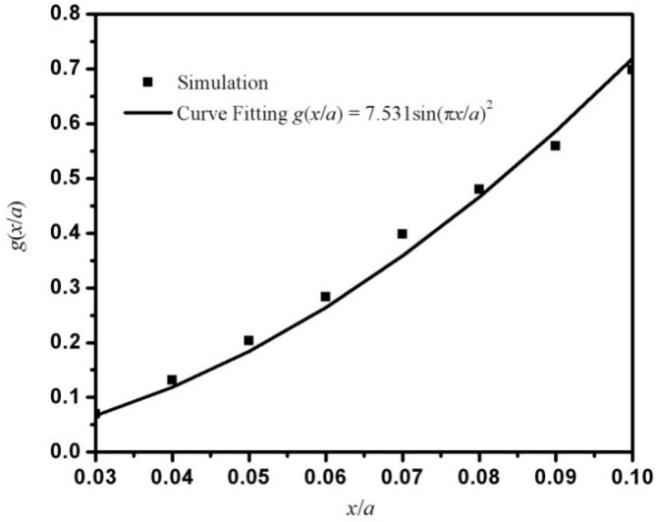

(a)

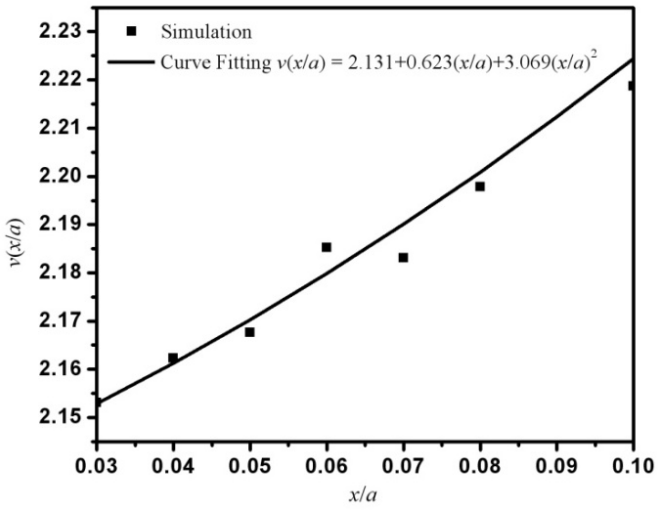

(b)

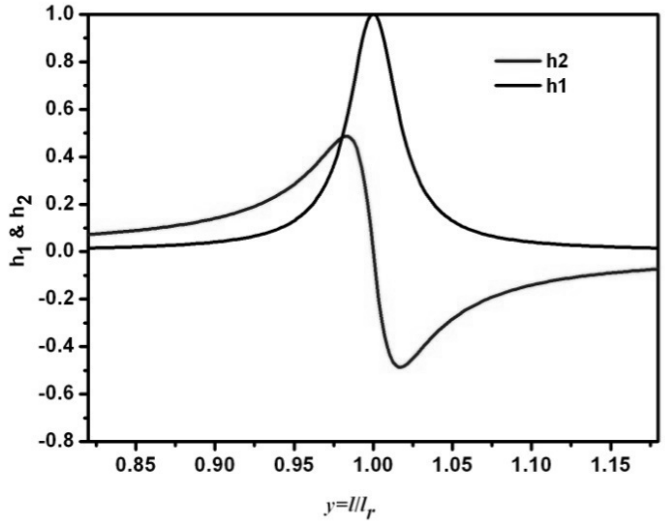

(c)

Figure 4.2: (a) $g(x)$, (b) $v(x)$, and (c) $h(y)$, of isolated longitudinal slot with slot width 0.18mm in the broad wall of SIW with width of 2.4 mm

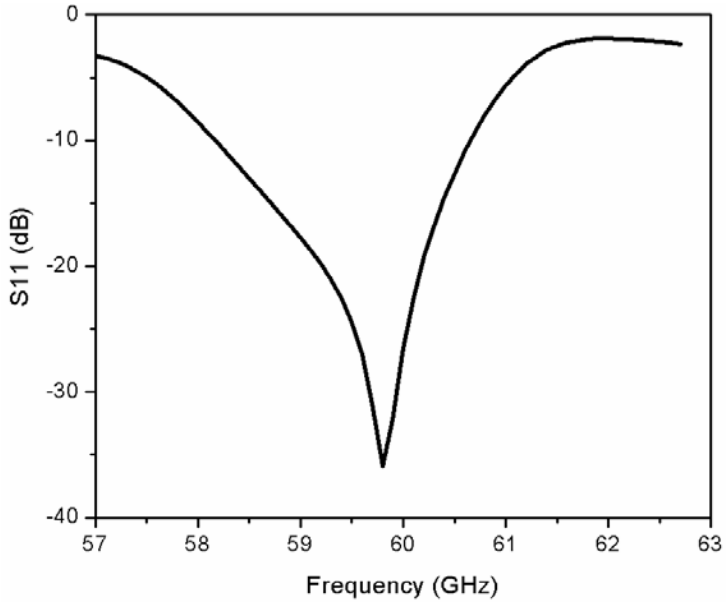

Figure 4.3: Simulated return loss of the SIW slot array antenna

Based on the above analysis, the entire antenna is finally simulated by HFSS. As shown in Figure 4.3, simulated bandwidth for 10 dB return loss is 2.3 GHz from 58.5 GHz to 60.7 GHz. Figure 4.4 shows simulated results of E-plane and H-plane radiation patterns at 59.5 GHz. The 3-dB

beamwidth of E-plane radiation pattern is about 140^{o} which is very suitable for 4×4 Bulter matrix beamforming architecture. The antenna also provides a high gain of about 13 dBi.

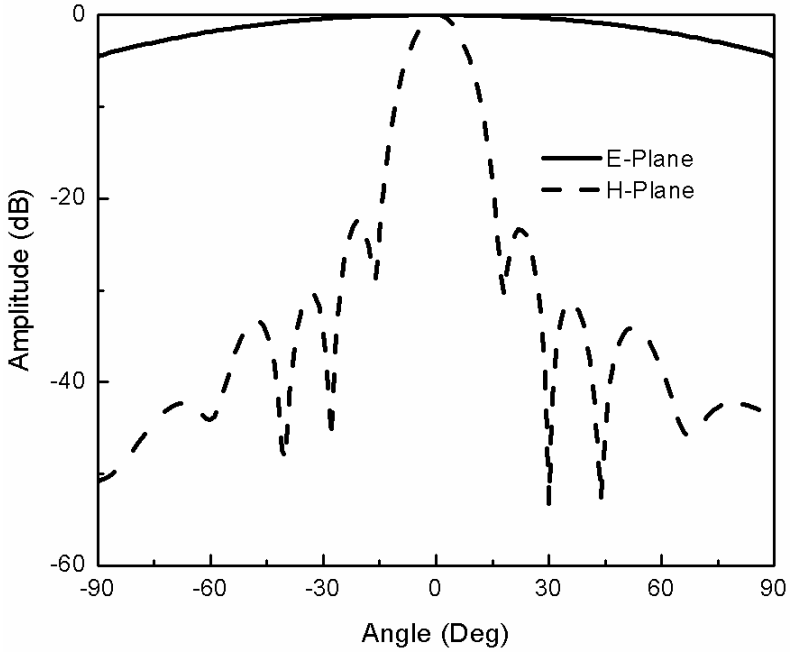

Figure 4.4: Simulated normalized radiation patterns in H-plane and E-plane at 59.5 GHz

4.4 60 GHz RF Front-End Design

Recently, many millimetre-wave front-ends or sub-systems based on SIW technology have been developed. Most sub-systems only developed SIW passive circuits such as filters and antennas to be integrated with active commercial components. In this chapter, we developed 60 GHz SIW hybrid integrated sub-system in the first place using SIW components from passive circuits to active circuits except of LNA.

In this design, the circuit from output of slot antenna to input of IF circuits block is called 60 GHz RF front-end, which is composed of an SIW Bulter matrix, filters, sub-harmonically pumped mixers, 60 GHz LNAs and 30 GHz LO source, as shown in Figure 4.5. In previous chapters, we took advantages of SIW technology to design some novel active components, such as VCO and mixer, which will be employed in the RF Front-end. First of all, the SIW Bulter matrix is proposed. Next, a 60 GHz SIW band-pass filter is designed between Bulter matrix and LNA. After that, a section of conductor back coplanar waveguide (CBCPW) is used to connect and match LNA circuit and filter. Further, 60 GHz LNA is used to amplify the received signal

after filter. Afterwards, the 60 GHz sub-harmonically pumped mixer is developed as a frequency down-converter. Finally, the LO is designed using an SIW VCO and tripler according to the requirements of the sub-system.

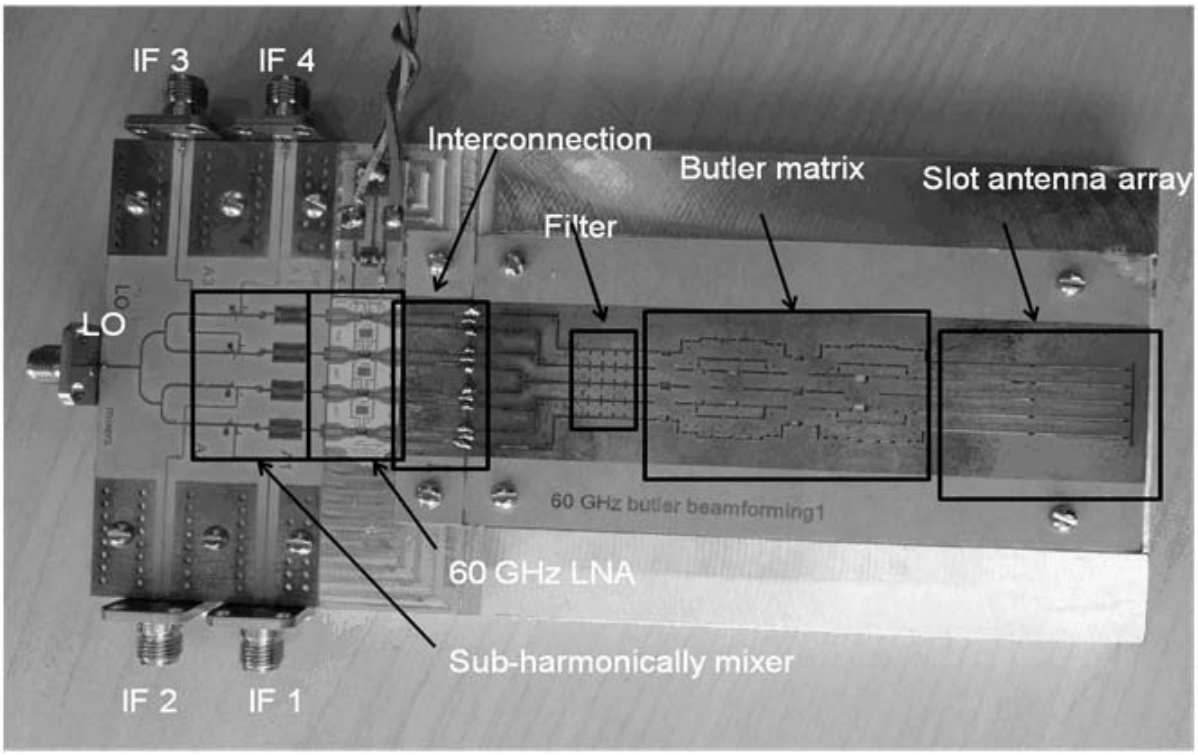

Figure 4.5: Photograph of the RF Front-end with the antenna array

4.4.1 60 GHz SIW Butler Matrix

Since its invention as a feeding structure for antenna arrays in the 1960s [175], the Butler matrix has been used extensively in radar, electronic warfare, and satellite systems for decades [176]-[177]. More recently, with an increasing demand for broadband wireless access technologies, techniques for maximizing the capacity and improving the transmission quality and coverage of a base station or an access point are currently under intense research. Considerable attention is being paid to the implementation of smart antenna systems with the Butler matrices [178]-[180]. Due to the large electrical size, the Butler matrices operating below or around 10 GHz are generally developed with the consideration of its physical size. But in millimetre-wave range, the physical size is inherently diminished, whereas the propagation loss is inevitably increased. The power losses are, therefore, a major concern for millimetre-wave circuit design. Accordingly, the millimetre-wave Butler matrices are usually realized by simple, but effective structures fabricated

on low-loss substrates to reduce the power losses. Therefore, SIW technology is a better choice to build a Butler matrix compared to microstrip. Some examples in the literature are implemented by SIW technology [181]-[182].

Figure 4.6 shows a block diagram of the conventional 4×4 Butler matrix composed of 90^o hybrids, crossovers, and the associated phase shifters. As different input ports are excited, the Butler matrix is treated as a beamforming network to provide four output signals with equal power levels and the progressive phases of $+45^o$, -45^o,$+135^o$ and -135^o , respectively. Hence, one can switch the direction of the radiation main beam by exciting the designated input port as shown in Figure 4.6.

In our designed Bulter matrix, the 90^o hybrids and crossovers are realized with the SIW short-slot couplers [183]. Phase shifters are SIW broadband self-compensating phase shifters [184]. For easily integrating the antennas on the same substrate, Rogers/duroid 6002 with 20 mil thickness and dielectric constant ε_r =2.94 is employed to implement the Butler matrix. Descriptions of the designs of the SIW 90^o Hybrid, SIW crossover and SIW phase shifter follow. Finally, the SIW Butler matrix is simulated and measured with the SIW slot array antenna.

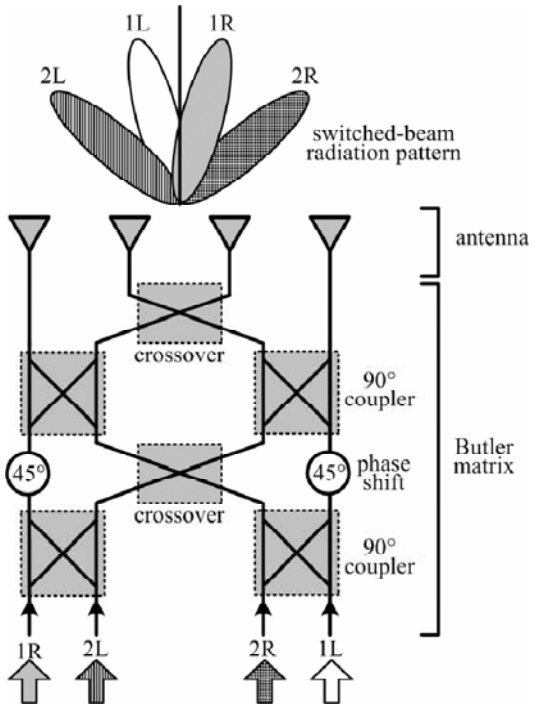

Figure 4.6 : Configuration of the Butler matrix network with antenna

1) 90^o Hybrid Coupler and Crossover

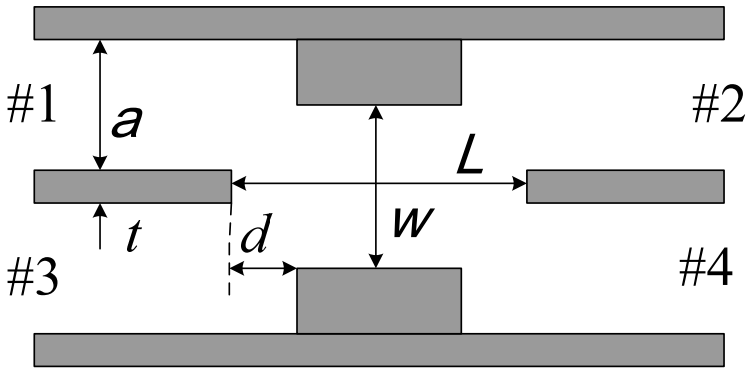

Figure 4.7: Structure of the SIW 90^o hybrid coupler or crossover

Figure 4.7 shows the structure of the SIW 90^o hybrid coupler or crossover. A stepped structure is installed in the coupled region in the conventional structure. The compact waveguide cross coupler and 90^o hybrid coupler can be designed by using the method as was introduced in [183]. In this structure, *a* is the width of the SIW, *t* is the thickness of the SIW metallic wall, *W* and *L* are respectively the width and length of the coupling area. Both couplers are designed at 59.5 GHz and simulated by HFSS software. Table 5.1 lists parameters of the SIW 90^o hybrid coupler and crossover. Figure 4.8 and Figure 4.9 show simulated S parameters of the SIW 90^o hybrid coupler and crossover.

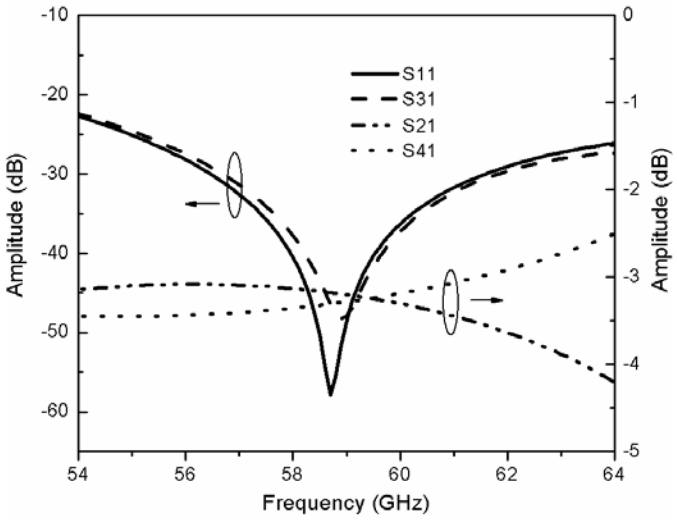

Figure 4.8: S parameters of the SIW 90^o hybrid coupler

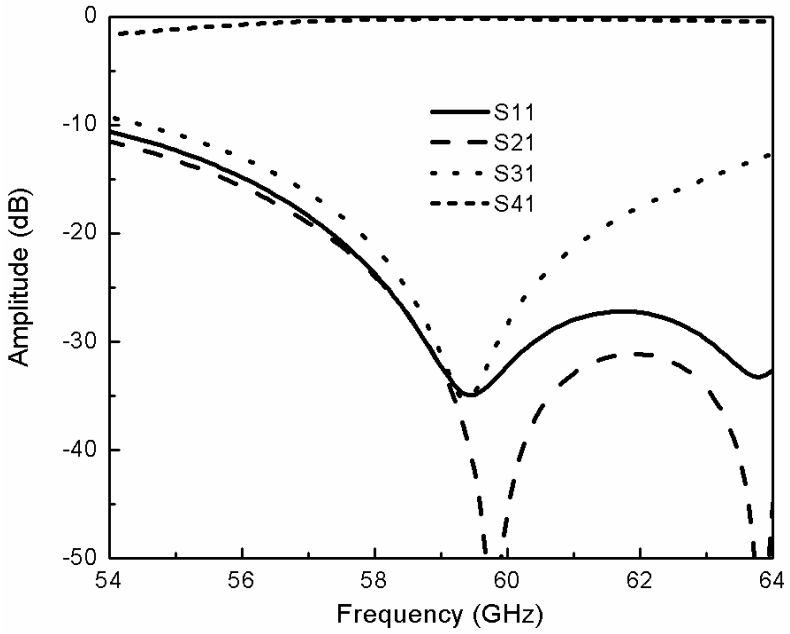

Figure 4.9: S parameters of the SIW crossover

Table 4.1 Parameters of the SIW 90^o hybrid coupler or crossover

SIW 90^o hybrid		**SIW crossover**	
t= 0.3 mm	a= 2.4 mm	t= 0.3 mm	a= 2.4 mm
L= 3 mm	W = 5.6 mm	L= 4.78 mm	W = 3.44 mm
d=0.77 mm		d=1.34 mm	

2) Phase shifter

Usually the SIW or conventional rectangular waveguide phase shifter in Bulter matrix is realized by delay line or equal-length unequal-width structure. But both types of phase shifter are narrow band because the TE_{10} mode in the SIW or conventional rectangular waveguide has dispersion characteristics. In order to get a wideband SIW phase shifter, a self-compensating SIW phase shifter, which can achieve a relative flat phase shift over a wide band, has been developed [184]. This new phase shifter is proposed based on a very interesting phenomenon that the varying

tendencies of phase shift obtained by delay line and equal-length unequal-width structure versus frequency are just opposite over frequency. Thus, a concept of phase compensation can be applied to expand the useful bandwidth of a phase shifter. Specifically, the phase shift will simultaneously be accomplished by combining different electrical lengths (delay line) and different phase velocities of waves (unequal-width). To achieve flat relative phase differences between ports of the Bulter matrix, the self-compensating SIW phase shifter is adopted in our design.

Figure 4.10 shows the structure of a phase shifter consisting of delay line (SIW bends) and a section of wider SIW. SIW bends are used to extend SIW length as delay lines. More phase shifts are introduced by SIW bends at higher frequency. Oppositely, more phase shifts are produced by wider SIW at lower frequency. Therefore, a flat phase shift over a wide band can be achieved by combining these two phase shifting features. To minimize reflection, one post is placed and optimized at the corner of each bend as described in [185]. *b* and *c* are parameters of the position of the post. The diameter of the post is *d*. L_S is the length of the bend, which acts as the delay line in this structure. *W* and L_W are the width and length of the wider SIW. By optimization of L_S, *W* and L_W, we can generate a flat relative phase shift over a wide band. Thickness of SIW wall *t* and SIW width *a* are the same as the coupler designed above. 45^o and 0^o phase shifters are designed according to the analysis of self-compensating SIW phase shifter. Table 4.2 lists parameters of the SIW 45^o and 0^o phase shifters.

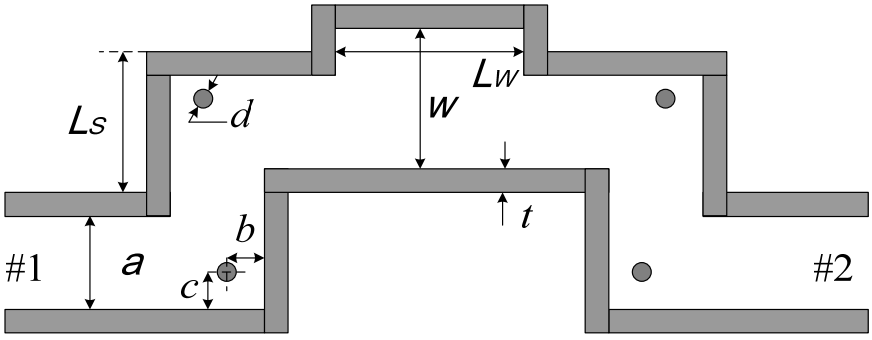

Figure 4.10: Structure of the SIW phase shifter

Table 4.2 Parameters of the SIW phase shifter

45^o phase shifter		**0^o phase shifter**	
b= 1 mm	*c*= 0.9 mm	*b*= 0.98 mm	*c*= 0.95 mm
Ls= 2.1 mm	L_W = 9.1 mm	*Ls*= 2.05 mm	L_W = 6 mm
d=0.3 mm	*W*=2.79 mm	*d*=0.3 mm	*W*=2.55 mm

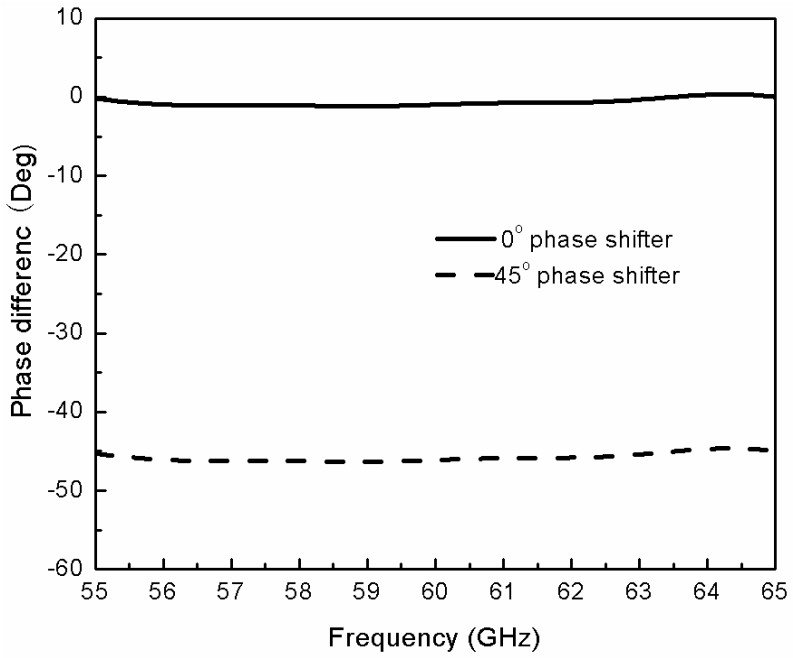

Figure 4.11: Simulated phase differences between crossover and both phase shifters

45^o or 0^o phase shifters are required to yield a shifting phase which equals to 45^o or 0^o plus shifting phase caused by crossover. Simulated phase differences between crossover and both phase shifters are shown in Figure 4.11. Results indicate that this phase shifter could generate a flat relative phase shift over a wide band.

3) Simulations and Experiments of the Butler Matrix

To validate the design, the Butler Matrix is simulated using HFSS and measured with the slot antenna. However, we cannot directly measure the developed 8-ports Butler matrix because we do not have enough V-band connectors. That is, it is not an accurate and guaranteed way to using many V-band connectors to test multi-port circuits. So we only obtain simulated results of the Butler Matrix and measured S parameters and radiation patterns with the integrated antenna.

Fig 4.12 shows the simulated return losses of the Butler matrix. Return losses of all ports are less than -15 dB from 55 to 63 GHz. Isolation characteristics are shown in Figure 4.13. Figure 4.14 and 4.15 show the transmission coefficients including magnitudes and relative phases with port 1 and port 2 excitations. From 57.5 to 62 GHz, the amplitude imbalances and relative phase imbalances are less than 1 dB and 8^{o}, respectively. Simulated transmission coefficients indicate that the entire Bulter matrix has insertion loss of about 1.7 dB at 59.5 GHz.

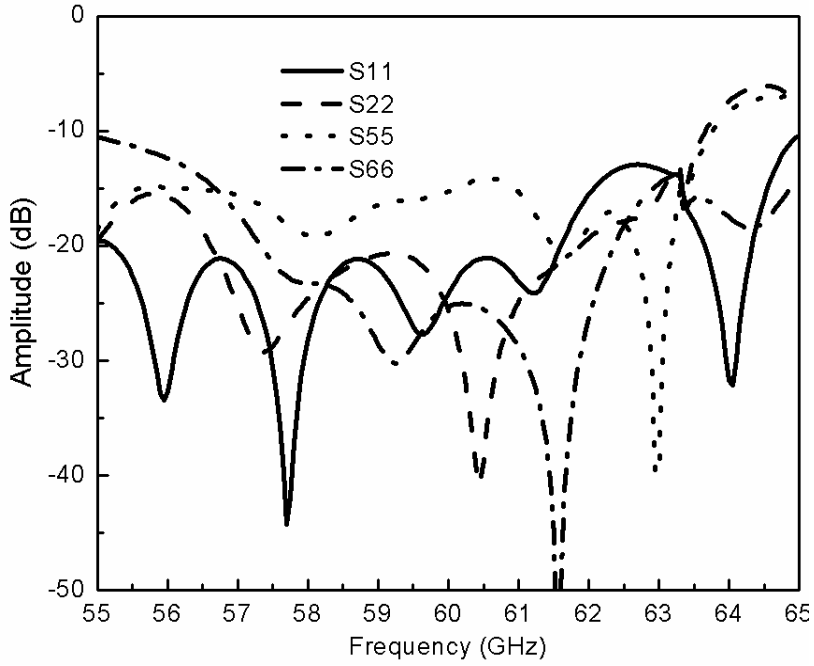

Figure 4.12: Simulated return losses of the Butler matrix

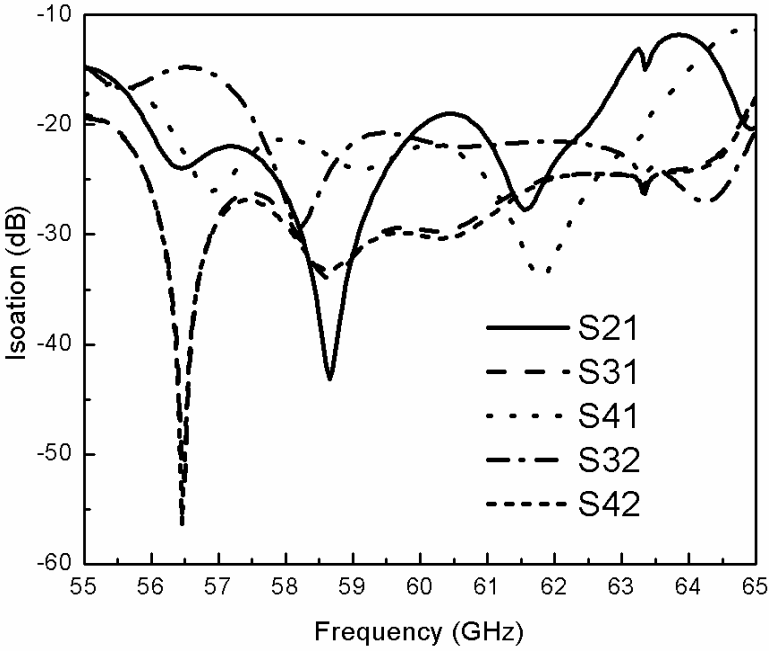

Figure 4.13: Isolation characteristics of the Butler matrix

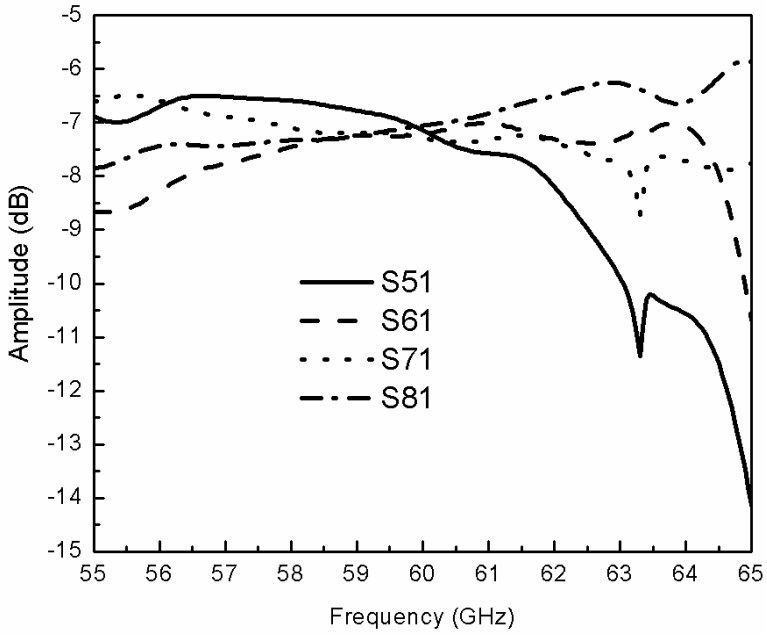

(a)

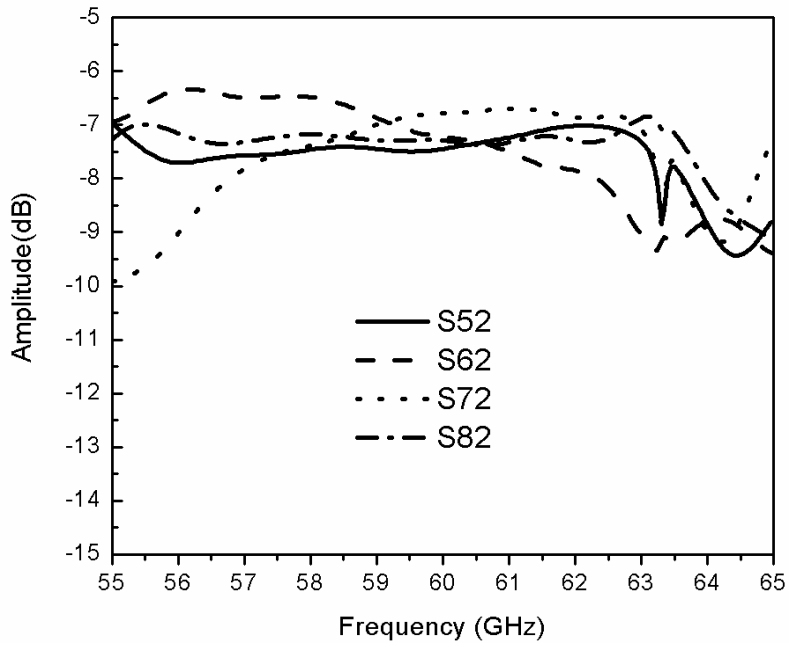

(b)

Figure 4.14: Magnitudes of -transmission coefficients of the SIW Butler matrix (a) port 1 excitation. (b) port 2 excitation.

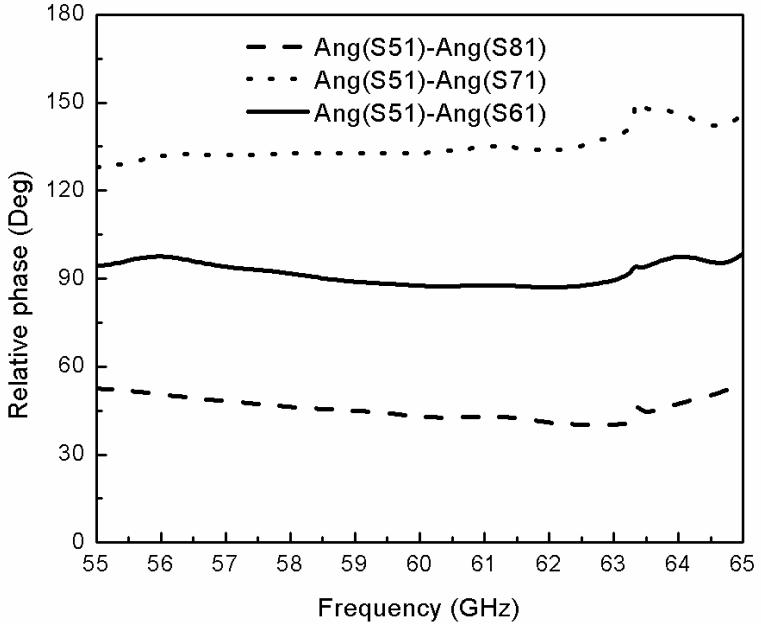

(a)

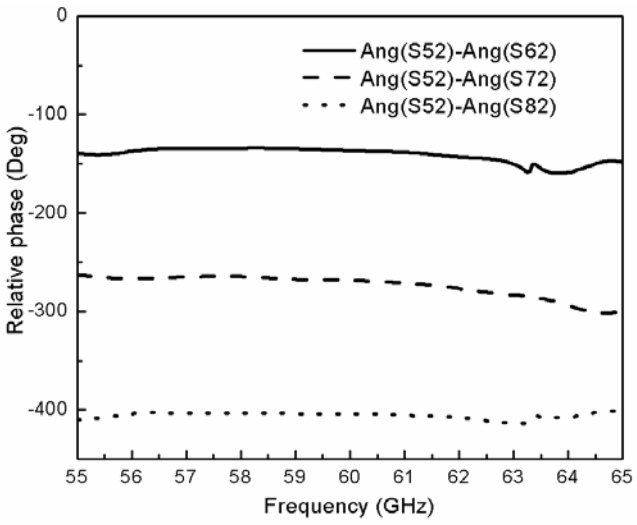

(b)

Figure 4.15:Relative phases of the transmission coefficients of the SIW Butler matrix, (a) port 1 excitation. (b) port 2 excitation

The Butler matrix integrated with the slot antenna array is measured. Return losses and isolations are greater than -13 dB from 55 to 65 GHz. E-plane radiation patterns are tested at 59.5 GHz, as shown in Figure 4.12. From the measured E-plane radiation patterns, it can be observed that the main beam directions are $\pm 42^{o}$ corresponding to input port 2 and 3, $\pm 15^{o}$ to input port 4 and 1, respectively. The gain of the antenna array is calculated from the Friis transmission equation. The gain is about 16 dBi when port 1or 4 is excited. But the gain is about 13.5 dBi corresponding to input port 2 or 3.

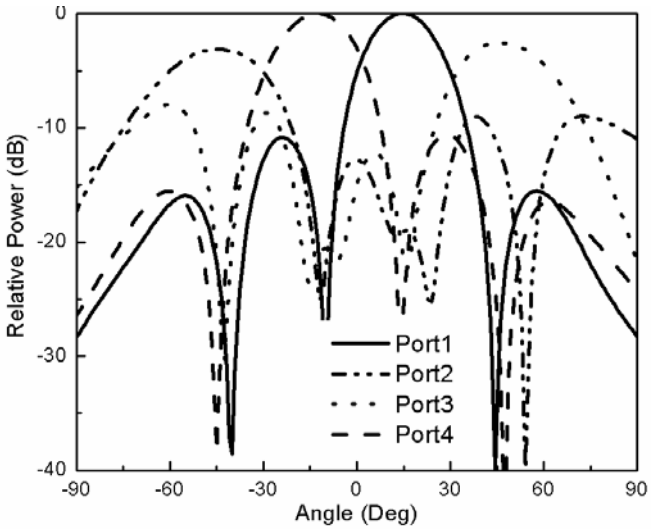

Figure 4.16: Measured E-plane pattern at the designed frequency (59.5 GHz)

4.4.2 60 GHz SIW Band-pass Filter

In a typical receiver architecture, it is necessary to apply a band-pass filter before LNA. 60 GHz SIW filter is naturally chosen for our sub-system because it has high performance and easy integration with the Butler matrix. A 4-order Chebyshev SIW cavity filter is designed, as shown in Figure 4.17. L_1 and L_2 are lengths of cavities, W_1, W_2 and W_3 are widths of the coupling gaps. The thickness of the coupling gap is the same as the thickness of the metallic wall of the SIW.

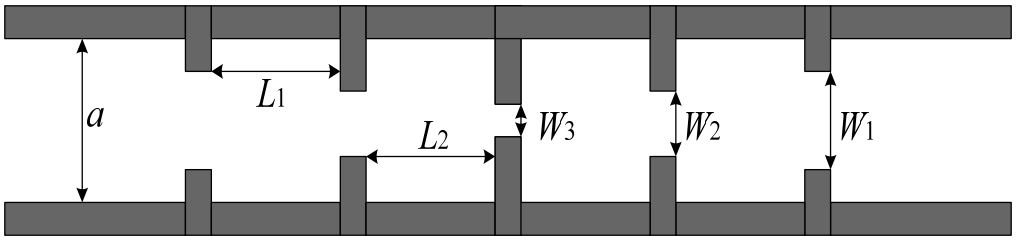

Figure 4.17: Physical description of the SIW cavity filter

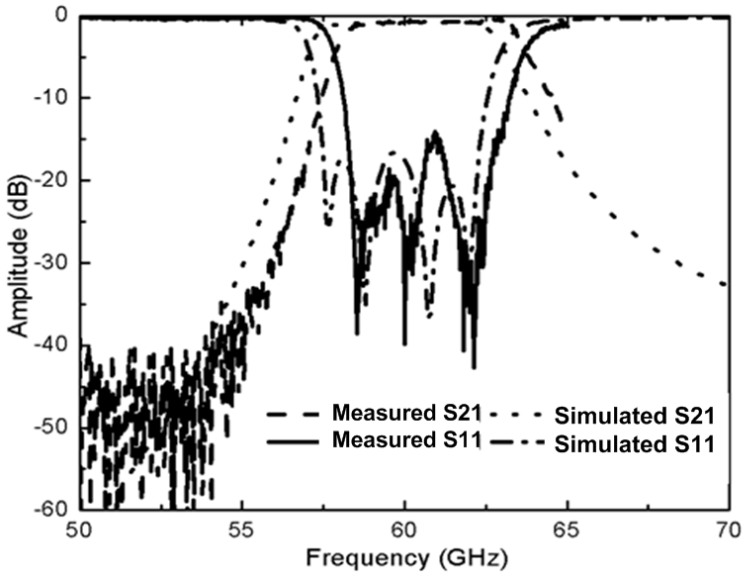

Figure 4.18: Simulated and measured frequency responses of the SIW band-pass filter

The SIW cavity filter is simulated using HFSS. Details of the parameters of the filter are a=2.3mm, L_1=1.363 mm, L_2=1.56 mm, W_1=1.308, W_2=0.988 and W_3=0.926. In our measurement, V-band test fixure and TRL calibration method are used. Two wide band CBCPW-to-SIW

transitions are also designed for measuring the filter [185]. Figure 4.18 shows simulated and measured frequency responses of the filter. Insertion loss and return loss in the pass band are around 1 dB and lower than -15 dB from 58 to 63 GHz, respectively. Measured results do not display the frequency response beyond 65 GHz because our V-band test fixture is working up to 65 GHz. Simulated and measured results indicate that the SIW filter has a very high performance in millimetre-wave band.

4.4.3 60 GHz LNA and Interconnects Consideration

In the sub-system under consideration, Hittite HMC-ALH382, which has a high dynamic range, four stages GaAs HEMT MMIC LNA operating between 57 and 65 GHz, is used to amplify the received RF signal. This die chip LNA features 20 dB of small signal gain, 4 dB of noise figure and an output power of +12 dBm at 1dB compression from a +2.5V supply voltage. It is necessary to use a MHMIC process to fabricate a LNA model with the HMC-ALH382 chip in a ceramic substrate with 10 mil thickness and dielectric constant ε_r =9.9, as shown in Figure 4.5. CBCPW is employed as the transmission line to connect the LNA chip and other components. The reasons to choose CBCPW as the transmission line rather than microstrip are listed in the follow. First of all, we need a narrow strip to connect the chip's pad which has a size of 4×4 mil. CBCPW can obtain narrower middle strip than microstrip in the same substrate. Another reason is that the LNA model can be easily connected with the 60 GHz band-pass filter which has a CBCPW output. In order to come up with a good interconnection between the LNA model and the filter, 50 Ω CBCPW with 4 mil width middle strip is transited to 50 Ω CBCPW with 10 mil width middle strip. The maximum width of the middle strip of the 50 Ω CBCPW is 10 mil in the designed ceramic substrate. Figure 4.19 displays measured frequency responses of the LNA model. The measured gain of the LNA is about 19 dB at 59.5 GHz.

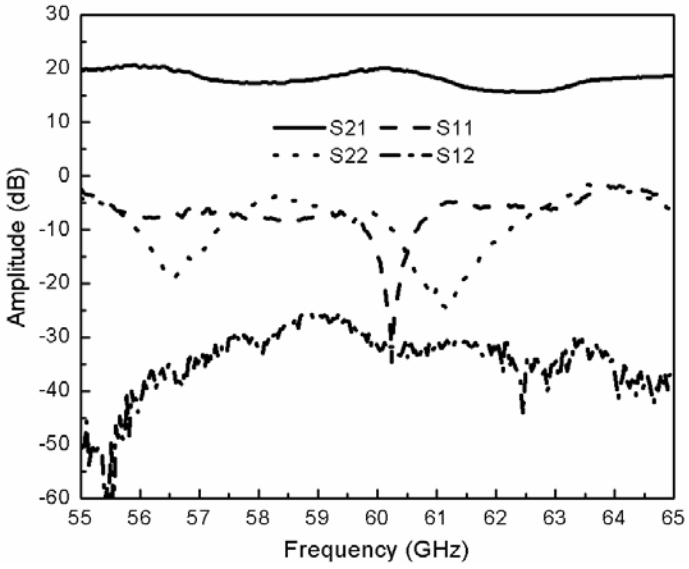

Figure 4.19: Measured frequency responses of the 60 GHz LNA model

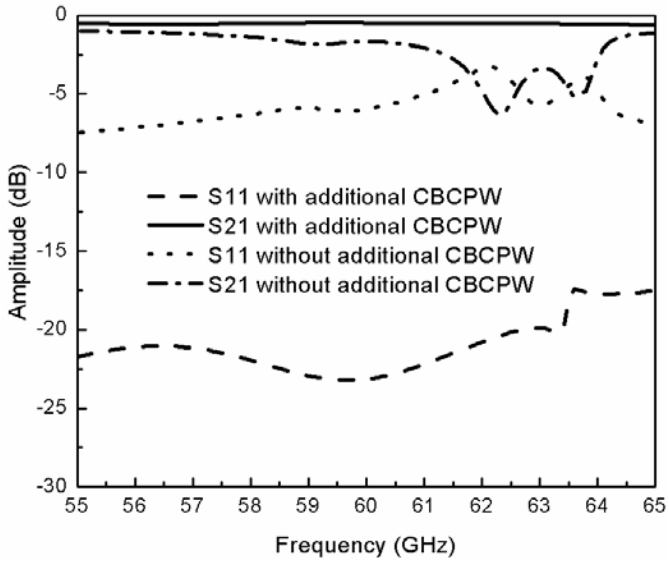

Figure 4.20: Simulated frequency responses of the connection with and without the additional CBCPW

A wideband SIW-to-CBCPW is designed to connect the LNA. For our PCB process, the minimum gap's width between two strips is 6 mil. So the minimum width of the middle strip is 35 mil on Rogers 6002 substrate with 20 mil thickness and dielectric constant ε_r =2.94. Figure 4.20 shows simulated frequency responses when the above both CBCPWs are connected, which indicates that the matching between two strips are very bad. In order to improve the matching between filter and the LNA, an additional 50 Ω CBCPW fabricated on Rogers 6002 substrate

with 10 mil thickness and dielectric constant ε_r =2.94 is inserted. In this additional 50 Ω CBCPW, the width of middle strip is 24 mil and the gap is 6 mil. Simulated frequency responses of the connection with additional 50 Ω CBCPW are shown in Figure 4.20. The insertion losses is less than 0.7 dB and return loss is greater than -15 dB from 55 to 65 GHz.

4.4.4 60 GHz Sub-harmoncially Pumped Mixer

The prototype of the sub-harmonically pumped mixer is similar to the up-converter proposed in Section 3.4, except that the SIW filter is replaced by a section of SIW in the 60 GHz mixer and a cross capacitor is added after the SIW. The section of SIW is designed with the cut-off frequency at 50 GHz. So high LO/RF and IF/RF isolations can be obtained. In this design, the mixer is designed with LO frequency of 29 GHz and IF frequency of 1.5 GHz. The circuit is designed and fabricated on Rogers/duroid 6010 substrate with dielectric constant of 10.2 and thickness of 0.254 mm. The Schottky anti-parallel diode pair used is MGS802 from Aeroflex/Metalics Inc.. Figure 4.21 shows the photograph of the designed mixer.

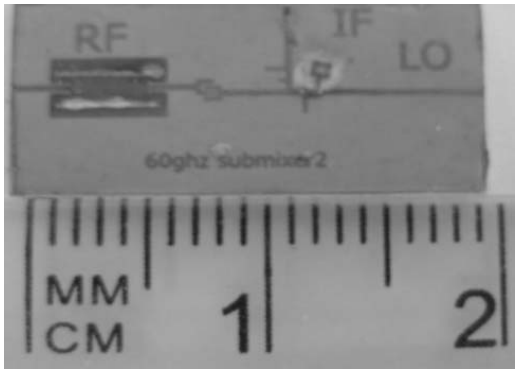

Figure 4.21: Photograph of the designed sub-harmonically pumped mixer

Measured conversion loss will remain 16 dB when LO input power level is larger than 11 dBm, where RF signal is fixed at 60 GHz with input power level of -20 dBm and LO frequency is 29 GHz as shown in Figure 4.22. Therefore, the minimized LO input power level of 11.5 dBm is chosen to pump the diode pair. Figure 4.23 shows simulated and measured conversion losses versus IF frequency when IF signal is swept from 58.4 to 62 GHz with a constant input power level of -20 dBm and LO signal is fixed at the frequency of 29 GHz with 11.5 dBm power level. At frequency of interest 59.5 GHz, the conversion loss is about 16.5 dB.

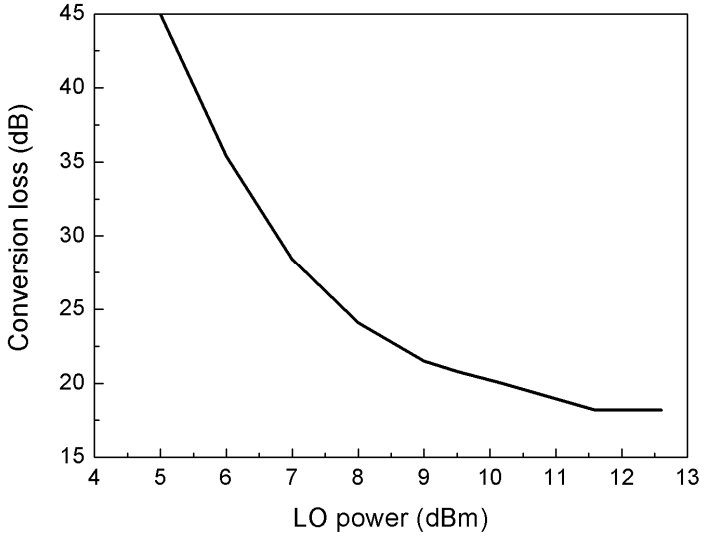

Figure 4.22: Measured conversion losses versus LO power level

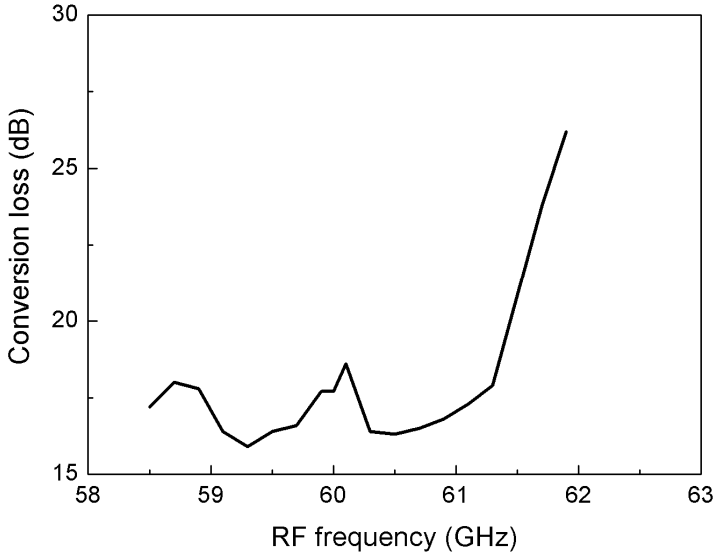

Figure 4.23: Measured conversion losses versus RF frequency

4.4.5 Ka-band LO Source Model

In order to drive the 60 GHz sub-harmonically pumped mixer, a Ka-band LO source model with an SIW VCO and an SIW frequency tripler is designed. Figure 4.24 shows the basic block diagram of the proposed Ka-band LO source. The RF power is developed by the SIW VCO presented in Section 2.5. This VCO can produce RF signal with output power of 6.5-9.8 dBm from 9.36-9.81 GHz. As X-band buffer amplifier, RFMD's broadband InGaP/GaAs MMIC

amplifier NBB-310 is to drive the SIW frequency tripler. We can get at least 15 dBm power level at the output of the amplifier. Through the SIW frequency tripler, the signal is converted from 9.36-9.81GHz to 28.08-29.43 GHz. To meet the power requirement of the LO of the sub-harmonically pumped mixer, Hittite's Ka-band PAs HMC566LP4 and HMC499LC4 are cascaded to obtain the power level of 20-22 dBm.

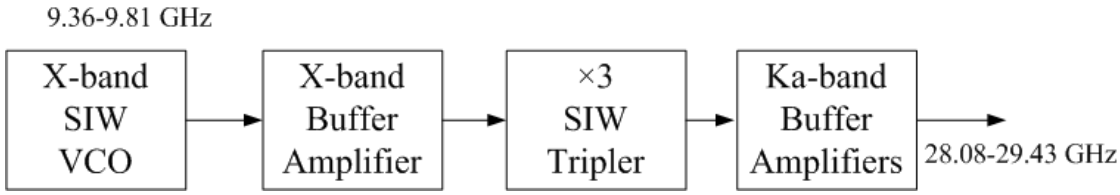

Figure 4.24: Basic block diagram of the Ka-band LO source

The designed tripler is a balanced passive one utilizing a planar Schottky anti-parallel diode pair MGS802 from Aeroflex/metalics Inc. Passive multiplier has advantages of wideband and stable without DC supply. Using anti-parallel diode pair to build a tripler, the even harmonics are suppressed inherently. That is, all even harmonics are shorted by anti-parallel diode pair. Figure 4.25 shows the photograph of the SIW frequency tripler. Left port and right port are output and input, respectively. At the input of the tripler, a $\lambda_{3f}/4$ open-circuited stub on the right side of a diode pair is used to provide shorted terminal for 3f frequency, where f is fundamental frequency. A section of SIW with the cut-off frequency of 25 GHz is fabricated on the left side of the diode pair to suppress fundamental and second harmonics and then provide very good f/3f isolation at output. The SIW technique provides an easy and low cost way to build a multiplier without the use of a band-pass filter. The circuit is fabricated on Rogers/duroid 6010 substrate with dielectric constant of 10.2 and thickness of 0.254 mm. The Ka-band frequency tippler exhibits a measured conversion loss of 14.8-16 dB for the input power of 11 dBm from 27 GHz - 36 GHz as shown in Figure 4.26. At output frequency of 29 GHz, the conversion loss is about 15 dB. Figure 4.27 displays the measured output power versus input power of the frequency tripler at the output frequency of 29 GHz.

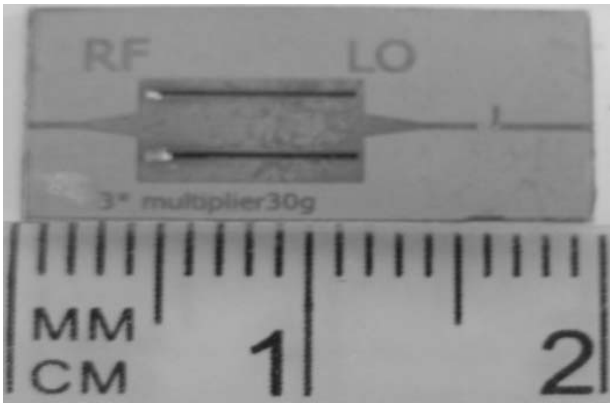

Figure 4.25: Photograph of the SIW frequency tripler.

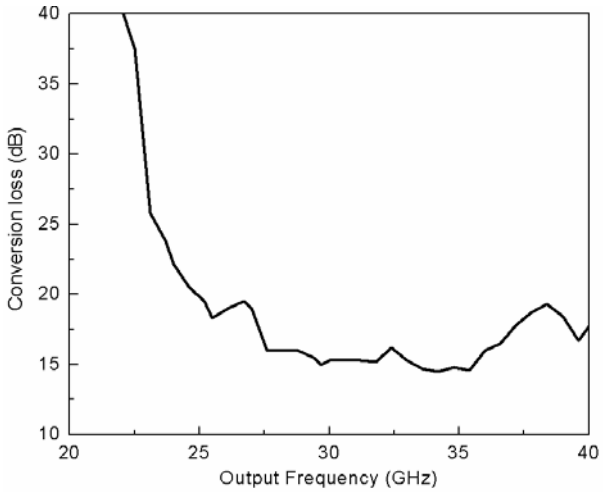

Figure 4.26: The conversion loss versus input frequency for the designed frequency tripler

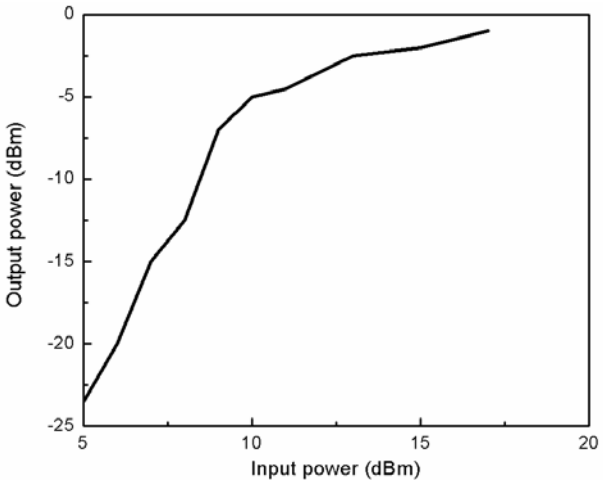

Figure 4.27: The output power versus input power at 29 GHz

Using the circuits described here, the source is constructed as shown in Figure 4.28. All circuits are integrated onto a base. The 29 GHz output is connected to a K-connector for measurement and connection with the sub-harmonically pumped mixer. From section 2.3, we have known that the tuning range of the SIW VCO varies from 9.356 GHz (0 V) with output power of 6.4 dBm to 9.816 GHz (13.3 V) with output power of 9.3 dBm. Fig 5.29 shows output frequency and power of the frequency tripler versus varactor tuning voltage in the designed SIW VCO. At 29 GHz, the output power is about 21.5 dBm. As we have pointed above, the mixer needs 11.5 dBm LO power to pump the diode pair. So the sub-system needs LO power of at least 17.5 dBm because there are four mixers in it. We can see that the designed Ka-band source can meet the power requirement for the LO.

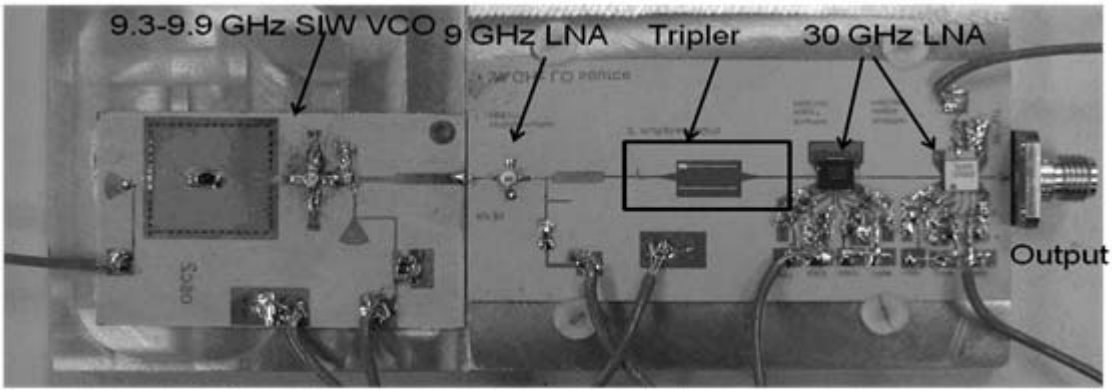

Figure 4.28Photograph of the Ka-band source model

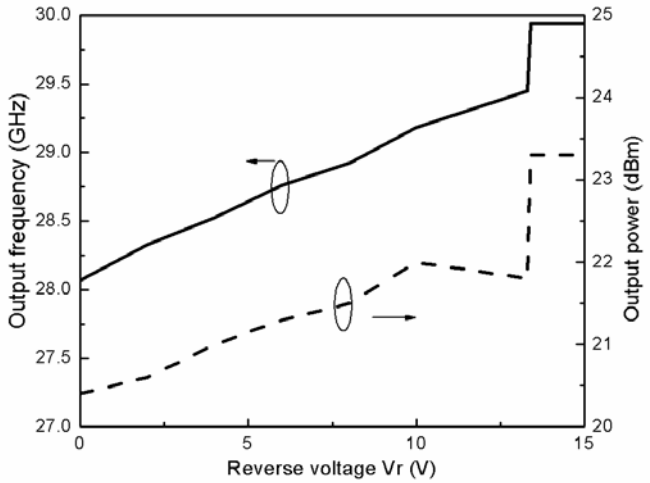

Figure 4.29: Output frequency and power of the frequency tripler versus varactor tuning voltage in VCO

4.4.6 IF Circuits Block and Digital Control Circuits Block

Section 4.4 described four received 59.5 GHz RF signals at four ports of the Butler matrix are amplified and frequency down-converted to four 1.5 GHz IF signals from IF1 to IF4, where IF1 to IF 4 mean four IF signals from channel 1 to 4, respectively. This part describes how to compare four IF signals and judge which channel received the maximum power, and then switch beam to the main direction.

The block diagram of IF circuit, which consists of IF low-pass filters, amplifiers, couplers, power detector and DC filter, is shown in Figure 4.30. The AVX low-pass filter has insertion loss of 0.5 dB and 3-dB bandwidth of 2.6 GHz. After AVX low-pass filter, Infineon Silicon Germanium Broadband MMIC Amplifier BGA614 is used to amplify IF signal. The amplifier has a typical gain of 16 dB and a noise figure of 2 dB. In order to generate four IF signals of comparison, four 10 dB couplers are used, which were purchased from Johanson Technology, Inc. Then, we input four coupling signals to power detector AD8313 from Analog Device and four main IF signals to SP4T switch AS204 from Skyworks Inc., respectively. Detector AD8313 has a wide bandwidth of 0.1 GHz to 2.5 GHz and a high dynamic range of 70 dB to ±3.0 dB. Figure 4.30 shows typical logarithmic response and error versus input power. The minimum detectable input signal power is about -75 dBm with output DC voltage of about 0.5 V. The AS204-80 is a high-isolation SP4T FET IC non-reflective switch with driver. The insertion loss is 0.5 dB and the isolation is 43 dB at 1.5 GHz. The switch is controlled by the TTL 2:4 decoder as shown in Table 4.3, where J1-J5 are signal ports, CTL1 and CTL2 are the control voltage levels. J2-J5 ports are connected with channel 1-4 correspondence with port 1-4 of the Bulter matrix. Figure 4.312 shows the photograph of the fabricated IF circuit. At each IF input port, the minimum IF input power of -65 dBm can be detected with an output DC voltage of 0.53 V. That is, only 1.5 GHz IF signal from mixer with above -65 dBm can be detected to judge which output of the Bulter matrix has the maximum received signal.

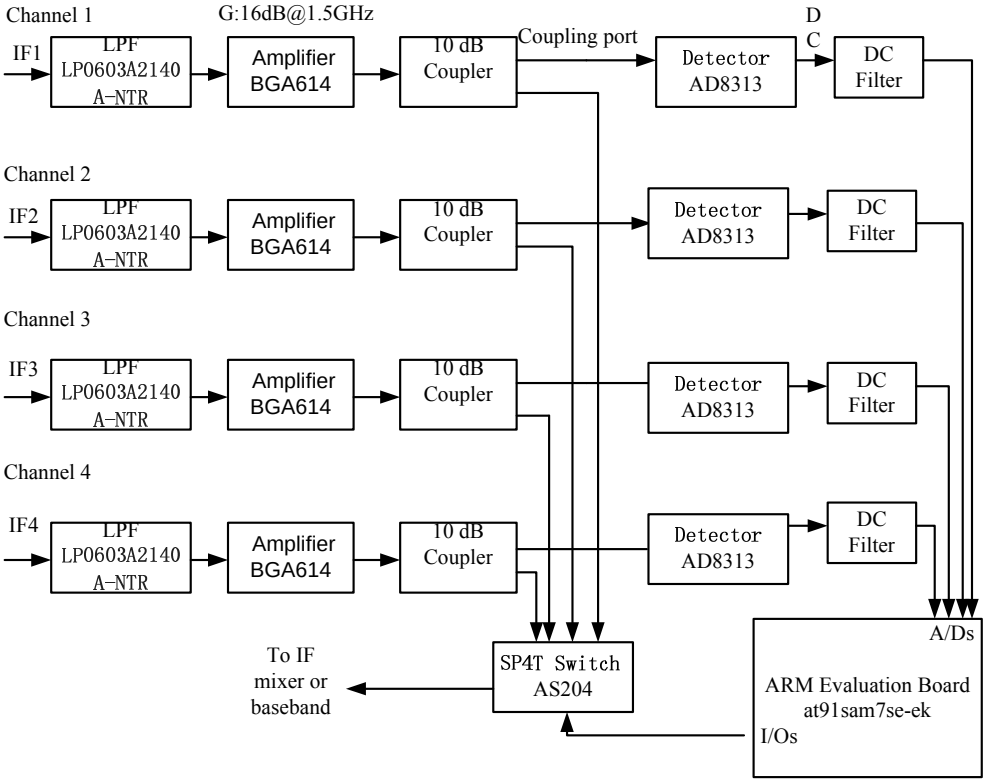

Figure 4.30: Block diagram of IF circuit with control block

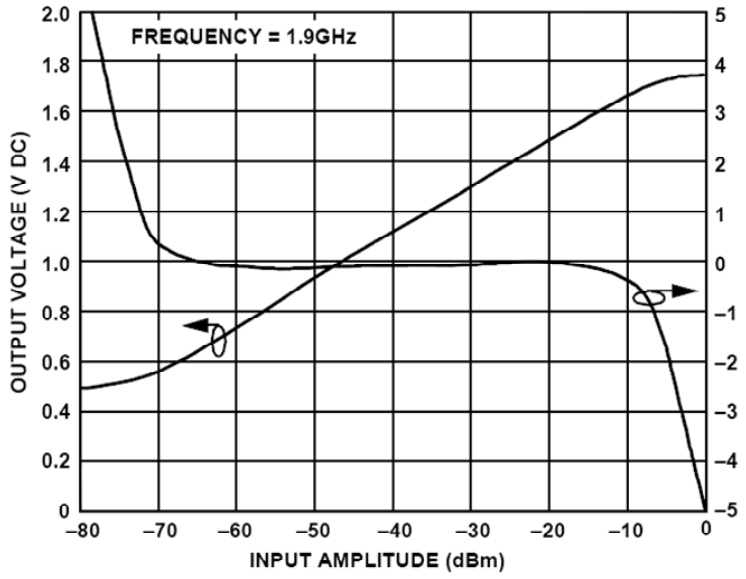

Figure 4.31: Typical logarithmic response and error versus input power

Table 4.3 Switch status versus control input

Insertion Loss Path J_1 to:	Control Input	
	CTL1	CTL2
J_2	0	0
J_3	1	0
J_4	0	1
J_5	1	1

"0" = 0 to 0.5 V.
"1" = 2.4 to 5 V.

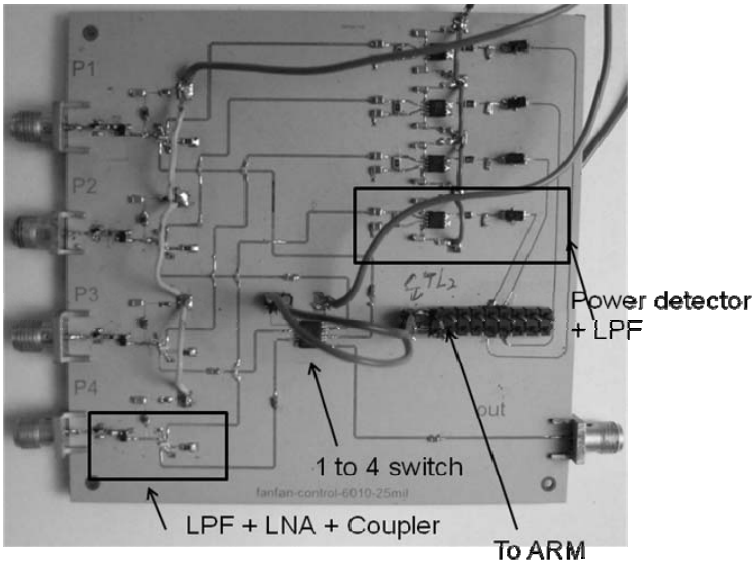

Figure 4.32: Photograph of the fabricated IF circuits

Passing through the DC filter, four detected DC signals are then converted to digital signals by ADCs and sent into (DSP) model. In this design, we use Atmel AT91SAM7SE512 as the DSP unit. AT91SAM7SE512 is an ARM processor that provides integrated ADCs. This ADC has 10-bit resolution mode, and conversion results are reported in a common register for all channels, as well as in a channel-dedicated register. The interval time between two samplings is 1 ms, which is enough for indoor communication because most people walk at an average rate of 1.2-1.4 m/s. By default, both initial control voltages to CTL1 and CTL2 are 0 V. That is, J1 and J2 are connected in the switch. In another words, the switch is connected with channel 1. By the algorithm of comparison, the channel with the highest voltage among four digital signals is decided. Then corresponding control voltages are feedback to CTL1 and CTL2 of the switch. For

example, if IF4 is selected by the comparing algorithm as the strongest signal, J1 and J5 are connected and then sub-system is switched to the beam corresponding to the output 4 of the Butler matrix in channel 4. In the ARM core, the comparison algorithm is programmed by assembly C and output 3.3V and 0 V control voltages for logic "1" and "0". The ARM evaluation board AT91SAM7SE-EK is used in this design, as shown in Figure 4.33.

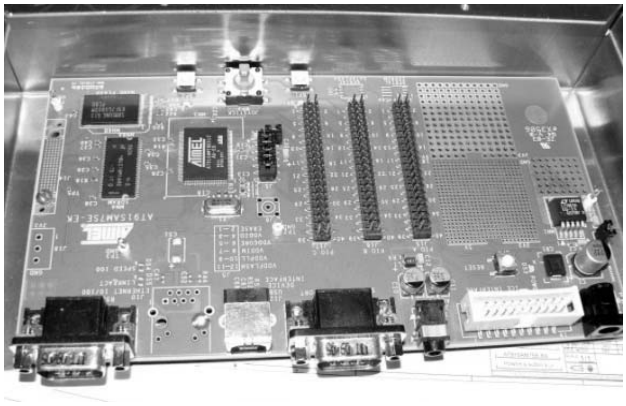

Figure 4.33: Photograph of ARM evaluation board AT91SAM7SE-EK

4.5 Experiments and Results

The entire sub-system is measured using a 60 GHz experimental setup built as shown in Figure 4.34. In the setup, a 60GHz horn antenna (Quinstar QWH-VPRR00) with 24 dBi gain at 59.5 GHz and an Anritsu 37397C vector network analyzer (VNA) are used as the transmit antenna and the transmit signal source, respectively. There is a V-band cable connected between horn antenna and VNA, which has an insertion loss of 12 dB. The receiver is fixed on a stand with distance *d* away from the transmit antenna. The distance d can be changed by adjusting the transmit antenna's position. In fact, the receiver in the center of the circle with a radius of d and the transmit antenna is on the circumference of the same circle. We can manually rotate the transmit antenna around the receiver from -90^{o} to $+90^{o}$ to measure the beams of the sub-system. To observe how the beams are witched while the transmit antenna is rotated around the receiver, the output IF signal of the SP4T switch is fed to signal analyzer R&S FS2040. Meanwhile, Ka-band LO circuits and IF circuits are connected with the receiver fixed in the stand.

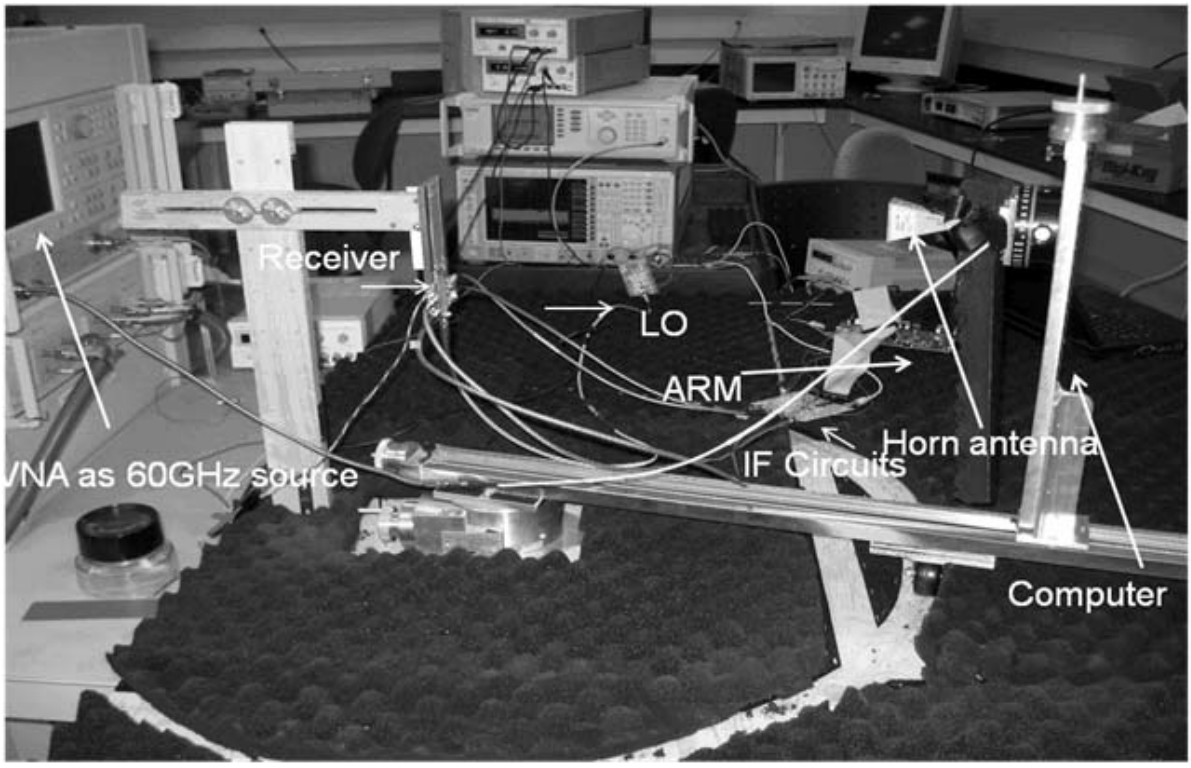

Figure 4.34: Experimental setup of the 60 GHz beamforming sub-system

Before we test and demonstrate the switchable function of the sub-system, the total channel gain of the RF front-end including antenna is calculated by received IF signals at the output of the mixer. Channel gain G_C can be expressed as:

$$G_C = P_R L_P / P_T G_T = 4 G_R G_A / L_B L_F C_L L_I \tag{4.2}$$

where P_R is the received IF signal power, L_P is path loss in free space, P_T is the transmitted signal power, G_T is the gain of the transmitted antenna, G_R is the gain of the received slot antenna, G_A is the gain of the LNA, L_B is the loss of the Butler matrix, L_F is the insertion loss of the filter, C_L is the conversion loss of the sub-harmonically pumped mixer and L_I is the insertion loss of the interconnection line CPW.

In the measurement, IF powers from mixers of channels 1 and 2 are measured while P_T is set as 7 dBm at 59.5 GH and distance d is 30 cm as well as the beam of transmitted antenna is aligned to beams 1 and 3 of the sub-system, respectively. L_P is 61 dB which can be calculated by

$$L_P(dB) = 20 \log\left(\frac{4\pi d}{\lambda}\right) \tag{4.3}$$

Figure 4.35 show calculated and measured gains of channels 1and 2 according to measured IF signals. In channel 1 and channel 2, the measured gains are about 13.5 dB and 11 dB, respectively. However, the measured gains are less than the calculated counterparts by about 3 dB, which may be caused by the additional insertion losses of interconnects and the Butler matrix. The channel gain decreases sharply at low frequency because there is the stop-band of 60 GHz band-pass filter. However, the channel gain goes down slowly at high frequency because frequency is out of the working frequency of the antenna. From the above section, it is known that IF circuits can receive the minimum IF signals of -65 dBm. Therefore, the minimum received RF signal power of channels 1 and 2 are -78.5 dBm and -76 dBm.

After performance measurements of each channel, we connect RF front-end, IF circuits and ARM evaluation board to test the proposed switchable function of the sub-system. The test method is to observe the IF signals from IF circuits in the signal analyzer while we rotate the transmitted horn antenna around the receiver. Measured IF relative power versus rotating angle is plotted in Figure 4.36. It has been found that the measured results not only agree well with the measured E-plane pattern in Figure 4.16, but also indicate that the beam can be successfully and adaptively switched to track the transmitted beam.

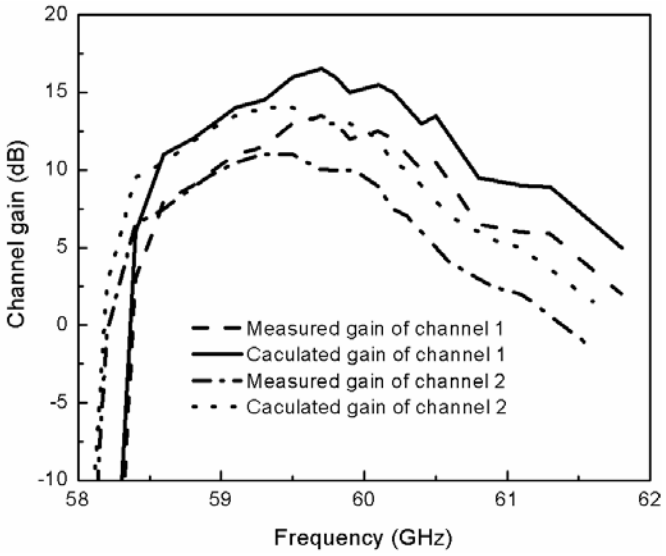

Figure 4.35: Calculated and measured gains of channels 1 and 2

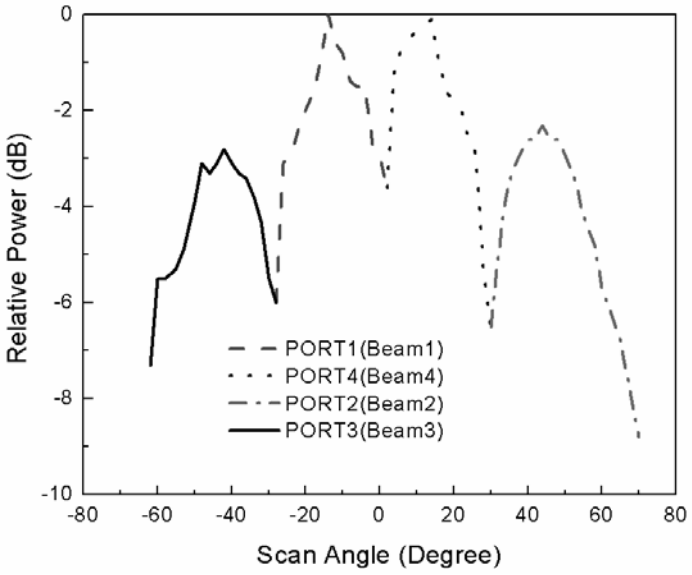

Figure 4.36: Measured normalized received IF signal power versus scan angle at 59.5 GHz

4.6 Conclusion

A low-cost switched-beam receiver system is thus developed and demonstrated employing all 60 GHz components based on the SIW Technology such as slot antenna, 4×4 Butler matrix network, band-pass filter, sub-harmonically pumped down-conversion mixer and LO source. In this system, IF control circuit block and adaptive algorithm in ARM are developed, respectively. Finally through a comparison algorithm in ARM processor, four beams are switched adaptively with different main beam of the transmitted signal. Thus, the realized sub-system may be very suitable for the low-cost 60 GHz indoor communication.

CONCLUSION AND FUTURE WORK

Communication systems operating at millimetre-wave frequencies are expected to have a bright future. Upcoming high definition video streaming and other applications like high-speed data synchronization of mobile devices require huge bandwidth capacities that can be offered by millimetre-wave technology. The unlicensed 60-GHz band could have a particular impact in this sector. On the other hand, the SICs technology as a promising scheme with advantages of low-cost, small size, relatively high power, high Q, low radiation loss and high-density integration over microwave and millimetre wave range has been investigated recently. Therefore, this thesis research is focused on further study of SIW technology to propose and develop various innovative and original microwave and millimetre-wave passive and active components. Theses innovative components structure can improve the integration between SIW components and other planar components. Then a part of proposed structures or components are applied in designs of millimetre-wave integrated antenna arrays and 60 GHz smart antenna sub-system. The other innovative components' concepts are proposed and demonstrated at lower microwave frequency.

So far, the conducted research work has resulted in a number of journals and conference publications (several others submitted or planned), such as IEEE Trans. on MTT, IEEE Microwave Components and Wireless Letters, IET Microwave and Antenna Propagation, IEEE MTT-S, etc.

The principal scientific contributions of this thesis work can be summarized in the following:

- Original designs of slotline-to-SIW, 180^0 reverse-phase T-junction and planar magic-Ts. As a demonstration of their concept, they were fabricated and tested at X-band. As an application of the magic-T, an X-band singly balanced mixer is developed.
- Original design of a super wideband filter by integrating HMSIW and a microstrip low-pass filter. This filter is demonstrated from 7.1 to 16 GHz.
- Original design of ALSTA structure fed by substrate parallel plate waveguide. This antenna is designed at 12-50 GHz.
- Original design of low impedance SIW bias line of PA for the first time and developed for harmonic suppressions as well as performance improvement. A C-band PA is realized as a

demonstration.

- Electrically tunable SIW and HMSIW cavity resonators are proposed and analyzed for the first time. We discuss the tuning range and Q factor of the both resonators. A low phase noise X-band VCO is realized to validate the tunable SIW cavity resonator.
- X-band spatial power amplifier is designed based on the SIW ALTSA.
- Original design of a Ka-band 2×2 up-converter mixer antenna array is proposed based on the SIW ALTSA.
- Original design of a Ka-band 1×4 rectenna array is reported with the SIW technology.
- A 60 GHz switched-beam receiver sub-system based on the SIW technology is realized and demonstrated for the first time. In this sub-system, we realize a 60 GHz front-end using our designed SIW 4×4 Butler matrix network, SIW antenna, SIW band-pass filter, SIW sub-harmonically pumped down-converter mixer and 30 GHz SIW LO source. It is found theoretically and experimentally that beam of the developed sub-system is adaptively switched by the controlled signals according to the criterion of the maximum received signal.

In these component level contributions, our proposed components such as VCO, rectifier, tripler and mixer are deployed to integrate with other SIW components in order to realize our millimetre-wave integrated antenna array sub-systems and 60 GHz smart antenna system. Although other components such as magic-T, wideband filter, wideband antenna and PA were realized at various low microwave frequencies, these innovative structures are proved with simulated and measured results and they are readily scaled up to millimetre-wave frequency band for other system applications.

In the future, certain improvements for the 60 GHz switched-beam receiver sub-system could be made. First of all, we can improve the performance of the SIW components in the system. For example, FET devices can be used to design the SIW sub-harmonically pumped mixer and tripler for improving the conversion loss of them, a high-gain wideband SIW antenna covering 57-64 GHz can be better choice for this system, PLL or DDS techniques can be used to design our SIW LO source for a stable source for the system. Second, we can integrate all circuits in one base or one substrate. Finally, the modulation signal can be used to test the communication performance.

From the system's view, we can update our switched-beam system to a continuously electrical digital scanning beamforming system which can be developed by using millimetre-wave shifter based on SIW technique to replace the beamforming network. In such a system, we will decrease the cost of millimetre-wave components such as LNA, mixer and LO. However, such system will increase the cost of digital circuit. In another hand, we can develop another high efficient beamforming network based on SIW technology or other substrate integrated structures like SINRD and SIIG. As for future investigations of the SICs techniques, many other fabrication processes such as LTCC, MEMS, thin film, can be used to design high-performance and compact millimetre-wave components and systems. In addition, using semiconductor processes will extend the development range in connection with frequency used to several-hundred GHz or THz. Meanwhile, SIC and MMICs can be integrated very well.

REFERENCES

[1] K. Wu. D. Deslandes, and Y. Cassivi, "The substrate integrated circuits - A new concept for high-frequency electronics and optoeletronics," Telecommunications in Modern Satellite, Cable and Broadcasting Service, 2003. TELSIKS 2003. 6th International Conference, vol. 1, Oct., 2003. Pages: P-III – P-X.

[2] K. Wu, "Integration and interconnect techniques of planar and non-planar structures for microwave and millimeter-wave circuits - current status and future trend," in Proc. Asia-Pacific Microwave Conference, vol. 2, Taipei, Taiwan, Dec. 2001, pp. 411–416.

[3] D. Deslandes and K. Wu, "Integrated microstrip and rectangular waveguide in planar form," IEEE Microwave and Wireless Components Letters, vol. 11, no. 2, pp. 68–70, Feb. 2001. 175

[4] F. Xu, Y. L. Zhang, W. Hong, K. Wu and T. J. Cui, "Finite-difference frequency-domain algorithm for modeling guided-wave properties of substrate integrated waveguide," IEEE Trans. Microwave Theory Tech., vol.51, no.11, pp.2221-2227, 2003.

[5] F. Xu, K. Wu, and W. Hong, "Equivalent Resonant Cavity Model of Arbitrary Periodic Guided-Wave Structures and Its Application to Finite-Difference Frequency-Domain Algorithm," IEEE Trans. Microwave Theory Tech., vol.55, no.4, pp.697-702, 2007.

[6] L. Yan, and W. Hong, "Investigations on the propagation characteristics of the Substrate Integrated Waveguide based on the Method of Lines," IEE Proc.-H: Microwaves Antennas Propag.，vol.152, no.1, pp.35-42, 2005.

[7] Y. Cassivi and K. Wu, "Substrate integrated non-radiative dielectric waveguide," IEEE Microwave and Wireless Components Letters, vol. 14, no. 3, pp. 89–91, Mar. 2004.

[8] A. Patrovsky and K. Wu, "Substrate integrated image guide (SIIG)—a planar dielectric waveguide technology for millimeter-wave applications," IEEE Transactions on Microwave Theory and Techniques, vol. 54, no. 6, pp. 2872–2879, Jun. 2006.

[9] W. Hong, et al (Invited Talk) "Half Mode Substrate Integrated Waveguide: A New Guided Wave Structure for Microwave and Millimeter Wave Application," Joint 31st Int. Conf. on

Infrared and Millimeter Waves and 14th Int. Conf. on Terahertz Electronics, Shanghai, Sept. 18-22, 2006.

[10] B. Liu, W. Hong, Y. Q. Wang, Q. H. Lai and K. Wu, "Half mode substrate integrated waveguide (HMSIW) 3dB coupler," IEEE Microwave Compon. Lett., vol.17, no.1, pp.22-24, 2007.

[11] B. Liu, W. Hong, Y. Zhang, H. J. Tang, X. X. Yin, and Ke Wu, "Half Mode Substrate Integrated Waveguide 180 3-dB Directional Couplers," IEEE Trans. Microwave Theory Tech., vol.55, no.12, pp.2586-2592, 2007.

[12] Y. J. Cheng, W. Hong, and K. Wu, "Half Mode Substrate Integrated Waveguide (HMSIW) Directional Filter," IEEE Microwave Compon. Lett., vol.17, no.7, pp.504-506, 2007.

[13] Y. Q. Wang, W. Hong, Y. D. Dong, B. Liu, H. J. Tang, J. X. Chen, X. X. Yin, and K. Wu, "Half Mode Substrate Integrated Waveguide (HMSIW) Bandpass Filter," IEEE Microwave Compon. Lett., vol.17, no.4, pp.265-267, 2007.

[14] J. F. Xu, W. Hong, H. J. Tang, Z. Q. Kuai, and K. Wu, "Half-mode substrate integrated waveguide (HMSIW) leaky-wave antenna for millimeter-wave applications," IEEE Antennas Wirel. Propag. Lett., vol.7, pp.85-88, 2008.

[15] Y. D. Dong, W. Hong, Z. Q. Kuai, C. Yu, Y. Zhang, J. Y. Zhou, and J. X. Chen, "Development of ultrawideband antenna with multiple band-notched characteristics using half mode substrate integrated waveguide cavity technology," IEEE Trans. Antennas Propag., vol.56, no.9, pp. 2894-2902, 2008.

[16] G. H. Zhai, W. Hong, and K. Wu et al, "Folded half mode substrate integrated waveguide 3 dB coupler," IEEE Microwave Compon. Lett., vol.18, no.8, pp.512-514, 2008.

[17] N. Grigoropoulos, B. S. Izquierdo, and P. R. Young, "Substrate integrated folded waveguides (SIFW) and filters," IEEE Microwave Wireless Compon. Lett. Vol.15, pp.829-831, 2005.

[18] W. Che, L. Geng, K. Deng, and Y. L. Chow, "Analysis and experiments of compact folded substrate-integrated waveguide," IEEE Trans. MTT, vol.56, pp.88-93, 2008.

[19] Yan Ding, and Ke Wu, “A 4x4 Ridge Substrate Integrated Waveguide (RSIW) Slot Array Antenna,” IEEE antenna and wireless propag. Lett., vol. 8, pp.561-564, 2009.

[20] Patrovsky and K. Wu, “Substrate integrated circuits (SICs)—providing a low-cost and low-loss approach for millimeter-wave circuit and system integration (invited paper),” in Proceedings 8th MINT Millimeter-Wave Int. Symp. and 9th Topical Symp. on Millimeter Waves, Seoul, Korea, February 26-27, 2007, Seoul, South Korea, Feb. 2007, pp. 9–14.

[21] L.Matthaei, L.Young and E.M.T.Jone, Microwave filters impedance matching networks, and coupling structures. New York: McGraw-Hill, 1964.

[22] W. A. Tyrell, "Hybrid circuits for microwaves," Proc. IRE, 35. 1947.

[23] I.D. Robertson, MMIC Design. London, U.K.: IEE Press, 1995.

[24] F. C. de Ronde, “A new class of microstrip directional coupler,” in Rec. IEEE Int. Microwave Symp., May 1970.

[25] G. J. Laughlin, “A new impedance-matched wideband balun and magic tee,” IEEE Tram. Microwave Theoty Tech., vol. MTT-24, pp. 135–141, Mar. 1976.

[26] C.-H. Ho, L. Fan, and K. Chang, "New uniplanar coplanar waveguide hybrid-ring couplers and magic-T's," IEEE Trans. Microwave Theory & Tech., vol. 42, no. 12, pp. 2440-2448, December 1994.

[27] J. P. Kim and W. S. Park, "Novel configurations of planar multilayer magic-T using microstrip-slotline transitions," IEEE Trans. Microwave Theory & Tech., vol. 50, no. 7, pp. 1683-1688, July 2002.

[28] M. Aikawa and H. Ogawa, "A new MIC magic-T using coupled slot lines," IEEE Trans. Microwave Theory & Tech., vol. 28, no.6, pp. 523-528, June 1980.

[29] T. Hiraoka, T. Tokumitsu and M. Aikawa, "Very small wideband MMIC magic-T' s using microstrip lines on a thin dielectric film," IEEE Trans. Microwave Theory & Tech., vol. 37, no. 10, pp. 1569-1575, October 1989.

[30] M. Davidovitz, "A compact planar magic-T junction with aperture-coupled difference port," IEEE Microwave & Guided Wave Lett., vol. 7, no. 8, pp. 217-218, August 1997.

[31] M.W. Katsube, Y. M. M. Antar, A. Ittipiboon, and M. Cuhaci, “A novel aperture coupled microstrip magic-T,” IEEE Microwave Guided Wave Letter, vol. 2, pp. 245–246, June 1992.

[32] M. Davidovitz, “A compact planar magic-T junction with aperture-coupled difference port,” IEEE Microwave Guided Wave Lett., vol. 7, pp.217–218, Aug. 1997.

[33] T. M. Shen, T.Y. Huang and R. B. Wu, “A laminated waveguide magic-T in multilayer LTCC,” IEEE MTT-S int. Microw. Symp. Dig., pp. 713-716, June. 2009.

[34] L. Han, K. Wu and S. Winkler, “Singly balanced mixer using substrate integrated waveguide magic-T structure,” European Conf. on, Wireless Tech., EuWiT 2008, pp. 9-12, 2008.

[35] D. Deslandes, and K. Wu, “Integrated microstrip and rectangular waveguide in planar form,” IEEE Microw. Wireless Compon. Lett., vol. 11, pp. 68-70, Feb. 2001.

[36] D. Deslandes, and K. Wu, "Analysis and design of current probe transition from grounded coplanar to substrate integrated rectangular waveguides,” IEEE Trans. Microw. Theory Tech., vol. 53, pp. 2487-12494, Aug. 2005.

[37] W. Hong, B. Liu, Y. Q. Wang, Q. H. Lai, H. J. Tang, X. X. Yin, Y. D. Dong, Y. Zhang and K. Wu “Half Mode Substrate Integrated Waveguide: A New Guided Wave Structure for Microwave and Millimetre Wave Application,” Joint 31st Int. Conf. on Infrared and Millimetre Waves and 14th Int. Conf. on Terahertz Electronics, Shanghai, Sept. 18-22, 2006.

[38] B. Liu, W. Hong, Y. Q. Wang, Q. H. Lai and K. Wu, “Half mode substrate integrated waveguide (HMSIW) 3dB coupler,” IEEE Microw. Wireless Compon. Lett., vol.17, no.1, 22-24, Jan. 2007.

[39] B. Liu, W. Hong, Y, Zhang, J. X. Chen and K. Wu, "Half-mode substrate integrated waveguide (HMSIW) double-slot coupler,” Electron. Lett., vol. 43, pp. 113-114, Jan. 2007.

[40] M. Skolnik, G. Andrews, and J. P. Hansen, “Ultrawideband microwave- radar conceptual design,” IEEE Trans. Aerosp. Electron.Syst., vol. 10, no. 10, pp. 25–30, Oct. 1995.

[41] G. R. Aiello and G. D. Rogerson, “Ultra-wideband wireless systems,” IEEE Micro, vol. 4, no. 2, pp. 36–47, Jun. 2003.

[42] S. B. Cohn, “Parallel-coupled transmission-line-resonator filters,” IRE Trans. Microw. Theory Tech., vol. MTT-6, no. 4, pp. 223–231, Apr. 1958.

[43] W. Menzel, L. Zhu, and K.Wu, “On the design of novel compact broadband planar filters,” IEEE Trans. Microw. Theory Tech., vol. 51, no. 2, pp. 364–370, Feb. 2003.

[44] L. Zhu, H. Bu, and K. Wu, “Aperture compensation technique for innovative design of ultra-broadband microstrip bandpass filter,” in IEEE MTT-S Int. Micro. Symp. Dig., Jun. 1999, pp. 315–318.

[45] L. Zhu, S. Sun, and W. Menzel, “Ultra-wideband (UWB) bandpass filters using multiple-mode resonator,” IEEE Microw. Wireless Compon. Lett., vol. 15, no. 11, pp. 796–798, Nov. 2005.

[46] R. Li and L. Zhu, “Compact UWB bandpass filter using stub-loaded multiple-mode resonator,” IEEE Microw. Wireless Compon. Lett., vol. 17, no. 1, pp. 40–42, Jan. 2007.

[47] L. H. Hsieh and K. Chang, “Compact, low insertion-loss, sharp-rejection, and wideband microstrip bandpass filters,” IEEE Trans. Microw. Theory Tech., vol. 51, no. 4, pp. 1241-1246, Apr. 2003.

[48] S. G. Kim and K. Chang, “Ultrawide-band transitions and new microwave components using double-sided parallel-strip lines,” IEEE Trans. Microw. Theory Tech., vol. 52, no. 9, pp. 2148–2152, Sep. 2004.

[49] J. T. Kuo and E. Shih, “Wide bandpass filter design with three-line microstrip structures,” in IEEE MTT-S Int. Microw. Symp. Dig., May 2001, pp. 1593–1596.

[50] H. Ishida and K. Araki, “Design and analysis of UWB bandpass filter with ring filter,” in IEEE MTT-S Int. Microw. Symp. Dig., Jun. 2004, pp. 1307–1310.

[51] K. M. Shum, W. T. Luk, C. H. Chan, and Q. Xue, “A UWB bandpass filter with two transmission zeros using a single stub with CMRC,” IEEE Microw. Wireless Compon. Lett., vol. 17, no. 1, pp. 43–45, Jan. 2007.

[52] K. Li, D. Kurita, and T. Matsui, “An ultrawideband bandpass filter using broadside-coupled microstrip-coplanar waveguide structure,” in IEEE MTT-S Int. Microw. Symp. Dig., Jun. 2005, pp. 675–678.

[53] H. Wang, L. Zhu, and W. Menzel, “Ultra-wideband bandpass filter with hybrid microstrip/CPW structure,” IEEE Microw. Wireless Compon. Lett., vol. 15, no. 12, pp. 844–846, Dec. 2005.

[54] N. Thomson and J. S. Hong, “Compact ultra-wideband microstrip/coplanar waveguide bandpass filter,” IEEE Microw. Wireless Compon. Lett., vol. 17, no. 3, pp. 184–186, Mar. 2007.

[55] C. L. Hsu, F. C. Hsu, and J. T. Kuo, “Microstrip bandpass filters for ultra-wideband (UWB) wireless communications,” in IEEE MTT-S Int. Microw. Symp. Dig., Jun. 2005, pp. 679–682.

[56] J. Garcia-Garcia, J. Bonache, and F. Martin, “Application of electromagnetic bandgaps to the design of ultra-wide bandpass filters with good out-of-band performance,” IEEE Trans. Microw. Theory Tech., vol. 54, no. 12, pp. 4136–4140, Dec. 2006.

[57] H. J. Carlin and W. Kohler, “Direct synthesis of bandpass transmission line structures,” IEEE Trans. Microw. Theory Tech., vol. MTT-13, no.5, pp. 283–297, May 1965.

[58] M. C. Horton and R. J. Wenzel, “General theory and design of optimum quarter-wave TEM filters,” IEEE Trans. Microw. Theory Tech., vol. MTT-13, no. 5, pp. 316–327, May 1965.

[59] R. Levy, “A new class of distributed prototype filters with applications to mixed lumped/distributed component design,” IEEE Trans. Microw. Theory Tech., vol. MTT-18, no. 12, pp. 1064–1071, Dec. 1970.

[60] W. Menzel, M. S. R. Tito, and L. Zhu, "Low-loss ultrasymmetrical/ asymmetrical multiple-mode stepped- wideband (UWB) filters using suspended stripline," in Proc. Asia-Pacific Microw. Conf., Dec. 2005, pp.2148-2151.

[61] W. Hong, B. Liu, Y. Q. Wang, Q. H. Lai, H. J. Tang, X. X. Yin, Y. D. Dong, Y. Zhang and K. Wu (Invited Talk), “Half Mode Substrate Integrated Waveguide: A New Guided Wave Structure for Microwave and Millimetre Wave Application,” Joint 31st Int. Conf. on

Infrared and Millimetre Waves and 14th Int. Conf. on Terahertz Electronics, Shanghai, Sept. 18-22, 2006.

[62] Z. C. Hao, W. Hong, J. X. Chen, X. P. Chen, and K. Wu, "Compact Super-Wide Bandpass Substrate Integrated Waveguide (SIW) Filters", IEEE Trans. Microw. Theory Tech., vol.53, No.9, pp.2968-2977, 2005.

[63] K. S. Yngvesson et al., "Endfire tapered slot antennas on dielectric substrates," IEEE Trans. Antennas Propag., vol. 33, pp. 1392-1400, 1985.

[64] K. S. Yngvesson, T. L. Korzeniowski, Young-Sik Kim, E. L. Kollberg, and J. F. Johansson, "The tapered slot antenna- A new integrated element for millimetre-wave applications," IEEE Trans. Microwave Theory Tech, vol. 37, No.2, pp. 365-374, 1989.

[65] Y.-S. Kim, and K. S. Yngvesson, "Characteristics of tapered slot antenna feeds and feed array," IEEETrans. Microwave Theory Tech., vol. 37, pp. 1559-1564, 1990.

[66] Z. C. Hao, W. Hong, J.X. Chen, X. P. Chen, and K. Wu, "A novel feeding technique for antipodal linearly tapered Slot Antenna Array," 2005 IEEE MTT-S Int. Microwave Symp. Dig., pp. 1641–1643, 2005.

[67] I.Nesic, "Endfire Slot Line Antennas Excited by a Coplanar Waveguide," 1991 IEEE AP-S Int. Symp. Dig., pp. 700-702, 1991.

[68] I.Wu, L. Shen, G. Y. Deng, Y. Shen and J.Litva, "Experimental Study of a Wide Band LTSA Which is Fed by an Inverted Microstrip Line (IML)," 1998 IEEE Int. AP-S Symp. Dig., vol. 4, pp. 2328-2331, 1998.

[69] Z. N. Chen, K. Hirasawa and K. Wu, "A broadband monopole in a parallel plate waveguide," 1999 IEEE APMC., vol. 3, pp. 732-735, 1999.

[70] K. H. Chuang, S. H. Pyun, S. Y. Chuang and J. H. Choi, "Design of a wideband TEM horn antenna," 2003 IEEE Int. AP-S Symp. Dig., vol. 1, pp. 229-232, 2003.

[71] R. Basset, "High-power GaAs FET device bias considerations," Fujitsu Compound Semiconductor Inc., Application Note, No. 010.

[72] Poza, "Microwave engineering," Artech house, 1998.

[73] E. L. Holzman, and R. S. Robertson, “Solid-state Microwave Power Oscillator Design,” Artech house, 1992.

[74] T. Itoh,, “Analysis of microstrip resonators,” IEEE Trans. Microwave Theory Theory Tech., Vol. MTT-22, No.11, pp.946-952, Nov. 1974

[75] K. Wu. D. Deslandes, and Y. Cassivi, “The substrate integrated circuits - A new concept for high-frequency electronics and optoeletronics,” Telecommunications in Modern Satellite, Cable and Broadcasting Service, 2003. TELSIKS 2003. 6th International Conference, vol. 1, Oct., 2003. Pages: P-III – P-X.

[76] D. Deslandes, and K. Wu, "Integrated microstrip and rectangular waveguide in planar form," IEEE Microw. Wireless Compon. Lett., vol. 11, pp. 68-70, Feb. 2001.

[77] J. X. Chen, W. Hong, Z. C. Hao, H. Li, and K. Wu, “Development of a low cost microwave mixer using a broad-band substrate integrated waveguide (SIW) coupler” IEEE Microw. Wireless Compon. Lett., vol. 16, NO. 2, pp. 84–86, Feb. 2006.

[78] A. Piloto, K. Leahy, B. Flanick and K. A. Zaki, "Waveguide filters having a layered dielectric structures," U.S. Patent 5 382 931, Jan. 17, 1995.

[79] F. F. He, K. Wu, W. Hong, H. J. Hong, H. B. Zhu and J. X. Chen, “A planar magic-T using substrate integrated circuits concept” IEEE Microw. Wireless Compon. Lett., vlo. 18, pp. 386-388, 2008.

[80] G. Q. Luo, W. Hong, Q. H. Lai, K. Wu, and L. L. Sun, “Design and experimental verification of compact frequency-selective surface with quasi-elliptic bandpass Response” IEEE Trans. Microw. Theory Tech.., vol. 55, NO. 12, pp.2481-2487, 2007.

[81] A. Suntives, and R. Abhari, “Design and application of multimode substrate integrated waveguides in parallel multichannel signaling systems” IEEE Trans. Microw. Theory Tech.., vol. 57, NO. 6, pp.1563-1571, June, 2009.

[82] H. J. Tang, W. Hong, J. X. Chen, G. Q. Luo and K. Wu, “Development of millimeter-wave planar diplexers based on complementary characters of dual-mode substrate integrated waveguide filters with circular and elliptic cavities” IEEE Trans. Microw. Theory Tech.., vol. 55, NO. 4, pp.776-782, April, 2007.

[83] D. S. Eom, J. Byun, and H. Y. Lee, "Multilayer substrate integrated waveguide four-way out-of-phase power divider" IEEE Trans. Microw. Theory Tech.., vol. 57, NO. 12, pp.3469-3476, 2009.

[84] H. W. Chen, H. C. Lu and T. W. Huang, "The analysis of relation between Q-factor and phase noise by using substrate integrated waveguide cavity oscillators," in Proc. Asia-Pacific Microwave Conf., Dec. 2005.

[85] J. C. Bohorquez, B. Potelon, C. Person, E. Rius, C. Quendo, G. Tanne and E. Fourn, "Reconfigurable Planar SIW Cavity Resonator and Filter" 2003 IEEE MTT-S Int. Microwave Symp., pp.947-950,June 2006.

[86] R. S. Kwok and J. F. Liang, "Characterization of high-Q resonators for microwave-filter applications," IEEE Trans. Microw. Theory Tech., vol. 47, NO. 1, pp. 111-114, 1999.

[87] Y. Cassivi, L, Perregrini, K. Wu, and G, Conciauro, "Low-cost and high-Q millimeter-wave resonator using substrate integrated waveguide," in Proc. Eur. Microw. Conf., Milano, Italy, 2002, pp.1-4.

[88] Y. Cassivi and K.Wu, "Low cost microwave oscillator using substrate integrated waveguide cavity," IEEE Microw. Wireless Compon. Lett., vol. 13, no. 2, pp. 48–50, Feb. 2003.

[89] C. L. Zhong, J. Xu, Z. Y. Yu and Y. Zhu, "Ka-band substrate integrated waveguide gunn oscillator," IEEE Microw. Wireless Compon. Lett., vol. 18, no. 7, pp. 461–463, Feb. 2008.

[90] H. Jacobsson, B. Hansson, H. Berg and S. Ggevorgian, "Very low phase-noise fully-integrated coupled VCOs," RFIC Symp., pp.467-470, Aug. 2002

[91] K. Hu, F. Herzel, and J. C. Scheytt, "An X-Band low-power and low-phase-noise VCO using bond wire Inductor, " Adv. Radio Sci., vol. 7, pp. 243-247, 2009.

[92] S. Ko, H. D. Lee, D-W Kang and S. Hong, "An x-band CMOS quadrature balanced VCO," 2004 IEEE MTT-S Int. Microwave Symp.,vol.3, pp.2003-2006.

[93] H. Jacobsson, B. Hansson, H. Berg and S. Ggevorgian, "Very low phase-noise fully-integrated coupled VCOs," RFIC Symp., pp.467-470, Aug. 2002

[94] H. A. Wheeler, “Small antennas,” IEEE Trans. Antennas Propagat., vol. AP-23, pp. 462–469, July 1975.

[95] J. R. Copeland, W. J. Roberston, and R. G. Verstraete, “Antennafier arrays,”IEEE Trans. Antennas Propagat., vol. AP-12, pp. 227–233, Mar. 1964.

[96] H. H. Meinke, “Active antennas,” N. Z. Eng., vol. 19, pp. 697–705, Dec.1966.

[97] A. P. Anderson, W. S. Davies, M. M. Dawoud, and D. E. Galanakis, “Notes on transistor-fed active-array antennas,” IEEE Trans. Antennas Propagat., vol. AP-19, pp. 537–539, July 1971.

[98] M. M. Dawoud and A. P. Anderson, “Calculations showing the reduction in the frequency dependence of a two-element array antenna fed by microwave transistors,” IEEE Trans. Antennas Propagat., vol. AP-20, pp. 497–499, July 1972.

[99] M. M. Dawoud and A. P. Anderson, “The performance of transistor fed monopoles in active antennas,” IEEE Trans. Antennas Propagat., vol. AP-21, pp. 371–374, May 1973.

[100] M. I. Kontorovich and N. M. Lyapunova, “Active antennas,” Radio Eng. Electron. Phys., vol. 19, pp. 126–127, 1974.

[101] T. S. M. Maclean and P. A. Ramsdale, “Short active aerials for transmission,” Int. J. Electron., vol. 36, pp. 261–269, Feb. 1974.

[102] M. M. Dawoud and A. P. Anderson, “Experimental verification of the reduced frequency dependence of active receiving arrays,” IEEE Trans. Antennas Propagat., vol. AP-22, pp. 342–344, Mar. 1974.

[103] P. K. Rangole and S. S. Midha, “Short antenna with active inductance,” Electron. Lett., vol. 10, pp. 462–463, Oct. 1974.

[104] J. P. Daniel and C. Terret, “Mutual coupling between antennas-optimization of transistor parameters in active antenna design,” IEEE Trans. Antennas Propagat., vol. AP-23, pp. 513–516, July 1975.

[105] B. Grob, Basic Electronics, 6th. New York: McGraw-Hill, 1959, ch.8.

[106] J. Lin and T. Itoh, “Active integrated antennas,” IEEE Trans. Microwave Theory Tech., vol. 42, pp. 2186–2194, Dec. 1994.

[107] R. A. York and Z. B. Popovic, Active and Quasi-Optical Arrays for Solid-State Power Combining. New York: Wiley, 1997.

[108] L. Wandinger and V. Nalbandian, "Millimetre-wave power combining using quasioptical techniques," IEEE Trans. Microwave Theory Tech., vol. MTT-31, pp. 189–193, Feb. 1983.

[109] J. W. Mink, "Quasi-optical power combing of solid-state millimetre-wave sources," IEEE Trans. Microwave Theory Tech., vol.34, pp. 273–279, Feb. 1986.

[110] J. A. Navarro and K. Chang, Integrated active antennas and spatial power combining, John Wiley & Sons, Inc, New York, 1996.

[111] N. S. Cheng, T. P. Dao, M. G. Case, D. B. Rensch and R. A. York, "A 120-watt X-band spatially combined solid state amplifier, " IEEE Trans. Microwave Theory Tech., vol.47, pp. 2557–2561, 1999.

[112] J. J. Sowers, D. J. Pritchard, A. E. White, W. Kong, O. S. A. Tang, D. R. Tanner and K. Jablinskey, "A 36W V-band solid state source, " MTT-S Int. Microwave Symp Dig, Anaheim, CA, pp. 235–238, 1999.

[113] W. W. Lam, C. F. Jou, H. Z. Chen, K. S. Stolt, N. C. Luhmann and D. B. Rutledge, "Millimetre-wave diode-grid phase shifters," IEEE Trans. Microwave Theory Tech., vol. vol.36, pp. 902-907, 1988.

[114] R. R. Swisher, F. Lecuyer, I. F. F. Chiao and M. P. Delisio, "A balanced diode grid mixer," MTT-S Int. Microwave Symp. Dig, Anaheim, CA, pp. 555-558, 1999.

[115] C. F. Jou, W. W. Lam, H. Z. Chen, K. S. Stolt, N. C. Luhmann and D. B. Rutledge, "Millimetre-wave diode-grid frequency doubler," IEEE Trans. Microwave Theory Tech. vol.36, pp.1507-1504, 1988.

[116] R.N. Simons, R.Q. Lee, and T. D. Perl "Non-Planar Linearly Tapered Slot Antenna With Balanced Microstrip Feed," IEEE AP-S International Symposium, vol. 4, Chicago II, pp. 2109-2112, 1992.

[117] K. S. Yngvesson, T. L. Korzeniowski, Young-SIK Kim, E. L. Kollberg, and J. F. Johansson "The Tapered Slot Antenna – A New Integrated Element for Millimetre-Wave

Applications," IEEE Trans. Microwave Theory Tech., vol. 37, No.2, pp. 365-374, Feb. 1989.

[118] K. S. Yngvesson, D. H. Schaubert, T. L. Korzeniowski, E. L. Kollberg, T. Thungern, and J. F. Johansson "Endfire Tapered Slot Antennas on Dielectric Substrates," IEEE Trans. Antennas Propagat., vol. AP-33, pp. 1392-1399, Dec. 1985.

[119] A. Nesic, "Endfire Slot Line Antennas Excited by a Coplanar Waveguide," IEEE AP-S International Symposium, Digest, pp. 700-702, 1991.

[120] C. Wu, L. Shen, G. Y. Deng, Y. Shen and J. Litva, "Experimental Study of a Wide Band LTSA Which is Fed by an Inverted Microstrip Line (IML)," IEEE AP-S International Symposium, pp. 2328-2331,vol. 4, 1998.

[121] Z. C. Hao, W. Hong, J.X. Chen, X. P. Chen, K. Wu, "A novel feeding technique for antipodal linearly tapered Slot Antenna Array", in IEEE MTT-S Int. Microwave Symp. Dig. 2005, pp. 1641 – 1643.

[122] Z. C. Hao, "investigations on the substrate integrated waveguide technology," Ph.D. dissertation, Dept. Radio Eng., Southeast Univ., Nanjing, Oct, 2005.D. Stephens, P. R. Young, and I. D. Robertson, "W-band substrate integrated waveguide slot antenna," Electronics Letters, vol. 41, NO. 4, Feb. 2005.

[123] K. Chang and C. Sun, "Millimetre-wave power-combining techniques," IEEE Trans. Microw. Theory Tech., vol. MTT-31, no. 2, pp. 91-107, Feb, 1983.

[124] J. A. Navarro, Y. H. Shu and K. Chang. "Wideband integrated varactor-tunable active notch antennas and power combiners," IEEE MTT-S Int. Microwave Symp. Dig. vol.3, pp. 1257-1260, 1991.

[125] R.N. Simons and R.Q. Lee, "Space power amplification with active linearly tapered slot antenna array," IEEE MTT-S Int. Microwave Symp. Dig.vol.2 pp. 623- 626 June 1993.

[126] D. Deslandes and K. Wu, "Single-substrate integration technique of planar circuits and waveguide filters, " IEEE Trans Microw. Theory Tech vol. 51, pp. 593-596, 2003.

[127] P. E. Glaser, "Power from the sun; Its future," Science, vol. 162, pp.857–886, 1968.

[128] Naoki Shinohara and Hiroshi Matsumoto, “Experimental study of large rectenna array for microwave energy transmission,” IEEE Trans. Microwave Theory Tech., vol. 46, pp. 261–268, MARCH 1998.

[129] J. O. McSpadden, F. E. Little, M. B. Duke, and A. Ignatiev, “An in-space wireless energy transmission experiment,” in Proc. IECEC Energy Conversion Engineering Conf., vol. 1, Aug. 1996, pp. 468–473.

[130] W. C. Brown, “The history of power transmission by radio waves,” IEEE Trans. Microwave Theory Tech., vol. MTT-32, pp.1230–1242, Sept. 1984.

[131] W.C. Brown, “Electronic and mechanical improvement of the receiving terminal of a free-spacemicrowave power transmission system,” Raytheon Co.,Wayland,MA, Tech. Rep. PT-4964, NASAReport No. CR-135194, NASAContract No. NAS 3-19722, p. 66, Aug. 1977.

[132] T.-W. Yoo, and K. Chang, “Theoretical and experimental development of 10 and 35 GHz rectennas,” IEEE Trans. Microwave Theory Tech, vol. 40, NO. 6, pp. 1259-1266, June 1992.

[133] J.O. McSpadden, L. Fan, and K. Chang, “Design and experiments of a high-conversion-efficiency 5.8-GHz rectenna,” IEEE Trans. Microwave Theory Tech., vol. 46, pp. 2053-2060, Dec. 1998.

[134] J. O. McSpadden and K. Chang, “A dual polarized circular patch rectifying antenna at 2.45 GHz for microwave power conversion and detection,” in IEEE MTT-S Int. Microwave Symp. Dig., 1994, pp. 1749–1752.

[135] L. W. Epp, A. R. Khan, H. K. Smith, and R. P. Smith, “A compact dual-polarized 8.51-GHz rectenna for high-voltage (50 V) Actuator applications,” IEEE Trans. Microwave Theory Tech., vol. 48, pp. 111–120, Jan. 2000.

[136] J. A. Hagerty, F. B. Helmbrecht, W. H. Mccalpin, R. Zane, and Z. B. Popovic “Rceycling ambient microwave energy with broad-band rectenna arrays,” IEEE Trans. Microwave Theory Tech, vol. 52, NO. 3, pp. 1014-1024, March, 2004.

[137] B. Strassner, and K. Chang, “Highly efficient C-band circularly polarized rectifying antenna array for wireless microwave power transmission,” IEEE Trans. Microwave Theory Tech, vol. 51, NO. 6, pp. 1347-1356, June 2003.

[138] M. Ali, G. Yang, and R. Dougal, “A new circularly polarized rectenna for wireless power transmission and data communication,” IEEE Antennas Wireless Propag. Lett., vol. 4, pp. 205–208, 2005.

[139] Y.-J. Ren and K. Chang, “5.8 GHz circularly polarized dual-diode rectenna and rectenna array for microwave power transmission,” IEEE Trans. Microw. Theory Tech., vol. 54, no. 4, pp. 1495–1502, Apr. 2006.

[140] J. Heikkinen and M. Kivikoski, “Low-profile circularly polarized rectifying antenna for wireless power transmission at 5.8 GHz,” IEEE Microw. Wireless Compon. Lett., vol. 14, no. 4, pp. 162–164, Apr. 2004.

[141] B. Strassner and K. Chang, “5.8-GHz Circularly Polarized Dual-Rhombic-Loop Traveling-Wave Rectifying Antenna for Low Power-Density Wireless Power Transmission Applications,” IEEE Trans. Microw. Theory Tech., vol. 50, no. 8, pp. 1870–1876, Aug. 2003.

[142] “Amendment of Parts 2, 15 and 97 of the Commission’s Rules to Permit Use of Radio Frequencies Above 40 GHz for New Radio Applications,” Federal Communications Commission,

[143] 1995 [Online].Available: ftp://ftp.fcc.gov/pub/Bureaus/Engineering_Technology/Orders/1995/fcc95499.txt

[144] “Frequency Range 29.7 MHz to 105 GHz and Associated European Table of Frequency Allocations and Utilizations,” European Radiocommunication Commission, 1998 [Online]. Available: http://www. ero.dk

[145] P. Smulders, “Exploiting the 60 GHz band for local wireless multimedia access: Prospects and future directions,” IEEE Commun. Mag., vol. 40, no. 1, pp. 140–147, Jan. 2002.

[146] B. Bosco, R. Emrick, S. Franson, J. Holmes, and S. Rockwell, “Emerging commercial applications using the 60 GHz unlicensed band: Opportunities and challenges,” in Proc. Wireless and Microwave Technology Conf., Dec. 2006, pp. 1–4.

[147] K. Ohata et al., "Wireless 1.25 Gb/s transceiver modules utilizing multilayer co-fired ceramic technology," presented at the Int. Solid-State Circuits Conf., Feb. 7–9, 2000.

[148] K. Maruhashi et al., "Wireless uncompressed-HDTV-signal transmission system utilizing compact 60-GHz-band transmitter and receiver," in IEEE MTT-S Int. Microwave Symp. Digest, Jun. 2005, pp. 1867–1870.

[149] S. Collonge, G. Zaharia, and G. E. Zein, "Influence of human activity on the propagation characteristics of 60 GHz indoor channels," IEEE Trans. Wireless Commun., vol. 3, no. 6, pp. 2396–2406, Nov. 2004.

[150] J. Laskar et al., "Circuit and module challenges for 60 GHz Gb/s radio," in Proc. IEEE/ACES Int. Conf. on Wireless Commun. and Applied Computational Electromagnetics, Apr. 2005, pp. 447–450.

[151] R. Hardacker, "Method and System for Multiple 60 GHz System Antennae," U.S. patent 20060160489, Jul. 20, 2006.

[152] Y. Murakami et al., "A switchable multi-sector antenna for indoor wireless lan systems in the 60-GHz band," IEEE Trans. Microw. Theory Tech., vol. 46, pp. 841–843, Jun. 1998.

[153] P. F. M. Smulders et al., "Application of five-sector beam antenna for 60 GHz wireless LAN," IEEE Electron. Lett., vol. 38, no. 18, pp. 1054–1055, Aug. 2002.

[154] J. C. Liberti and T. S. Rappaport, Smart Antennas for Wireless Communications: IS-95 and Third Generation CDMA Applications. Englewood Cliffs, NJ: Prentice Hall, 1999.

[155] H. Tanaka and T. Ohira, "A single-planar integrated self-heterodyne receiver with a built-in beam-steerable array antenna for 60-GHz-band video transmission systems," in IEEE MTT-S Int. Microwave Symp. Digest, Jun. 2004, vol. 2, pp. 735–738.

[156] G. Grosskopf et al., "Maximum directivity beam-former at 60 GHz with optical feeder," IEEE Trans. Antennas Propag., vol. 1, no. 11, pp. 3040–3046, Nov. 2003.

[157] M. Bona, L. Manholm, J. P. Starski, and B. Svensson, "Low-cost compact Butler matrix for a microstrip antenna," IEEE Trans. Microw. Theory Tech., vol. 50, no. 11, pp. 2069–2075, Sep. 2002.

[158] G. Tudosie, H. Barth, and R. Vahldieck, “A compact LTCC Butler matrix realization for phased array applications,” in Proc. IEEE MTT-S Int. Microwave Symp. Dig., Jun. 2006, pp. 441–444.

[159] A.-S. Liu, H.-S. Wu, C.-K. C. Tzuang, and R.-B. Wu, “Ka-band 32-GHz planar integrated switched-beam smart antenna,” in Proc. IEEE MTT-S Int. Microwave Symp. Dig., Jun. 2005, pp. 565–568.

[160] C.-W.Wang, T.-G. Ma, and C.-F. Yang, “A new planar artificial transmission line and its applications to a miniaturized Butler matrix,” IEEE Trans. Microw. Theory Tech., vol. 55, no. 12, pp. 2792–2801, Dec. 2007.

[161] M. Ando, and J. Hirokawa, “High-gain and high-efficiency single-layer slotted waveguide array in 60GHz band,” in Proc. 11th Int. Conf. Antennas Propag., Edinburgh, UK, 1997, vol.1, pp: 464-468.

[162] Y. P. Zhang, M. Sun, and L. H. Guo, “On-chip antennas for 60-GHz radios in silicon technology," IEEE Trans. Electron Devices, vol. 52, pp. 1664-1668, July 2005.

[163] S. R. Rengarajan, M. S. Zawadzki, and R. E. Hodges, “Design, analysis, and development of a large Ka-band slot array for digital beam-forming application,” IEEE Trans. Antennas Propagat., vol.57, no.10, pp. 3103-3109, Oct. 2009.

[164] M. Ando, and J. Hirokawa, “System integration of planar slot array antennas for mmWave wireless applications,” in Proc. XXVIIIth URSI, New Delhi, India, 2005.

[165] J. Hirokawa and M. Ando, “Millimetre-Wave Post-Wall Waveguide Slot Array Antennas,” in IEEE AP-S Int. Antennas Propagat. Symp, pp. 4381-4384, June 2007.

[166] L. Yan, W. Hong, G. Hua, J. Chen, K. Wu and T. J. Cui, “Simulation and Experiment on SIW Slot Array Antennas,” IEEE Microw. Wire. Comp. Lett., vol. 14, no. 9, pp. 446-448, 2004.

[167] W. Hong, B. Liu, G.Q. Luo, Q.H. Lai, J.F. Xu, Z.C. Hao, F.F. He and X.X. Yin, “Integrated microwave and millimetre wave antennas based on SIW and HMSIW technology,” presented in International Workshop on Antenna Technology: Small and Smart Antennas Metamaterials and Applications, pp. 69-72, March 2007.

[168] P. Chen, W. Hong, Z. Kuai, and J. Xu, "A double layer substrate integrated waveguide blass matrix for beamforming applications," IEEE Microw. Wire. Comp. Lett., vol. 19, no. 6, pp. 374-376, June 2009.

[169] S. Cheng, H. Yousef and H. Kratz, "79GHz Slot Antennas Based on Substrate Integrated Waveguides (SIW) in a Flexible Printed Circuit Board," IEEE Trans. Antennas Propagat., vol. 57, no. 1, pp. 64-71, 2009.

[170] X.-P. Chen "60 GHz SIW antenna" IEEE Trans. Antennas Propagat., vol. 57, no. 1, pp. 64-71, 2009.

[171] X.-P. Chen, L. Li, and K. Wu, "Multi-Antenna System Based on Substrate Integrated Waveguide for Ka-Band Traffic-Monitoring Radar Applications," in Proc. 39th European Microw. Conf. Symp., Roma, Italy, 2009, pp. 417-420.

[172] R. J. Stegen, "Slot radiators and arrays at X-band," IEEE Trans. Antennas Propagat., vol. AP-1, pp. 62–64, Feb. 1952.

[173] R. S. Elliott, "An improved design procedure for small arrays of shunt slots," IEEE Trans. Antennas Propagat., vol. AP-31, pp. 48–53, Jan. 1983.

[174] R. S. Elliott, Antenna Theory and Design. New Jersey: John Wiley & Sons, 2003, ch. 8.

[175] J. Butler and R. Lowe, "Beam-forming matrix simplifies design of electrically scanned antennas," Electron. Design, no. 9, pp. 170–173, Apr.1961.

[176] B. Pattan, "The versatile Butler matrix," Microw. J., vol. 47, no. 11, pp, 126–138, Nov. 2004.

[177] D. Parker and C. Zimmermann, "Phased arrays—Part II: Implementations, applications, and future trends," IEEE Trans. Microw. Theory Tech., vol. 50, no. 3, pp. 688–698, Mar. 2002.

[178] C. A. Balanis and P. I. Ioannides, Introduction to Smart Antennas.San Rafael, CA: Morgan & Claypool, 2007.

[179] M. Barba, J. E. Page, J. A. Encinar, and J. R. Montejo-Garai, "A switchable multiple beam antenna for GSM-UMTS base stations in planar technology," IEEE Trans. Antenna Propag., vol. 54, no. 11, pp. 3087–3094, Nov. 2006.

[180] A. Grau, J. Romeu, S. Blanch, L. Jofre, and F. D. Flaviis, “Optimization of linear multielement antennas for selection combining by means of a Butler matrix in different MIMO environments,” IEEE Trans. Antenna Propag., vol. 54, no. 11, pp. 3251–3263, Nov. 2006.

[181] P. Chen, W. Hong, Z. Kuai, J. Xu, H. Wang, J. Chen, H. Tang, J. Zhou, and K. Wu, “A multibeam antenna based on substrate integrated waveguide technology for MIMO wireless communications,” IEEE Trans. Antenna Propag., vol. 57, no.6, pp. 1813–1821, Jun. 2009.

[182] Chih-Jung Chen, and Tah-Hsiung Chu, “Design of a 60-GHz Substrate Integrated Waveguide Butler Matrix—A Systematic Approach“IEEE Trans. Microw. Theory Tech., vol. 58, no. 7, pp. 2792–2801, Dec. 2007.

[183] S. Yamamoto, J. Hirokawa, and M. Ando, “A half-sized post-wall short-slot directional coupler with hollow rectangular holes in a dielectric ubstrate,” IEICE Trans. Electron., vol. 88, no. 7, pp. 1387–1394, Jul. 2005.

[184] Yu Jian Cheng, Wei Hong, and Ke Wu,, “Broadband Self-Compensating Phase Shifter Combining Delay Line and Equal-Length Unequal-Width Phaser “IEEE Trans. Microw. Theory Tech., vol. 58, no1, pp. 2792–2801, Jan. 2010.

[185] Z.-C. Hao, W. Hong, J.-X. Chen, X.-P. Chen, and K. Wu, “A novel feeding technique for antipodal linearly tapered slot antenna array,” Proc. IEEE MTT-S Int. Microw. Symp. Dig., Jun. 12–17, 2005, pp. 1641–1643.

[186] X.-P. Chen, and K. Wu, “Low-loss ultra-wideband transition between conductor-backed coplanar waveguide and substrate integrated waveguide,” in IEEE MTT-S Int. Microwave Symp., June 7-12, Boston, MA, 2009.

APPENDIX 1 – PUBLICATIONS RESULTING FROM THIS RESEARCH WORK

Published papers:

[1] FanFan He, Ke Wu, Wei Hong, Xiaoping Chen and Liang Han, "A Planar Magic-T Structure Using Substrate Integrated Circuits Concept and Its Mixer Applications," IEEE Transactions on Microwave Theory and Techniques, vol.59, no.1, pp.72-79, Jan. 2011.

[2] FanFan He, Ke Wu, Wei Hong, Xiaoping Chen and Liang Han, "A Low Phase Noise VCO Using a Novel Tunable Substrate Integrated Waveguide Resonator" IEEE Transactions on Microwave Theory and Techniques, vol.58, no.12, pp.3452-3458, Dec. 2010.

[3] Fanfan He, Ke Wu, Xiao-Ping Chen, Liang Han and Wei Hong, "A Planar Magic-T Structure Using Substrate Integrated Circuits Concept," 2010 IEEE MTT-S International Microwave Symposium, Anaheim, California, USA, 23-28 May 2010, pp. 720-724.

[4] Fanfan He, Wei Hong, Ke Wu, Jixin Chen, Hongbing Zhu and Hongjun Tang, "Substrate Integrated Waveguide Sub-harmonically Pumped Up-converter Antenna for Spatial Power Combining," IET Proceedings Microwaves, Antennas and Propagation, vol.8, no.3, pp.1172-1178, 2009.

[5] Fanfan He, Ke Wu, and Wei Hong, "Antipodal Linearly Tapered Slot Antenna System Using Substrate Parallel Plate Waveguide Feeding Structure," in proc. of the 39th European Wireless Technology Conference, Rome, Italy, Sep. 28-29, 2009, pp. 88-91.

[6] Fanfan He, Xiao-Ping Chen, Ke Wu, and Wei Hong, "Tunable reflective integrated substrate waveguide cavity resonator," in Proc. Asia-Pacific Microwave Conference, Singapore, Dec. 7-10, 2009, pp.119-123.

[7] Fanfan He, Ke Wu, Wei Hong, Hongjun Tang, Hongbing Zhu and Jixin Chen, "Suppression of Second and Third Harmonics Using lambda/4 Low-Impedance Substrate Integrated Waveguide Bias Line in Power Amplifier", IEEE Microwave and Wireless Components Letters, vol.18, no.7, pp.479-481, 2008.

[8] Fanfan He, Ke Wu, and Wei Hong, "A Planar Magic-T Using Substrate Integrated Circuits Concept," IEEE Microwave and Wireless Components Letters, vol.18, no.6, pp386-388, 2008.

[9] Fanfan He, Wei Hong, Ke Wu Jixin Chen and Hongjun Tang, "Substrate Integrated Waveguide rectenna array using antipodal linearly tapered slot antenna," Sciencepaper online (in Chinese), vol.3, no.1, pp.59-64, Jan. 2008.

[10] Fanfan He, Ke Wu, and Wei Hong, "A Wideband Bandpass Filter by Integrating a Section of High Pass HMSIW with a Microstrip Lowpass Filter," Global Symposium on Millimetre Waves, Nanjing, China, Apr.21-24, 2008, pp 282-284.

[11] Xiaoping-Chen, Ke Wu, Liang Han, and Fanfan He, "Low-Cost High Gain Planar Antenna Array for 60-GHz Band Applications," IEEE Transactions on Antennas and Propagation, vol.58, no.6, pp.2126-2129, June 2010.

[12] Liang Han, Ke Wu, Xao-Ping Chen, and Fanfan He, "Accurate analysis of finite periodic substrate integrated waveguide structures and its applications," 2010 IEEE MTT-S International Microwave Symposium, Anaheim, California, USA, 23-28 May 2010, pp. 1-4.

[13] H. B. Zhu, W. Hong, TIAN Ling, TANG Hong-Jun, CHEN Ji-Xin, HE Fan-Fan. "A Ka-band Broadband Power Amplifier Design Based on Flexible Substrate Integrated Waveguide Technology". Journal of Millimetre Wave and Infrared (in Chinese), vol.29, no.3, pp.180-184, 2010.

[14] Wei Hong, Hongbing Zhu, Hongjun Tang, Jixin Chen, Ling Tian, and Fanfan He (Invited Paper), "Recent Research Advances in Substrate Integrated Power Combining/Amplifying Technologies," 2010 Global Symposium on Millimetre Waves (GSMM'2010), Korea, April 14-16, 2010.

[15] Zhu Hong-bing, Hong Wei, Tian Ling, Fanfan He, Chen ji-xin and Tang Hong-jun , "Multiway Power Divider/Combiner with Multilayer Substrate Integrated Waveguide Technology for Developing Broadband Power Combining Amplifiers," Journal of Microwavs (in Chinese) , vol.24, no.6, pp.55-59, 2008.

[16] Hongbing Zhu, Wei Hong, Ling Tian, Fanfan He, and Bing Liu, “Experimental Investigations on Substrate Integrated Flexible Waveguide,” in Proc. Asia-Pacific Microwave Conference, Bangkok, Thailand, Dec. 11-14, 2007, pp.1-4.

[17] Wei Hong, Bing Liu, G.Q. Luo, J.F. Xu, Z.C. Hao, F.F. He, and X.X. Yin, “Integrated Microwave and Millimetre Wave Antennas Based on SIW and HMSIW Technology,” International Workshop on Antennas Technology, Cambridge, March 21-23, 2007, pp.69.

[18] L. Han, K. Wu, X.-P. Chen, and F. He, "Packaged microstrip line diplexer," Accepted by Microwave Journal.

Submitted papers:

[1] Fanfan He, Ke Wu, Wei Hong and Xiao-Ping Chen “Realization of a Low Cost 60 GHz Smart Antenna Receiver Sub-System Based on Substrate Integrated Waveguide Technology” submitted to IEEE Transactions on Microwave Theory and Techniques.

[2] Fanfan He, Ke Wu, Wei Hong, Liang Han and Xiao-Ping Chen “Half mode substrate integrated waveguide tunable resonator” submitted to EUMC 2011.